⑫

SYSTEMS, SCIENCE AND SOFTWARE

VSC-TR-80-2

SSS-R-80-4569

THE CONTRIBUTION OF TWO-DIMENSIONAL SOURCE EFFECTS
TO THE FAR-FIELD SEISMIC SIGNATURES OF
UNDERGROUND NUCLEAR EXPLOSIONS

T. C. BACHE
T. G. BARKER
N. RIMER
J. T. CHERRY

TOPICAL REPORT

JULY 1980

P. O. BOX 1620 LA JOLLA CALIFORNIA 92038 TELEPHONE (714) 453 0060

REPORT DOCUMENTATION PAGE		READ INSTRUCTIONS BEFORE COMPLETING FORM
1. REPORT NUMBER VSC-TR-80-2	2. GOVT ACCESSION NO. AD-A123664	3. RECIPIENT'S CATALOG NUMBER
4. TITLE (and Subtitle) THE CONTRIBUTION OF TWO-DIMENSIONAL SOURCE EFFECTS TO THE FAR-FIELD SEISMIC SIGNATURES OF UNDERGROUND NUCLEAR EXPLOSIONS		5. TYPE OF REPORT & PERIOD COVERED Topical Report
		6. PERFORMING ORG. REPORT NUMBER SSS-R-80-4569
7. AUTHOR(s) T. C. Bache, T. Barker, N. Rimer, J. T. Cherry		8. CONTRACT OR GRANT NUMBER(s) F08606-79-C-0008
9. PERFORMING ORGANIZATION NAME AND ADDRESS Systems, Science and Software P.O. Box 1620 La Jolla, CA 92038		10. PROGRAM ELEMENT. PROJECT. TASK AREA & WORK UNIT NUMBERS Program Code No. 6H169 ARPA Order No. 2551
11. CONTROLLING OFFICE NAME AND ADDRESS		12. REPORT DATE JULY 1980
		13. NUMBER OF PAGES 200
14. MONITORING AGENCY NAME & ADDRESS(If different from Controlling Office) VELA Seismological Center 312 Montgomery Street Alexandria, Virginia 22314		15. SECURITY CLASS. (of this report) Unclassified
		15a. DECLASSIFICATION. DOWNGRADING SCHEDULE

16. DISTRIBUTION STATEMENT (of this Report)

Approved for Public Release, Distribution Unlimited.

17. DISTRIBUTION STATEMENT (of the abstract entered in Block 20, if different from Report)

18. SUPPLEMENTARY NOTES

19. KEY WORDS (Continue on reverse side if necessary and identify by block number)

Nuclear monitoring; Seismic source theory; Under nuclear explosions; Synthetic seismograms; Seismic yield determination

20. ABSTRACT (Continue on reverse side if necessary and identify by block number)

Two-dimensional calculations of underground explosions are able to include free surface interaction effects and the depth dependence of overburden pressure and material properties, as well as the complex constitutive models for geologic materials developed in one-dimensional (spherically symmetric) studies. Eleven axisymmetric calculations of explosions in granite are analyzed in this study to determine the two-dimensional effects on the far-field body and surface waves and the magnitudes m_b and M_s. Seven of these are hypothetical 150 KT

explosions at depths from 159 to 1000 meters calculated by Applied Theory, Inc. (ATI). These show depth effects that are different, though not strikingly so, from those calculated with one-dimensional source models. The other four calculations were done by Systems, Science and Software (S-Cubed). The first was for a specific event (PILEDRIVER), and the depth and yield were varied for the other three. The near- and far-field data for PILEDRIVER were matched rather well, except that the spallation was too large in the calculation.

Synthetic body and surface waves from the S-Cubed two-dimensional sources are compared to those from analogous one-dimensional sources to isolate the two-dimensional effects. These are not important for the deep events or for the first arriving P wave from the shallow events. They do strongly enhance the surface wave amplitudes (by a factor of two or three) for the two shallow calculations, including that for PILEDRIVER, and reduce the m_b by 0.1 - 0.2 units. The m_b effects can clearly be attributed to spallation and the accompanying reduction of the pP amplitude, which are overpredicted by the calculations. The M_s enhancement must be due to the same causes, though they are not easily isolated.

TABLE OF CONTENTS

TABLE OF CONTENTS (continued)

TABLE OF CONTENTS (continued)

PER HP

Codes
and/or
Dist   Spal

A

LIST OF FIGURES

LIST OF FIGURES (continued)

LIST OF FIGURES (continued)

LIST OF FIGURES (continued0

LIST OF FIGURES (continued)

I. INTRODUCTION AND SUMMARY

1.1 BACKGROUND

To successfully monitor a test ban treaty prohibiting or limiting underground nuclear explosions, it is necessary to understand the seismic signatures of these events. An important part of the research effort to improve this understanding has been the development and application of deterministic methods to compute the seismic wave signatures of nuclear explosions. In nearly all of this work the source is assumed to be spherically symmetric and the earth is assumed to be plane-layered. Theoretical seismograms can then be computed with widely available methods and compared to observations. This procedure has been quite successful and most of the important controlling parameters have been identified and their effects have been quantified to some degree. However, many important issues remain unresolved.

Most of the important questions that remain regarding the generation of seismic waves by underground explosions are associated with multi-dimensional effects. For example, there is not yet a clear understanding of the effect on the seismic radiation of nearby interfaces, the free surface (allowing spallation), the overburden pressure, nonhydrostatic prestress, and zones of weakness in the near source environment. The one-dimensional calculations now incorporate detailed constitutive models that include realistic models for pore collapse, effective stress, yielding, and cracking due to shear and tension failure. These constitutive models, have been generalized to two-dimensions for the axisymmetric finite difference source calculations analyzed in this report. While they do not include all the multi-dimensional effects we have listed, they do include some of the most important, and so represent a significant step forward in the development of realistic theoretical simulations of the seismic waves from underground explosions.

1

1.2 AXISYMMETRIC CALCULATIONS OF NUCLEAR EXPLOSIONS

In this report we present a detailed analysis of the seismic waves from eleven two-dimensional finite difference calculations of underground nuclear explosions in granite. Seven of these calculations were done by J. Trulio and N. Perl of Applied Theory, Inc. (ATI) and four by N. Rimer and J. T. Cherry of Systems, Science and Software (S-Cubed). They share the same axisymmetric geometry, though the details are different.

The two-dimensional, axisymmetric explosion calculations include the presence of a free surface, the dependence of overburden pressure on depth and, for the S-Cubed calculations, some dependence of material properties on depth. These are probably the most important higher order corrections to the one-dimensional models. The depth-dependence of overburden pressure is a property of all test sites. Further, our understanding of geologic structures is normally based on plane-layered models. Therefore, axisymmetry is a natural geometry, and specification of the geometry and material properties in two-dimensions is more straightforward than characterizing the entire near-source environment by a homogeneous material.

The most important two-dimensional effects are associated with the nonlinear interaction of the stress waves with the free surface. Surface spallation is an obvious, even dominant, phenomenon observed in the near-field, yet it has never been included in seismic wave propagation studies in a very satisfactory way. Perhaps more important, there is ample evidence that the free surface phase pP is more complex than predicted by elastic theory with spherically symmetric sources, but, again, this remains mostly in the realm of speculation. With the axisymmetric calculations, we are able to study these important effects.

The objectives of the parameter variations in the ATI and S-Cubed suites of calculations are somewhat different. The ATI calculations were all done at the same yield, 150 kt, in a hypothetical granite halfspace. Only the depth was varied, from 159

2

to 1000 meters. The philosophy of the S-Cubed calculations was to begin by modeling a specific event, PILEDRIVER, at the Nevada Test Site. The constitutive model and source geology (three layers) were chosen for this event. The computed and observed ground motions were compared at some twenty-five near-field gauge locations. The comparison was quite good, except that the calculation overpredicted the amount of cracking (spallation) within 300 meters of ground zero. This turns out to be important when comparing synthetic and observed far-field seismograms.

The other three S-Cubed source calculations were the same, except the depth and yield were varied from the values appropriate for PILEDRIVER. The four calculations were as follows:

Depth (Meters)	Yield (Kt)
463	60 (PILEDRIVER)
1000	150
1000	20
400	20

1.3   OUTLINE OF THE ANALYSIS

The analyses of the seven ATI and four S-Cubed calculations are described separately, but follow parallel lines. First, we describe the near-field ground motions predicted by the calculations in some detail. Then we present theoretical seismograms for these calculations and analyze their implications. This outline is apparent in the section headings listed below:

Section II: ATI Granite Calculations

Section III: M_s and m_b Estimates for ATI Granite Calculations

Section IV: S-Cubed Granite Calculations

Section V: M_s and m_b Estimates for S-Cubed Granite Calculations

3

Section VI: Comparison of Predicted and Observed
Seismograms for PILEDRIVER

Section VII: Comparative Analysis of ATI and
S-Cubed Granite Calculations.

A key step in this study is the linkage between the near-field ground motions computed by the finite difference programs and the analytical techniques used to propagate seismic waves in realistic earth models. A rigorous method for accomplishing this linkage is described in Appendix A, "Synthetic Seismograms from Complex Source Calculations." The details and examples presented in this appendix are mostly for the calculation of the normal mode (Rayleigh waves) displacements in a plane-layered earth model, but ray theory methods for propagating body waves can be used within the same theoretical framework.

To compute synthetic seismograms at large distances for the finite difference source calculations, it is necessary to monitor the tractions and displacements on some (hypothetical) surface which entirely encloses the region of nonlinear material response. Our discussion of the source calculations in Sections II and IV is concerned with the characteristics of the monitored ground motions on this elastic surface.

An important constraint on the numerical results is the requirement, based on conservation of momentum, that the total downward force and impulse (on the surface enclosing the source region) vanish at late time. It turns out (Appendix A) that the inevitable numerical errors that cause deviation from this requirement can dominate the solution at long periods. Therefore, a major theme in Sections II and IV is the application of a "correction" to adjust the computed vertical force and impulse to zero at the last time step.

The synthetic seismogram results are presented in Sections III and V. The vertical force "correction" is also an issue in these sections, because it would be unsatisfactory for an ad hoc correction, which is what we apply, to dominate the answer. Our

4

conclusion is that the vertical force terms, after correction, do not play an important role. All of the solution checks we are able to make indicate that the body and surface wave synthetic seismograms accurately represent the seismic waves generated by these theoretical sources.

The synthetic seismogram analyses in Sections III and V are focussed on comparing the seismic waves from the two-dimensional sources with those from analogous one-dimensional, reduced displacement potential (RDP) sources. For the S-Cubed calculations, we are able to compare to the RDP source computed with the same constitutive model in spherical symmetry. No such one-dimensional calculation was available for the ATI granite, so we compare to the RDP predicted by the semi-empirical model of Mueller and Murphy (1971).

Most of the calculations are for hypothetical events, so direct comparison with observed seismograms is only possible for the PILEDRIVER calculation done by S-Cubed. This comparison is made in Section VI. Finally, in Section VII, the results of all eleven calculations are plotted together for direct comparison.

1.4 CONCLUSIONS

This study is primarily an investigation of the influence of burial depth on the seismic signals from underground explosions. For the most part, the results are interesting, but not terribly exciting, because they are pretty much in accord with our expectations. The key exception is the surface wave results for the S-Cubed calculations.

The most important result of this study is that the S-Cubed calculations show M_s to be a strong function of depth. The shallow S-Cubed calculations have surface wave amplitudes that are a factor of two or three larger than those from a comparable one-dimensional source calculation. This effect is probably exaggerated because the free surface interaction effects are too large in the S-Cubed calculations, but would remain important even if the near surface material were strengthened. On the other hand, the ATI

5

calculations show no strong dependence of M_s on depth, even though the shallow ATI sources cratered. We do not know why the two sets of calculations give such different results.

The important conclusions are listed at the end of several sections of the report. Summaries for the ATI and S-Cubed calculations are given separately in Sections 3.7 and 5.10. Our conclusions about the comparison of synthetic and observed seismograms are listed in Section 6.4, and all of Section VII should be read as a summary.

The main results are listed below:

ATI Calculations

- Neither m_b nor M_s are strongly dependent on depth. The most effect was on M_s at shallow depths.

- Compared to the Mueller/Murphy RDP source, the depth dependence in both amplitude and corner frequency is less for the ATI sources.

- The pP phase appears to be smaller than expected from elastic theory.

S-Cubed Calculations

- Two-dimensional effects are not very important for the two deep explosions (20 kt and 150 kt at 1000 meters). Both m_b and M_s are little different from the values estimated from an RDP source computed with the same constitutive model at the same depth.* This is true even though considerable cracking and spallation occur in the two-dimensional calculations.

---

* These results are essentially tests of the entire computational procedure. It is gratifying that these two very different and complex procedures arrive at the same results.

6

- For body waves the first arriving P wave is essentially the same for one- and two-dimensional sources.*

- The two-dimensional effects enhance the surface wave amplitudes for the shallow events (60 kt at 463 meters and 20 kt at 400 meters) by a factor of two or three. We must qualify this by pointing out that these shallow calculations have very strong surface interaction effects. Comparison with PILEDRIVER data indicates that the free surface interaction is overpredicted, at least for that event. Less free surface interaction would presumably give less enhancement of the surface wave amplitudes.

- For the shallow events, the m_b^c is different than predicted with an RDP source, though by less than 0.2 units.

- Analysis of the spectra show that in no case is pP a spectral shadow of P, as it is for an RDP source and elastic propagation.

- Phases that seem to be associated with spall closure can be seen on the shallow source body wave records. However, they are not easily associated with identifiable crack closure patterns in the source calculation.

The comparison of observed and calculated body and surface waves for PILEDRIVER in Section VI leads to the conclusion that the two are in rather good agreement. This conclusion is subject to the qualifications one often faces in this kind of comparison. For the surface waves, it is the need to account for the non-axisymmetric

---

* See footnote on previous page.

7

component, usually attributed to tectonic stress release. Adding a recent estimate for this component by Rivers and von Seggern (1979) to our solution, we get good agreement with the data.

For body waves the comparison is complicated by the apparent presence of strong azimuthal effects in the radiated short period energy (Hadley and Hart, 1979). However, our conclusion is that the computed PILEDRIVER source (in one- or two-dimensions) has about the right direct P amplitude. However, the two-dimensional source calculation appears to include too much non-linear interaction with the free surface. The later portion of the P waveform does not match the data, apparently because pP is too greatly suppressed and because the seismic energy from spall closure is too large or is timed incorrectly. This "overprediction" of surface interaction effects is expected since comparison of theoretical and observed near-field motions and plots of the cracking near the source indicate that there was too much spallation in the calculation.

All the theoretical M_s and m_b values are plotted together in Section VII. They are shown versus source depth and versus yield, including the observed values for HARDHAT, SHOAL and PILE-DRIVER. The most dramatic difference between the ATI and S-Cubed calculations is the strong dependence of M_s on depth predicted by S-Cubed, but not by ATI sources. This must be a reflection of the different constitutive models used.

The constitutive models used by S-Cubed (in spherically symmetric source calculations) lead to RDP source functions that are strongly peaked, with the value near 1 Hz a factor of five or more larger than the value at long periods. The peaking is due to the incorporation of an effective stress law and the choice of unconfined compressive strength (0.75 kbar), based on laboratory data for fractured granite and results of comparison with near-field ground motion observations (Rimer, personal communication).

While we do not have RDP source functions for the ATI granite, comparison of M_s and m_b for the ATI two-dimensional calculations indicates that the RDP peaking is probably less than a factor of

3

two. Due primarily to this difference, the m_b for the S-Cubed calculations is about 0.5 units higher than that for ATI calculations of the same yield. The ATI M_s values fall between those for the shallow and deep S-Cubed calculations.

1.5   CONTRIBUTORS

This report was written by Dr. Thomas C. Bache, who directed this project, with important technical contributions from the listed authors and several others on the technical staff at S-Cubed, ATI and Pacific Sierra Research, Inc. (PSR). Developing and programming the techniques for linking synthetic seismogram methods with the finite difference calculations required the collaboration of many members of the S-Cubed staff. Much of the basic theoretical development was done by Dr. Steven M. Day and Mr. Henry J. Swanger. Dr. Terrance G. Barker worked out the details and programmed the body wave method, while Dr. Akilesh Maewal did much the same for the surface waves. All the body wave calculations in the report were done by Dr. Barker, while Dr. Bache did the surface wave calculations. Mr. Bruce Mason did much of the computer interfacing for these calculations.

Interpretation of the output of the source calculations required the assistance of Drs. J. T. Cherry and N. Rimer of S-Cubed and Dr. J. Trulio and Mr. N. Perl of ATI. Mr. Lee Woodie of PSR has also been studying the ATI calculations and made some helpful suggestions, especially about the vertical force and impulse corrections. Dr. David Hadley of Sierra Geophysics kindly gave us a copy of his plot of the WWSSN observations of PILEDRIVER.

A portion of the analysis of the ATI calculations was done under subcontract to PSR. This support, which was arranged and monitored by Dr. Frank Thomas of PSR is gratefully acknowledged.

Preparation of the manuscript was mainly done by Ms. Susan Glatz. Ms. Darlene Roddy and Ms. Elyse Tessary also contributed, especially in the layout of the figures. The figure drafting was done by Ms. Carolyn Hunt.

9

II. ATI GRANITE CALCULATIONS

2.1 INTRODUCTION

We will subsequently be analyzing the output of seven source calculations done by J. Trulio and N. Perl of Applied Theory, Inc. The purpose of this analysis is to determine the body and surface wave magnitudes (m_b and M_s) associated with the simulated seismic events, and this is done with the method described in Appendix A.

Our intention in this section is to describe the characteristics of the source calculations and the computed near-source ground motions. An important constraint on the numerical results is the requirement, based on conservation of linear momentum, that the total downward force and impulse vanish at late-time. Due to numerical errors that are inevitable in source calculations of this kind, this requirement is not satisfied exactly. The data are therefore "corrected" by imposing an additional time step that causes the force and impulse to vanish. This correction is described in Section 2.4. It is the "corrected" data that are used for the synthetic seismogram calculations described in Section III.

2.2 SOURCE DESCRIPTION

The seven ATI calculations are for 150 KT explosions in a granite halfspace characterized by

P wave velocity:	$\alpha =$	4.403 km/sec,
S wave velocity:	$\beta =$	2.542 km/sec,
Density	$\rho =$	2.661 gm/cm^3.

This material is intended to represent NTS granite. A similar series of calculations is described by Perl, et al. (1979) and Perl and Trulio (1979). The computational method and constitutive model for the NTS granite is described in these reports.

The seven calculations were done in a cylindrical (axisymmetric) geometry and differ only in the source depth. These are:

10

ATI Identifier	Depth (m)	Number of Monitoring Stations
4701	159.4	64
4702	207.2	66
4703	253.0	66
5127	398.9	66
5128	531.3	64
5129	797.0	64
5130	1000.0	63

All calculations were carried out to 2.5 seconds.

The source data provided to S-Cubed were the time histories of the "excess" tractions (i.e., tractions relative to their initial equilibrium values), T_r^M, T_z^M (r,z,t), and velocities, $\dot{u}_z^M$, $\dot{u}_r^M$ (r,z,t), at stations on a surface surrounding the region of inelastic material response. The number of monitoring stations for each calculation is listed above. The position of these stations for a typical calculation is shown in Figure 1.

Also provided to S-Cubed were the area of the surface upon which the tractions were assumed to act and the components of the unit vector (n_r, n_z) normal to that area. All of these quantities are necessary for calculating seismograms in the far-field, as described in Section III and Appendix A.

In Figure 2 we show the time histories of the monitored quantities at several positions on the monitoring surface for ATI Number 5127. The motions are not entirely stopped at 2.5 seconds when the calculations were terminated. However, they are small at this time and the decision to terminate the calculation seems reasonable.

In the Appendix A, Section A.5, we discuss the behavior of the surface wave solution for periods that are large compared to duration of the source calculation. The most important data for

11
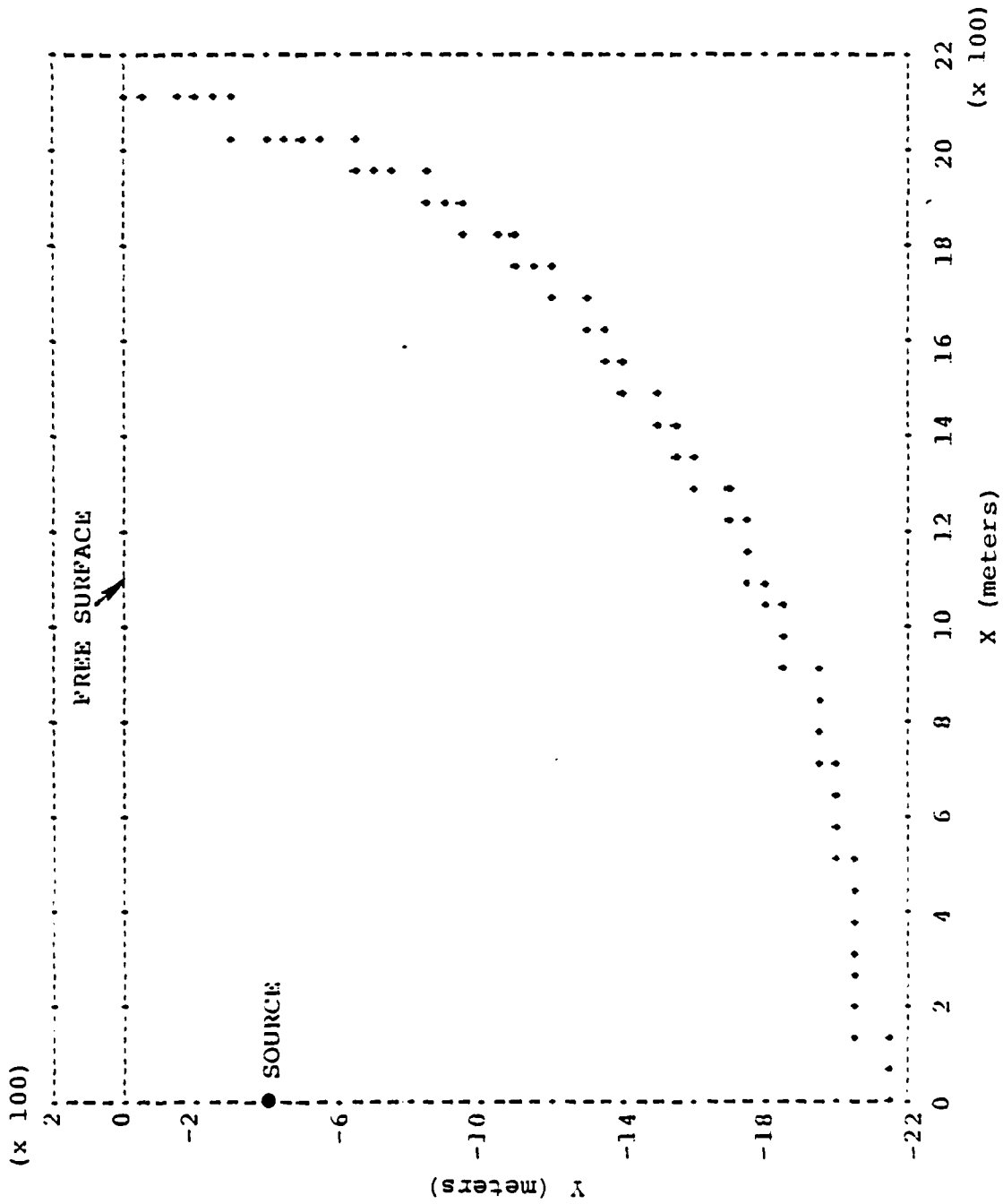
Figure 1. The monitoring positions for ATI #5127.

12
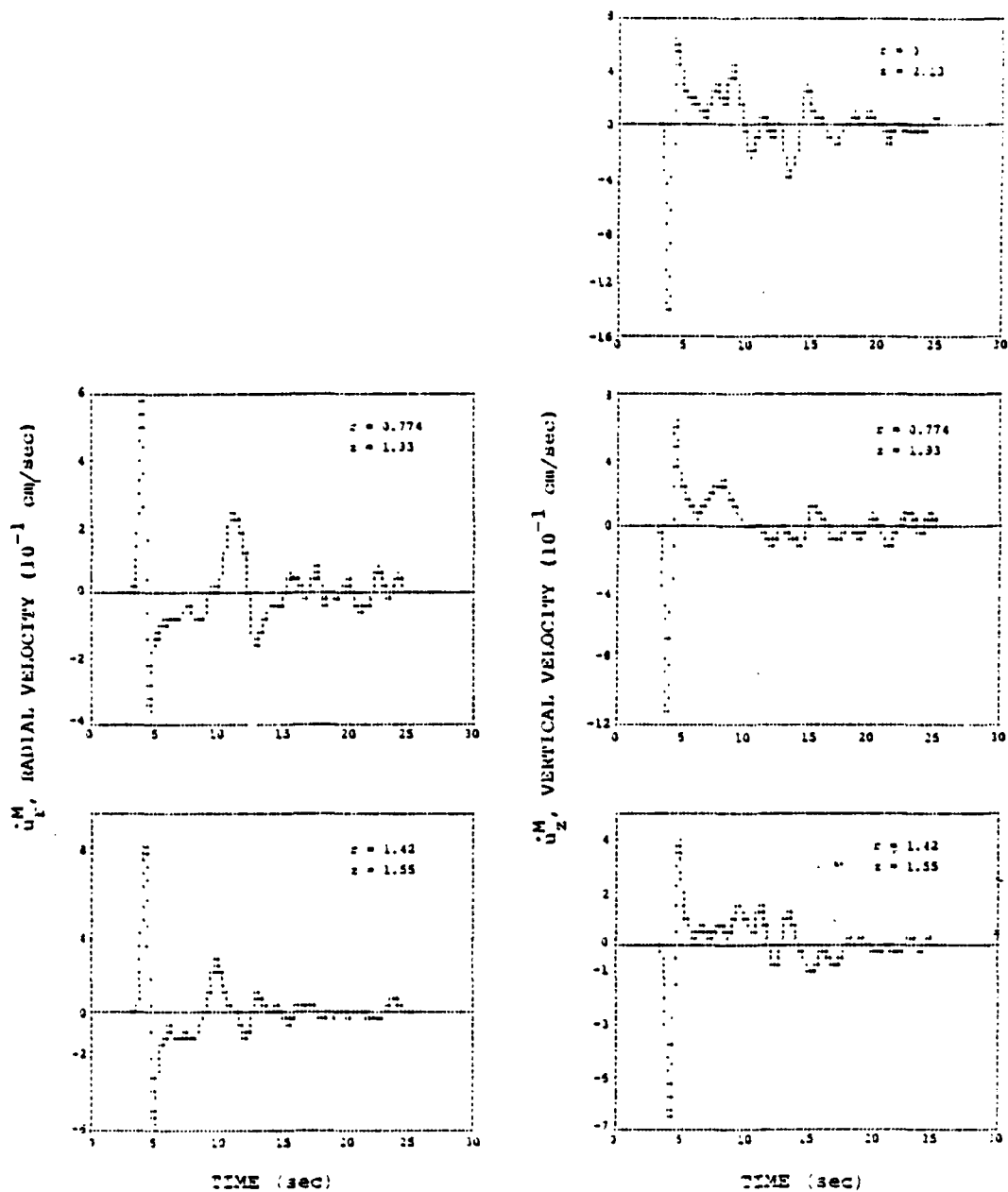
Figure 2. The monitored velocities and tractions are plotted at selected positions (given in terms of their coordinates in kilometers) for ATI #5127. As will be explained in Section 2.4, the ATI calculations have positive z up and minus signs in the stress-strain relation. To be consistent with the theory of Appendix A, it is necessary to change the signs of the vertical velocity and radial traction. We also show the values of the tractions at an imposed final time step.

13

Figure 2. (Continued)

14
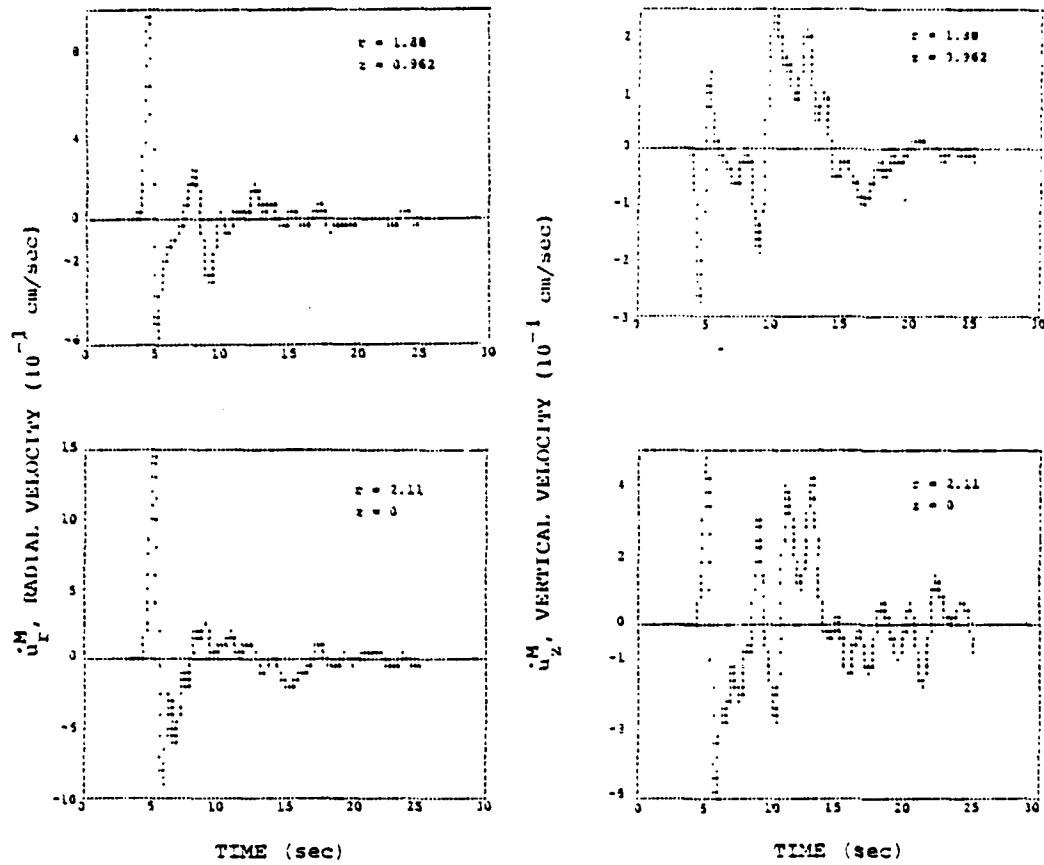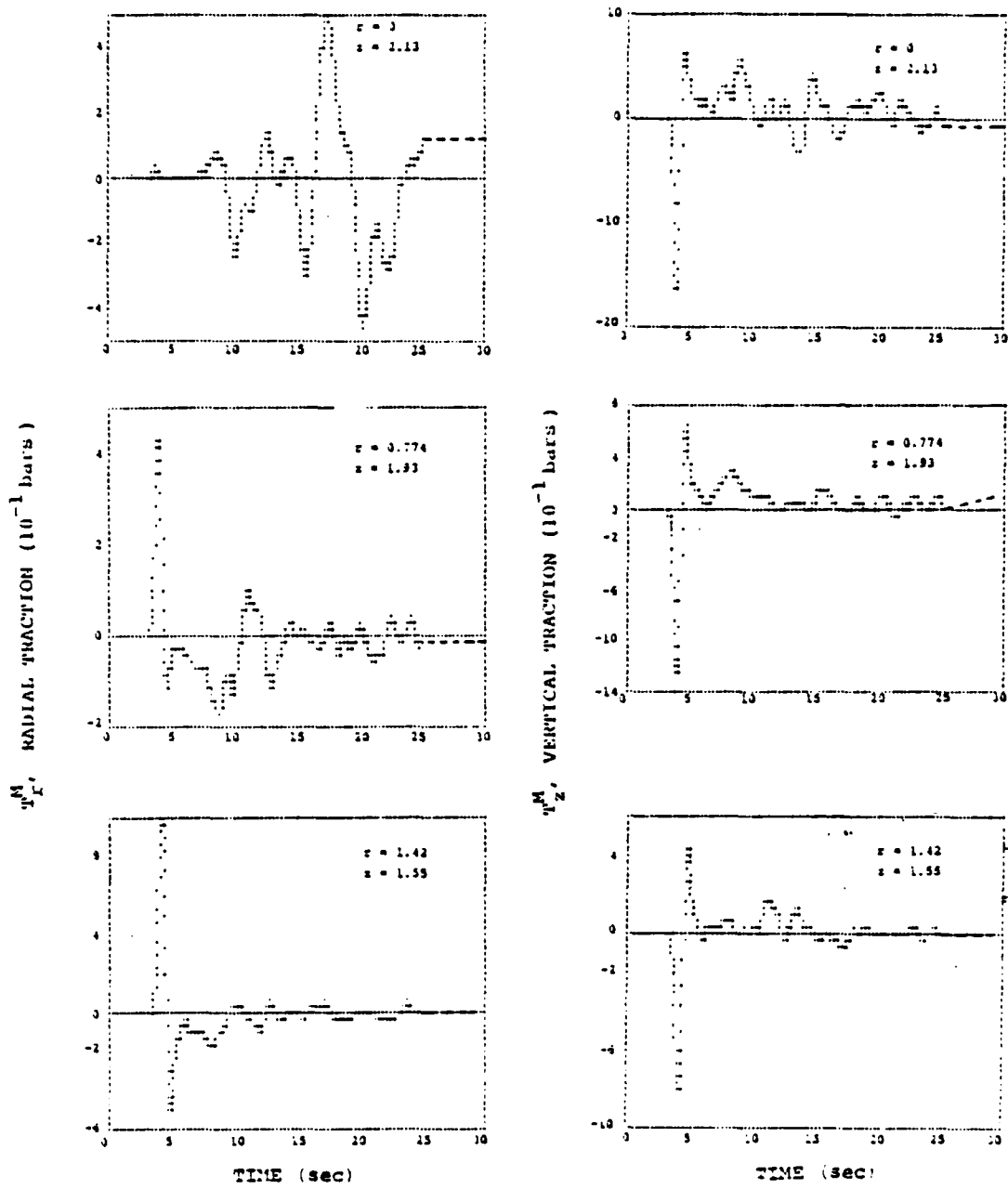
Figure 2. (Continued)

Figure 2. (Continued)

16
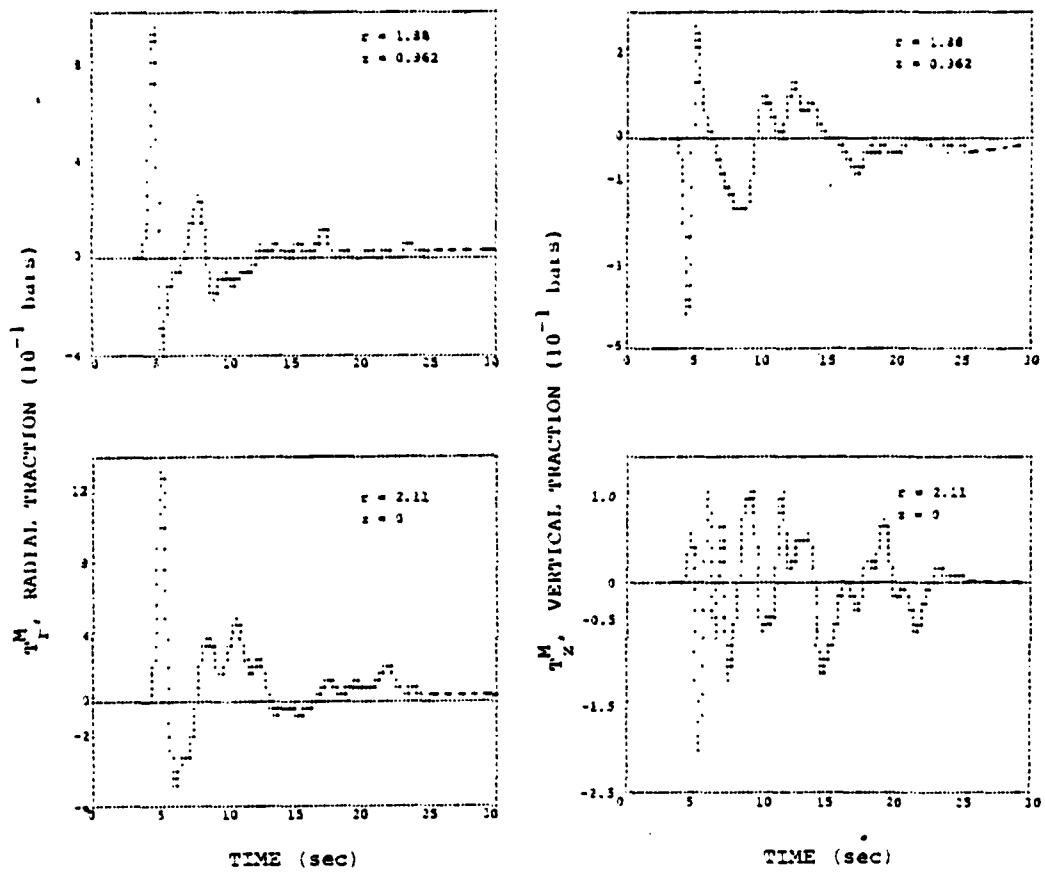
this solution are the static values of T_r^M, T_z^M and u_r^M. These static tractions appear to be small compared to the peak values and are probably difficult to compute accurately for this reason.

In Figure 3 we plot the values of the monitored solutions at the last time point versus position. Since the velocities should be nearly zero at this time, their angular dependence may not be too significant. However, the angular variation of the tractions is important. Their rapid oscillation with position suggests that numerical errors may be present at these low stress levels. This could lead to significant errors in the long period solutions, so we will be checking this part of the solution with care.

2.3 THE VERTICAL FORCE AND IMPULSE

An important indicator of the numerical accuracy of the calculations is the total vertical force and impulse:

$$F_z(t) = \int_S T_z^M (r,z,t) \, dA \, ,$$

$$I_z(t) = \int_0^t F_z(\tau) \, d\tau, \tag{1}$$

where S is the monitoring surface. The four deepest explosions were fully contained (N. Perl, personal communication). Then for these calculations there are no external forces or body forces influencing the monitored solutions. In this case, conservation of linear momentum requires that the force and impulse vanish at late time. Each of the shallowest three calculations formed a crater. But the ejected material must return to the surface at late time and, again, linear momentum will be conserved, though the calculation might not be run long enough to satisfy this condition.

In Figure 4 we show the vertical force and impulse for the seven ATI calculations. In each case these quantities are non-zero

17
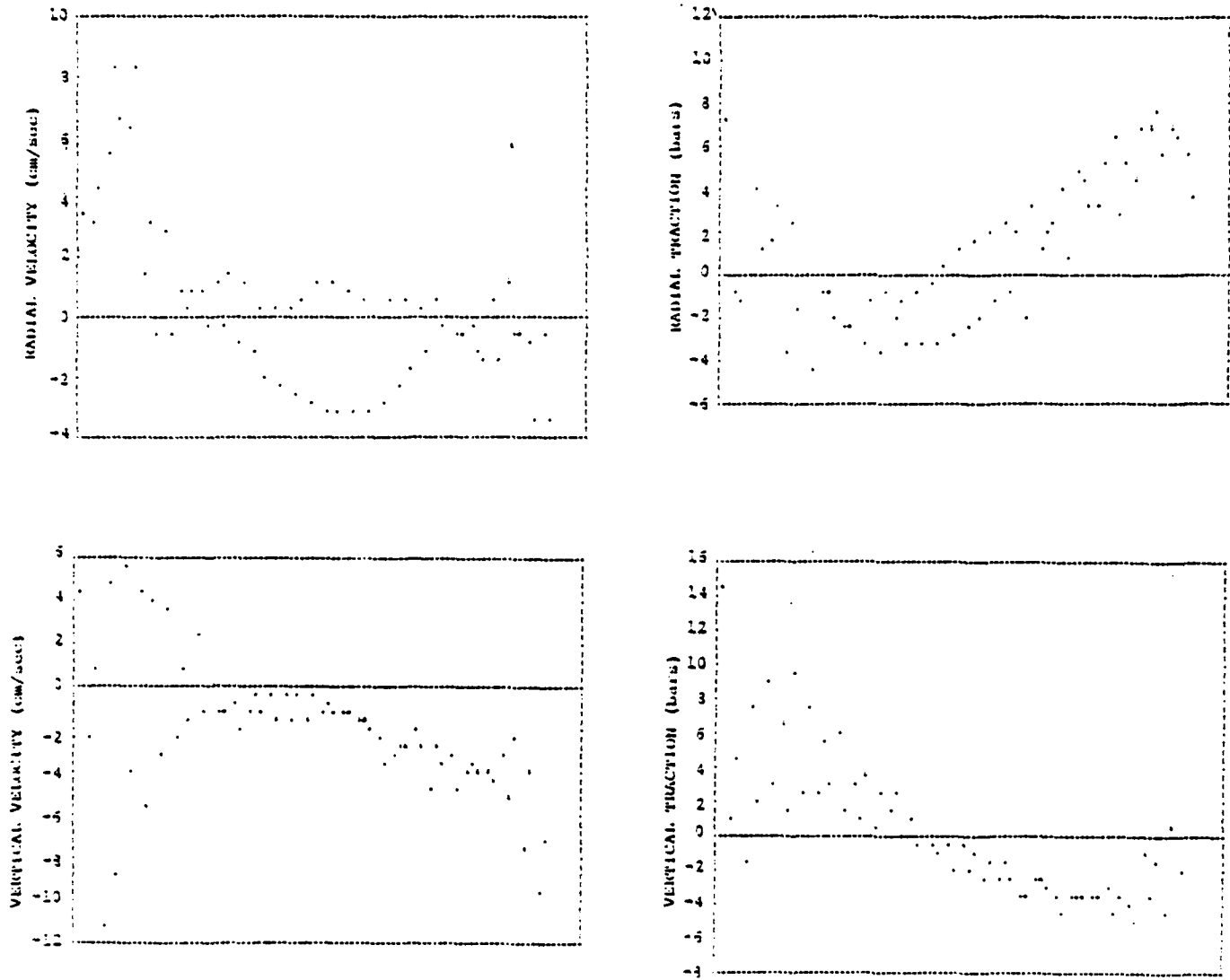
Figure 3. The monitored velocities and tractions for ATI #5127 are plotted versus position for the last time cycle. The monitoring station positions are shown in Figure 1 and are plotted from r = 0, z = 2.1 at the left to r = 2.1, z = 0 at the right.

18
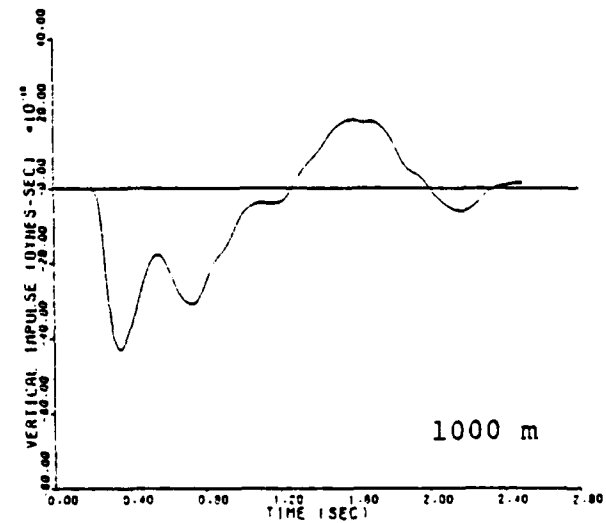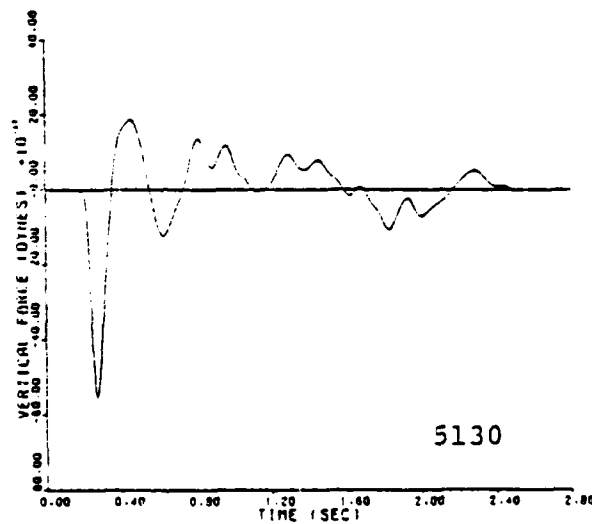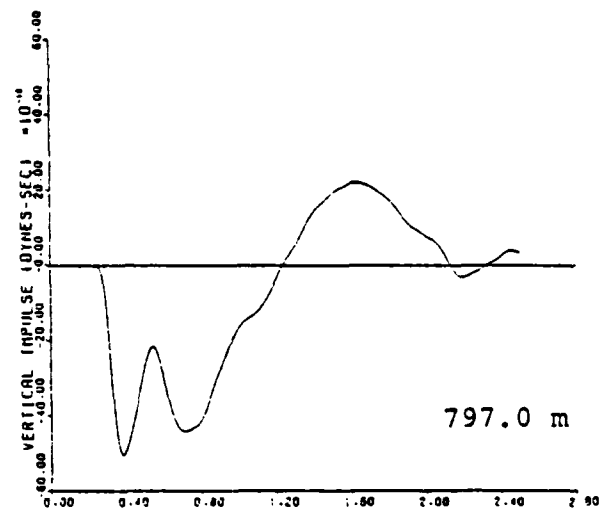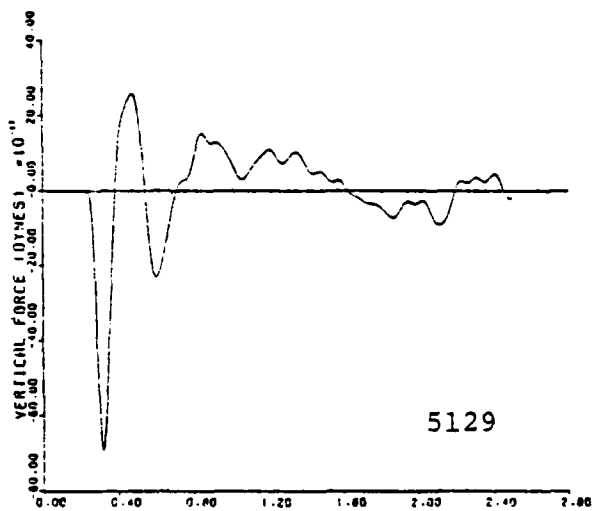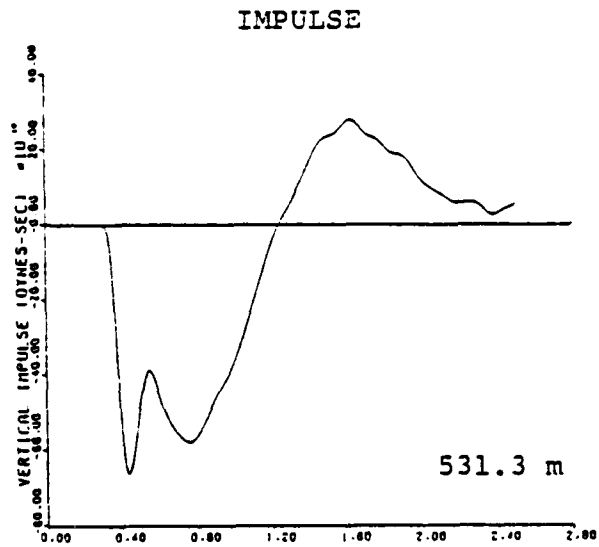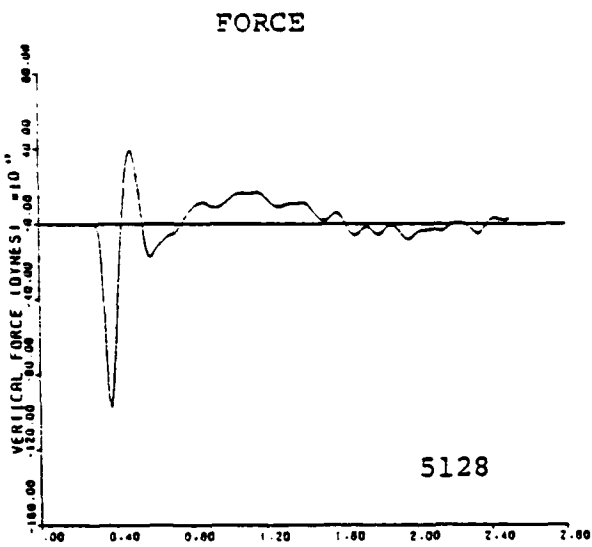
Figure 4. The vertical force and impulse are plotted for the seven ATI calculations. The actual force is 10^{17} times the number printed on the axes while the factor for the impulse is 10^{16}.

19

FORCE

5127

IMPULSE

398.5 m

Figure 4. (Continued)

20

Figure 4. (Continued)

21
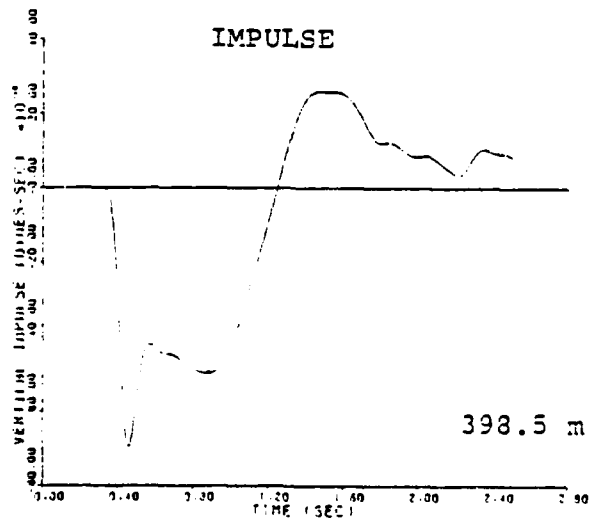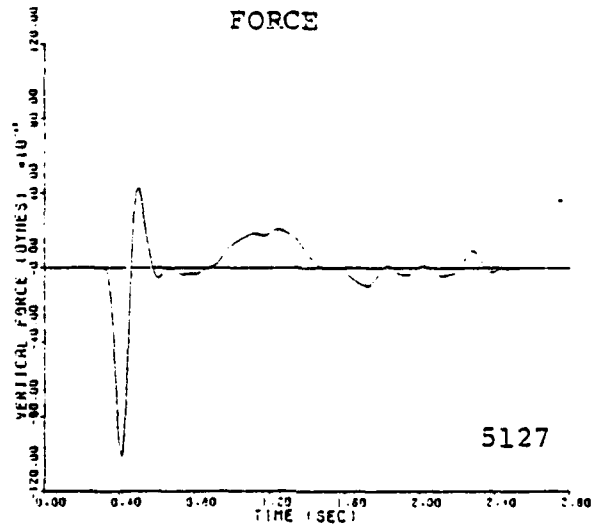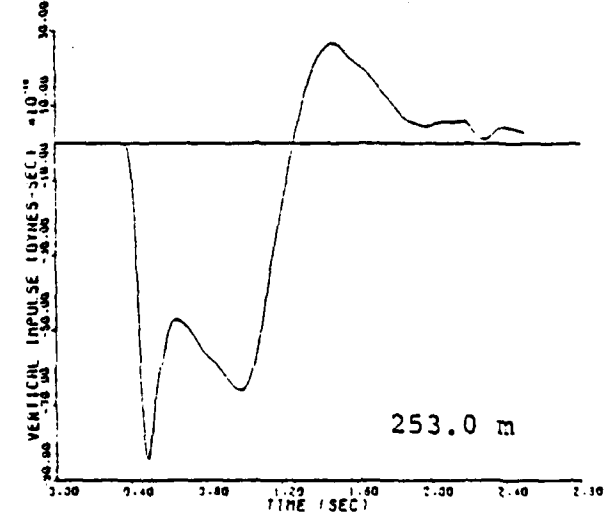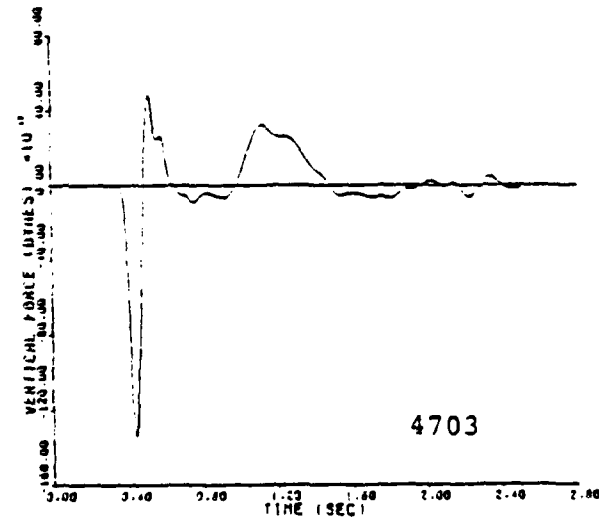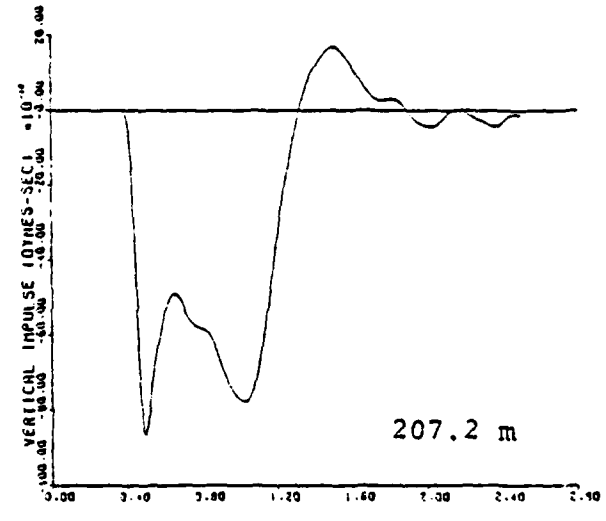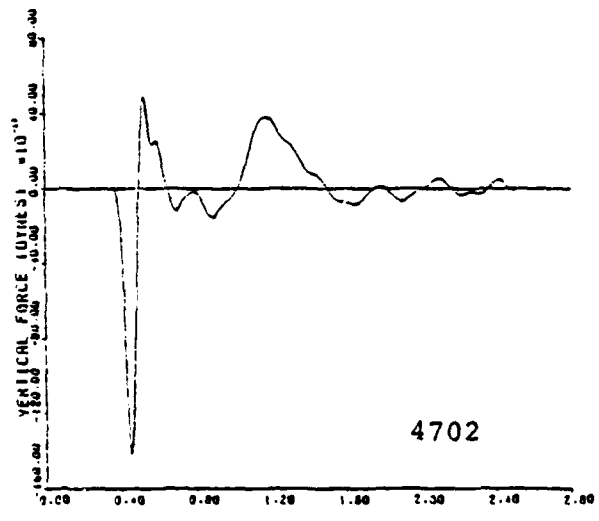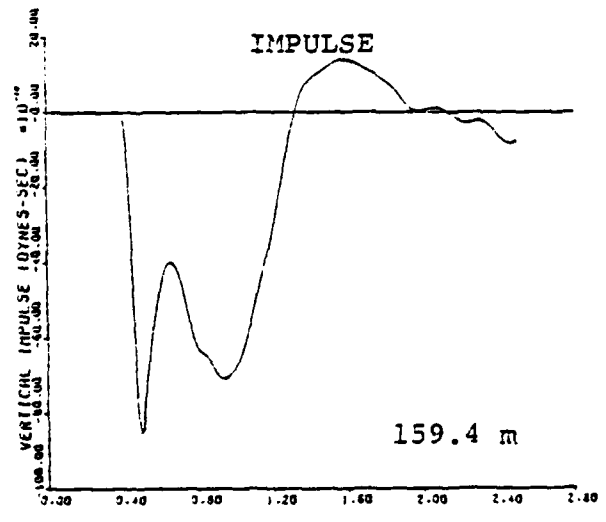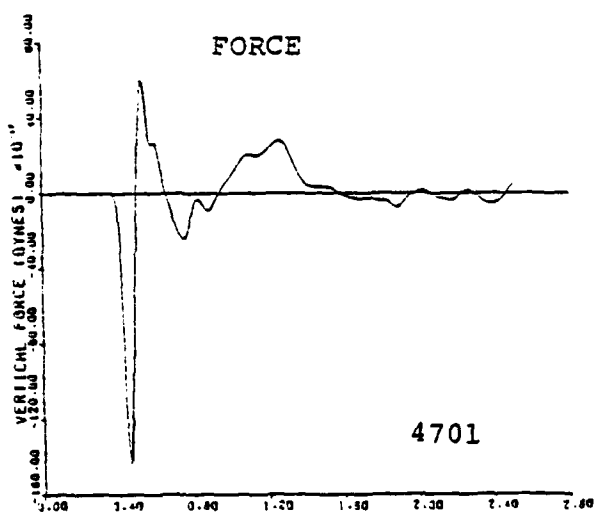
at the last time step (at 2.5 seconds), though they are small. The shallow calculations that cratered show no systematic differences from the deeper contained source calculations.

In Section A.5 of Appendix A we discuss the low frequency asymptotic behavior of the surface wave solution. If $F_z(t)$ and $I_z(t)$ are finite, the dominant term in the solution depends on the static value of the vertical force. If the force approaches zero in such a way that the impulse remains non-zero, the vertical force term is of the same order as other terms in the low frequency asymptotic solution and so will make an important contribution. However, if

$$\lim_{t \to \infty} F_z(t) = \lim_{t \to \infty} I_z(t) = 0 \quad , \tag{2}$$

the vertical force term is a higher order term that makes little contribution at long periods. Conservation of linear momentum requires that (2) be satisfied, and our asymptotic analysis shows that this is an important constraint on the long period solution.

2.4 CORRECTING THE DATA TO ZERO THE VERTICAL FORCE AND IMPULSE

A straightforward procedure may be devised to correct the T^M to satisfy the conditions (2). Basically, we assume that the final values of the force and impulse are nonzero, either because there are some numerical errors, or because the calculation is not quite finished (i.e., some small motions are still propagating through the monitoring surface). We then add an additional time step to correct the monitored solutions to satisfy (2). This is an ad hoc procedure that is least troublesome if the correction is "small"; that is, if we start with calculations where (2) is nearly satisfied, as is the case here.

Our procedure for "correcting" the monitored tractions is as follows. Let $t = T_1$ at the final time step of the calculation. Then assume that

22

$$F(T_1) = K,$$

$$I_z(T_1) = -L \tag{3}$$

In practice, we will always have $K \neq 0$ and $L \neq 0$. Then we take another time step, $\Delta t = T_2 - T_1$ such that

$$F_z(T_2) = I_z(T_2) = 0. \tag{4}$$

This is done by setting

$$T_z^M(T_2) = T_z^M(T_1) + \delta T_z^M \tag{5}$$

at each point on the monitoring surface.

From (1) we see that the vertical force will be zero if we choose δT^M to satisfy

$$\int_S \delta T_z^M \, dA = -K \, . \tag{6}$$

If K and L have the same sign, we can zero the impulse by an appropriate choice for Δt. Let $F_z(t)$ be linear between T_1 and T_2. That is,

$$F_z(t) = K - (t - T_1) K / \Delta t \tag{7}$$

for $t \in [T_1, T_2]$. Then

$$\Delta t = \frac{2L}{K} \tag{8}$$

leads to $I_z(T_2) = 0$. If K and L have the opposite sign, a more complex functional form could be chosen for $F_z(t)$ between T_1 and T_2 to zero the impulse. However, in most cases we prefer to retreat to an earlier time step where K and L have the same sign and then apply the procedure outlined.

We have not yet shown how to select the δT^M to satisfy (6) while minimizing the perturbation to the individual T_z^M time histories. There are other possibilities, but we have chosen to minimize

23

$$\int_S \frac{(\delta T_z^M)^2}{|T_z^M|} \, dA \, , \tag{9}$$

while requiring that (6) be satisfied. This is a classic minimization problem which can be solved using a Lagrange multiplier. The solution is

$$\delta T_z^M = -\frac{K}{\Gamma} \left| T_z^M \right| , \tag{10}$$

where

$$\Gamma = \int_S \left| T_z^M \right| dA \, . \tag{11}$$

In summary, the tractions and displacements are computed to time T_1. Then another time step, Δt from (8), is added to take the calculation to a new final time T_2. The vertical tractions at T_2 are computed from (5), using (10) to compute δT_z^M. The other quantities are extended as follows:

$$u_r^M (T_2) = u_r^M (T_1) \, ,$$

$$u_z^M (T_2) = u_z^M (T_1) \, , \tag{12}$$

$$T_r^M (T_2) = T_r^M (T_1) \, .$$

In Table 1 we list the parameters used for correcting the vertical force and impulse from the ATI calculations. Note that for two of the calculations (4702 and 5130) some of the data provided were discarded and the processed data were terminated at a time when the force and impulse had opposite signs.

The important numbers in Table 1 are K/Γ and Δt. We see that the imposed final time step is not too large. Calculation 5127 is typical and the correction is indicated in Figure 5. The K/Γ give

24

TABLE 1

PARAMETERS FOR CORRECTING THE VERTICAL FORCE AND IMPULSE TO ZERO

ATI Identifier	Depth	T_1 (sec)	$F_z(T_1)$ (10^{17} dynes)	$I_z(T_1)$ (10^{16} dyne-sec)	Γ (10^{17} dynes)	K/Γ	Δt (sec)
4701	159.4	2.50	4.5	-7.8	7.2	0.62	0.35
4702*	207.2	2.45	2.6	-1.5	5.4	0.49	0.12
4703	253.0	2.50	-1.9	2.9	7.6	-0.25	0.30
5127	398.5	2.50	-4.1	8.3	8.1	-0.50	0.41
5128*	531.3	2.37	-2.2	2.8	8.5	-0.26	0.25
5129	797.0	2.50	-1.9	3.4	4.5	-0.42	0.36
5130	1000.0	2.50	-0.46	14.4	5.8	-0.08	0.63

* The last time step used for subsequent calculations is earlier than the last time step provided.
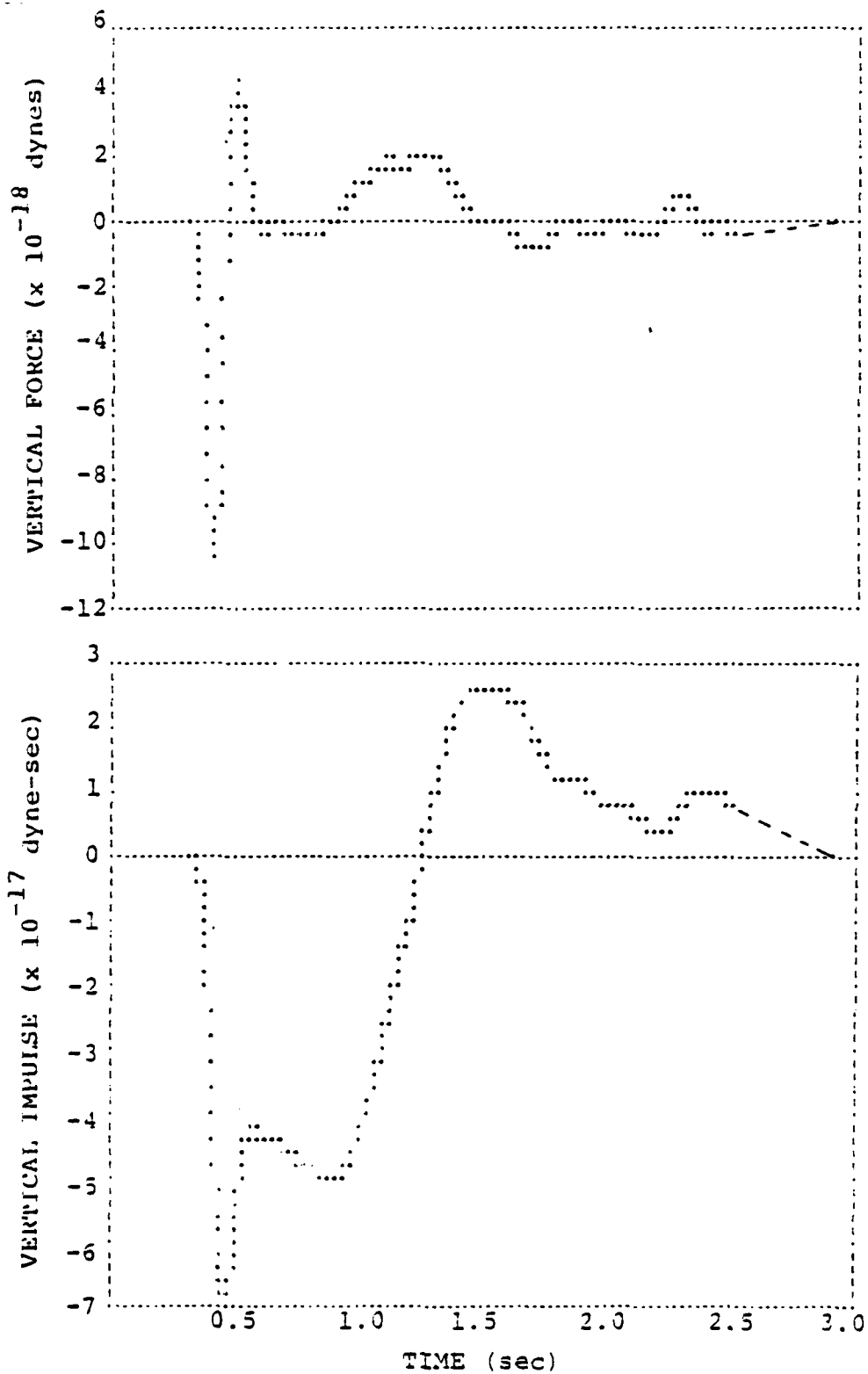
Figure 5. *The corrected vertical force and impulse for ATI #5127. The imposed time step is indicated with a broken line (for the impulse, this line is more properly drawn as a quadratic).*

26

the ratio of the traction correction (δT^M) to the computed value at the last time step, see (10). For all but number 5130, this correction is rather large. For example, for Number 5127 we have

$$\delta T_z^M = 0.50 \; \left| T_z^M \right|. \tag{13}$$

That is, to zero the vertical force and impulse, we impose an "upward" traction at each node that is half the size of the computed final value. The values of the tractions used in the calculations (including the imposed time step) were plotted in Figure 2. In many cases, the corrections are small in absolute terms because the final computed values were small to start with.

How important are these corrections? First, they mainly affect long period seismic waves. That is, the surface waves. Our asymptotic analysis in Appendix A shows that the contribution of the vertical traction to long period surface waves is rather small as long as the force and impulse do vanish. For these reasons, we do not expect the details of the correction to be very important. We will later show in Section 3.4 that this is indeed the case.

27

III. M_s and m_b Estimates for ATI Granite Calculations

3.1 INTRODUCTION

The ATI source calculations described in the previous section were processed with the methods described in Appendix A to compute synthetic body and surface wave seismograms in realistic earth models. From these seismograms conventional m_b and M_s were determined. In this section we describe these synthetic seismogram calculations and analyze the results.

The basic equation for the seismogram synthesis is (Section A.2).

$$u_i^F = -\int_{S_M} \left[G_j^i * T_j^M - S_{jk}^i * u_j^M \; n_k \right] dA \qquad (14)$$

where G_j^i and S_{jk}^i are Green's functions while T_j^M and u_j^M are the monitored tractions and displacements. For most of the development in Appendix A, the tractions are replaced by the actual stress components. In that form the basic equation for axisymmetric sources is (A.5). In terms of tractions, and a general monitoring surface like that in Figure 1, the vertical displacements are

$$u_z^F = -\int_S \left[G_r^z \; T_r^M + G_z^z \; T_z^M \right] dA + \int_S \left[S_{rr}^z \; u_r^M \; n_r + S_{zr}^z \; u_z^M \; n_r \right.$$

$$\left. + S_{rz}^z \; u_r^M \; n_z + S_{zz}^z \; u_z^M \; n_z \right] dA \quad . \qquad (15)$$

The G_j^i and S_{jk}^i are the azimuthally averaged Green's functions given in Appendix A. The T_j^M, u_j^M and n_j are the quantities provided by ATI. The quadratures reduce to a sum over the nodes with the dA being the appropriate incremental area. Equation (15) is used for all calculations in this section. The difference between body and surface waves is in the Green's functions.

28

3.2 FAR-FIELD RAYLEIGH WAVES IN A HALFSPACE

We begin our study of the Rayleigh waves excited by the ATI granite calculations by examining the Rayleigh pulse in a half-space. The waveform is simple and unusual features are easy to see. In dispersive real earth models, peculiarities due to the source are relatively difficult to identify.

The halfspace is that of the source calculations $(\alpha = 4.403$ km/sec, $\beta = 2.542$ km/sec, $\rho = 2.661$ gm/cm^3). The halfspace Rayleigh pulses were computed at 1000 kilometers and were filtered by a WWSSN 15-100 long period seismometer response. The effects of attenuation ($Q = 10$ in the top kilometer and 300 elsewhere) were included by multiplying the Rayleigh wave spectrum by the following factors:

Period (sec)	Attenuation Factor
25.0	0.73
20.0	0.65
14.0	0.48
10.0	0.31
6.25	0.097
5.0	0.0006

The halfspace Rayleigh pulse is shown in Figure 6 compared to the Rayleigh pulse from an RDP source at the same depth as the ATI explosion. The RDP is that of Mueller and Murphy (1971) for granite at a depth of 398.5 meters. There is little perceptible difference between the Rayleigh waves from the ATI sources and the RDP source. We do see a little long period "noise" on several of the seismograms for the ATI sources, but generally they look quite good.
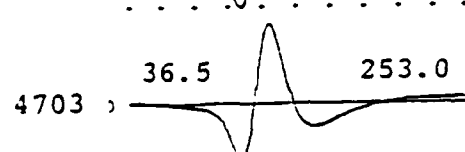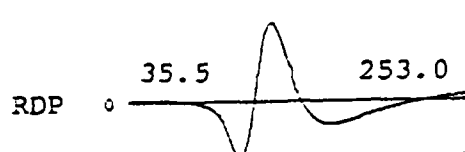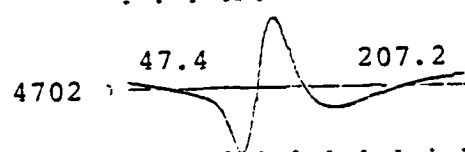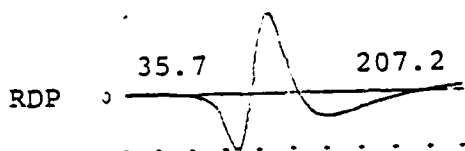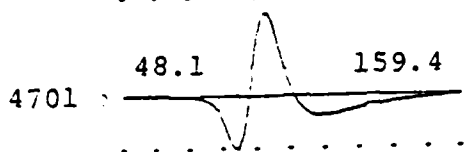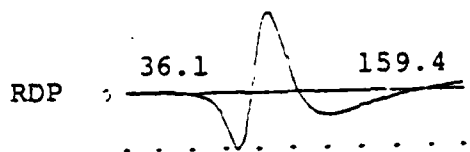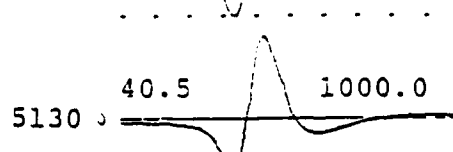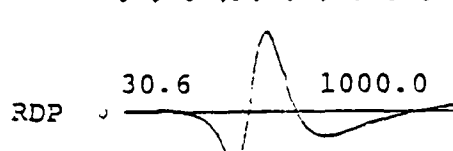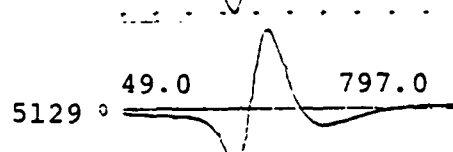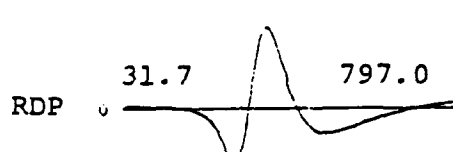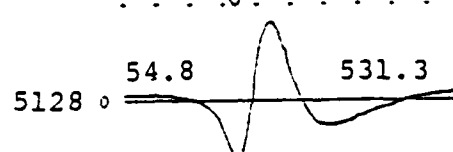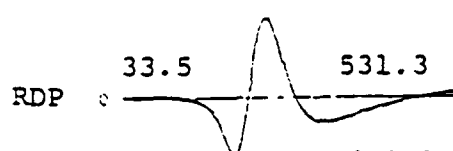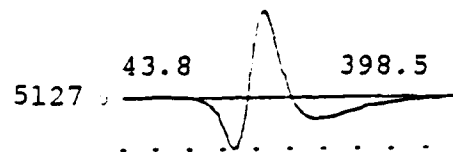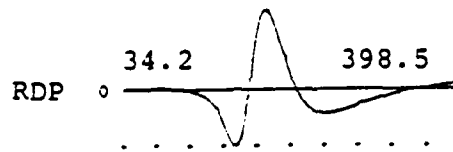
Figure 6. Halfspace Rayleigh waves are shown for seven ATI granite calculations and comparable calculations with an RDP source.

3.3 CONTRIBUTION OF VERTICAL TRACTIONS

As was discussed in Section 2.4, an ad hoc correction was introduced into the vertical tractions to force them to satisfy the required condition that the total downward force and impulse vanish at late time. The influence of this correction on the contribution of the vertical traction terms to the solution should become larger with increasing period. We do not expect 'the correction to have much influence on periods below two seconds that are important for m_b. However, the important periods for surface waves are much larger than two seconds.

In Figure 7 we compare the halfspace Rayleigh wave solution from Figure 6 to the Rayleigh wave computed with only the vertical tractions. The latter were computed with an incorrect sign, so the actual vertical traction Rayleigh wave is inverted compared to that in the figure. That is, it has the same polarity as the total solution. The Rayleigh wave spectra for these seismograms are plotted in Figure 8.

The dominant period of the total halfspace Rayleigh wave is about nine seconds. For the vertical traction component the dominant period is slightly shorter, about seven seconds. The peak-to-peak amplitudes and their ratios shown in Figure 7 are not corrected for the small difference in instrument response at these periods. If included, this correction would increase the ratios by about 15%.

For M_s our interest is in periods longer than nine seconds. The spectral comparison in Figure 8 shows that the vertical traction contribution is less for longer periods than it is at the period dominating the halfspace Rayleigh waves.

The ratios in Figure 7 and the spectral comparisons indicate that the contribution of the vertical tractions decreases with source depth. For the three shallowest depths, the vertical traction contribution is within a factor of two or three of the total solution for M_s periods. This is merely a suggestion that we

31
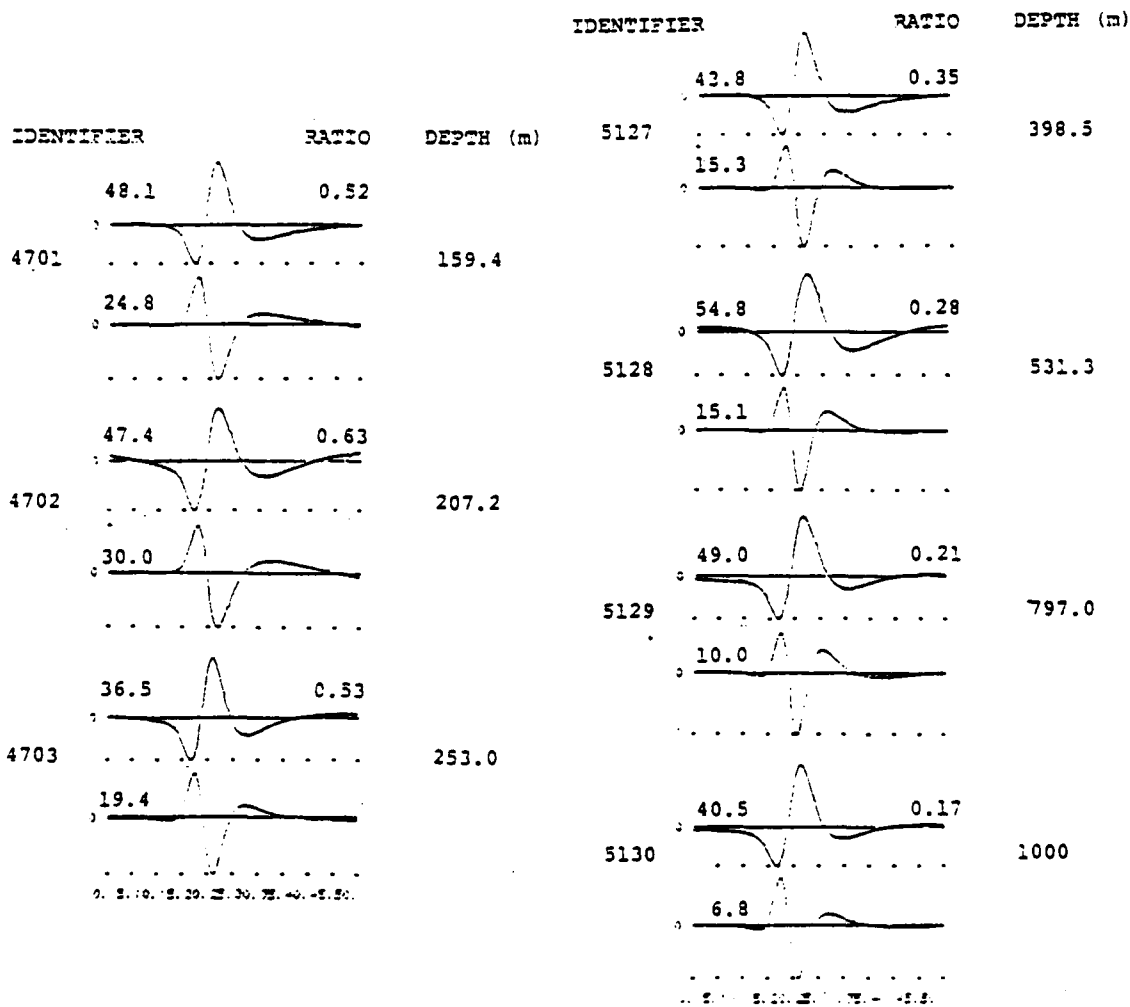
Figure 7. Comparison of halfspace Rayleigh waves for the total solution to those computed from only the vertical tractions. The latter are inverted. The peak-to-peak amplitudes are shown for each seismogram and the ratio is given for each pair.

32
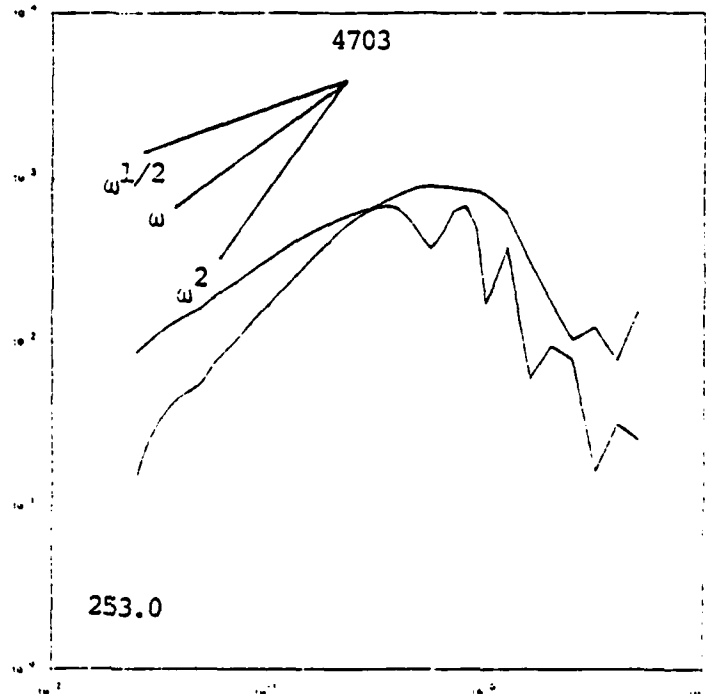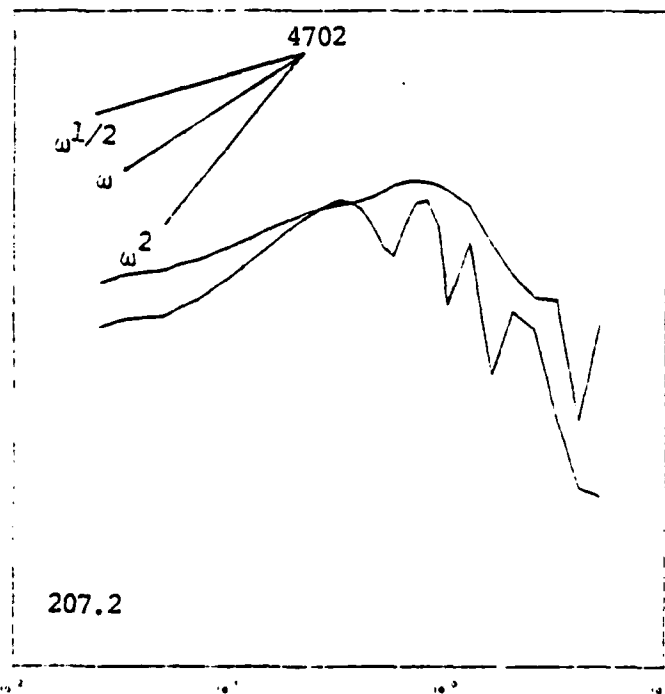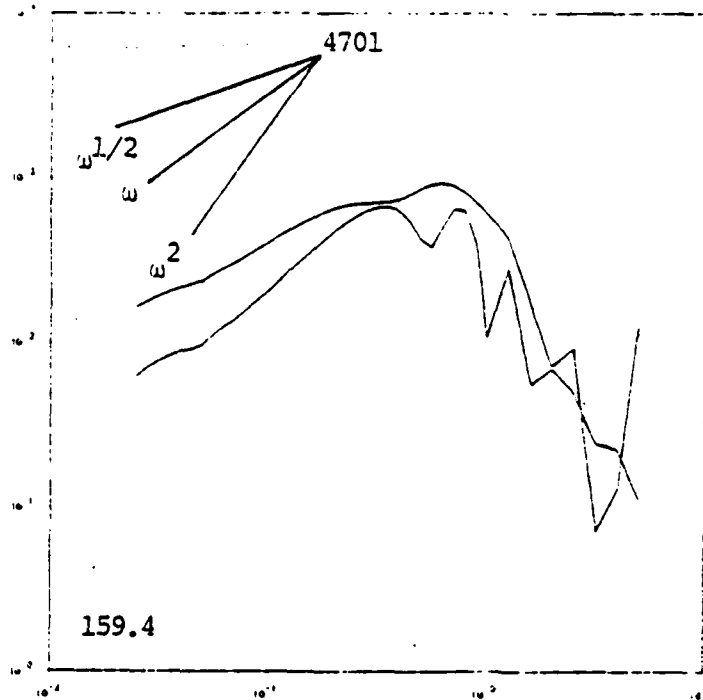
Figure 8. The Rayleigh wave spectra for the seismograms of Figure 7 are plotted. These spectra do not include the effect of Q or the seismometer. The smoother spectrum that is larger over most of the frequency range is the total spectrum.

FREQUENCY (Hz)

33

FREQUENCY (Hz)
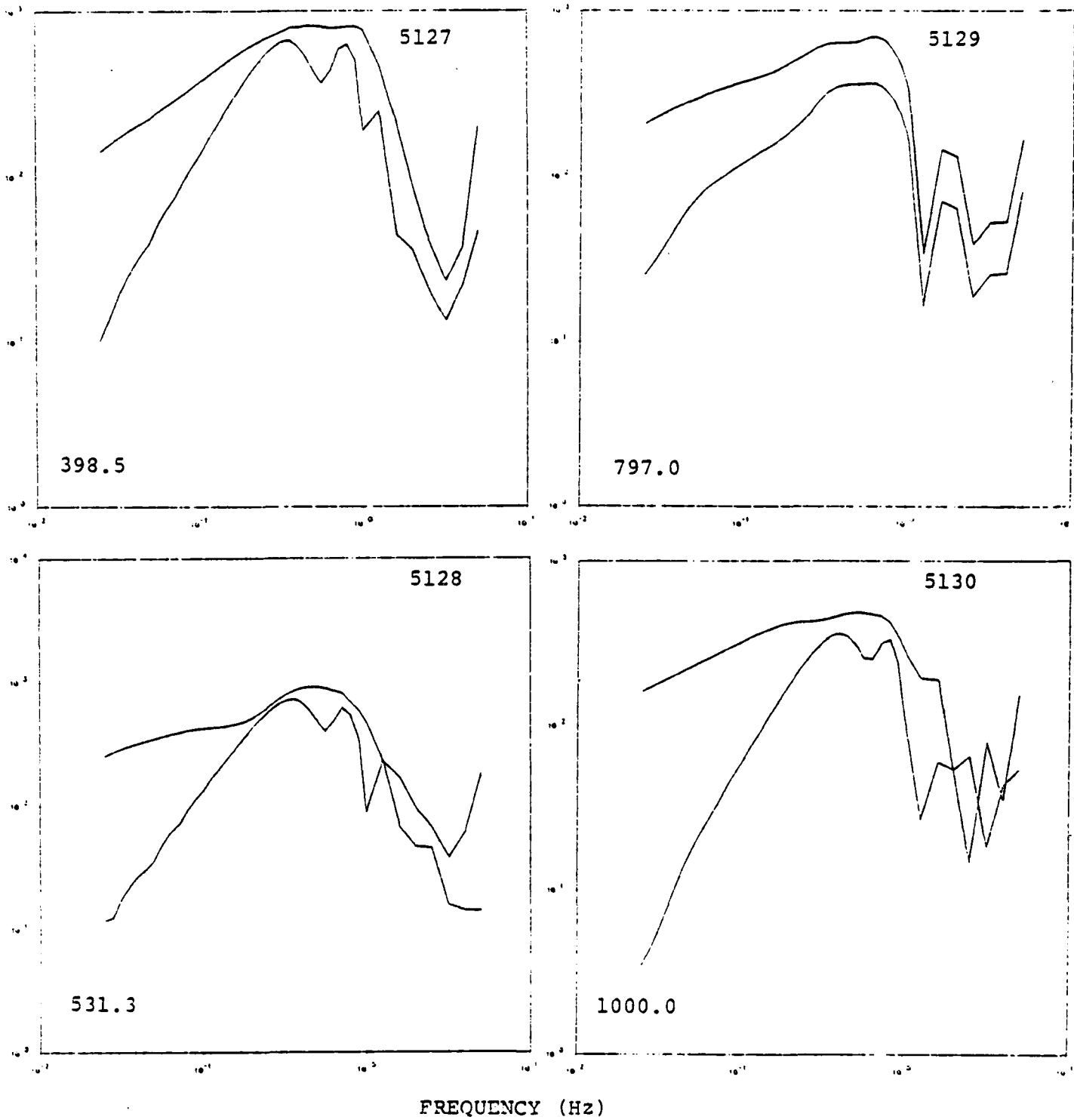
Figure 8. (continued)

34

should have less confidence in the solution at the shallower
depths. Of course, we have no way to estimate the relative
importance of errors from the ad hoc correction to the vertical
tractions (which, after all, forces them to satisfy a global
conservation law), compared to other errors in the calculations.

3.4 AN EQUIVALENT RDP FROM SURFACE WAVES

The standard way to represent the source for underground
nuclear explosions is in terms of a spherically symmetric point
source. An important motivation for doing multi-dimensional source
calculations is to study the influence of effects that cannot be
represented by a one-dimensional source. One way to do this is to
compare seismograms computed from the complex source with those from
a one-dimensional (reduced displacement potential or RDP) source.
Such a comparison was made in the time domain in Figure 6.

In Appendix B we point out that an "equivalent RDP" repre-
sentation can be computed for the two-dimensional source. This
equivalent source, called $\hat{\Psi}_e$, can be computed from the equation

$$\hat{\Psi}_e = \frac{\overline{W}_{AC}}{\overline{W}_{EX}} \hat{\Psi} , \qquad (16)$$

where $\overline{W}_{AC}$ is the spectrum of the Rayleigh waves from the
two-dimensional sources in Figure 6. The W_{EX} is the spectrum of
the corresponding seismogram computed with the reduced velocity
potential, $\hat{\Psi}$.

Another way to look at the $\hat{\Psi}_e$ is that it is the source that
we would deduce from Rayleigh wave recordings of an explosion, if we
had perfect knowledge of the path and if we assumed that the source
could be represented by an RDP.

The semi-empirical Mueller/Murphy model (Mueller and Murphy,
1971; Murphy, 1977) predicts that the long period source level (Ψ_∞)
depends on depth according to

35

$$h^{-1/3} \quad , \tag{17}$$

for explosions at a fixed yield. The Mueller/Murphy granite source functions for the seven depths of the 150 KT ATI calculations are shown in Figure 9.

The "equivalent RDP" representations for the ATI calculations were computed with (16) using the spectra of the seismograms in Figure 6. These are shown in Figure 10. The amplitude scales vary from case to case, so a Mueller/Murphy source function is plotted with each case for reference.

The high frequency behavior of the $\hat{\Psi}_e$ in Figure 10 is not what we expect for a true RDP source. We see that the amplitudes go off-scale. Mechanically, this is because the Rayleigh wave spectra for the RDP sources, $\overline{W}_{EX}$, fall off faster than ω^{-3} at high frequencies, while the spectra for the two-dimensional sources, $\overline{W}_{AC}$ (Figure 8), are not even monotonically decreasing at high frequency. Part of this may be due to numerical error, since the surface wave synthesis method may be losing accuracy at the high frequencies. However, there are also plausible physical explanations for the observed behavior of the $\overline{W}_{AC}$ and $|\hat{\Psi}_e|$. First, the free surface reflections in the inelastic ATI calculations are not perfect scaled replicas of the direct waves, as they are in the calculations of $\overline{W}_{EX}$. Second, the ATI calculations presumably include some contribution from spall closure. These physical explanations for the high frequency character of the $|\hat{\Psi}_e|$ are supported by the way the spectral holes shift to lower frequency with increasing depth.

3.5 FAR-FIELD RAYLEIGH WAVES IN A REALISTIC EARTH MODEL

The fundamental mode Rayleigh waves for the ATI source calculations were computed for a crust and upper mantle model for the central United States. The velocity model is essentially that given by McEvilly (1964) while the Q model is roughly compatible

36
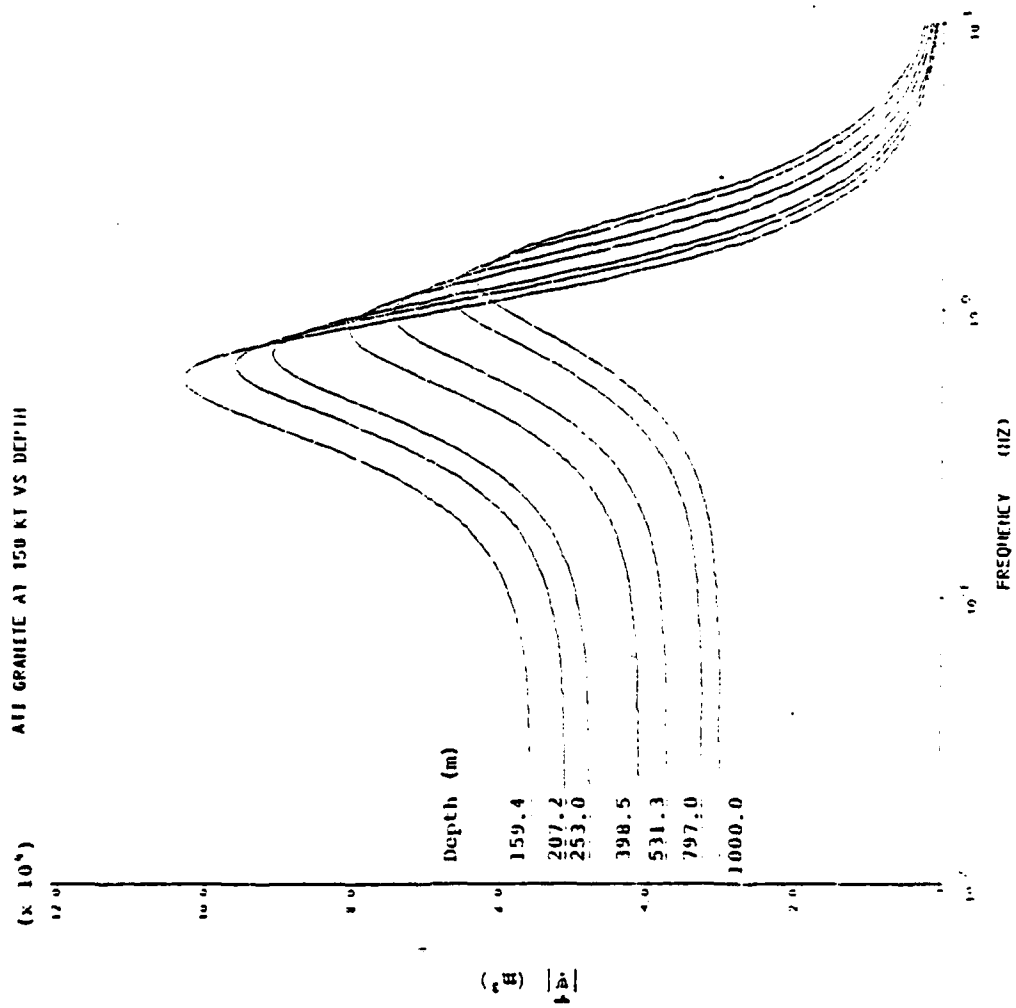
Figure 9. The spectral amplitude of the Mueller/Murphy reduced velocity potential for 150 KT explosions in granite.

37
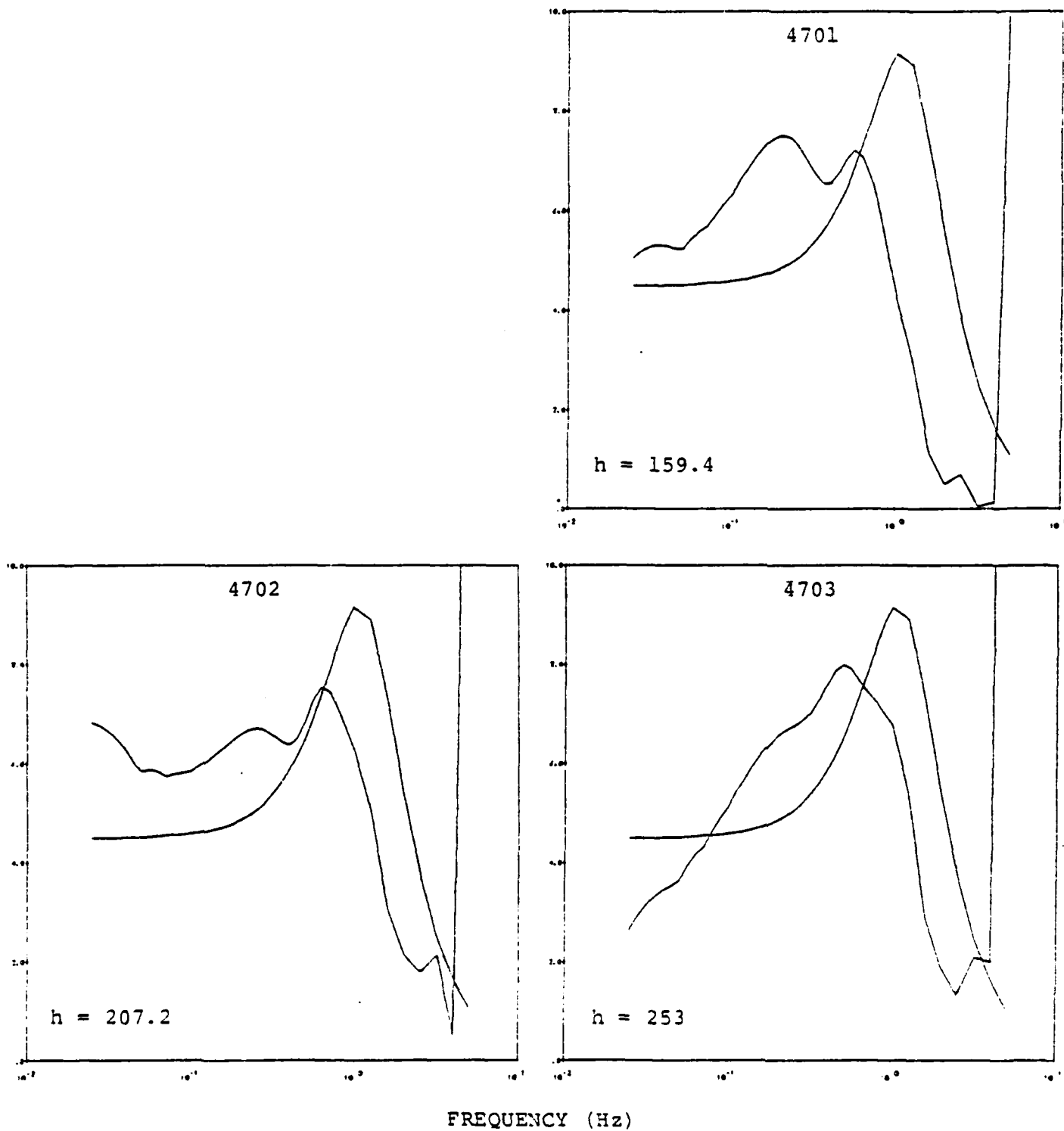
Figure 10. The |vₑ| from the seismograms in Figure 6 are plotted. The amplitude axes are in 10^4 m³. The Mueller/ Murphy |v| for a depth of 700 meters (see Figure 9) is shown for reference.
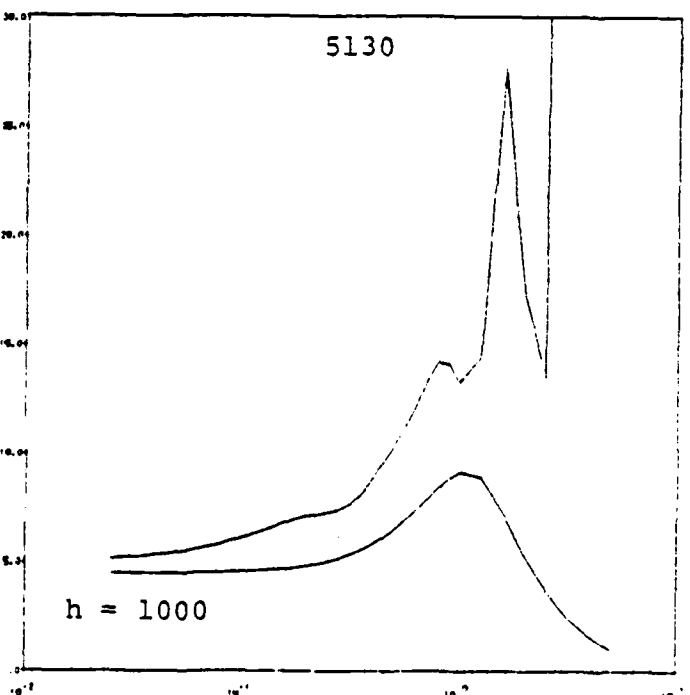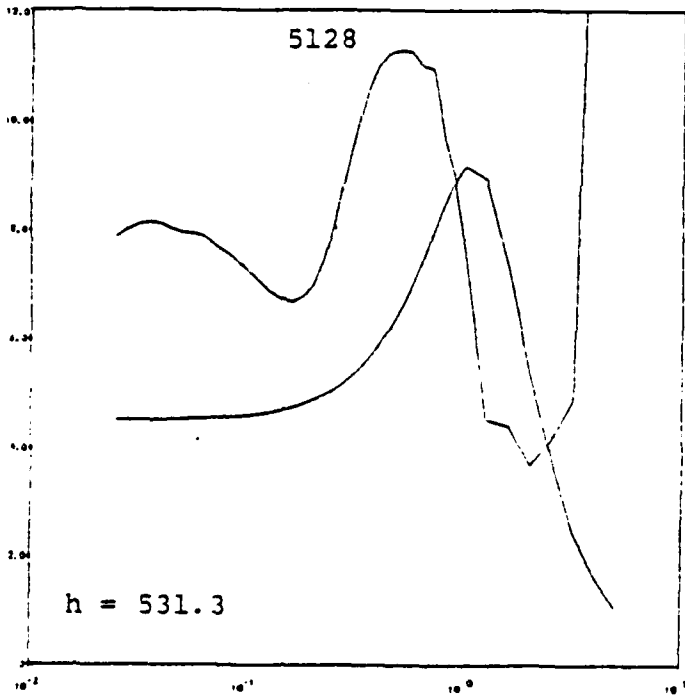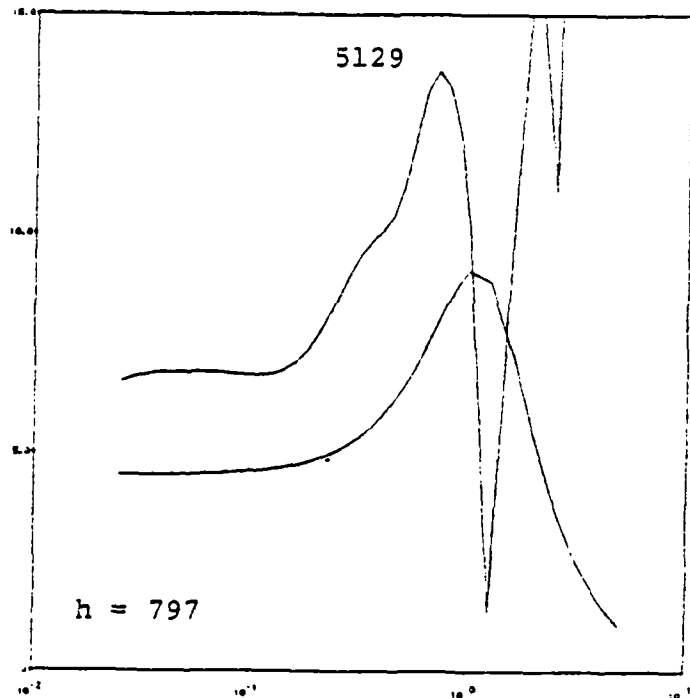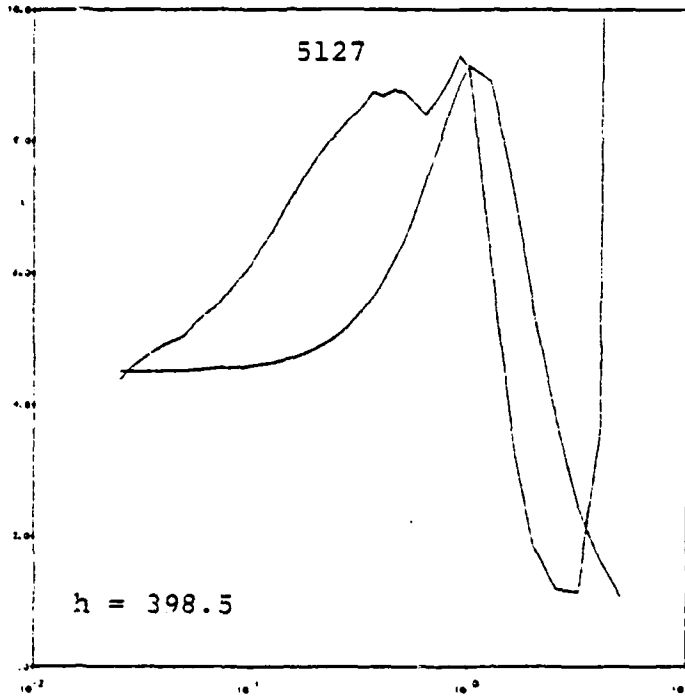
FREQUENCY (Hz)

Figure 10. (continued)

39

with the Rayleigh wave attenuation factors of Tryggvason (1965). These models are listed in Table 2. To account for the mismatch between the near-surface properties in the source region and those in the propagation model, we used the technique of Bache, Rodi and Harkrider (1978), which is described in Section A.4. With this method separate models are used for the source region and propagation path. The two differ only in the top three kilometers.

The computed Rayleigh waves are shown in Figure 11. The structure has a strong Airy phase near 16 seconds. The somewhat strange appearance of the waveform results from the simultaneous arival of 5 to 3 second waves from the inverse branch with the 20 to 22 second waves.

The amplitude for computing M_s was taken from the largest trough to the following peak. The period of this cycle is about 14 seconds. The M_s formula of Marshall and Basham (1972) was used. At 3000 kilometers this is

$$M_s = \log A + 1.38 + P(T) \qquad (18)$$

where A is the maximum zero-to-peak amplitude in millimicrons, $P(T)$ is a period-dependent path correction and 1.38 is the distance correction.

The M_s values are listed in Table 3 and are plotted versus source depth in Figure 12. As another display of the depth-dependence of the Rayleigh wave excitation, we also plot the logarithms of the Rayleigh wave spectral amplitudes at 20, 14 and 10 seconds. The depth dependence is greatest at 20 seconds and decreases at shorter periods. The M_s depth dependence lies between those for the 14 and 20 second spectral amplitudes.

A simpler display that is independent of the propagation model is to plot the logarithm of the spectral amplitude for the halfspace Rayleigh waves shown in Figure 7. These are shown in the figure for 20, 10, 5 and 1 second periods. The 20 and 10 second curves are

40

TABLE 2

CRUSTAL MODELS FOR SURFACE WAVE CALCULATIONS

Depth (km)	Thickness (km)	α (km/sec)	β (km/sec)	ρ (gm/cm^3)	Q
Source Region Model					
1	1	4.403	2.542	2.661	10
2	1	4.403	2.542	2.661	30
3	1	4.403	2.542	2.551	100
11	8	6.1	3.5	2.7	250
20	9	5.4	3.68	2.9	250
38	18	6.7	3.94	2.9	2000
62	24	8.15	4.75	3.3	200
102	40	8.2	4.61	3.3	85
120	18	8.7	4.80	3.6	85
		8.7	4.80	3.6	85

Propagation Path Model

Extend Layer 4 (α = 6.1 km/sec) to the surface

41

Calculation	Depth		M_s
4701	159.4		4.65
4702	207.2		4.70
4703	253.0		4.49
5127	398.5		4.61
5128	531.3		4.74
5129	797.0		4.69
5130	1000.0		4.62
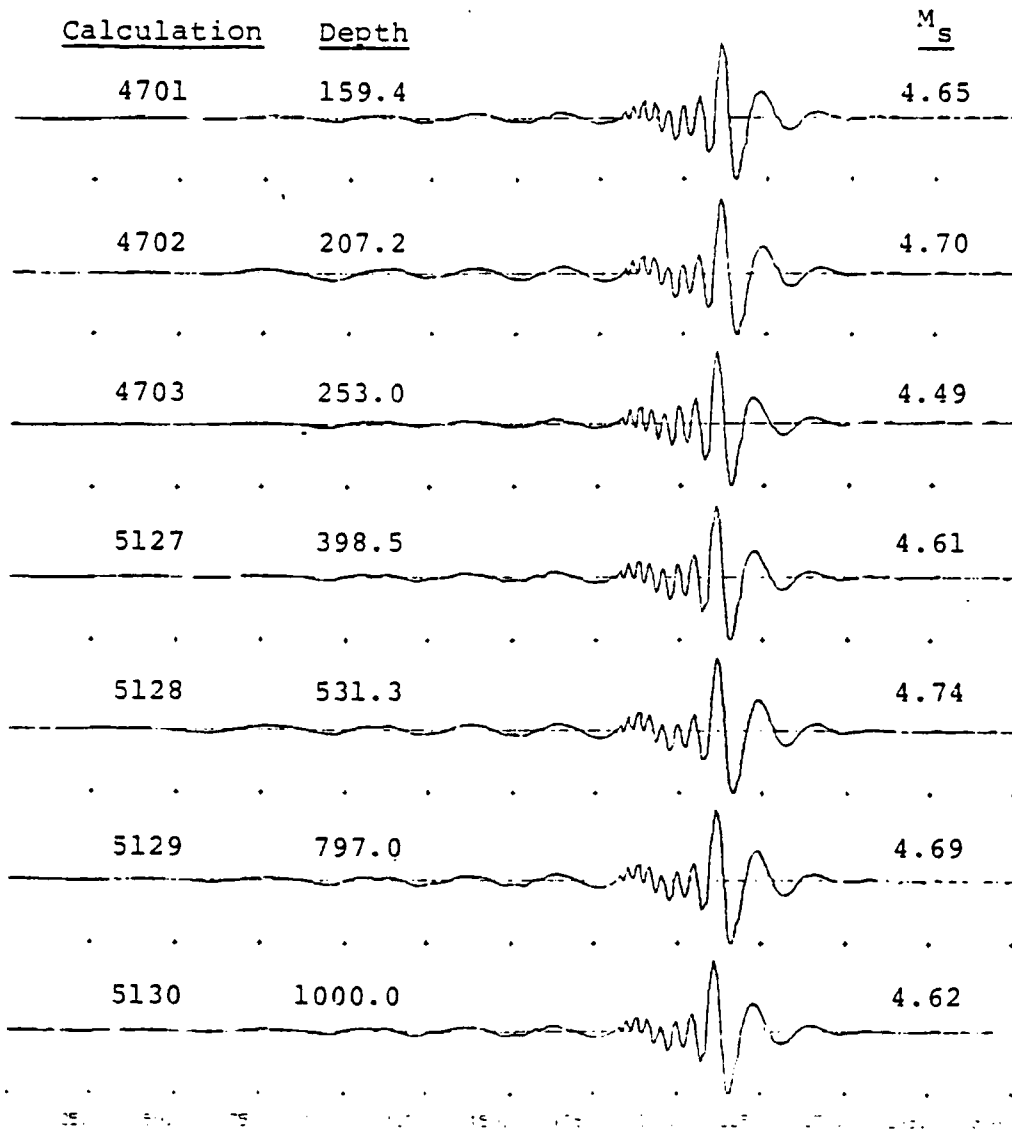
Figure 11. Rayleigh waves in a shield crustal model for seven ATI granite calculations. The range is 3000 km and the WWSSN 15 to 100 instrument response was included. Zero on the time scale corresponds to 750 seconds after source initiation.

42

TABLE 3

M_S FOR SEVEN ATI CALCULATIONS OF EXPLOSIONS IN GRANITE

Calculation	Depth (km)	A (microns)	T (sec)	M_S
4701	159.4	5.4	14.0	4.65
4702	207.2	5.0	15.0	4.70
4703	253.0	4.4	13.0	4.49
5127	398.5	5.0	13.8	4.61
5128	531.3	6.1	14.5	4.74
5129	797.0	5.5	14.4	4.69
5130	1000.0	4.9	14.1	4.62
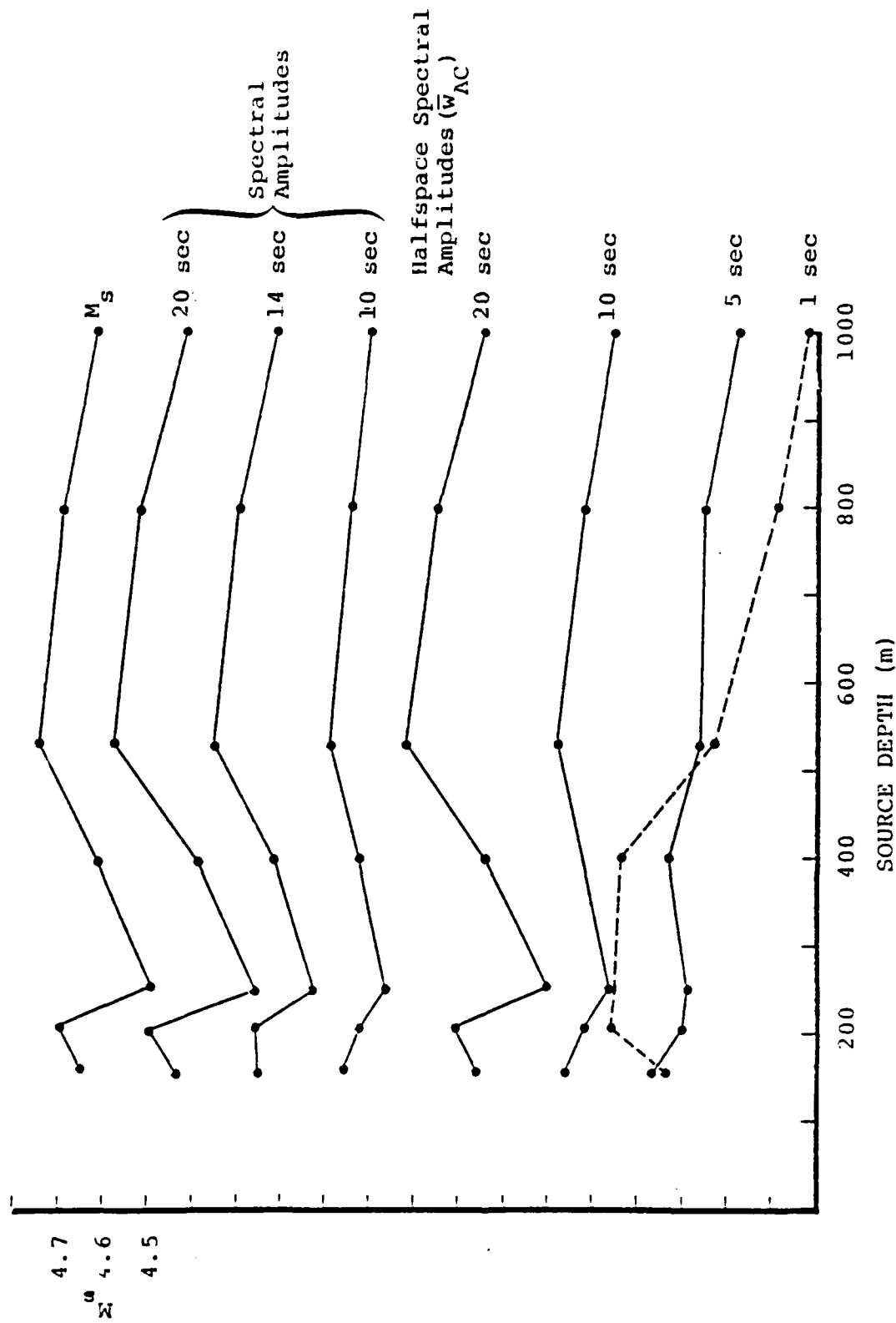
Figure 12. The M_S values and the logarithm of several spectral amplitudes are plotted versus source depth. The spectral amplitudes do not include the effect of Q or the seismometer and are on an arbitrary scale with one division on the axis corresponding to 0.1 on a log (base 10) scale.

44

nearly the same as those for the dispersive crustal model, as expected. We see that the dependence on depth continues to change as we go to shorter periods.

The spectral values in Figure 12 enhance our confidence that the M_s computed with the particular crustal model chosen is a true representation of the surface waves from the source calculations. The M_s increases slightly as the depth goes from 159 to 207 meters. There is a sharp decrease at 253 meters followed by an increase as depth increases to 531 meters. The M_s values then fall off for increasing depth.

Another interesting comparison is shown in Figure 13. In this plot, we show the M_s and 20 second spectral amplitude $(\overline{W}_{AC})$ from Figure 12 compared to the 20 second value of the equivalent RDP $(\overset{\wedge}{\overset{\cdot}{\tau}}_e)$ from Figure 10. The trend for all three measures of the surface wave excitation is the same.

Also shown in Figure 13 is the 20 second spectral amplitude of the Mueller/Murphy RDP from Figure 9. This is nearly the expected depth dependence of M_s predicted by the Mueller/Murphy model (the small dependence of the Rayleigh wave excitation on depth is ignored). At greater depths, where the interaction with the free surface may be nearly elastic, the depth dependence of the Rayleigh wave excitation for the ATI calculations is not too different from that for the Mueller/Murphy model. However, at shallow depths the two-dimensional calculations predict a much different depth dependence.

3.6   BODY WAVE MAGNITUDE

Synthetic body wave seismograms were computed using techniques similar to those for computing the Rayleigh waves. The basic equation is (15) with Green's functions appropriate for teleseismic body waves.

The body wave seismograms were for a range of 4000 km. The earth model included detailed crustal structures for the source and

45
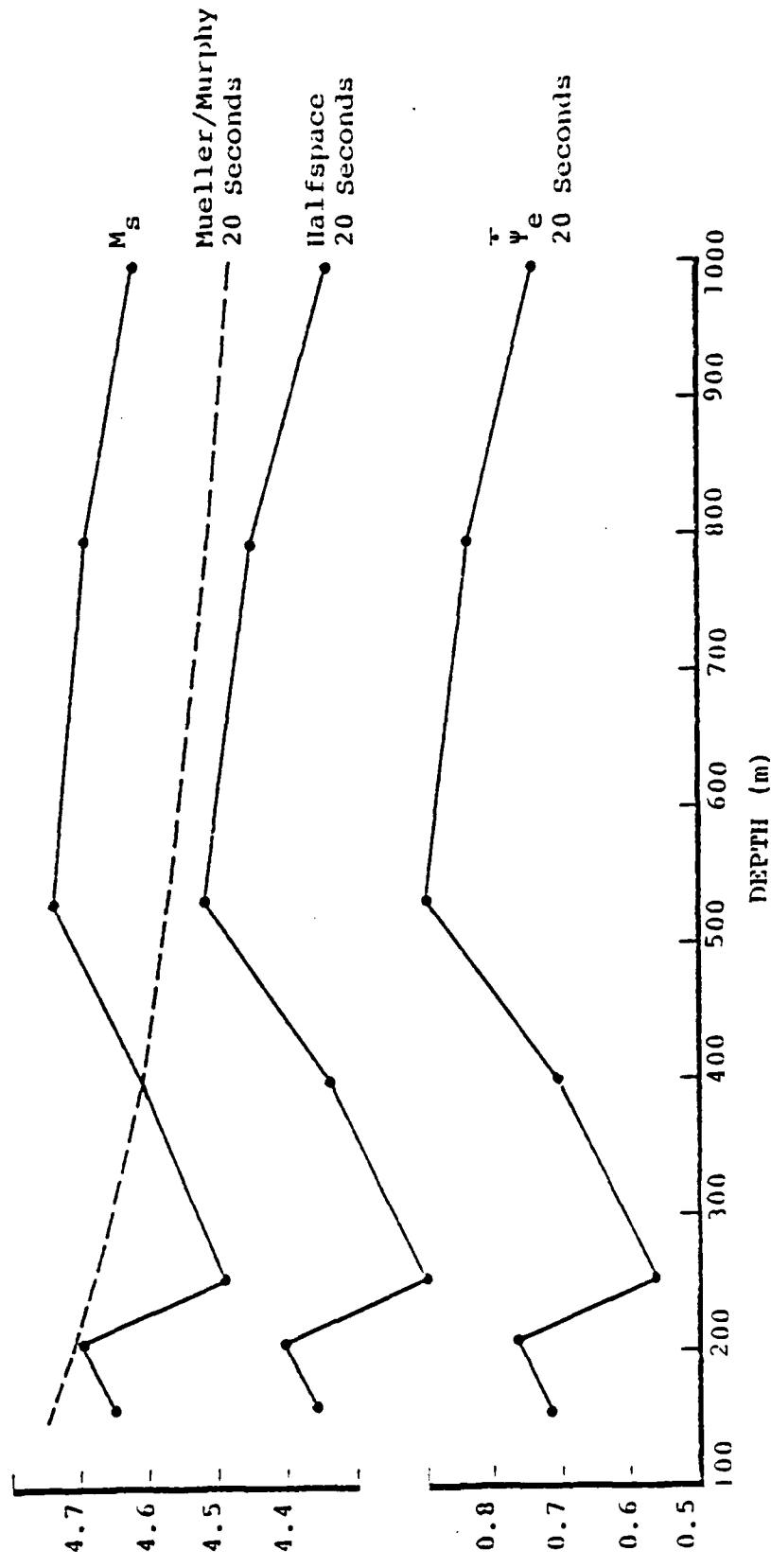
Figure 13. The M_s and the logarithm of several spectral amplitudes are plotted versus source depth. The three solid curves are for different ways to represent the relative amplitudes of the long period Rayleigh waves from the ATI calculations. The dashed curve is for the Mueller/Murphy RDP source.

16

receiver regions (Table 4). Rather than use a detailed upper mantle model, we represented this part of the path by a constant geometric spreading factor, which is reasonable for this range. For all the seismograms shown in this section (as well as for the S-Cubed sources discussed in Section V), we used 5.6×10^{-5} km^{-1} for the effective $1/R$. This value is somewhat arbitrary. Langston and Helmberger (1975) give about 7.6×10^{-5} km^{-1} for this range in a Jeffreys-Bullen earth model. We chose the ray parameter (source takeoff angle) to be appropriate for a range of 4000 km in the model HWNE (Helmberger and Wiggins, 1971). Later calculations indicated that 6.4×10^{-5} km^{-1} is the best estimate for the effective $1/R$ at this range in HNME. The seismograms are easily scaled for a $1/R$ different than the value we used.

The ray parameter for the body wave synthesis corresponds to a source takeoff angle of 20.3 degrees. The calculations are not very sensitive to this choice. It is also necessary to account for Q. This was done by multiplying the spectrum by the causal Q operator (Strick, 1970)

$$ \exp \left[-\pi f t^* \left[1 - \frac{2}{\pi} i \ln \left(\frac{1000}{f} \right) \right] \right], $$

where f is frequency in Hertz. Our calculations were done with $t^* = 0.3$. This is an important path dependent parameter which is much discussed and debated in the literature. We believe appropriate values for short period P wave synthesis range from 0.5 to 1.2, so our choice lies between. Finally, the seismograms were filtered by the response of the KS36000 seismometer. The amplitude response is plotted in Figure 14.

The synthetic body wave seismograms are plotted in Figure 15. Two amplitude measurements were made from each record, one on the "b" phase (first peak to first trough) and one on the "c" phase (first trough to second peak). Body wave magnitudes, m_b^b and m_b^c, were computed from these amplitudes using

47

TABLE 4

CRUSTAL MODELS FOR BODY WAVE CALCULATIONS

Depth (km)	Thickness (km)	α (km/sec)	β (km/sec)	ρ (gm/cm^3)
SOURCE REGION				
3.0	3.0	4.403	2.542	2.661
8.0	5.0	5.35	2.79	2.70
20.0	12.00	6.0	3.5	2.70
RECEIVER REGION				
1.70	1.70	4.0	2.31	2.3
3.00	1.30	5.1	2.94	2.5
20.00	17.00	6.0	3.5	2.8
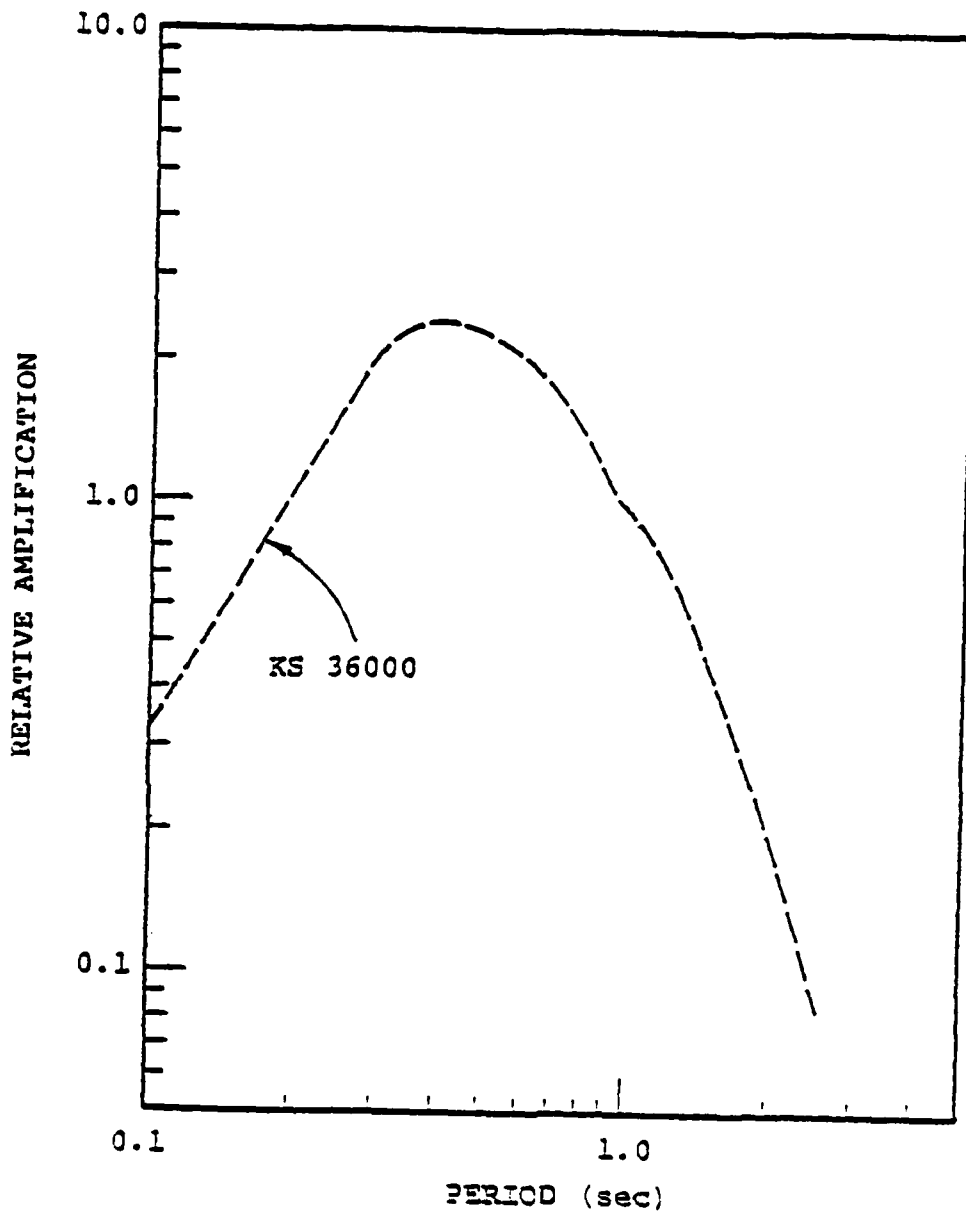
Figure 14. Amplitude response for the KS36000 seismometer.

49
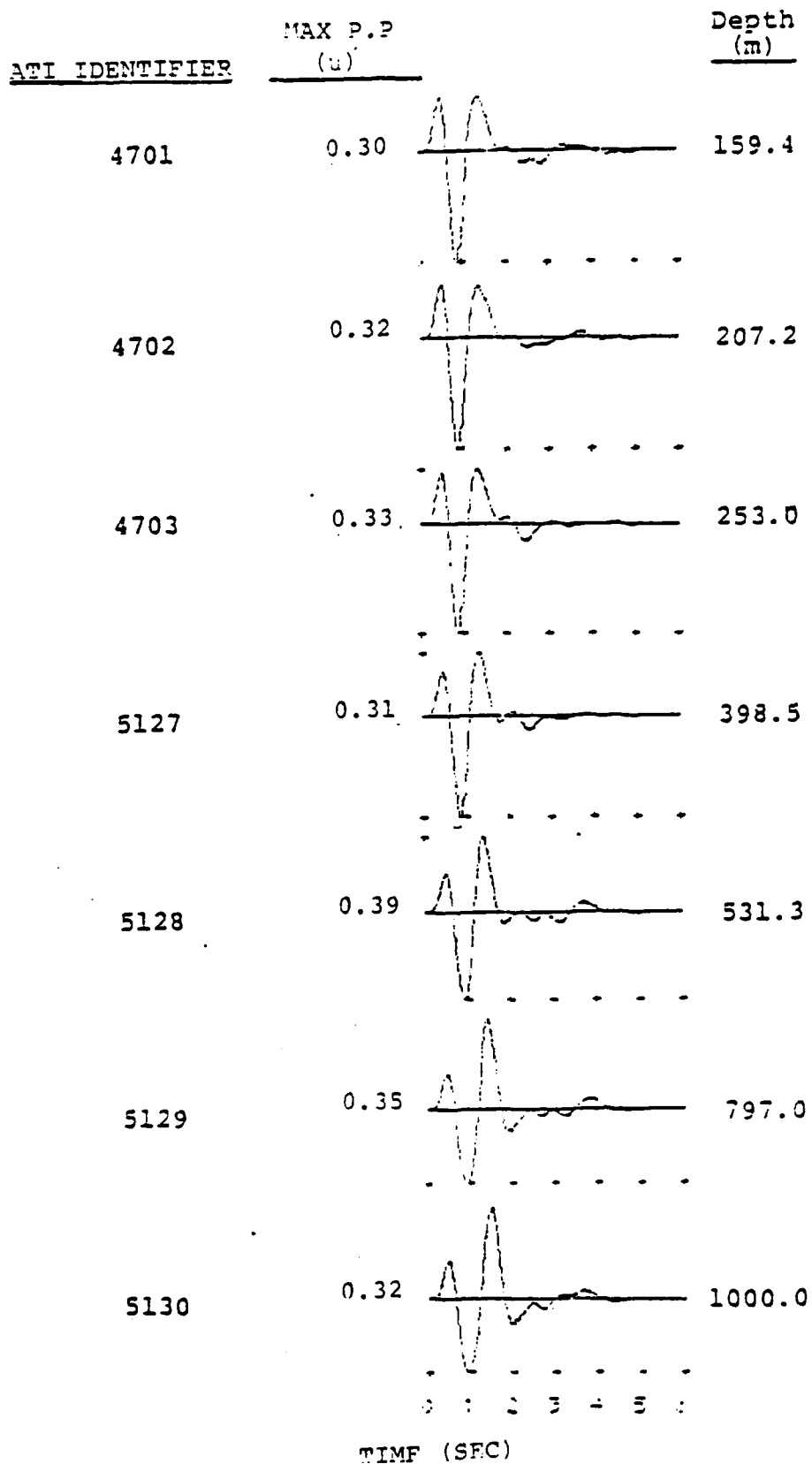
Figure 15. Synthetic body wave seismograms for seven ATI calculations of explosions in granite. The maximum peak-to-peak amplitude in microns at one Hertz is listed at the left of each seismogram.

50

$$m_b^A = \log \left(\frac{A}{T}\right) + 3.25, \tag{19}$$

where A and T are the appropriate amplitude (corrected for instrument response) and period and 3.25 is the distance correction for 4000 kilometers.

The magnitudes are listed in Table 5. Note that the apparent period of the b and c phases decreases slightly with depth to 253 meters (the maximum depth at which cratering occurred), then increases thereafter.

The m_b^b and m_b^c are plotted versus depth in Figure 16. Also plotted are the M_s from Figure 8 and the residuals, $m_b^b - M_s$ and $m_b^c - M_s$. The dependence of m_b and M_s on depth is quite similar except for the point at 253 meters depth. At that point there is a sharp minimum in the M_s that is not present in the body wave magnitudes.

3.7   ANALYSIS OF m_b DATA

The short period P wave seismograms for the two-dimensional ATI calculations can be studied by comparing them to analogous seismograms computed with a one-dimensional RDP source. Such a comparison is shown in Figure 17. The seismograms for the two-dimensional ATI sources from Figure 15 appear in the center column. In the left column we show seismograms at the same depth for a constant RDP source which is the Mueller/Murphy RDP computed at the shallowest depth, 159.4 meters. Thus, only the P-pP lag time changes with depth for the seismograms in the left column.

In the right column in Figure 17 we show the seismograms for the Mueller/Murphy RDP source with the depth scaling included. The source functions used for these seismograms were plotted in Figure 9. With increasing depth, the source function gets smaller and the peak moves to higher frequencies. The b phase magnitude, m_b^b, and the associated period, T_b, are listed with each seismogram and they have the expected trend.

51

TABLE 5

m_b FOR SEVEN ATI CALCULATIONS OF EXPLOSIONS IN GRANITE

Calculation	Depth	b (nm)	T_b (sec)	m_b^b	c (nm)	T_c (sec)	m_b^c
4701	159.4	200	0.78	5.56	262	0.88	5.72
4702	207.2	215	0.77	5.70	263	0.86	5.74
4703	253.0	209	0.76	5.69	256	0.84	5.73
5127	398.5	194	0.78	5.62	244	0.84	5.71
5.28	531.3	246	0.86	5.71	347	0.89	5.84
5129	797.0	219	0.92	5.62	340	0.97	5.79
5130	1000.0	202	0.93	5.59	325	1.01	5.76
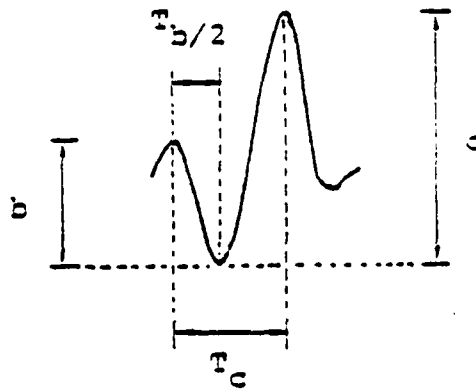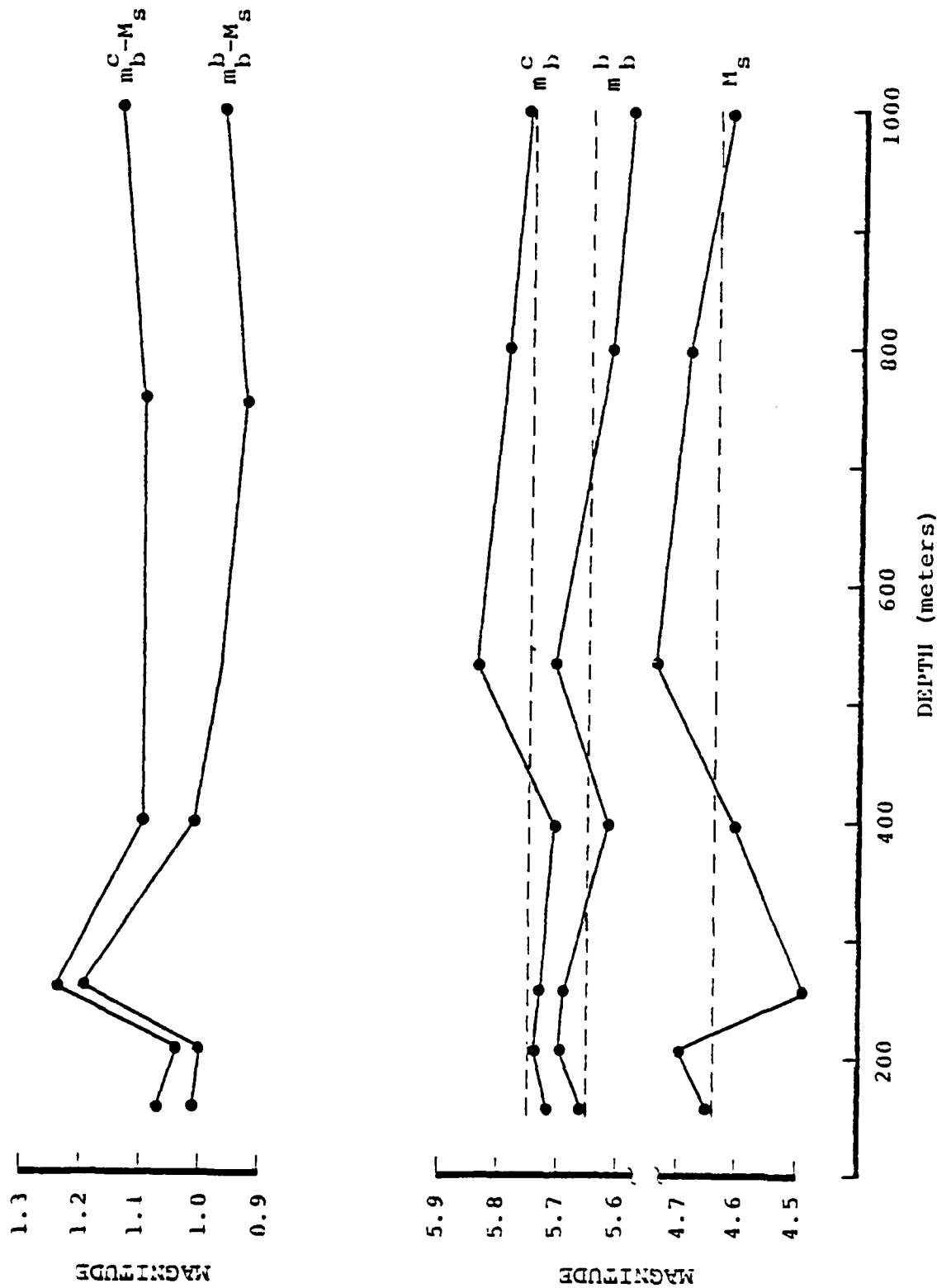
Figure 16. The body and surface wave magnitudes and their differences are plotted versus source depth. The dashed line is drawn for reference at the mean value of the magnitude.

53
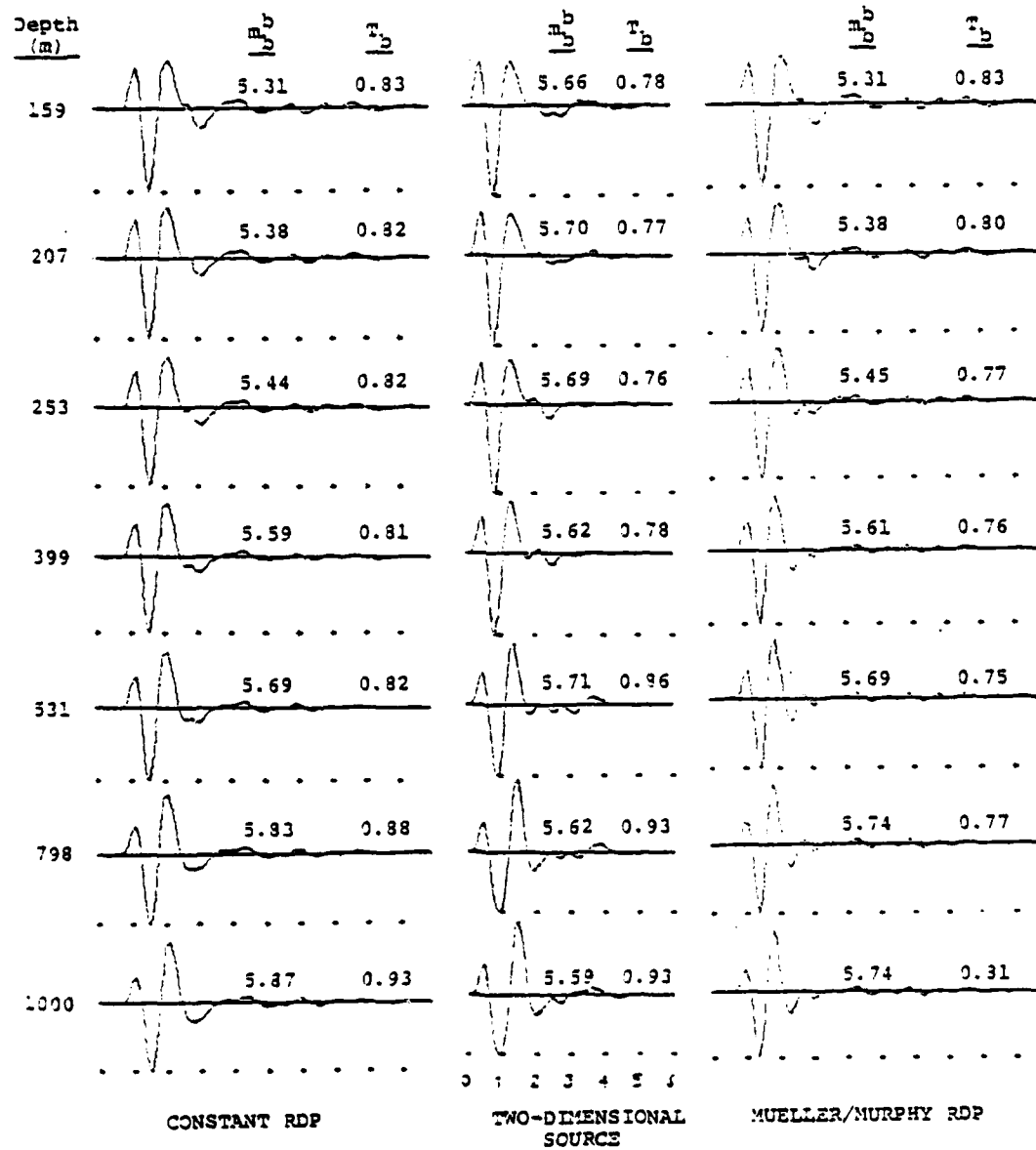
Figure 17. Comparison of the short period body wave seismogram for the ATI granite source calculations with seismograms computed with a spherically symmetric RDP source.

54

Comparison of the waveforms in Figure 17 suggests that the two-dimensional source calculations give body waves that do look much like the simpler P + pP seismograms from the one-dimensional sources. We see that the second peak is initially the same size as the first, then gets larger as the P and pP constructively interfere.

The ATI calculations include nonlinear material behavior all the way to the free surface. In fact, the first three formed a crater. Thus, we would expect the free surface reflected phase to be somewhat different from the pP of elastic theory.

In Figure 18 we again plot the body wave seismograms for the ATI calculations and compare them to seismograms computed with the Mueller/Murphy RDP. This time the source is modified to completely suppress the pP (left column) or to halve it. The waveform comparison suggests that substantial suppression of pP is not occurring for the greater source depths. However, this may be a more reasonable model at the shallow depths.

These seismogram comparisons are placed on a more quantitative basis in Figures 19, 20 and 21. In these figures, we compare the magnitude and period data taken from the seismograms in Figures 17 and 18.

In Figures 19 and 20 we plot the magnitude data from the seismograms. First, we point out that we are most concerned with comparing the trends with increasing depth. However, the absolute magnitudes are quite close, especially for depths of 350 to 550 meters. This is interesting, but we are not quite sure what it means.

From the comparisons in Figures 19 through 21, we draw the following conclusions:

- When the RDP source calculations include an elastic pP, as in Figure 17, the magnitude

55
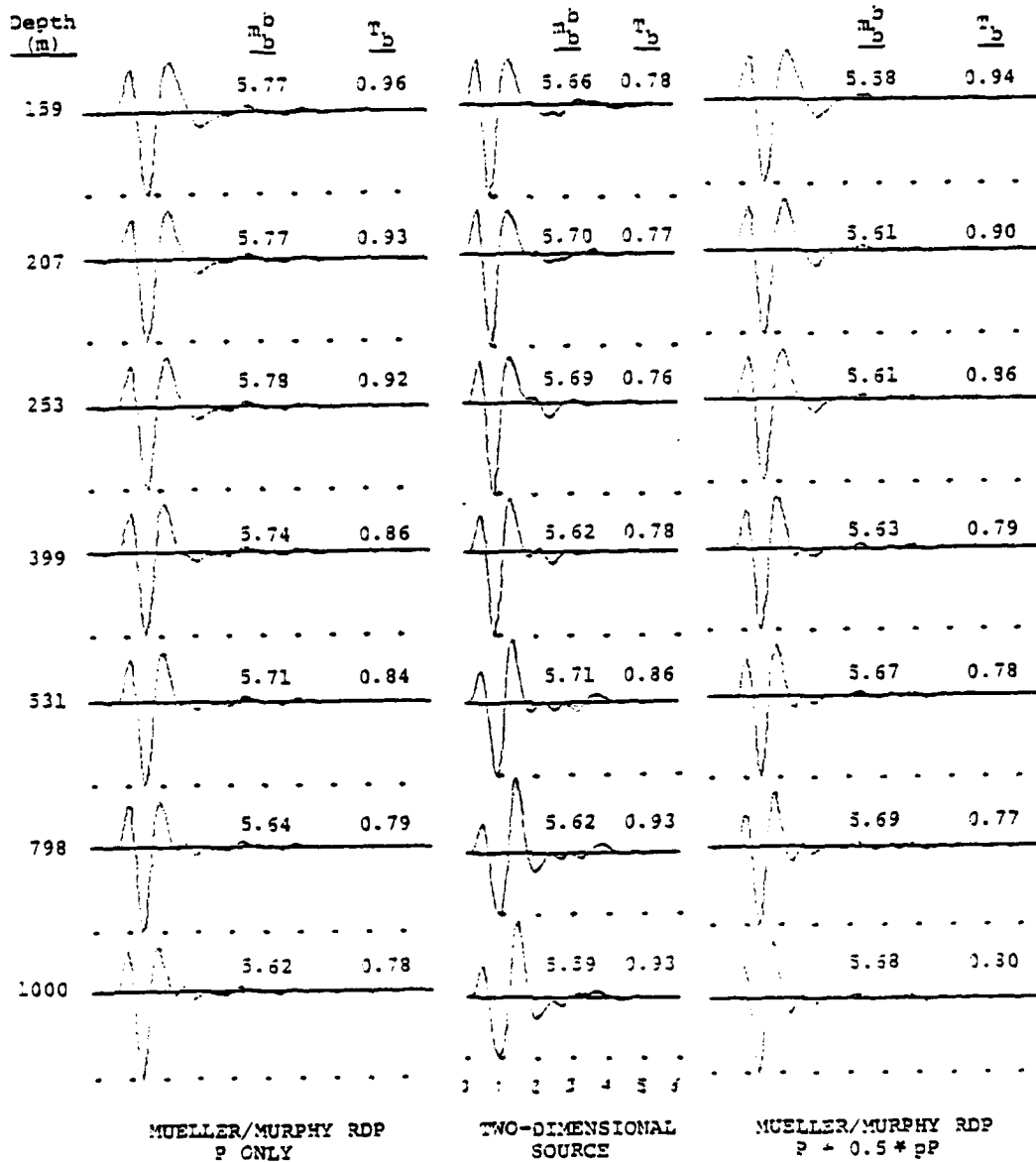
Figure 18. The body wave seismograms for the ATI sources are compared to those for modified versions of the Mueller/ Murphy RDP.
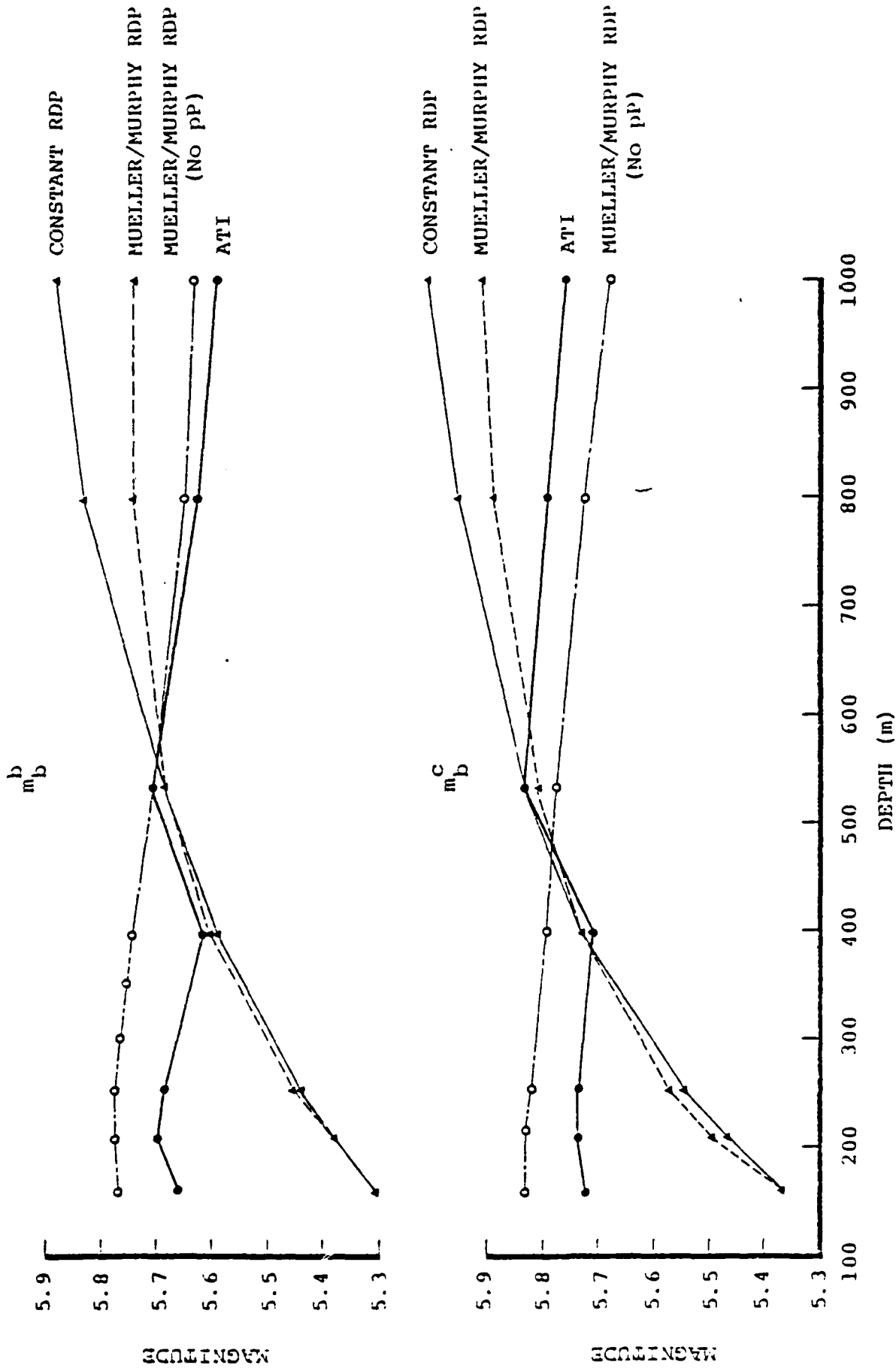
Figure 19. The magnitude data from the seismograms of Figures 17 and 18 are plotted versus source depth.

57
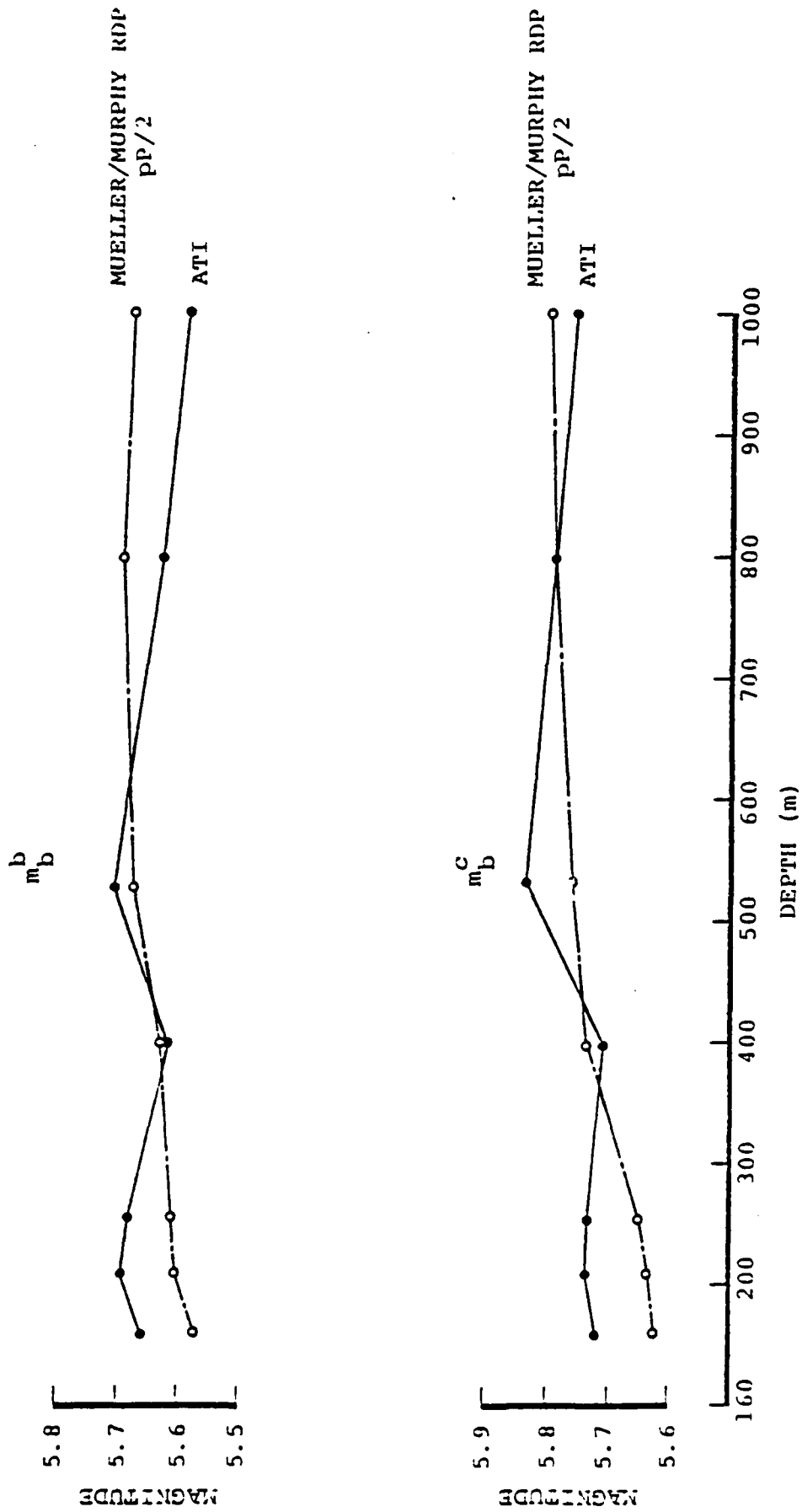
Figure 20. The magnitude data for two of the seismogram set given in Figure 18 are plotted versus source depth.

58
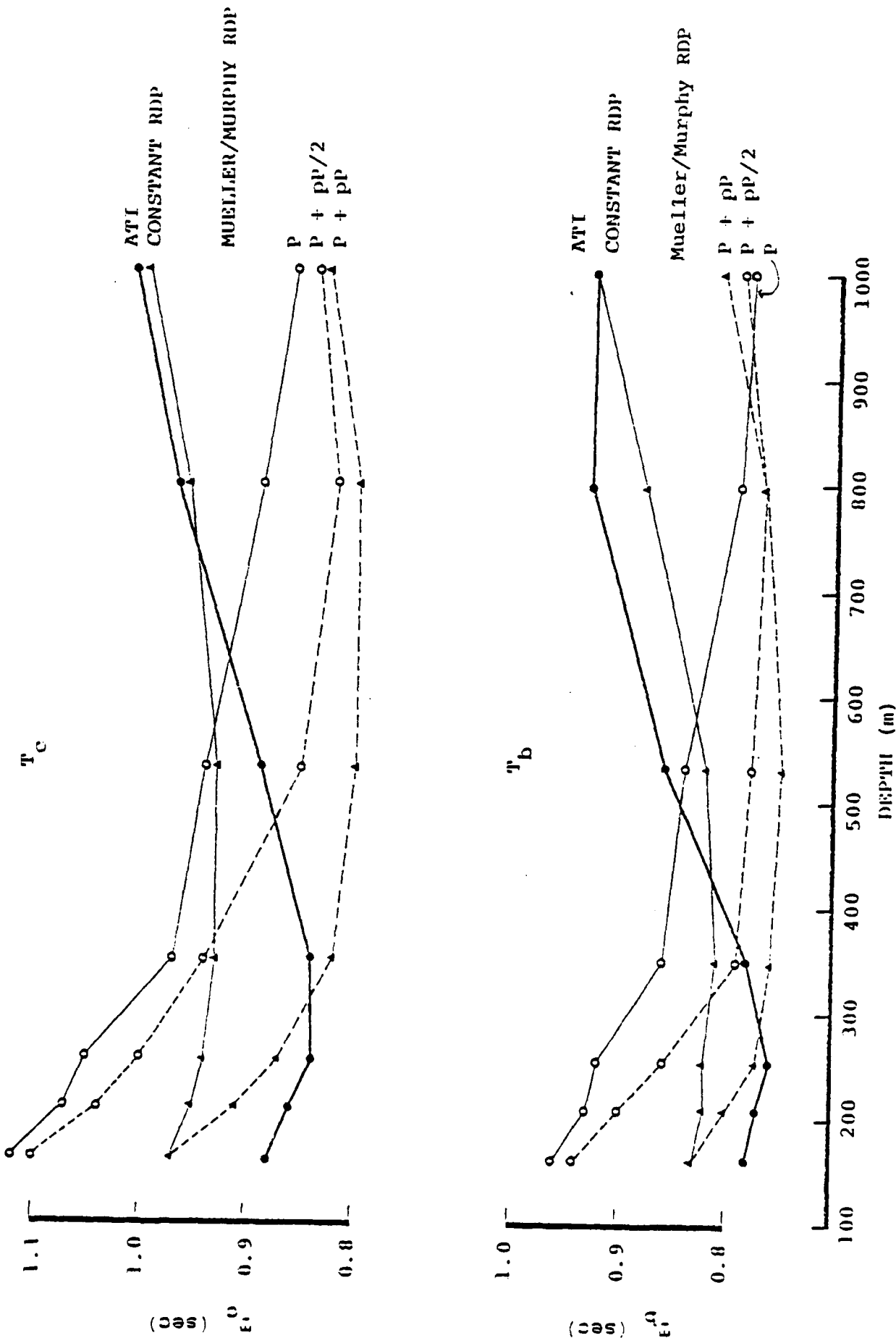
Figure 21. The periods measured from the seismograms in Figures 17 and 18 are plotted versus source depth.

65

increases with depth. The ATI 2-D calculations do not show this behavior, especially at shallow depths.

- The closest agreement with the magnitude depth dependence of the 2-D calculations is when all or part of pP is suppressed in the RDP source calculations. The filter that suppresses pP is certainly more complicated than the frequency-independent factor used here, but the ATI calculations seem to support the idea that some suppression has taken place.

- Comparison of the measured periods shows the worst agreement for the pP suppressed cases and the best agreement for the constant RDP source. This is an indication that the ATI calculations do not show the large corner frequency shift with depth predicted by the Mueller/Murphy model.

3.8 SUMMARY

We have computed body and surface wave seismograms for the ATI calculations and have determined the m_b and M_s associated with these calculations. The actual values of the magnitudes are to some degree dependent on the details of the path models chosen. However, the changes with source depth appear to be nearly path independent.

Neither m_b nor M_s is very strongly dependent on depth. The largest effect is on M_s for the shallow depths, with the value at 253 meters depth being most noticeable. The source coupling into both body and surface waves decreases steadily below 500 meters. At shallower depths, nonlinear free surface effects are likely to obscure the smoother effect of changing overburden pressure.

60

The results for the ATI calculations have been analyzed by comparing to seismograms computed with the one-dimensional reduced displacement potential model usually used to represent the seismic source function. This comparison highlights the influence of two-dimensional effects. The standard for comparison is the Mueller/Murphy semi-empirical RDP for granite, which is based upon observations of SHOAL. The magnitudes for the ATI two-dimensional calculations are in close agreement with those from the Mueller/Murphy model at depths near 400 meters. The long period level of the Mueller/Murphy model decreases more rapidly with depth than does that of the ATI calculations, as is seen in the M_s comparison in Figure 13. The M_s for the ATI calculations also includes the effect of nonlinear interaction with the free surface, including spallation, which is not easily quantified.

The m_b comparison between one- and two-dimensional sources was made in the previous section and our conclusions were summarized. Again, the depth dependence of both amplitude and corner frequency is less than predicted by the Mueller/Murphy model. The comparison indicates that the pP is influenced by nonlinear interaction with the free surface.

In the next two sections we will be describing similar two-dimensional calculations done by S-Cubed for explosions in granite. Then in Section VII we will discuss the entire set of two-dimensional granite calculations and summarize the important conclusions.

61

THIS PAGE LEFT BLANK

IV. S-CUBED GRANITE CALCULATIONS

4.1 INTRODUCTION

Four calculations of explosions in granite were done at
S-Cubed. These were two-dimensional, axisymmetric calculations;
that is, the geometry is essentially the same as for the ATI
calculations discussed in previous sections. In this section, we
describe the general features of these calculations and the stresses
and displacements monitored in the elastic response regime. These
data were processed with the techniques described in Appendix A to
construct synthetic seismograms and the results will be described in
Section V.

The S-Cubed calculations are intended to represent explosions
in the PILEDRIVER environment. The first of these was an attempt to
specifically model the PILEDRIVER event. Rimer, et al. (1979)
describe this calculations and compare computed velocity and
displacement time histories to the observed data at some 25
near-field gauges. This is essentially the entire near-field data
base.

The PILEDRIVER geometry used for the calculation and the gauge
locations are shown in Figure 22. The data were collected by SRI
(Hoffman and Sauer, 1969), except the shot level stations 8-SL and
16-SL which were collected by Sandia Laboratories (Perret, 1968).
The layered geologic model was constructed from P wave arrival time
data in these reports and in a description of the nearby HARDHAT
event (Swift, 1962). The shear wave velocity was based on an
assumed Poisson's ratio of about 0.3.

As described by Rimer, et al. (1979), the S-Cubed PILEDRIVER
calculation included an effective stress law to account for the
water present in the jointed granite below the water table. The
void crush-up that is important above the water table was accounted
for by a P-α model (Cherry, et al, 1975). Tensile cracking is

63
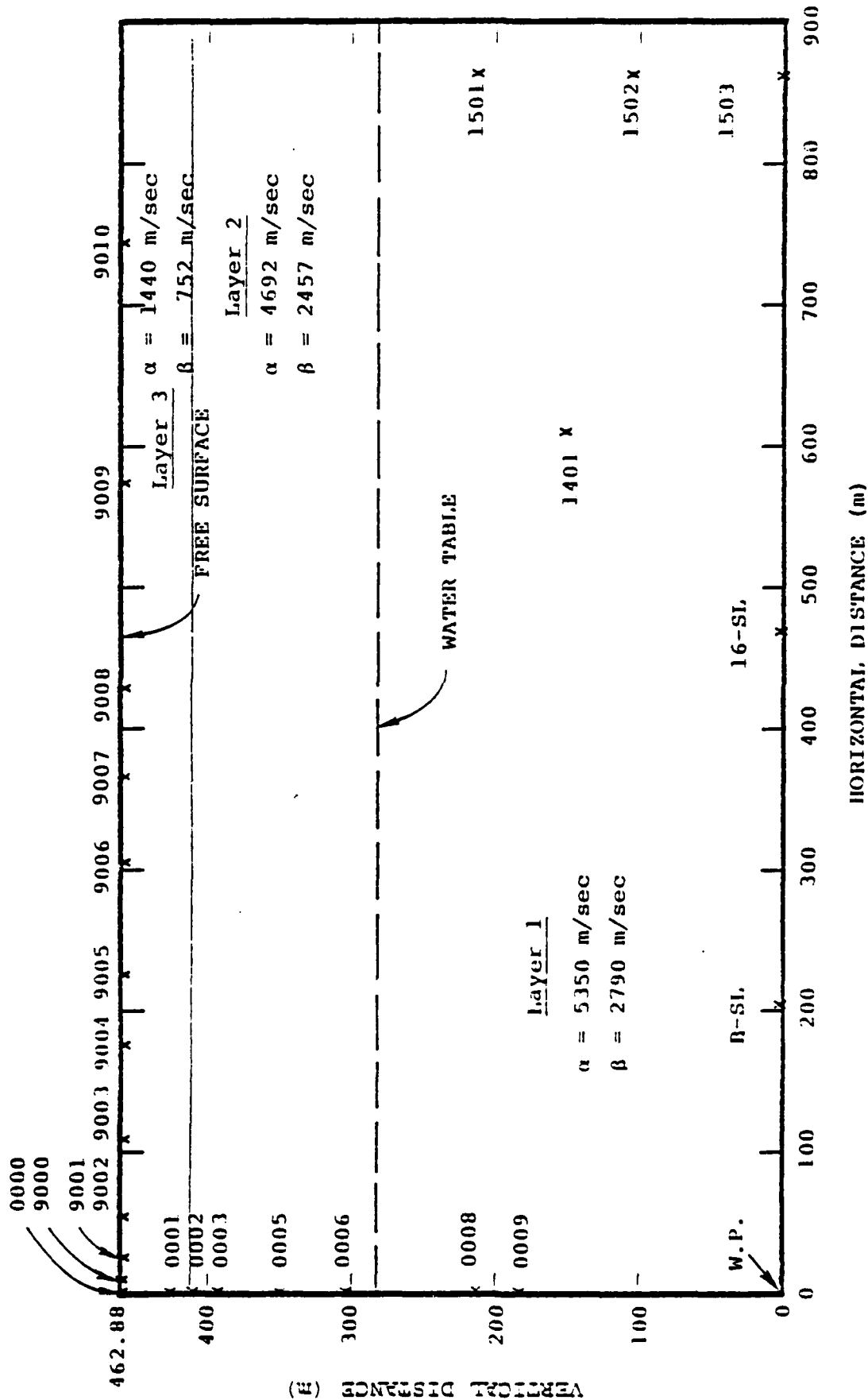
Figure 22. Assumed layered geology and location of gauge stations for PILEDRIVER and other S-Cubed granite calculations.

64

important in the entire region surrounding the explosion and especially near the surface where spallation and subsequent spall closure are important contributors to the ground motions.

In Figures 23 and 24 we compare the computed and observed velocity time histories at two of the stations, one at shot level and one on the surface. These, and the complete set of comparisons given by Rimer, et al. (1979), indicate that the main features of the ground motion have been modeled rather well. The main discrepancy is that spallation effects are too large within 300 meters of ground zero. There are other details that are not matched by the calculation, but much of the discrepancy can reasonably be attributed to the elementary axisymmetric geometry. Also, little information about the constitutive properties of the weathered rock near the surface was available. A poor model for this layer is probably the explanation for the surface spallation being too large.

Having made a satisfactory calculation of PILEDRIVER, the yield and burial depth were varied and three more calculations were done. These are the four S-Cubed granite calculations to be discussed in this report.

4.2 SOURCE DESCRIPTION

The four S-Cubed granite calculations were for three depths and three yields. These are:

Identifier	Depth (m)	Yield (kt)
PD1	460	60
GRAN1	1000	150
GRAN2	1000	20
GRAN3	400	20

The source region was a layered halfspace meant to represent the PILEDRIVER environment. This structure is given in Table 6. Note that the granite at the source depths is a higher velocity material than the ATI granite ($\alpha = 4.4$ km/sec, $\beta = 2.54$ km/sec). The shear modulus is 20% larger (206 kbar compared to 172 kbar).

65
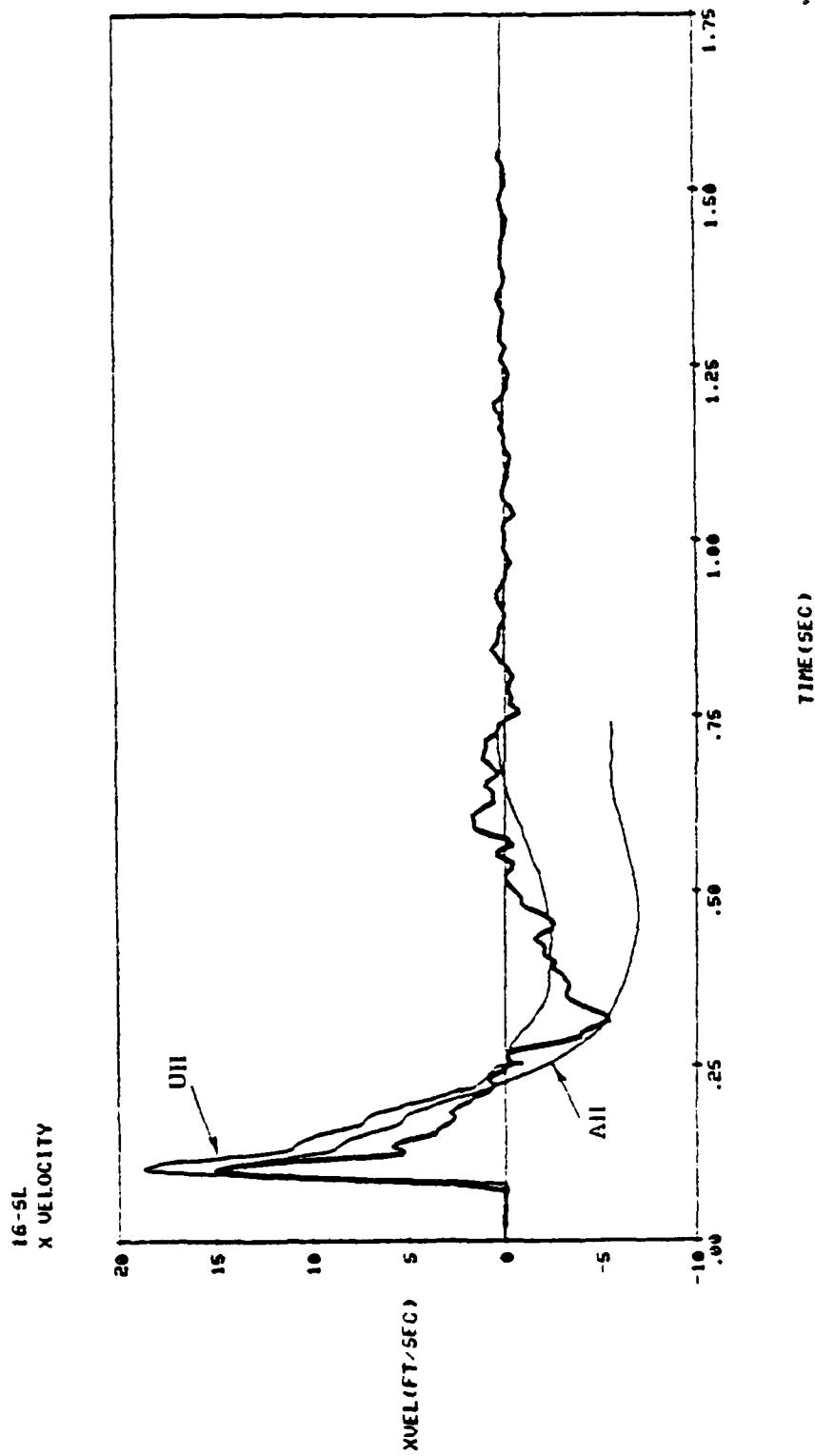
Figure 23. Measured and calculated (heavy line) horizontal velocities at shot level station 16-SL (range = 470 m). The data marked UH are from a velocity gauge while AH indicates an integrated accelerometer record.

66
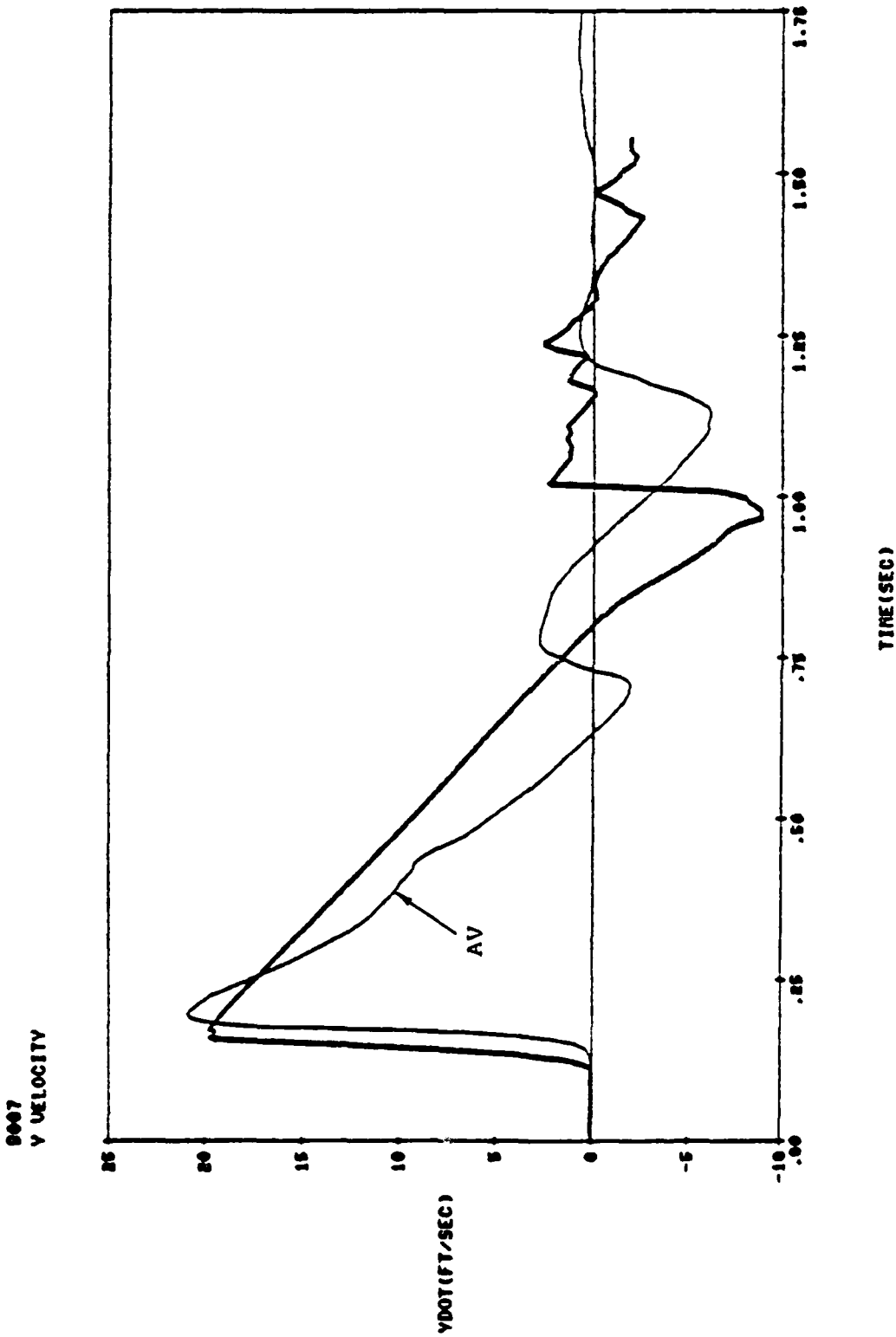
Figure 24. Measured and calculated (dark line) vertical velocities at free surface station 9007 (horizontal range – 368 m). The data were obtained by integrating an accelerometer record.

67

The velocities, $\dot{u}_z^M$, $\dot{u}_r^M$ (r,z,t), and stresses, σ_{rr}^M, σ_{zz}^M, σ_{rz}^M (r,z,t), were monitored at stations on a cylindrical surface surrounding the region of inelastic material response. The radius and depth to the bottom of this cylindrical surface are listed in Table 7, together with the number of monitoring stations on the side and bottom. The station spacing is about 25 meters for all but GRAN1, where it is 50 meters. This compares to the ATI calculations where the station spacing was about 50 meters.

In Figure 25 we plot some representative velocity and stress time histories for each of the calculations. The GRAN2 calculation is very close to completion, since the velocities are nearly zero on the monitoring surface. The others have been terminated at a time when motion is not entirely stopped at the monitoring surface. The GRAN1 is probably the worst in that respect.

Note that the monitored stresses attain static values that are a significant fraction of the peak values. This is in contrast to the ATI calculations where the static tractions were very small. The reason is the much smaller scaled distance to the monitoring surface in the S-Cubed calculations (the radius of the monitoring surface in the ATI calculations was about 2.1 kilometers). The static stresses decay approximately as $1/R^3$.

In Figure 26 we plot the values of the monitored stresses at the last time point versus position on the monitoring surface. These are remarkably smooth except near the free surface.

4.3 THE VERTICAL FORCE AND IMPULSE

For these calculations the vertical force and impulse are given by

$$F_z(t) = 2\pi \int_0^a \sigma_{zz}^M(r_0, b) \, r_0 dr_0 + 2\pi \int_0^b a \, \sigma_{zr}(a,z) \, dz, \quad (20)$$

TABLE 6

SOURCE REGION STRUCTURE FOR S-CUBED GRANITE CALCULATIONS

Depth (km)	Thickness (km)	α (km/sec)	β (km/sec)	ρ (km/sec)
0.05	0.05	1.44	0.752	2.65
0.18	0.13	4.69	2.46	2.65
∞	∞	5.35	2.79	2.65

TABLE 7

MONITORING STATIONS FOR S-CUBED GRANITE CALCULATIONS

Identifier	Source Depth (km)	Yield (kt)	Monitoring Depth (m)	Surface Radius (m)	Number of Stations Bottom	Side
P01	460	60	1057	1200	45	54
GRAN1	1000	150	1696	1088	22	36
GRAN2	1000	20	1391	1088	44	61
GRAN3	400	20	838	1088	44	39

69
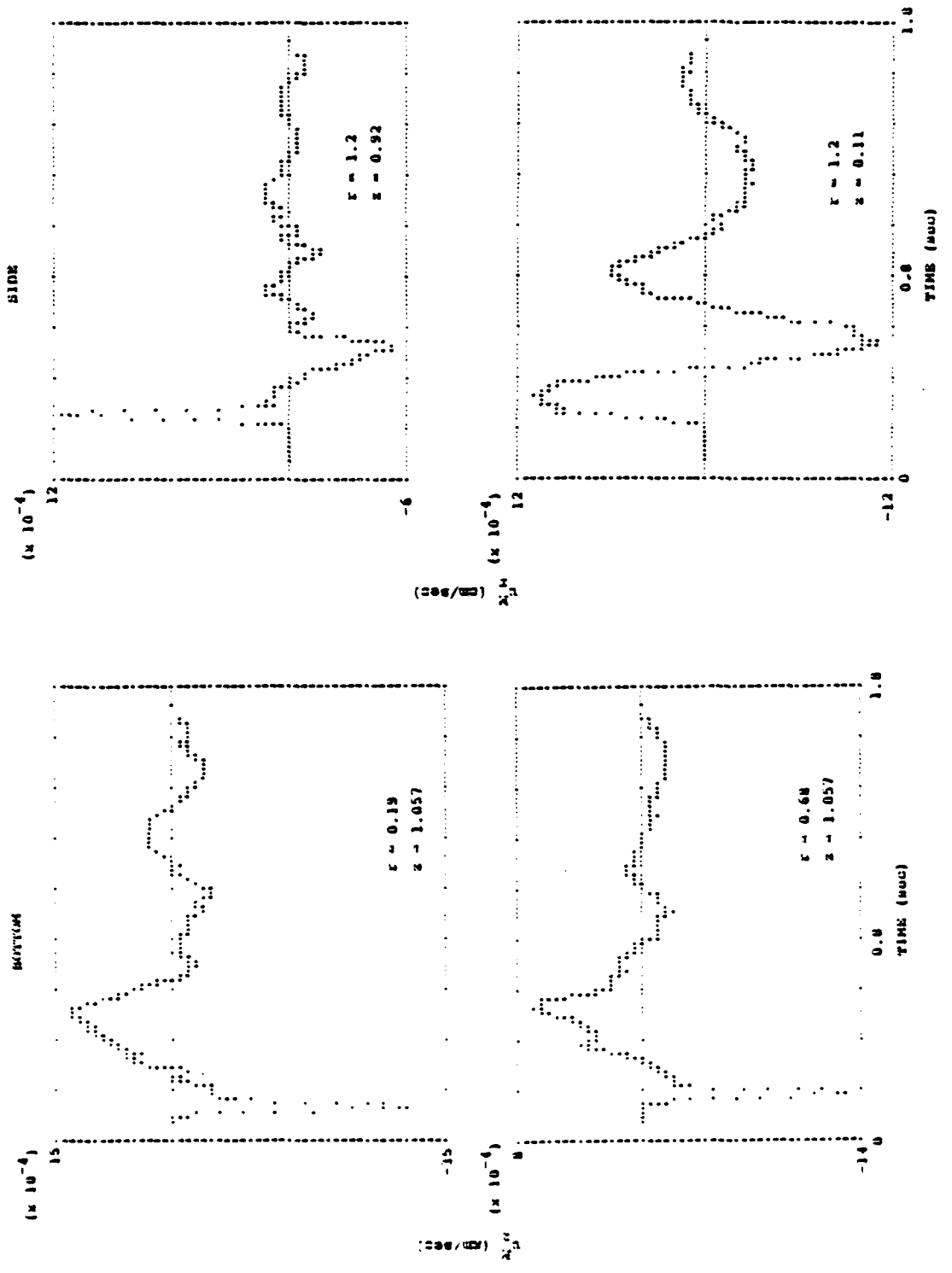
Figure 25. The monitored velocities and tractions are plotted at selected positions (r and z in kilometers). For consistent sign conventions, the u_z^m and σ_{rz}^m for PD1 must be inverted.
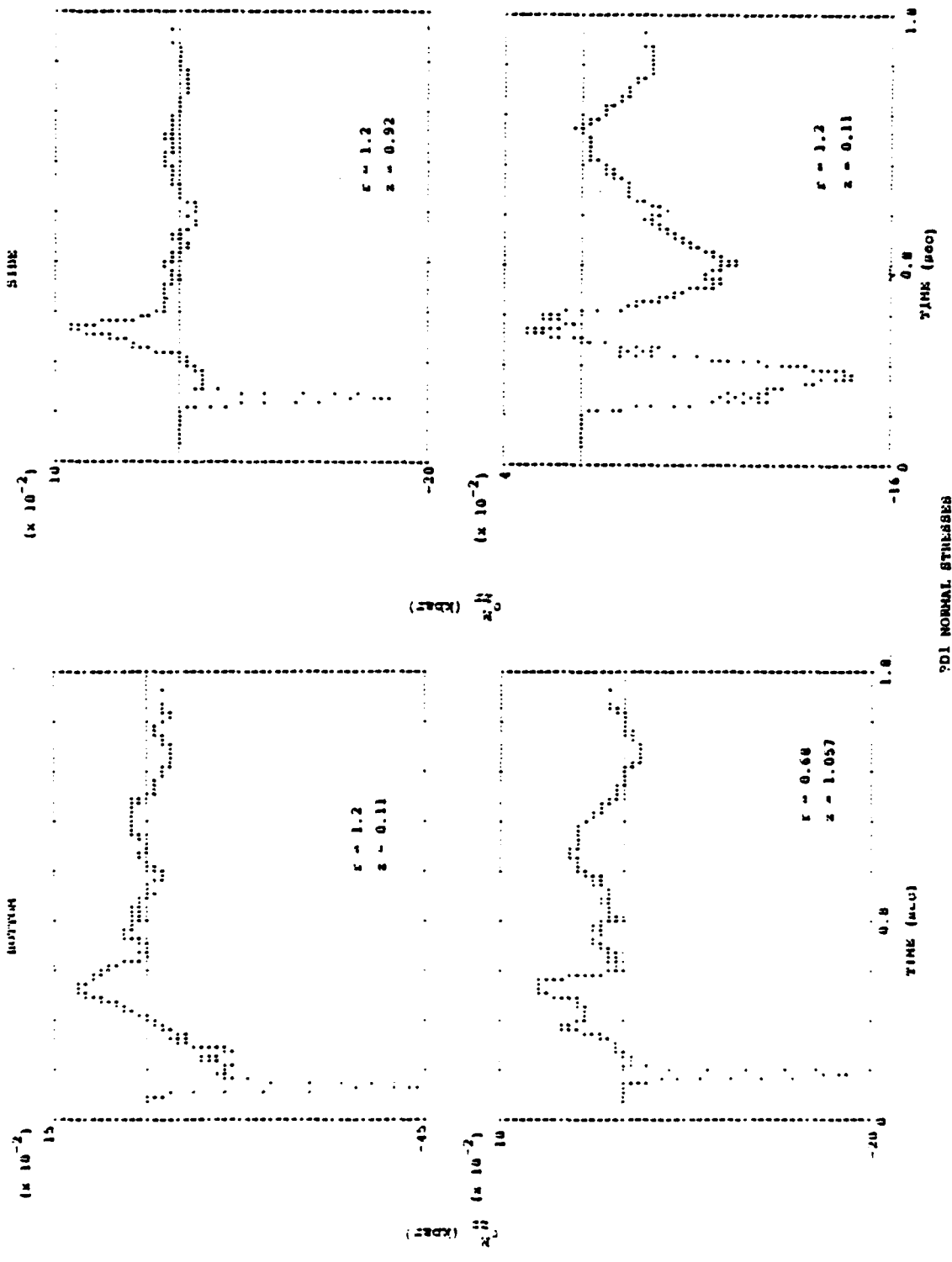
70

Figure 25. (continued)

71

Figure 25. (continued)

72

Figure 25. (continued)

73

Figure 25. (continued)

74
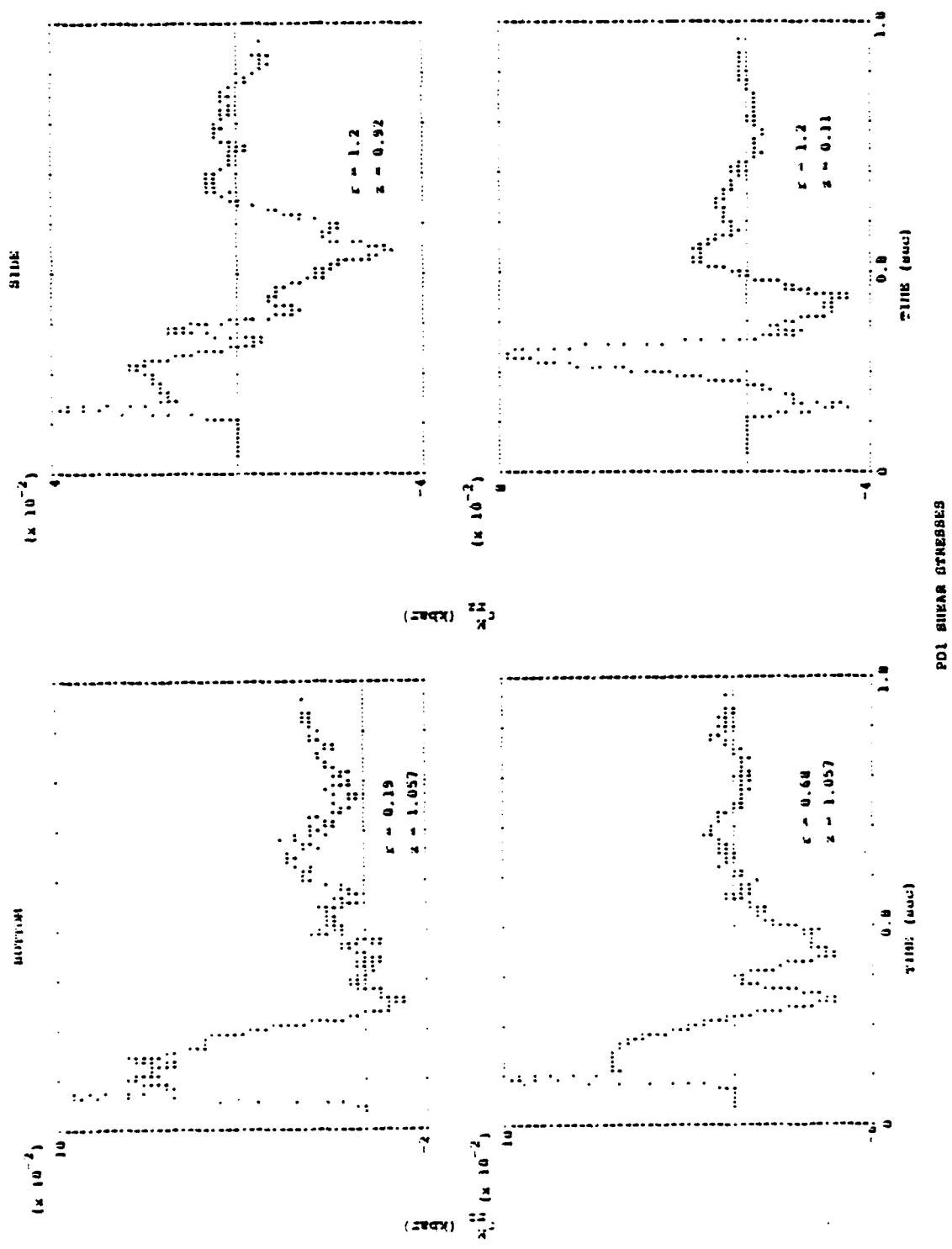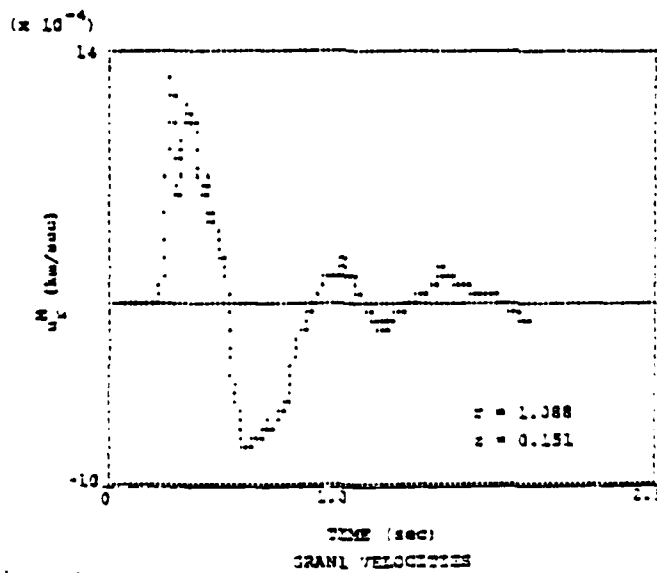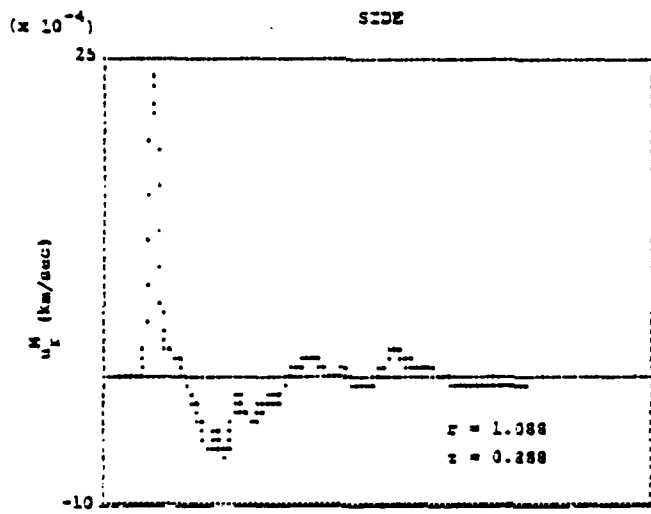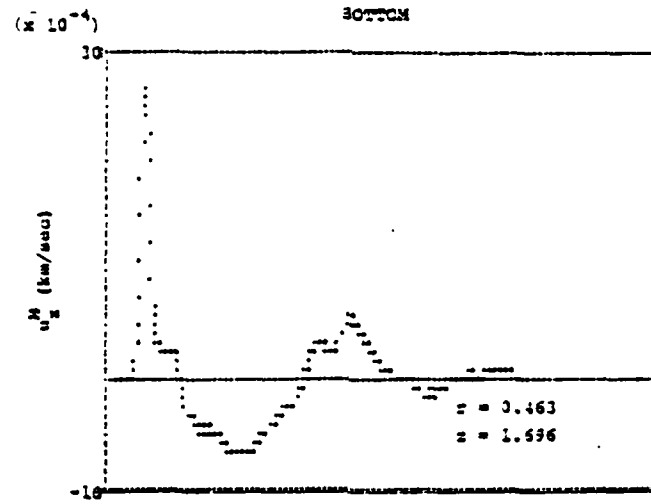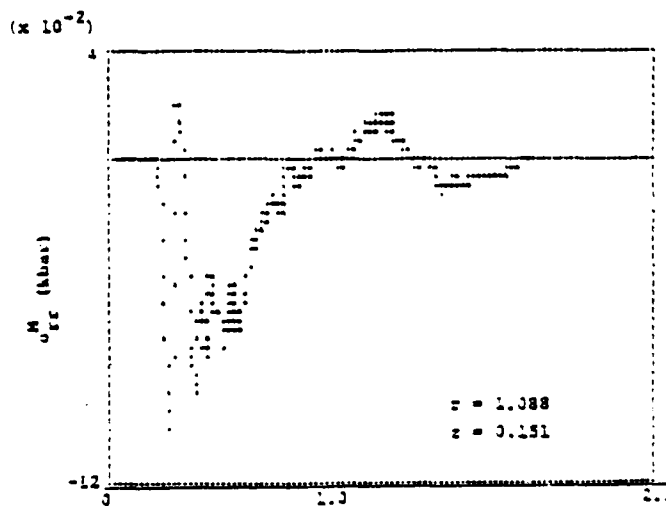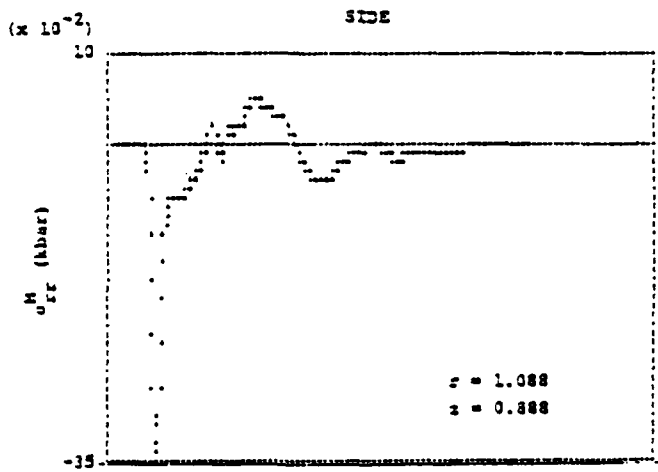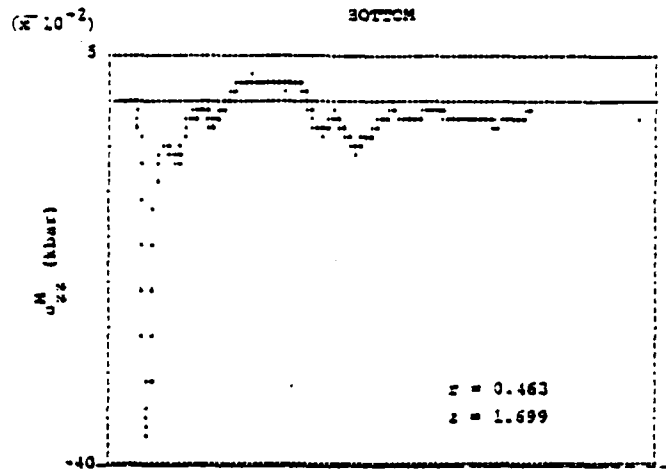
GRANI SHEAR STRESSES

Figure 25. (continued)

75
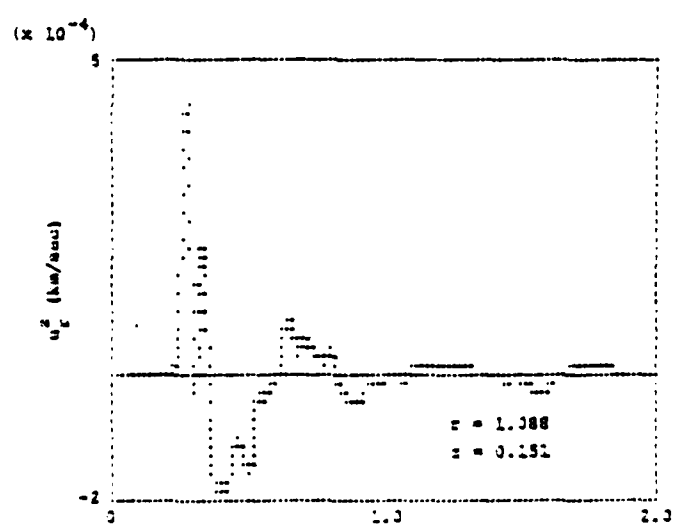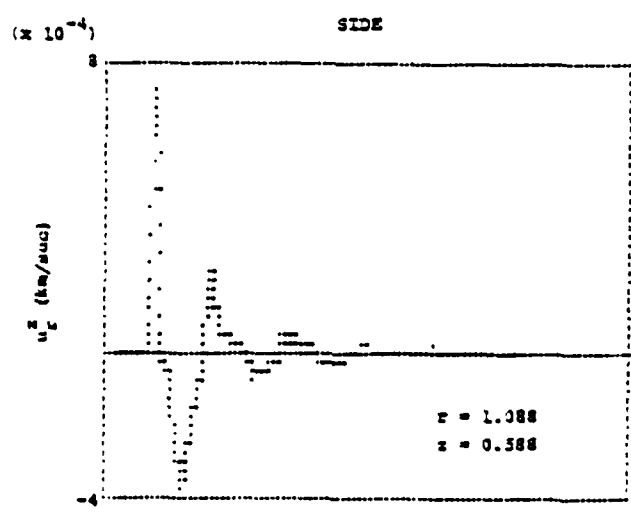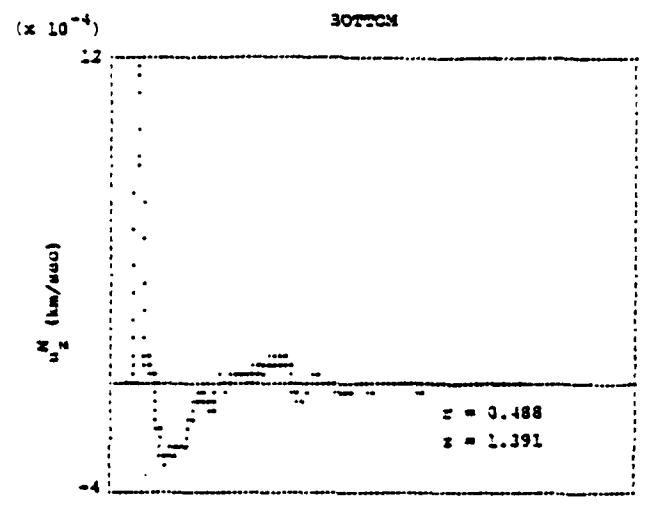
Figure 25. (continued)
GRAN2 VELOCITIES

Figure 25. (continued)

77

Figure 25. (continued)

Figure 25. (continued)

Figure 25. (continued)

80

Figure 25. (continued)

31
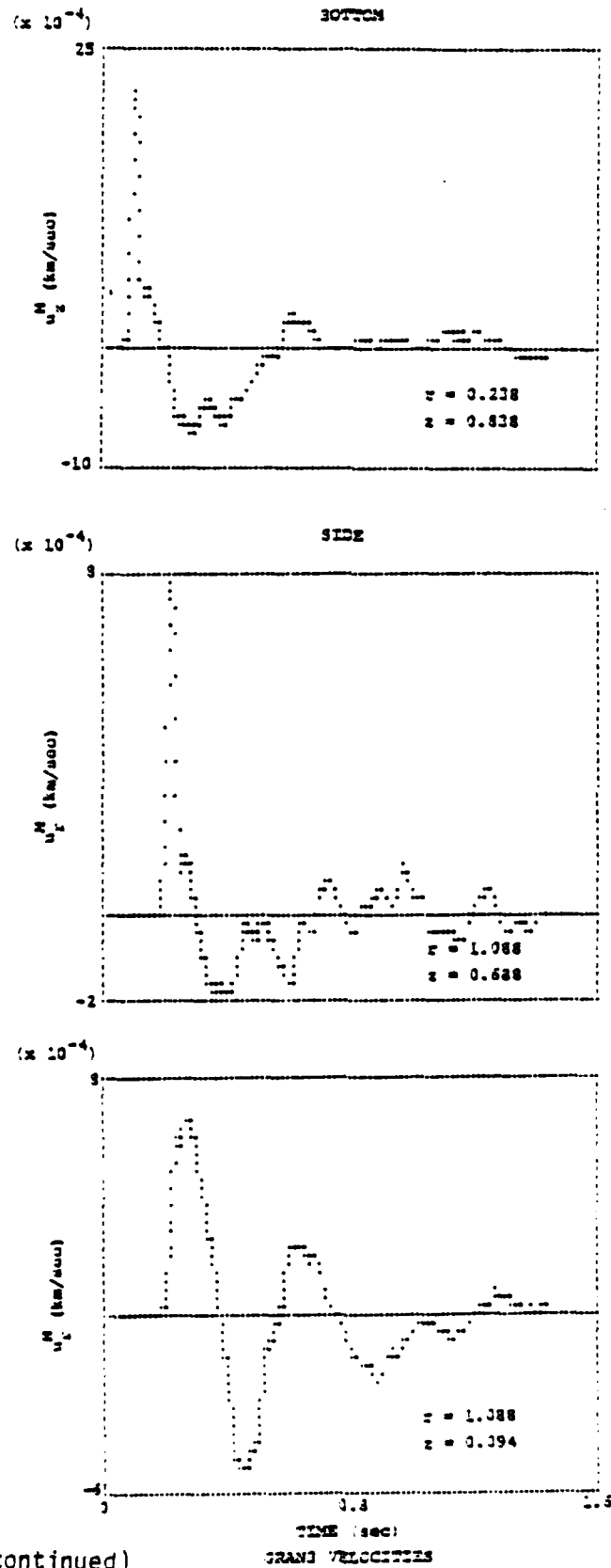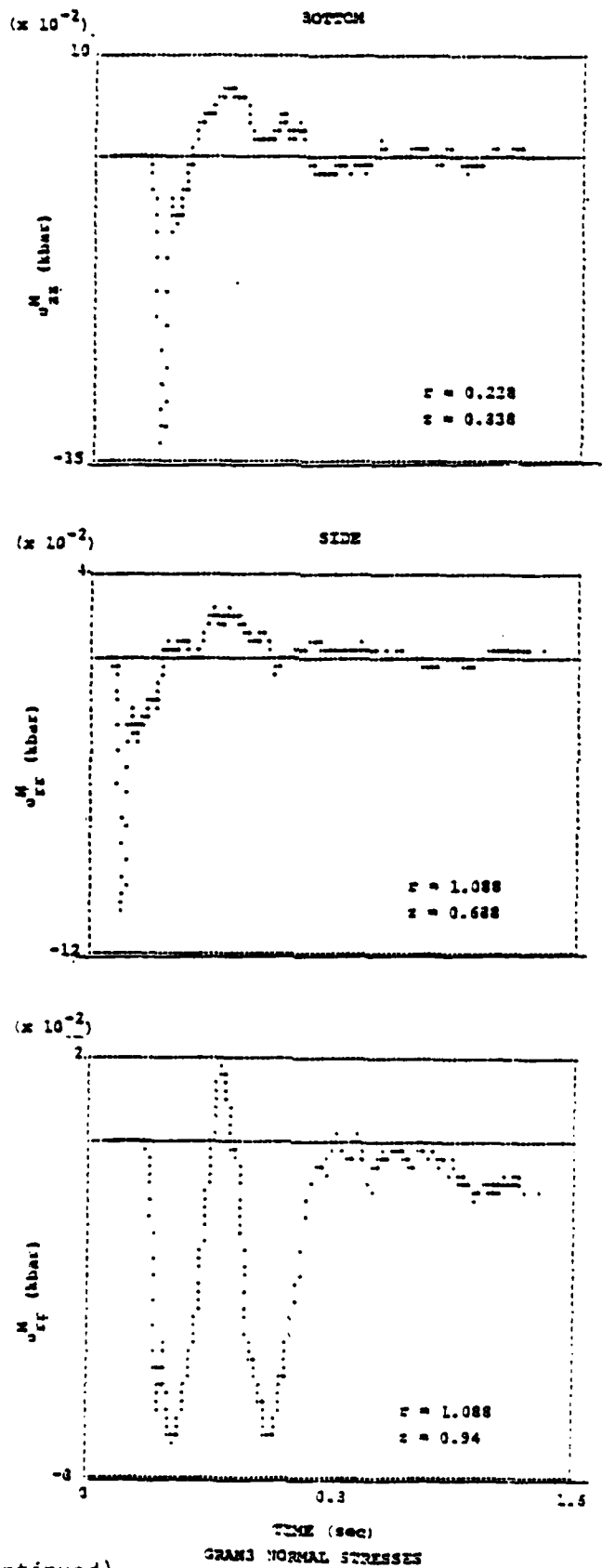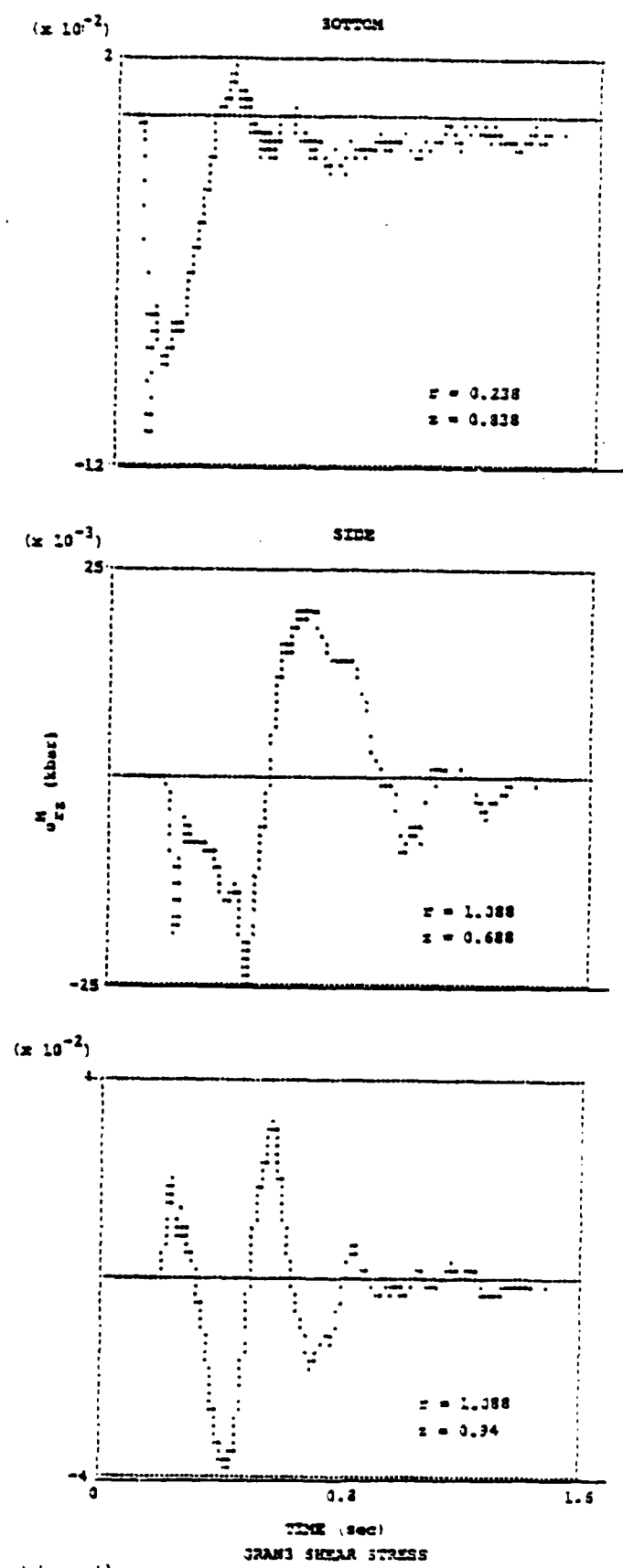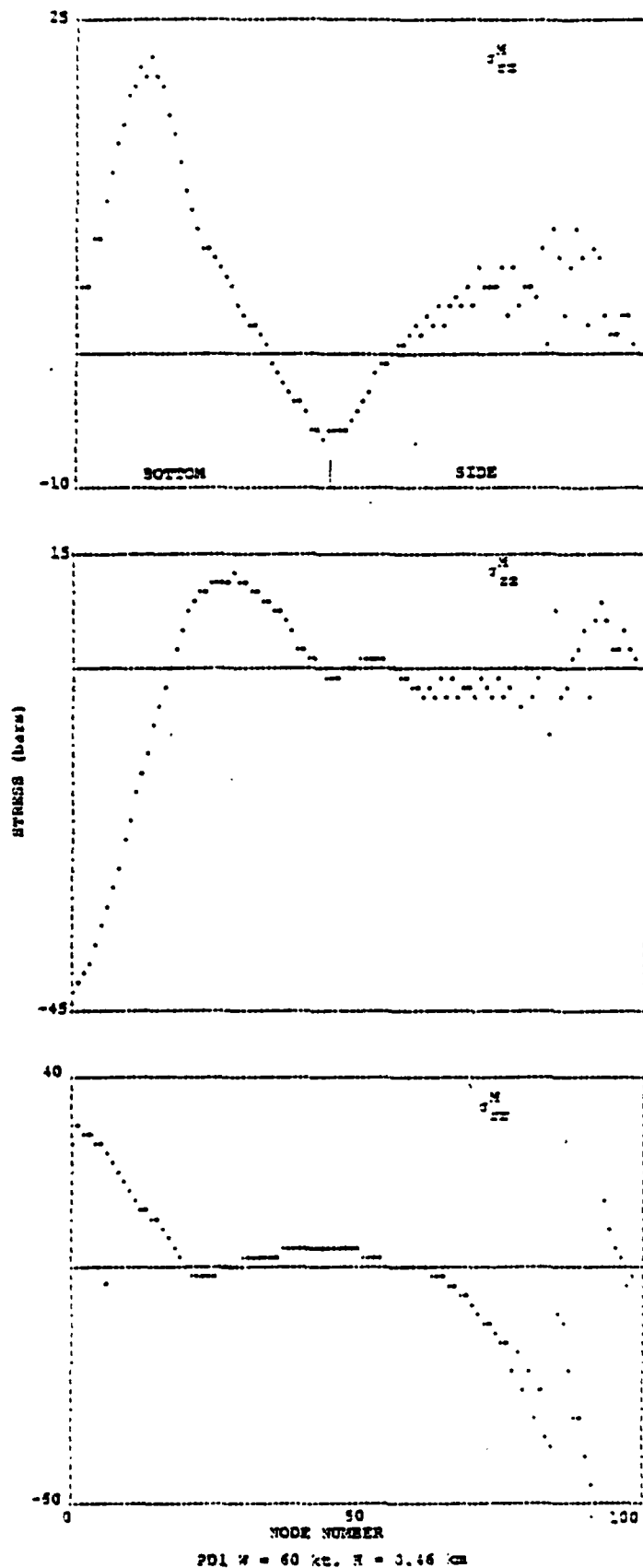
Figure 26. The monitored stresses at the last time point are plotted versus position. The abscissa is actually the node number, starting with 1 at the axis of symmetry and counting across the bottom and up the side of the cylindrical surface.
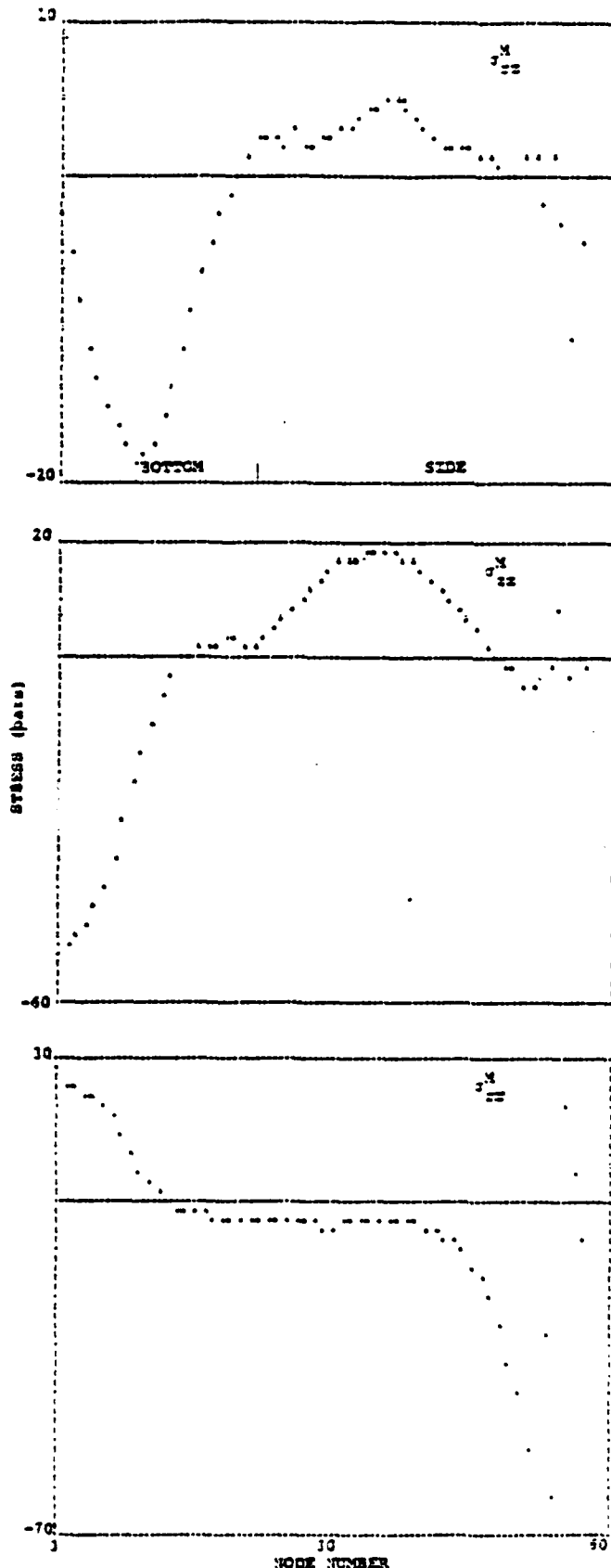
Figure 26. (continued)

83
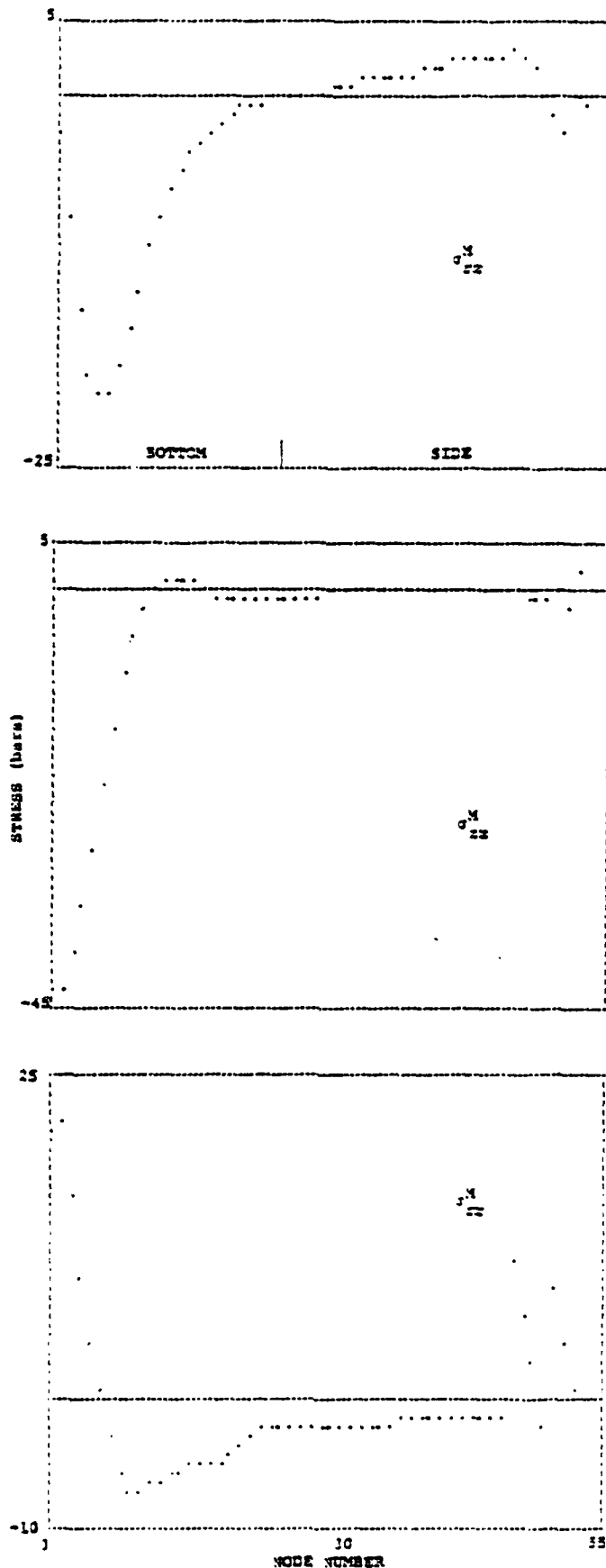
Figure 26. (continued)

Figure 26. (continued)

85
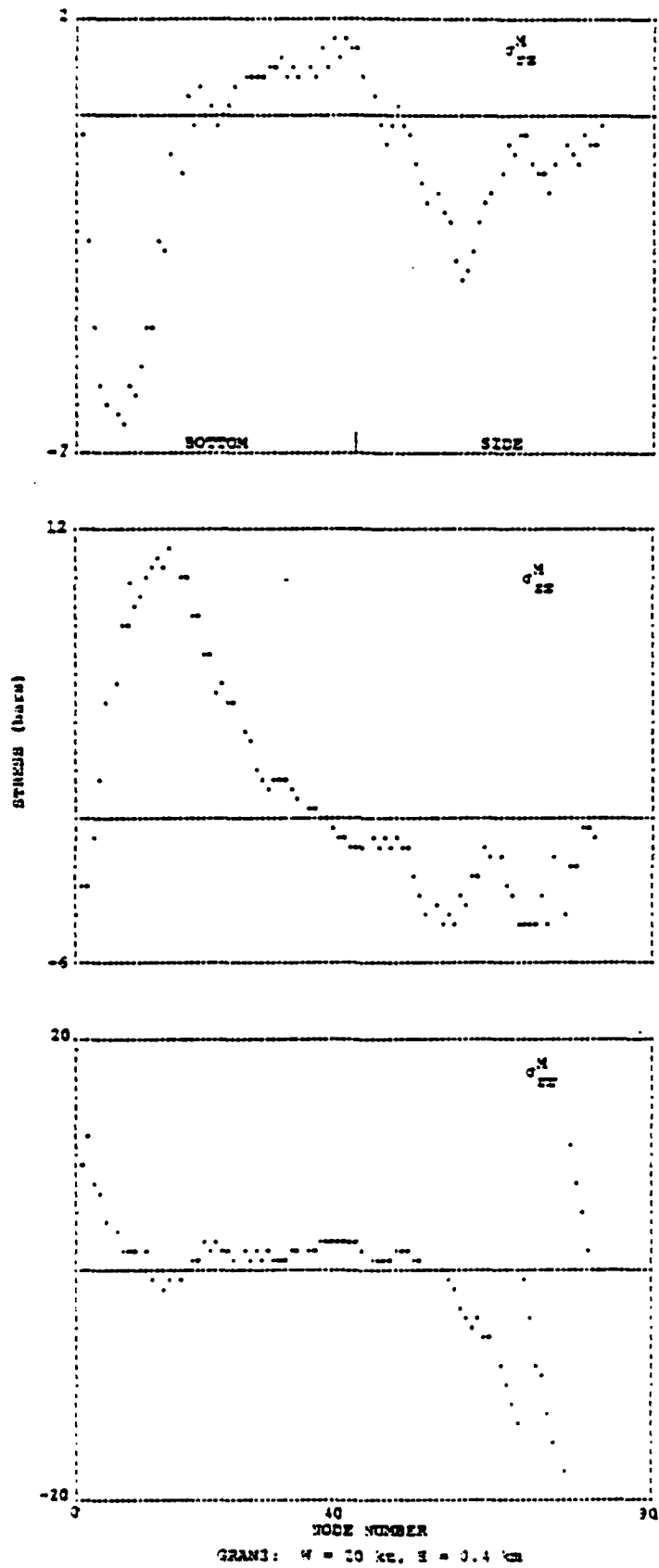
$$I_z(t) = \int_0^t F_z(\tau)d\tau,$$

where a is the radius and b is the depth of the cylindrical monitoring surface. The analogous equations for the ATI calculations are (1) in Section 2.3. In Sections 2.3 and 2.4 we discuss the downward force and impulse in a general way and point out that conservation of linear momentum requires that they vanish at late time. A procedure for applying a correction factor to the vertical tractions to force the calculation to satisfy these conditions was outlined in Section 2.4. In this case, we have the stresses rather than the tractions, and the implementation is slightly different. Once again, we assume that

$$F_z(T_1) = K \quad,$$

$$I_z(T_1) = -L \quad, \tag{21}$$

where $t = T_1$ at the last time step. Then if K and L have the same sign, we can zero the force and impulse in the following way. We add another time step $\Delta t = T_2 - T_1$, such that

$$F_z(T_2) = I_z(T_2) = 0 \quad. \tag{22}$$

This is done by setting

$$\sigma_{zz}^M(r,b,T_2) = \sigma_{zz}^M(r,b,T_1) + \delta\sigma_{zz}^M \quad, \quad 0 \leq r \leq a \quad,$$

$$\sigma_{rz}^M(a,z,T_2) = \sigma_{rz}^M(a,z,T_1) + \delta\sigma_{rz}^M \quad, \quad 0 \leq z \leq b \quad, \tag{23}$$

and taking

$$\Delta t = 2L/K. \tag{24}$$

The correction terms are computed from

$$\delta\sigma_{zz}^{M} = \frac{-K}{\bar{I}} \left| \sigma_{zz}^{M} \right| \quad , \tag{25a}$$

for stations on the bottom of the cylindrical monitoring surface, and

$$\delta\sigma_{rz}^{M} = \frac{-K}{\bar{I}} \left| \sigma_{rz}^{M} \right| \tag{25b}$$

for stations on the side, where

$$\bar{I} = \int_{0}^{a} \left| \sigma_{zz}^{M}(r_0,b,T_1) \right| r_0 dr_0 + \int_{0}^{a} \left| \sigma_{zr}^{M}(a,z,T_1) \right| a dz \quad . \tag{26}$$

The other quantities are extended to T_2 as follows:

$$
\begin{aligned}
u_z^{M}(T_2) &= u_z^{M}(T_1) \; , \\[6pt]
u_r^{M}(T_2) &= u_z^{M}(T_1) \; , \\[6pt]
\sigma_{rr}^{M}(T_2) &= \sigma_{rr}^{M}(T_1) \; , \\[6pt]
\sigma_{zz}^{M}(T_2) &= \sigma_{zz}^{M}(T_1) \; , \qquad 0 \le r \le a \; , \\[6pt]
\sigma_{rz}^{M}(T_2) &= \sigma_{rz}^{M}(T_1) \; , \qquad 0 \le z \le b \; .
\end{aligned} \tag{27}
$$

If K and L have opposite signs, it is much more difficult to zero the impulse. This happens to be the case for three of the four S-Cubed calculations. For the other, the Δt from (24) is too large for this method to be applied very satisfactorily.

In Figure 27 we show the force and impulse for each of the S-Cubed calculations. The force is nearly zero in every case, but the impulse is not. This is because there is a substantial amount of momentum remaining inside the monitoring surface at the end of

Figure 27. The vertical force and impulse for the four S-Cubed granite calculations are plotted. A dashed line indicates the imposed final time step which zeroes the force (the line is more properly plotted as a quadratic for the impulse).
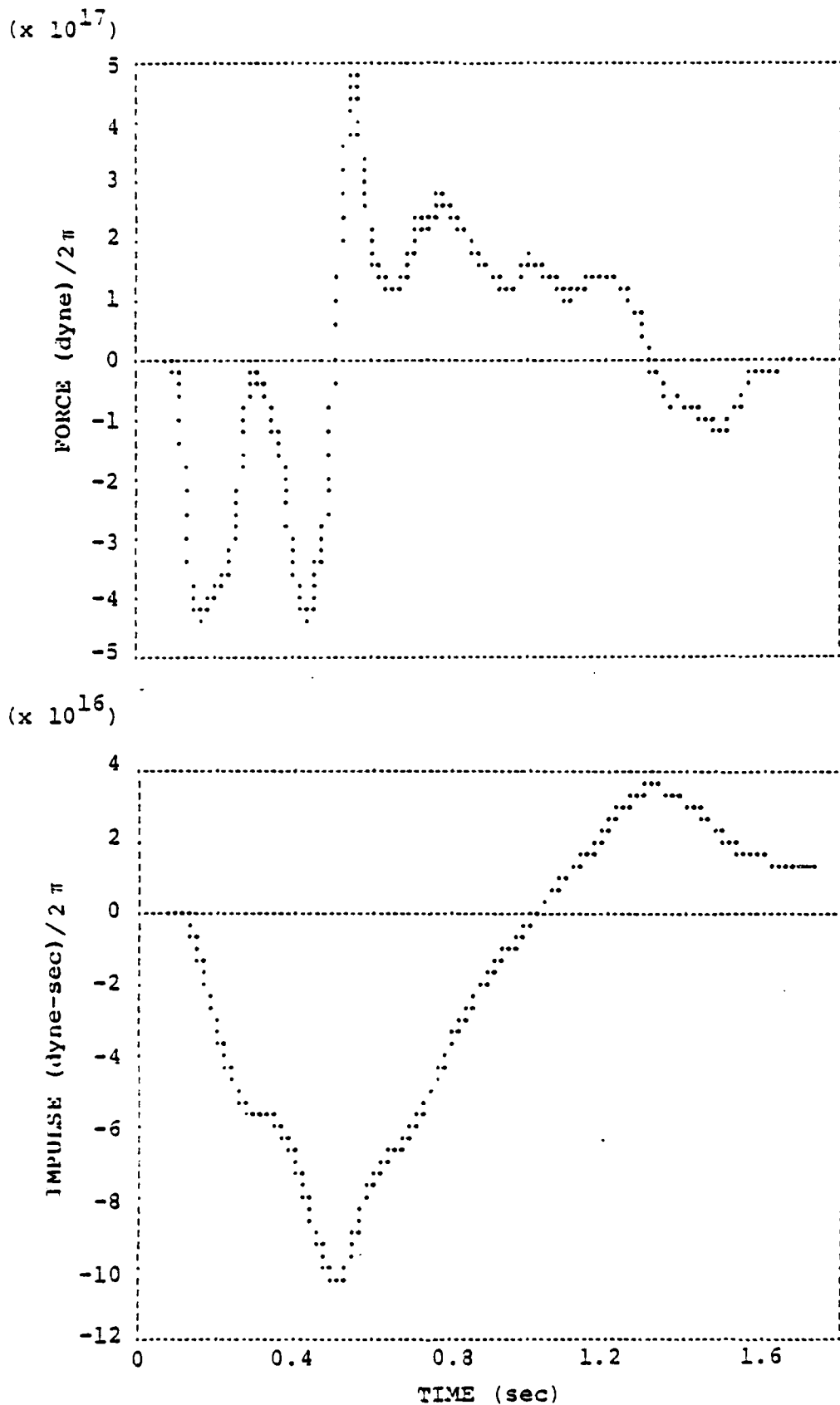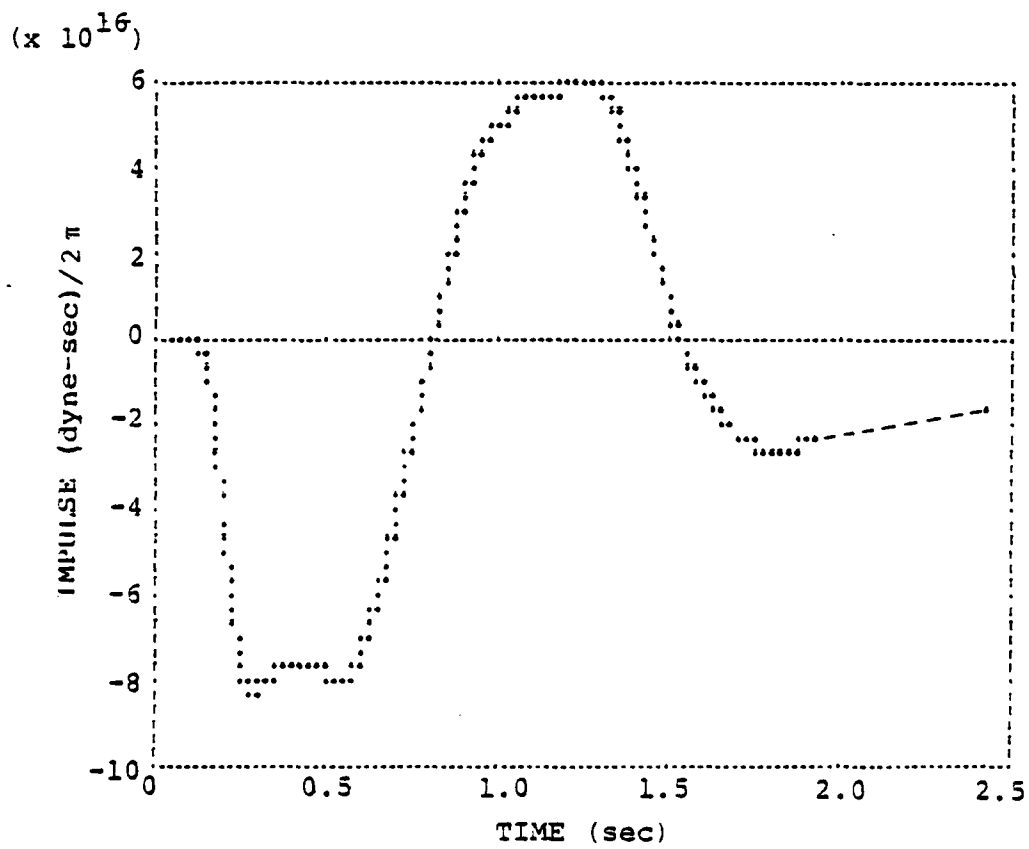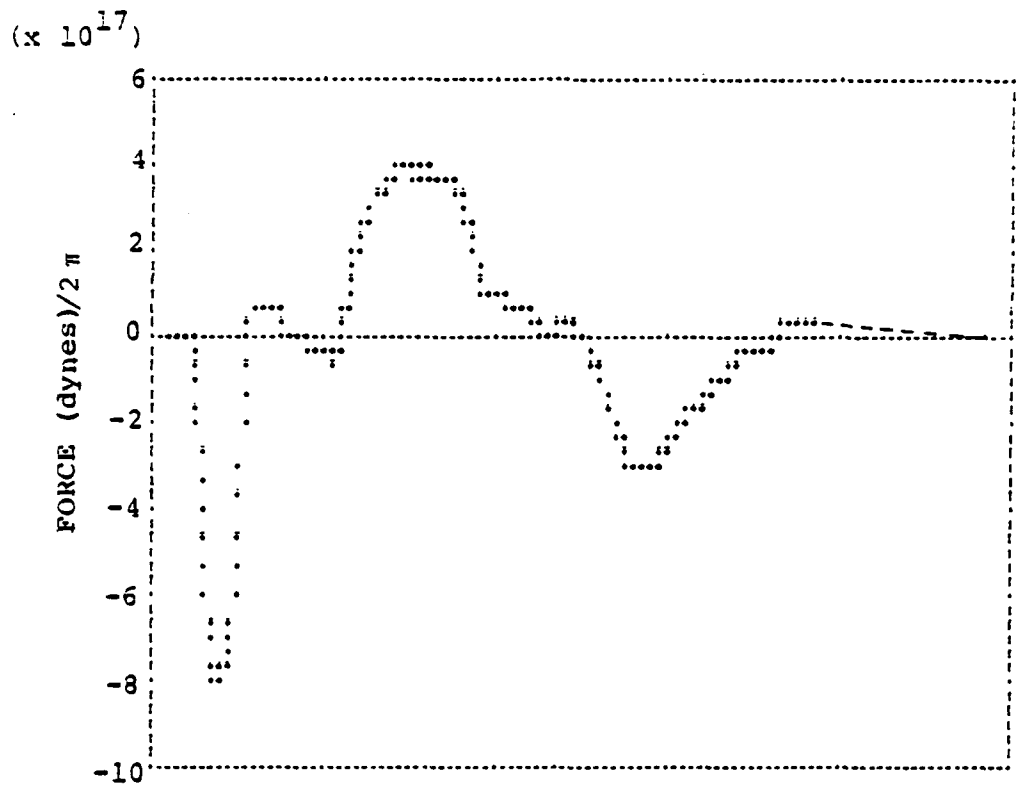
PILEDRIVER: $W = 60$ kt, $H = 0.46$ km

Figure 27. (continued)

89

Figure 27. (continued)

90

Figure 27. (continued)

91
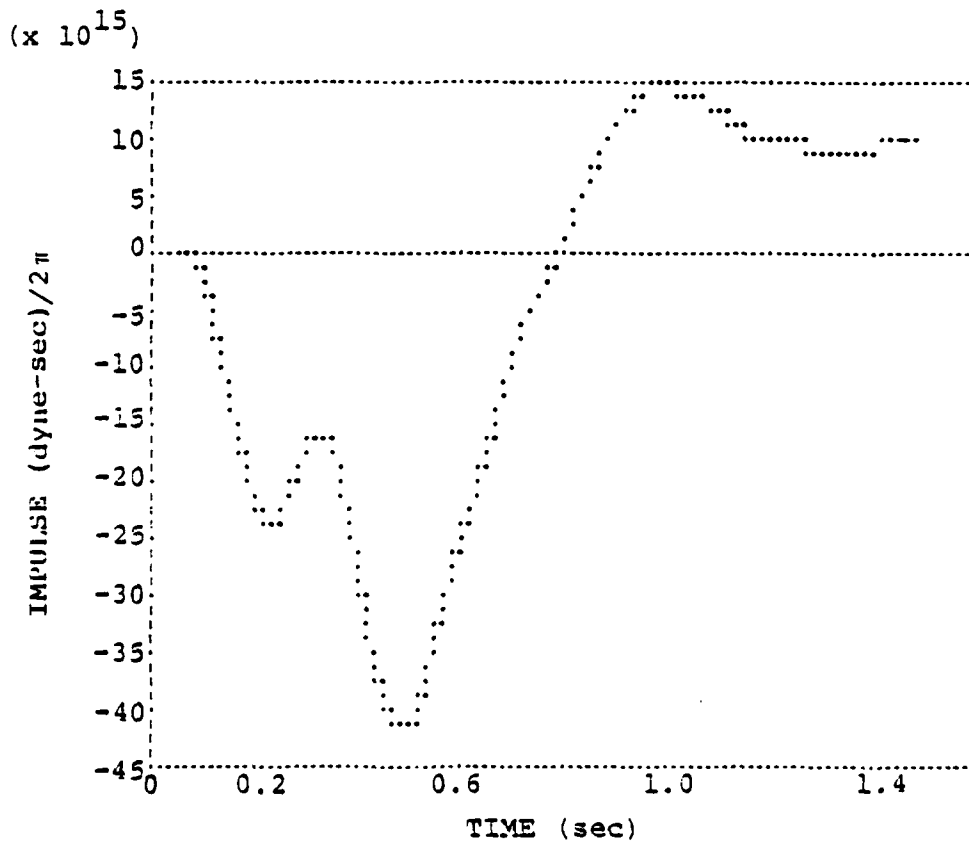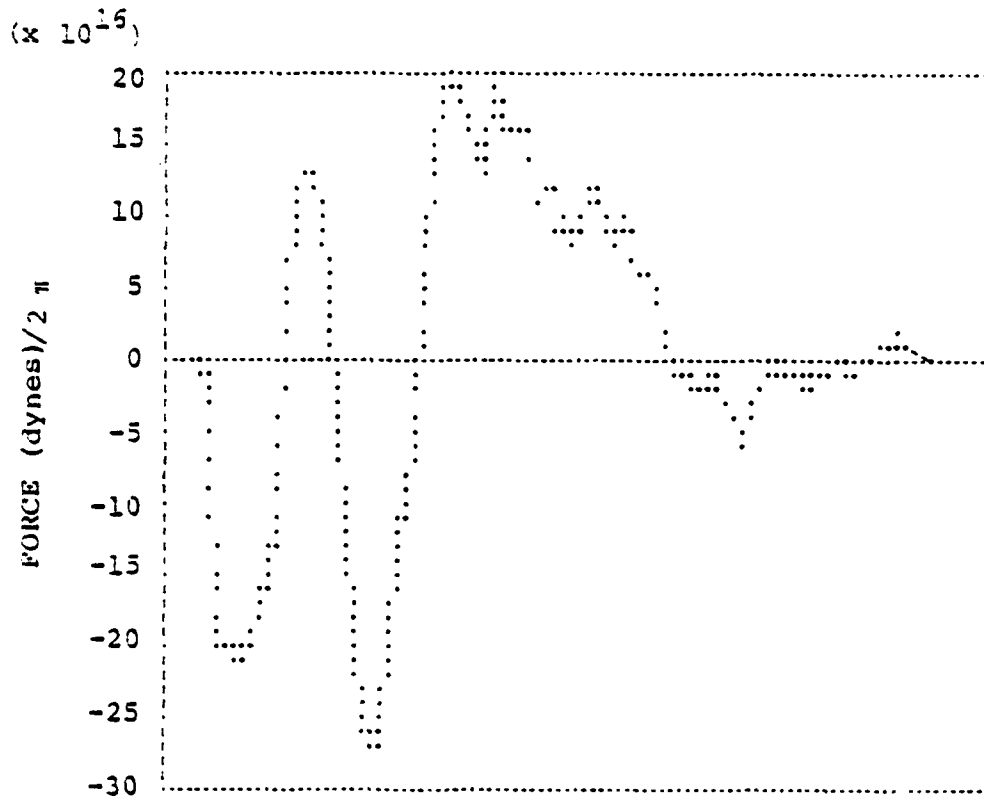
the calculation. The actual momentum within the cylindrical volume was calculated and, indeed, is in good (within a factor of 1.5) agreement with the $I_z(T_1)$ in Table 8, which was calculated from the surface integral (20). Most of the momentum is in material that has been spalled. This can be seen in crack density plots which will be discussed later, in Section 5.7. For GRAN1, which we know (Figure 25) is furthest from completion, the dominant momentum is still associated with upward motion. For the others, the positive impulse at the final time indicates that the spalled material is mainly moving downward, closing cracks.

As well as the impulse being far from zero, the condition that $K * L > 0$ is not satisfied in two of the four cases. Therefore, we decided to allow

$$I_z(T_2) \neq 0 . \tag{28}$$

Rather than using (24) to find the time step, we pre-selected Δt to be 0.5 seconds when $K * L > 0$ and 0.05 seconds when $K * L < 0$.

The parameters for correcting the force and impulse are given in Table 8. The corrections to the stresses, K/Γ in equation (25), are not very large, especially for PD1 and GRAN2.

The inability to zero the impulse means that the monitored solutions do not satisfy conservation of linear momentum. As is shown in Appendix A, this means that the contribution of the vertical force terms is larger than it should be at long periods. However, as we will demonstrate in the next section, the error turns out to be insignificant at the periods of interest.

92

TABLE 8

PARAMETERS FOR CORRECTING THE VERTICAL FORCE AND IMPULSE TO ZERO*

Identifier	Depth (m)	Yield (kt)	T_1 (sec)	$F_z(T_1)$ $(10^{15}$ dyne-sec)	$I_z(T_1)$ $(10^{15}$ dyne-sec)	$I_z(T_2)$ $(10^{15}$ dyne-sec)	Γ $(10^{16}$ dynes)	K/Γ	Δt (sec)
PD1	460	60	1.68	2.9	14.6	14.7	10.0	-0.29	0.05
GRAN1	1000	150	1.92	33.6	-23.5	-15.1	10.8	0.31	0.5
GRAN2	1000	20	1.68	-5.0	3.7	2.4	3.3	-0.15	0.5
GRAN3	400	20	1.43	9.1	9.7	9.9	3.2	0.29	0.05

* The true values of F_z, I_z and Γ are obtained by multiplying the listed values by 2π.

93

THIS PAGE LEFT BLANK

V. M_s AND m_b ESTIMATES FOR S-CUBED GRANITE CALCULATIONS

5.1 INTRODUCTION

The granite source calculations described in the previous section were processed with the methods described in Appendix A to compute synthetic body and surface wave seismograms in the same earth models used with the ATI sources in Section III. In this section we describe these calculations and analyze the results. The ATI and S-Cubed calculations will be compared in Section VII.

We begin by discussing the far-field Rayleigh waves in a half-space. These are easily compared to the simple Rayleigh pulse we expect for an explosion source. Analysis of these Rayleigh waves leads to the conclusion that the contribution of the vertical tractions, which we know to include some error, is not very large. Also, we use the halfspace Rayleigh waves to determine an equivalent RDP representation for the two-dimensional source. Finally, we compute Rayleigh waves in the central United States crustal model used earlier with the ATI sources.

The far-field body waves are shorter period and are associated with wave propagation along a particular takeoff angle. Thus, they are somewhat easier to understand. The effects of the nonlinear interaction with the free surface can be directly seen. In connection with these seismograms, we again compute an equivalent RDP to directly display the two-dimensional effects. We also look at spallation in some detail, presenting plots of the crack distribution for each calculation.

An especially important feature of these granite calculations is that we are able to compare with one-dimensional source calculations done with the same constitutive model. It is satisfying to see that the two-dimensional effects are in accordance with our intuitive expectations, being rather small for the deep events and important for the shallow ones. The direct (downward propagating) P wave from all the two-dimensional calculations is about the same as predicted with the one-dimensional source. These conclusions are summarized in Section 5.10.

5.2 FAR-FIELD RAYLEIGH WAVES IN A HALFSPACE

As with the ATI calculations (Section 3.2), we first look at the Rayleigh pulse in a halfspace. In this case, the source calculations were done in a three-layered model. For the propagation medium we chose a halfspace with $\alpha = 6.0$ km/sec, $\beta = 3.5$ km/sec, $\rho = 2.7$ gm/cm^3. The technique of Bache, Rodi and Harkrider (1978), which is described in Section A.4, was used for the transition between the two structures. The range was 1000 km and the WWSSN 15 - 100 instrument response was included. For attenuation, we had $Q = 10$ in the top kilometer and $Q = 300$ elsewhere in the propagation medium.

In Figure 28 we compare the halfspace Rayleigh pulse from the S-Cubed two-dimensional calculations to the Rayleigh pulses from RDP sources at the same depths and yields. The RDP sources were computed at two depths with the same constitutive model used in the two-dimensional calculations. The overburden pressure difference between 400 and 460 meters was ignored. These RDP source functions are plotted in Figure 29.

The Rayleigh pulses for the two-dimensional calculations have waveforms much like those from the RDP sources. There is no obvious indication of numerical difficulty. In the next two sections, we will examine this comparison more closely.

5.3 CONTRIBUTION OF VERTICAL TRACTIONS

As pointed out at the end of Section IV, these calculations could not easily be corrected to bring the total vertical force and impulse to zero at late time. The asymptotic behavior of the solution, discussed in Appendix A, indicates that the contribution of the vertical traction terms (σ_{rz} and σ_{zz}) is, therefore, too large at long period. Thus we know our surface wave solution is incorrect at very long periods, but the importance of this static offset error at the periods of interest for M_s can only be estimated by examining the numerical results.
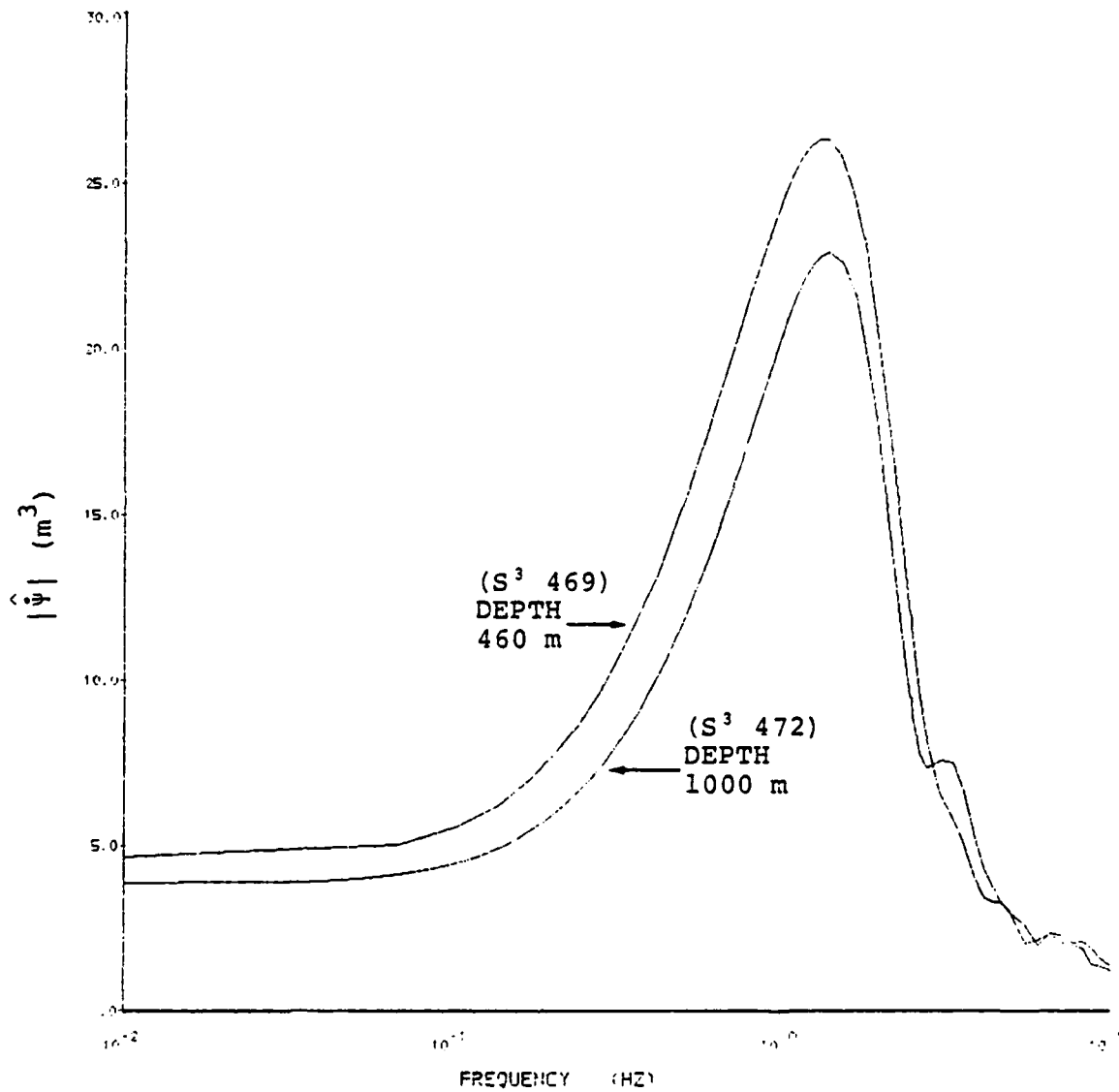
Figure 29. The spectral amplitude of the reduced velocity potential
is plotted for two spherically symmetric source calcula-
tions in the PILEDRIVER source material. The calcula-
tions differ only in the overburden pressure. The ampli-
tude axis is scaled to 0.02 KT, while the frequency axis
is scaled to 60 KT.

98

Source		A (microns)	T (sec)

RDP   26   6.5

PN1
(60 KT, 0.46 km)

2-D   57   6.6

RDP   50   6.5

GRAN1
(150 KT, 1 km)

2-D   64   6.1

RDP   5.0   7.1

GRAN2
(20 KT, 1 km)

2-D   5.2   6.8

RDP   7.4   6.8

GRAN3
(20 KT, 0.4 km)

2-D   2.1   6.7
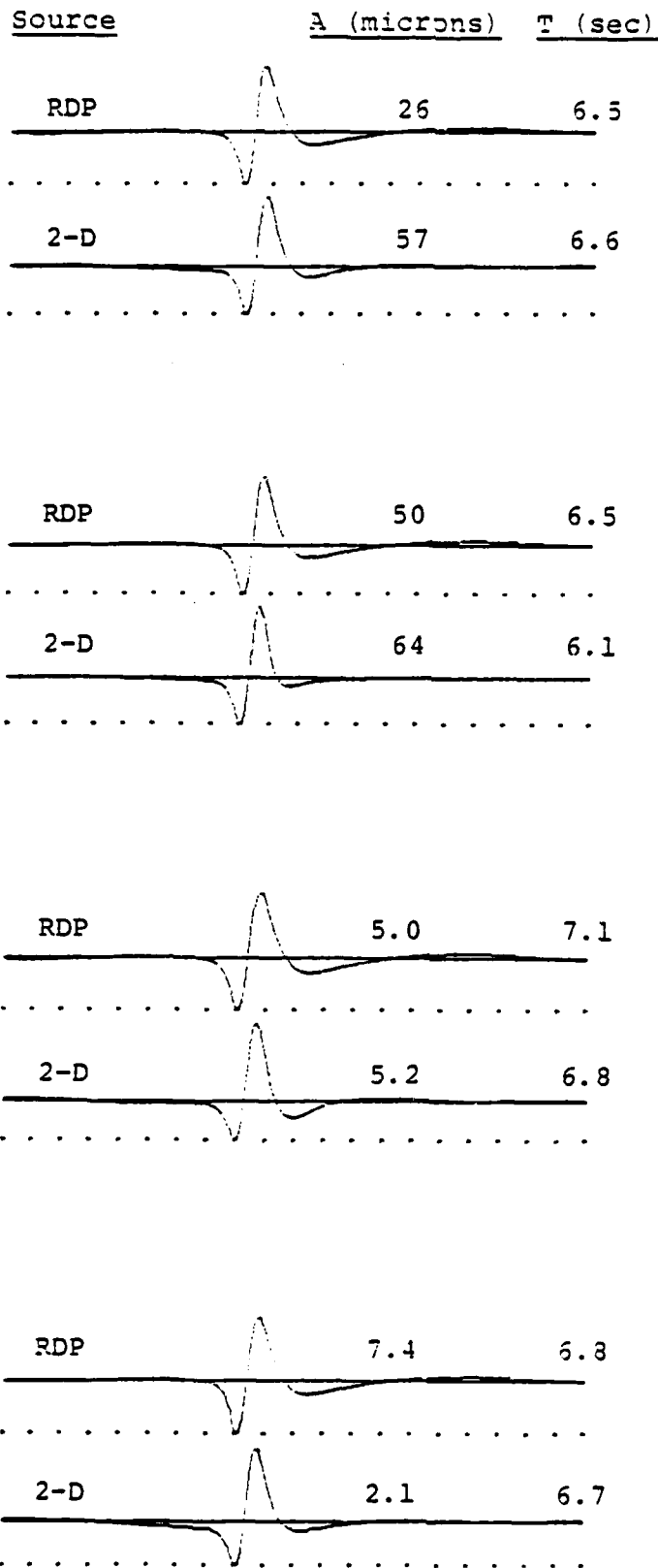
20 sec

Figure 28. Halfspace Rayleigh waves for the S-Cubed calculations are com-
pared to those computed with an RDP source. Listed with each
record is the peak-to-peak amplitude, which has been corrected
for the instrument response at the apparent period (T).

In Figure 30 we compare the halfspace Rayleigh wave solution from Figure 28 to the Rayleigh wave solution computed from only the vertical traction contribution. The Rayleigh wave spectra for these seismograms are plotted in Figure 31. The period of the Rayleigh pulses in Figure 30 is 6 to 8 seconds, and the spectral amplitude differences at those periods are fairly represented by the peak-to-peak amplitudes of the seismograms.

On each of the spectral plots in Figure 31, we have marked the frequency associated with the time (T_1) at which the calculation was terminated. As a rough approximation, we can say that the solution for frequencies higher than this is as accurate as the finite difference calculations, while moving to lower frequencies tends to exaggerrate the effect of errors in the calculated values at the last time step.

The contribution of the vertical force term is small at the periods of interest for the two deep source calculations, GRAN1 and GRAN2. This is consistent with the ATI calculations, Figure 8, where the vertical force contribution was relatively more important at shallow depths, even when the impulse had no static offset. Only for GRAN3 does the (incorrect) static offset in the vertical impulse appear to be causing significant errors. But even in this case, the Rayleigh wave solution is probably accurate for periods out to 20 seconds or so.

5.4   AN EQUIVALENT RDP FROM SURFACE WAVES

As discussed in Appendix 3 and in Section 3.4, another interesting way to display the propagated surface waves is in terms of an equivalent RDP. That is, we compute the RCP source which gives the same Rayleigh waves as the two-dimensional source. From (16) in Section 3.4, we see that the equivalent RDP, $\hat{\psi}_e$, is simply the ratio of the spectra of the seismograms in Figure 28 times the RDP used for those calculations, which are plotted in Figure 29.
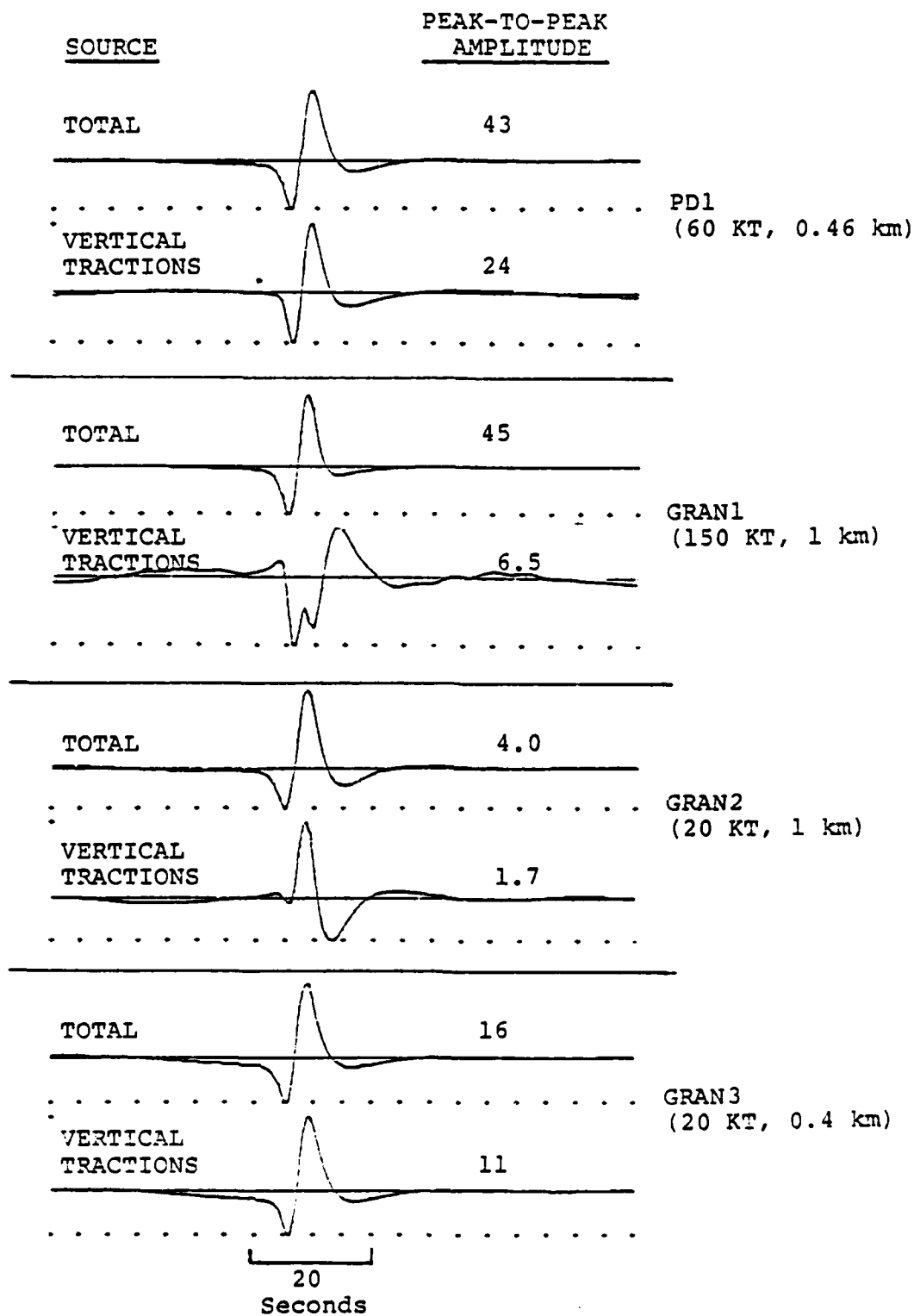
Figure 30. The complete halfspace Rayleigh waves for the S-Cubed granite calculations are compared to the solution computed with only the vertical traction terms. The peak-to-peak amplitudes in microns at 15 seconds are shown with each record.

100
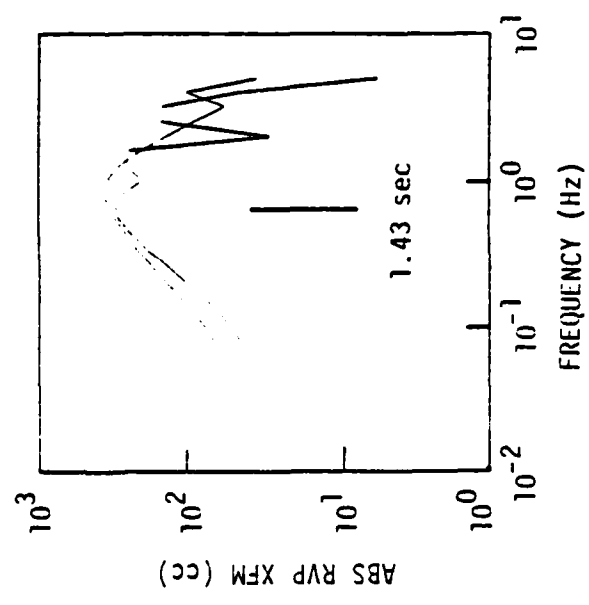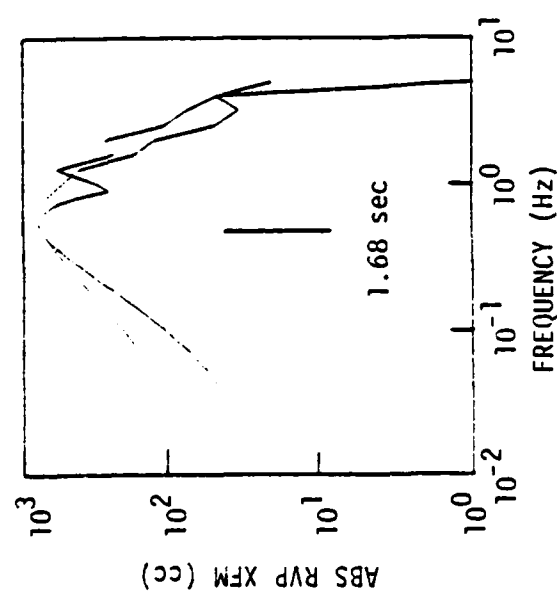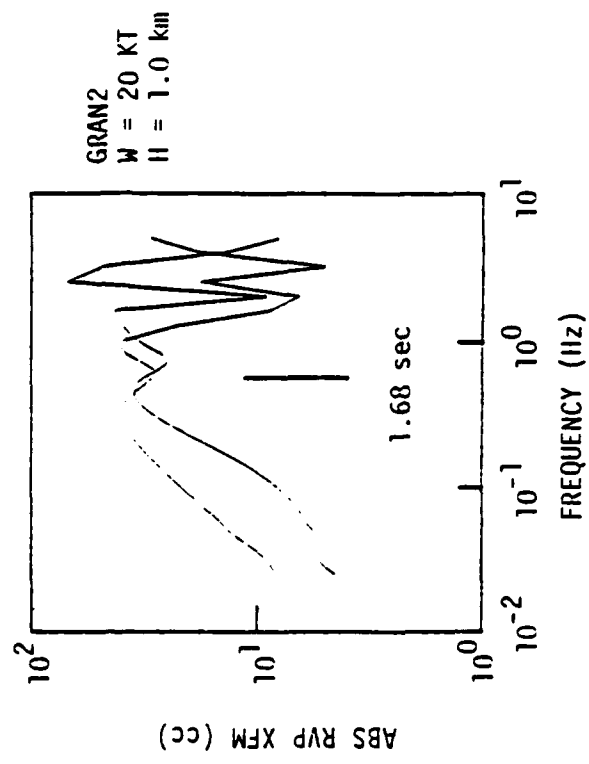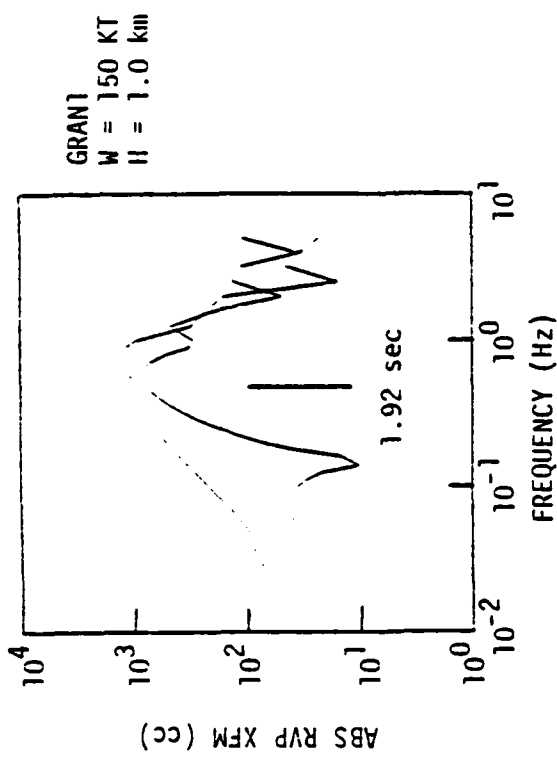
Figure 31. The Rayleigh wave spectra are plotted for the seismograms of Figure 30. These spectra do not include the effect of Q or the seismometer. The total spectrum is the larger at long period on each plot.

101

In Figure 32 we plot the $|\hat{\Psi}_e|$ for the four S-Cubed granite calculations. They are compared to $|\hat{\Psi}|$ for the RDP sources 469 or 472, scaled to the appropriate yield. Our remarks about the high frequency behavior of $|\hat{\Psi}_e|$ in Section 3.4 apply here. Again, the spectral "holes" shift to lower frequency with depth and are believed to be associated with the nonlinear interaction with the free surface, including spallation. We also point out that the long period errors expected in GRAN3 are apparent in the $|\hat{\Psi}_e|$ (it increases for periods longer than about 20 seconds). For the other calculations, the $|\hat{\Psi}_e|$ are nearly constant at long period, as they should be. This is another reason to believe that our failure to zero the vertical impulse is not important at the periods of interest.

Another display of the $|\hat{\Psi}_e|$ for the S-Cubed granite calculations is shown in Figure 33. The $|\hat{\Psi}_e|$ for all four calculations are plotted together at the top of the figure. It is the long period behavior (called Ψ_∞) that is of most interest. For the two deep explosions the Ψ_∞ deduced from the 2-D calculations is about the same. Further, this Ψ_∞ is nearly the same as that obtained from a 1-D calculation at the same depth. This is an important result that gives considerable confidence in the consistency of the whole procedure. If we refer back to the halfspace Rayleigh wave comparison in Figure 28, we also see, as expected, close agreement in the amplitudes of the RDP and 2-D seismograms for the deep events, GRAN1 and GRAN2. At shallow depths, the two-dimensional calculation predicts much larger (a factor of 2 to 3) surface waves than a one-dimensional calculation. We expect 2-D effects to be more important for shallow source depths, so this is not surprising.

At the bottom of Figure 33 the 1-D and 2-D source functions for PILEDRIVER are compared to the Mueller/Murphy granite source for PILEDRIVER. The S-Cubed 1-D source has nearly the same Ψ_∞, but is very different at frequencies above 0.1 Hz.

102
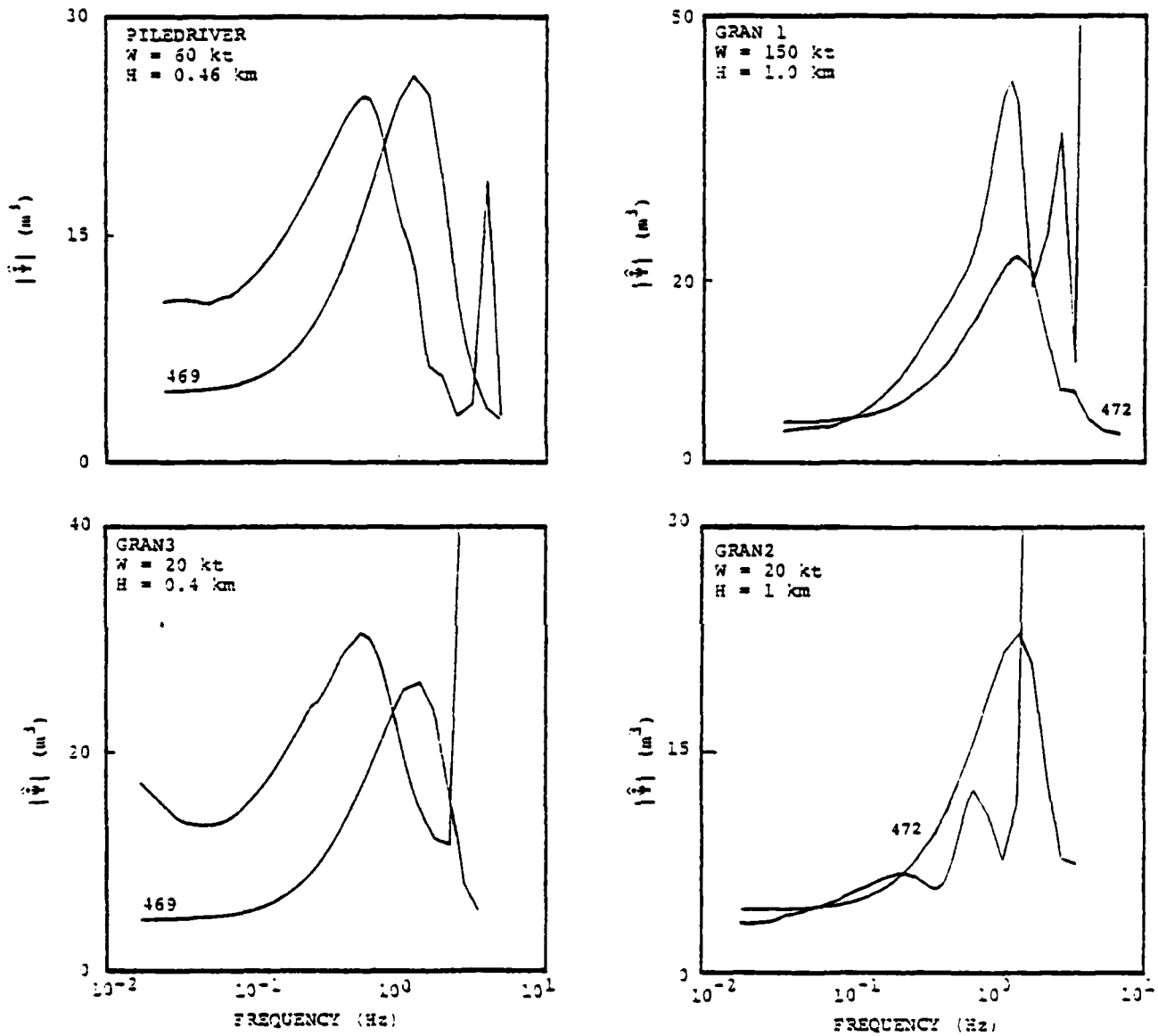
Figure 32. The $|\hat{\psi}_e|$ for the S-Cubed granite calculations are compared to source 469 or 472 (Figure 29), depending on the depth. The amplitudes have been scaled to a common yield, 0.02 KT and the frequencies have been scaled to 60 KT.

103
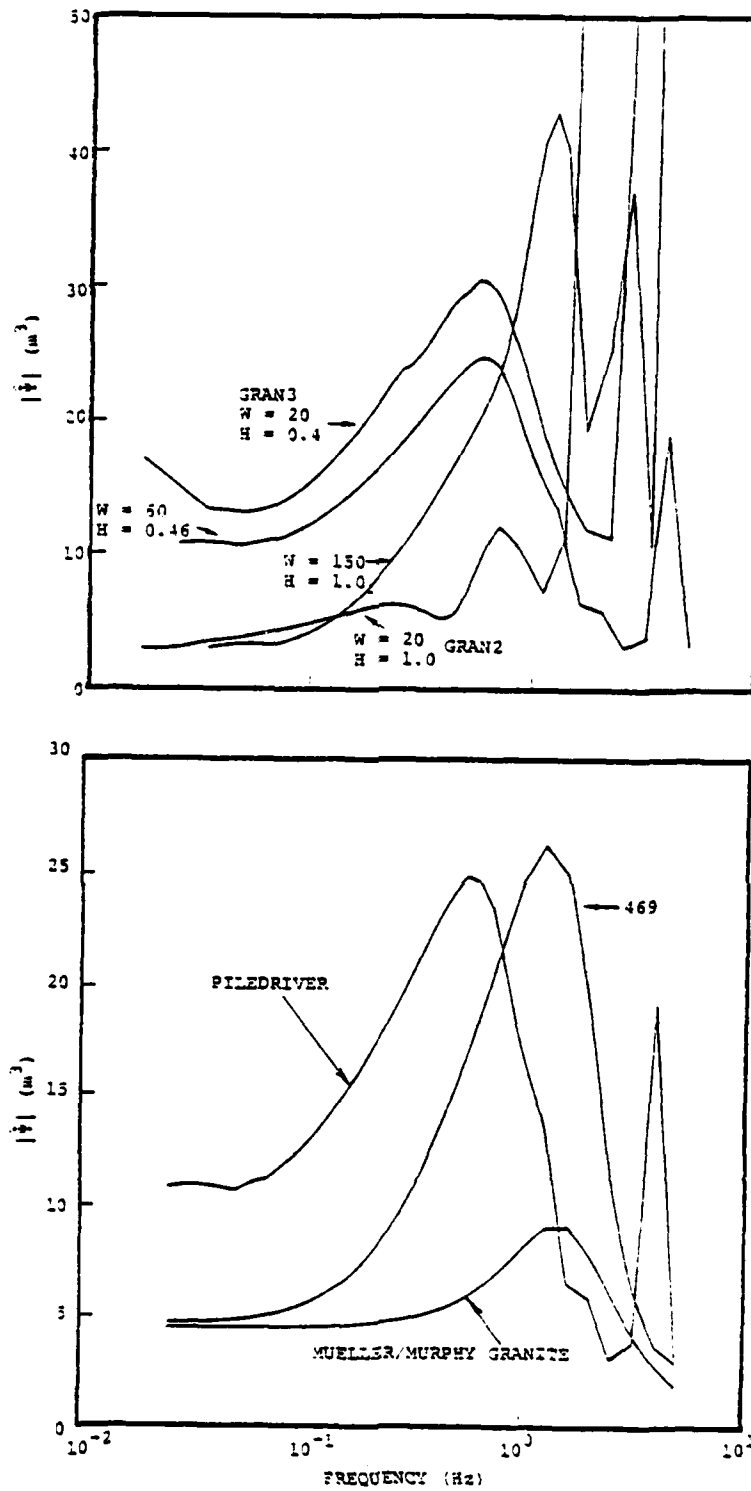
Figure 33. The spectral amplitude (scaled to 0.02 Kt) of the equivalent
RVP, $|\dot{\Phi}_e|$, is plotted for each of the S-Cubed granite calcu-
lations. At the bottom the PILEDRIVER $|\dot{\Phi}_e|$ is compared to
1-D source 469 and the Mueller/Murphy granite source at this
yield. The frequency axes are scaled to 60 kt.

104

5.5   FAR-FIELD RAYLEIGH WAVES IN REALISTIC EARTH MODELS

The fundamental mode Rayleigh waves were computed for the four S-Cubed granite calculations with the same path model used for the ATI sources (Section 3.5). This model is listed in Table 2, with the exception that the top three kilometers of the source region model were replaced by the source structure in Table 6.

The computed Rayleigh waves are shown in Figure 34. These are directly comparable to the surface wave synthetics in Figure 11 for the ATI source calculations. The M_s values were computed according to (18) and are listed in Table 9. These values will be discussed in more detail in Section VII where we compare them with the M_s from the ATI sources.

5.6   FAR-FIELD BODY WAVES

Short period body wave seismograms like those for the ATI sources in Figure 15 are plotted in Figure 35. We also plot the analogous seismograms for the 1-D sources 469 (PILEDRIVER and GRAN3) and 472. The only difference between the calculations here and those for the ATI sources in Section 3.6 is that the top three kilometers of the source region structure (Table 4) are replaced with the structure in Table 6.

The body wave magnitude values for the calculations in Figure 35 are listed in Table 10. These m_b were computed using (19). Note that the magnitudes for the 1-D source are very nearly the same as those for the 2-D sources, especially for the two deep events.

For the two deep sources, GRAN1 and GRAN2, the seismograms for the RDP and two-dimensional sources have very similar waveforms. The two-dimensional effects are much more prominent on the seismograms for the shallow sources. This is, of course, what we should expect.

105
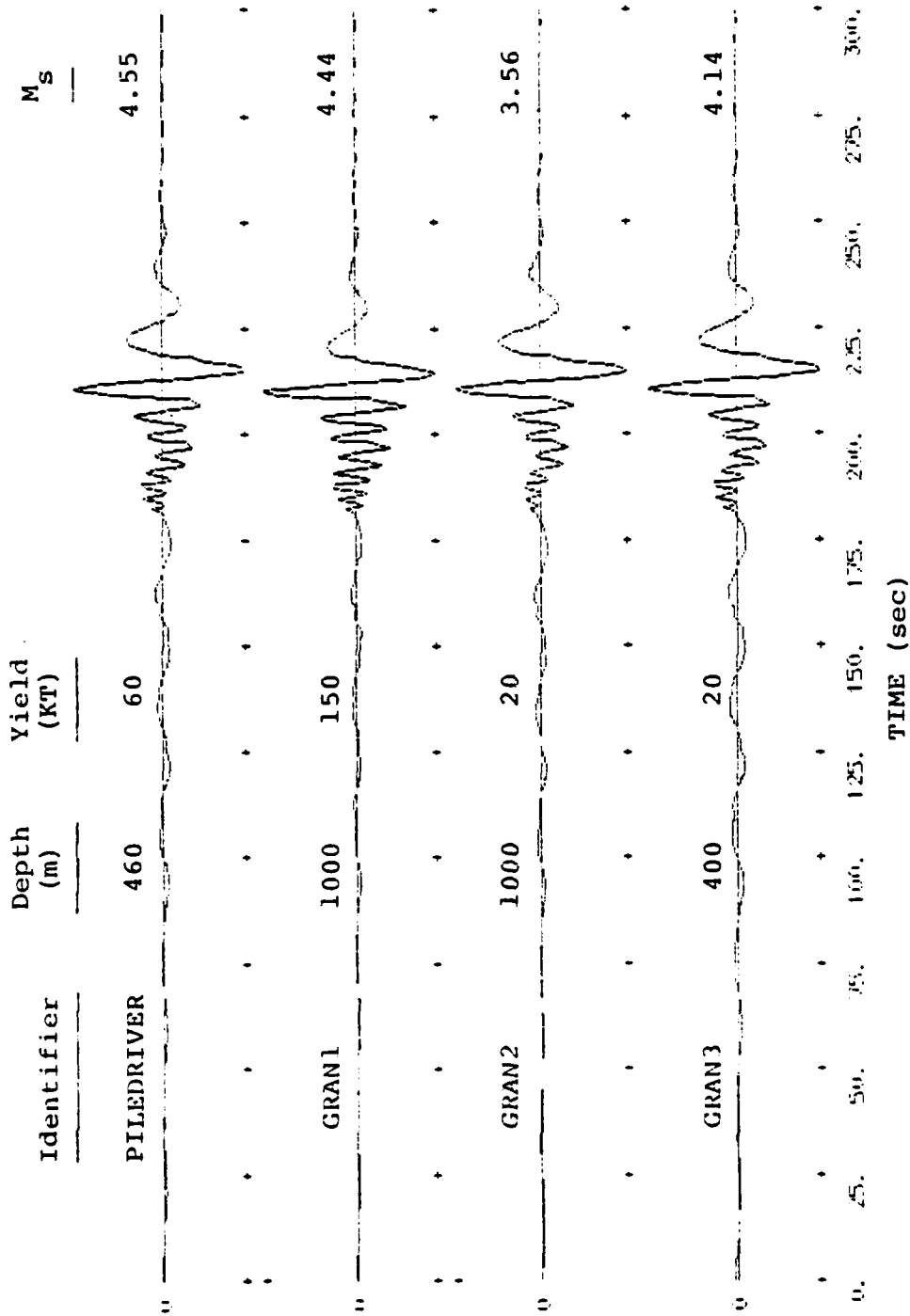
Figure 34. Rayleigh waves for the S-Cubed granite calculations. The range is 3000 km and the WWSSN 15 to 100 seismometer response is included.

106

TABLE 9

M_S FOR S-CUBED GRANITE CALCULATIONS

Calculation	Depth (km)	Yield (kt)	A (microns)	T (sec)	M_S
PILEDRIVER	0.46	60	8.7	13 8	4.55
GRAN1	1.0	150	8.7	12.4	4.44
GRAN2	1.0	20	1.0	13.0	3.56
GRAN3	0.40	20	3.3	13.9	4.14

107
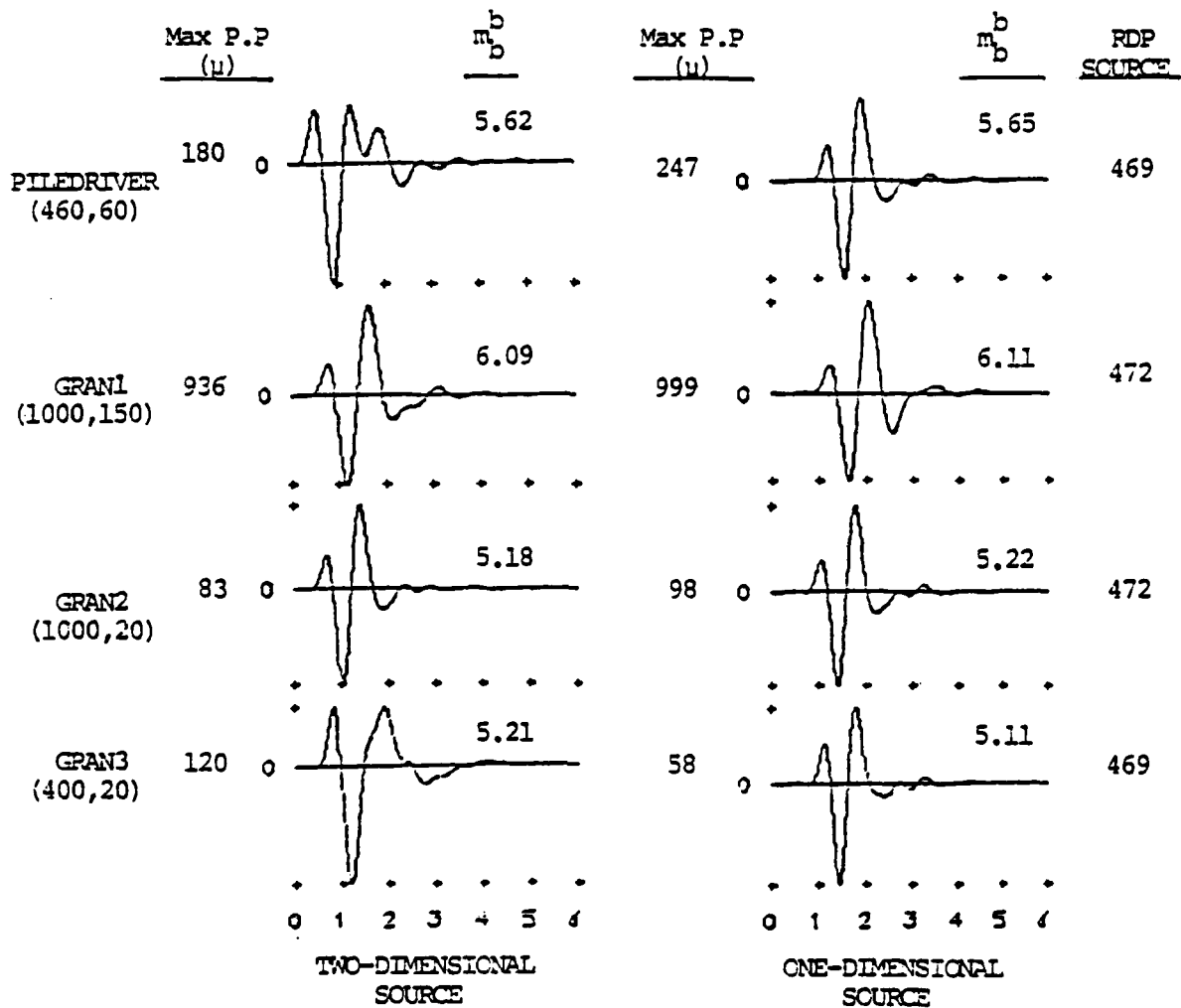
Figure 35. Body wave seismograms for the S-Cubed granite calculations are compared to seismograms with an RDP source. The peak-to-peak amplitudes listed with each seismogram have been corrected for the instrument response at the apparent period (T_c) in Table 10.

TABLE 10

m_b FOR S-CUBED GRANITE CALCULATIONS

Calculation	Depth (km)	Yield (kt)	b (nm)	T_b (sec)	m_b^b	C (nm)	Tc (sec)	m_b^c
TWO-DIMENSIONAL								
PILEDRIVER	0.46	60	169	0.73	5.62	180	0.75	5.63
GRAN1	1.0	150	553	0.81	6.09	936	0.85	6.29
GRAN2	1.0	20	57	0.67	5.18	83	0.70	5.32
GRAN3	0.4	20	64	0.71	5.21	120	1.07	5.30
ONE-DIMENSIONAL								
469	0.46	60	166	0.67	5.65	247	0.70	5.30
472	1.0	150	568	0.73	6.11	999	0.82	6.33
472	1.0	20	62	0.68	5.22	98	0.72	5.39
469	0.4	20	44	0.60	5.11	58	0.65	5.21

109

5.7 ANALYSIS OF SPALLATION

Probably the most important two-dimensional effect is the occurrence of spallation. This complex phenomenon degrades and distorts the free surface reflected waves and partitions some of the energy into spall closure phases. This is an extremely complex process which can be seen by examining displays of the crack porosity. We will show some attempts to reproduce the synthetic for the 2-D source by modifying the seismogram for the 1-D source by (1) suppressing pP by a constant factor, and (2) adding an impulsive force at the surface to represent spall closure. This was not very successful, apparently because this model is much too simple to represent this calculation.

In Figure 36 we show crack density plots for the PILEDRIVER calculation at three times. These and similar plots for the other three calculations (Figures 37 through 39) are in two different formats which are explained in the caption. The plot at 0.426 seconds shows the maximum extent of cracking near the surface. The entire first layer (Table 5), which is 50 meters thick, is "spalled" to a radius of 1 kilometer. The spalled region would have extended to even greater radii, but was terminated at this radius to ensure elastic behavior at the monitoring surface. Recall that in Section 4.1 we mentioned that the amount of spall is unrealistically large in the calculation, probably due to an inaccurate material model for the surface layer.

The plots at 0.68 seconds show that some of the near surface cracks have closed. Spall closure pulses corresponding to these cracks can be seen on the records at the free surface monitoring stations (e.g., Figure 24). At 1.68 seconds, the end of the calculation, many more of the near surface cracks have closed, but there is a substantial region still in free fall. Cracked material is distributed extensively through the grid even at this time. It is clear that spall closure is very complex and is distributed over more than a second in time. Certainly the pP must be degraded to a substantial degree in opening these cracks.

110

Cycle: 850   Time (msec):   425.5

463 m

1000 m
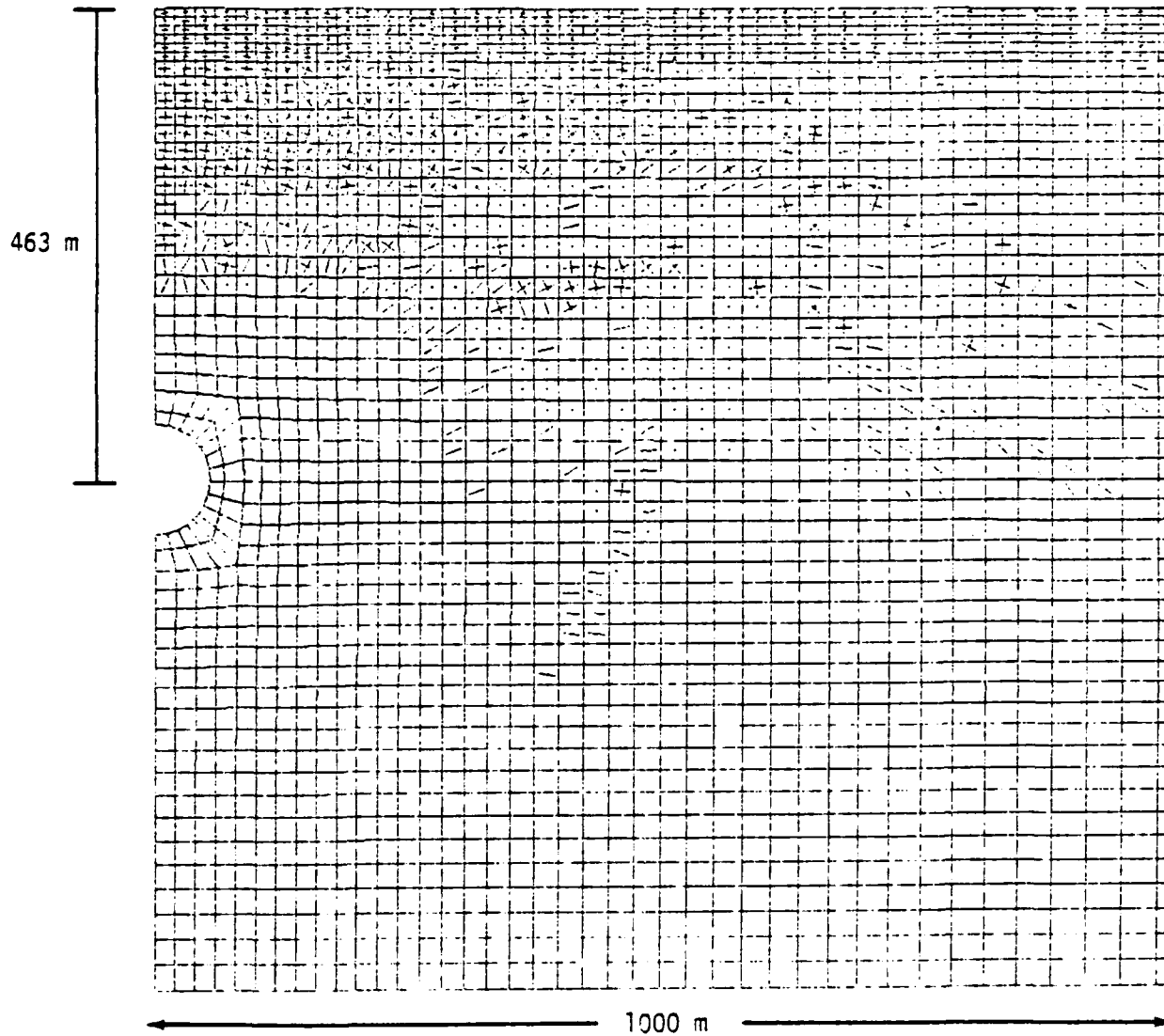
Figure 36.   The crack density is plotted at three times for the PILEDRIVER
             calculation. Dots or open boxes indicated hoop (out-of-plane)
             cracks. In-plane cracks open across the lines. The X or
             closed boxes indicate zones in which tensile failure has
             occurred in all three coordinate directions. These zones are
             thus decoupled from adjacent zones.

111

PILEDRIVER RUN 22A

CRACK ANGLES

CYCLE: 1200.   TIME(MSEC)   683.04002

Figure 36. (continued)

112
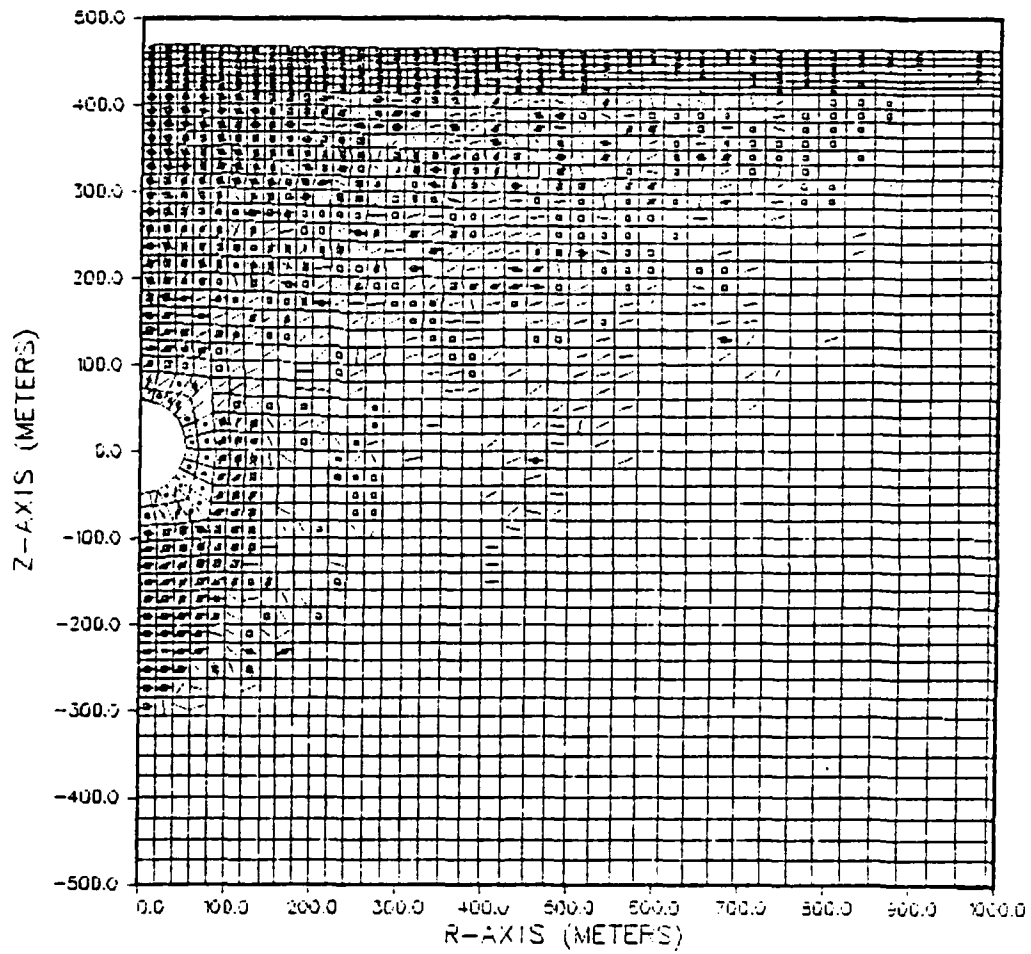
PILEDRIVER RUN 22A

CRACK ANGLES

CYCLE: 2100.   TIME(MSEC) 1678.54417

Figure 36. (continued)

113

Figure 37. The crack densities plotted at three times for GRAN2
(w = 20 KT and H = 1000 m).

114

GRANITE PUN 2

CRACK ANGLES

CYCLE: 1700.   TIME(MSEC)   750.43920
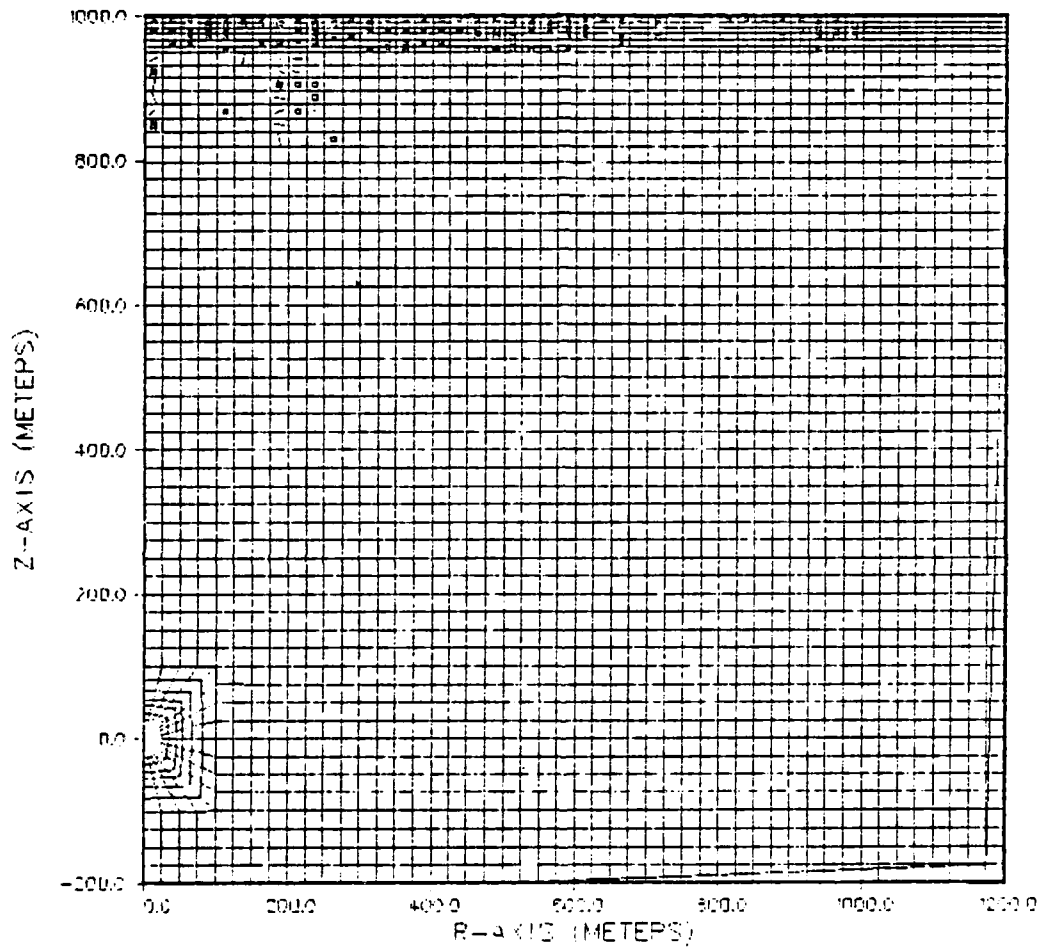
Figure 37. (continued)

GRANITE RUN 2

CRACK ANGLES

CYCLE: 2235. TIME(MSEC) 1681.23549

Figure 37. (continued)

116
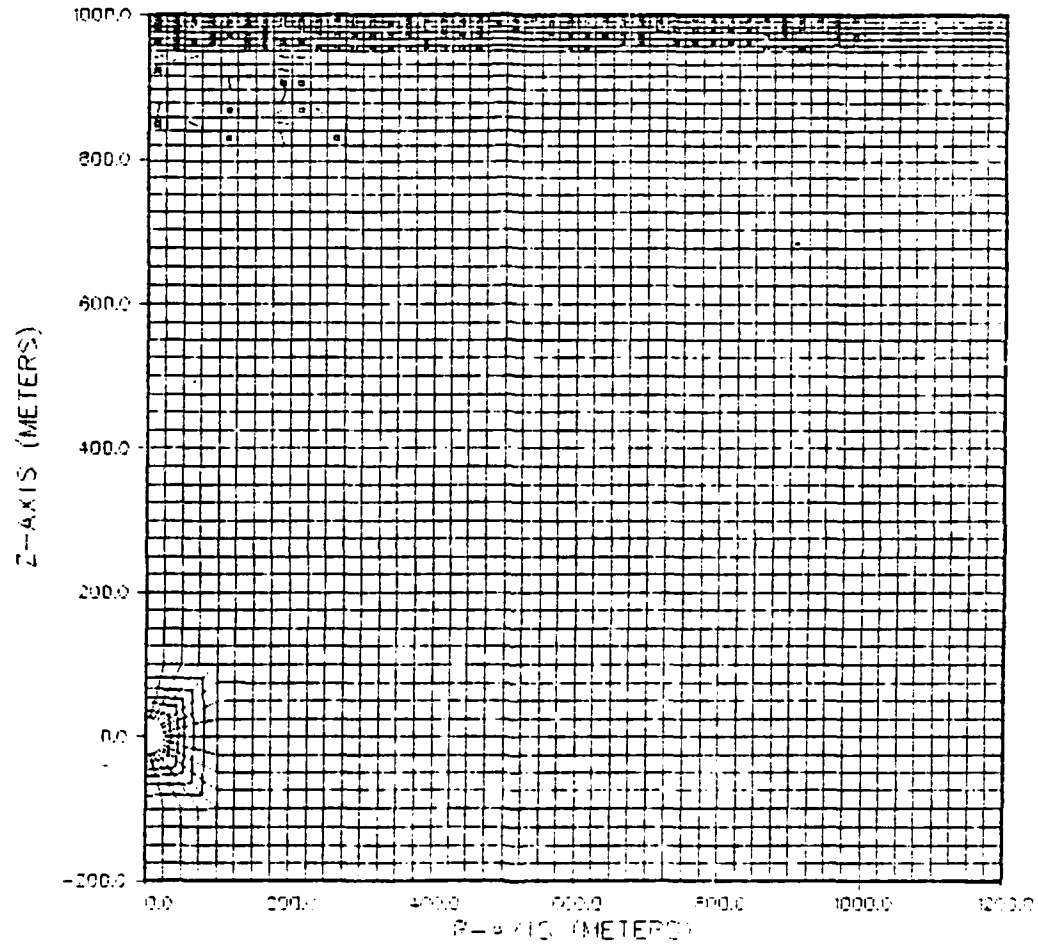
Cycle: 900   Time (msec) 566
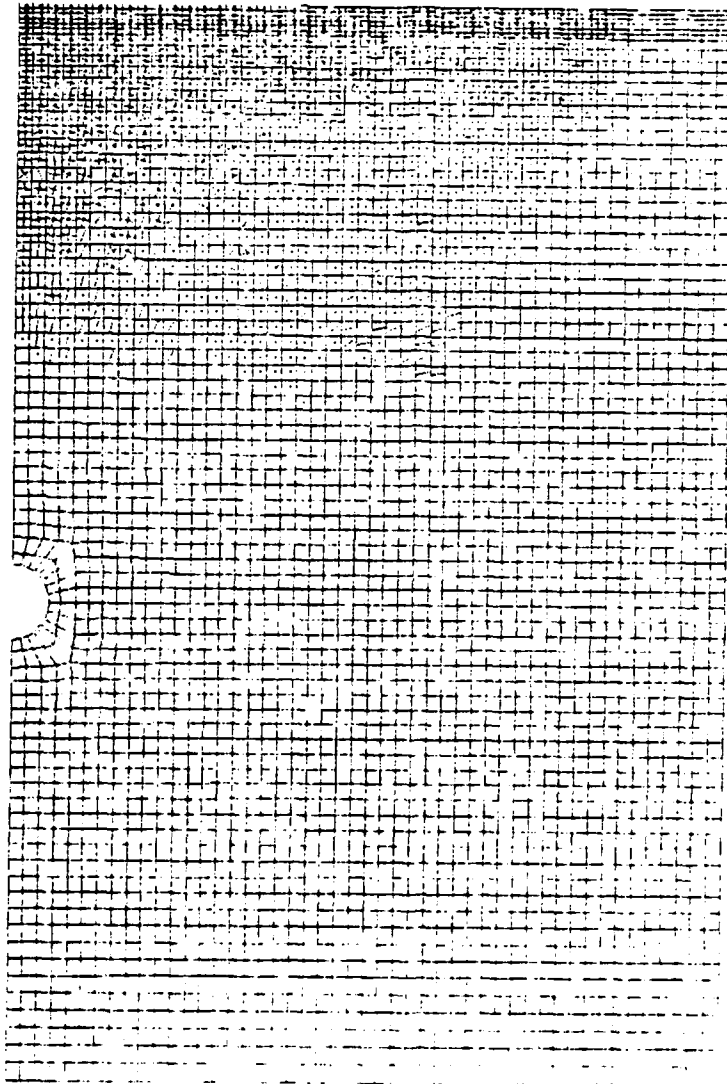
Figure 38.   The crack density is plotted at two times for
             GRAN1 (W = 150 KT and H = 1.0 km).

117

Cycle: 2500   Time (msec) 1887
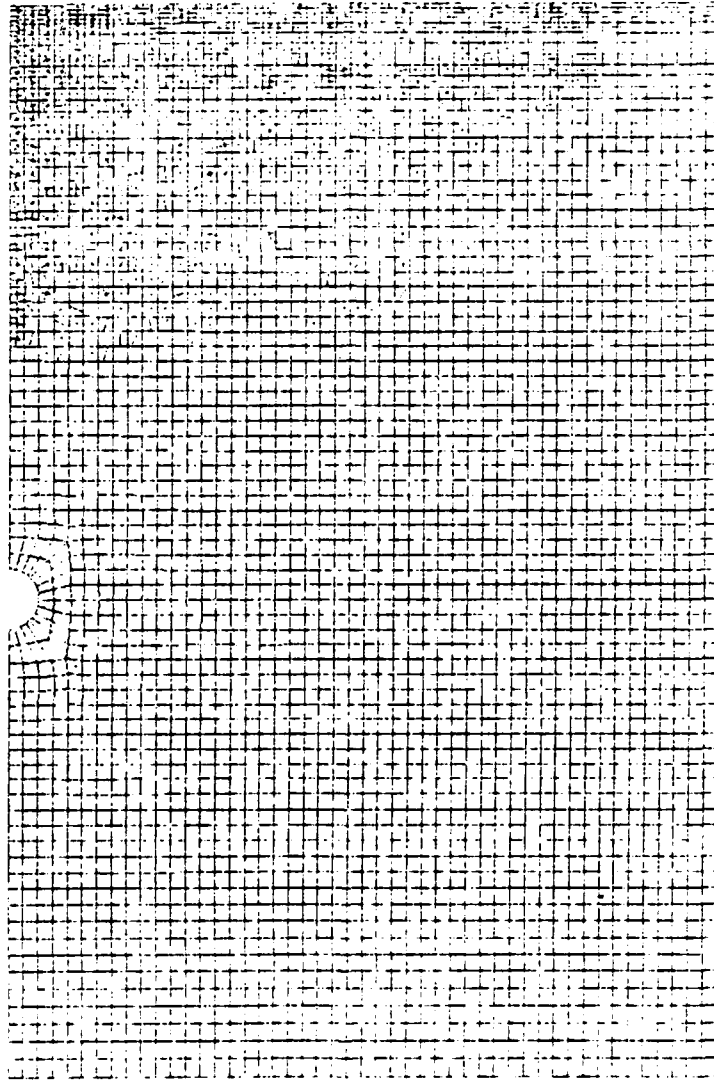
Figure 38. (continued)

118

Cycle: 1150   Time (msec):   449
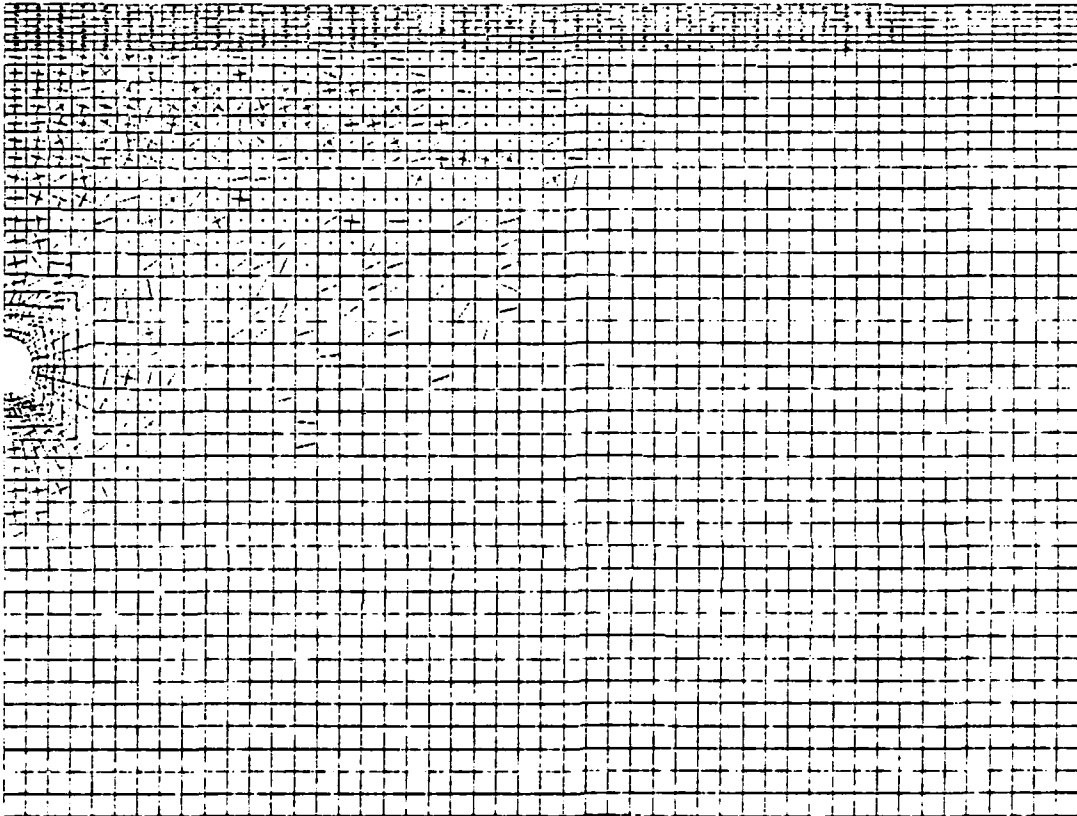
Figure 39.   The crack density is plotted at two times for GRAN3
             (W = 20 KT and H = 400 m).

119

GRANITE RUN 3A

CRACK ANGLES

CYCLE: 2050.   TIME(MSEC) 1431.86604
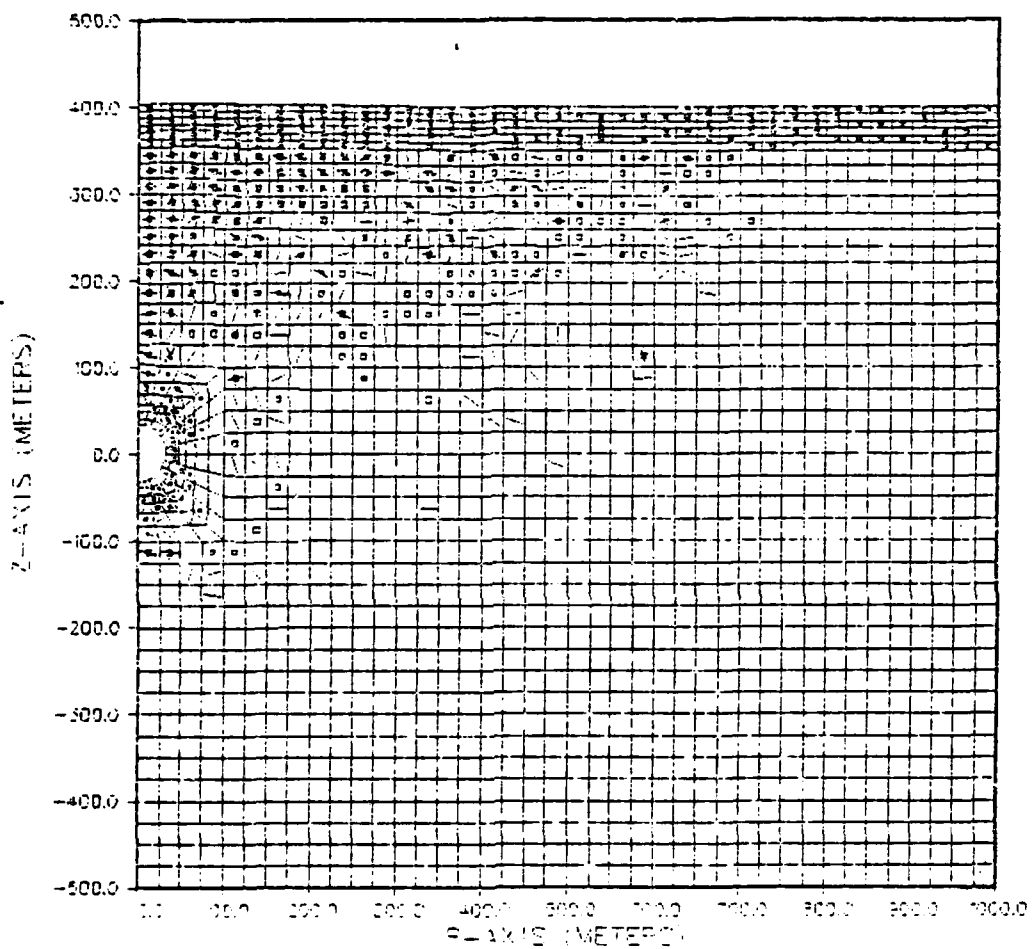
Figure 39. (continued)

120

In Figure 40, we again compare the seismograms for the one and two-dimensional PILEDRIVER sources (Figure 35), then repeat the comparison with the upgoing waves entirely suppressed. We see that suppressing the pP does improve the agreement, especially of the relative amplitudes of the three main peaks. The bottom two comparisons in the figure will be discussed in later paragraphs.

In Figure 37 we show the crack density at several times for GRAN2, which was an overburied explosion. This event had the least cracking of the four. Even so, we see that the 50 meter thick top layer is entirely spalled. Some cracks remain open at the last time, but not nearly as many as for PILEDRIVER.

In Figures 38 and 39 we show crack density plots for GRAN1 and GRAN3. Again, the first layer is entirely spalled. Many cracks remain open at the end of the calculation, and the cracked region extends to considerable depth. These two calculations are between PILEDRIVER and GRAN2 in the extent of cracking.

We should remark that the last crack density plot for each calculation shows the cracks that remain open when the calculation is terminated. There is clearly a substantial amount of momentum remaining inside the monitoring surface at this time. Thjis probably accounts for most of the "static" offset of the vertical impulse discussed in Section 4.3.

How much seismic energy is generated by the cracks that do close? In all four calculations, the entire first layer is spalled to a radius of 1000 meters. In most cases the spalled region is substantially thicker in the region directly above the explosion. The spall closure phases from such a large mass of material would make a huge seismic signal if they were in phase.

The volume of a cylinder with radius 1000 m and thickness 50 m is $50\pi \times 10^{12}$ cm^3. The density is 2.65 gm/cm^3, so the mass of this volume is

$$M = 4.16 \times 10^{14} \text{ gm.} \tag{29}$$

121
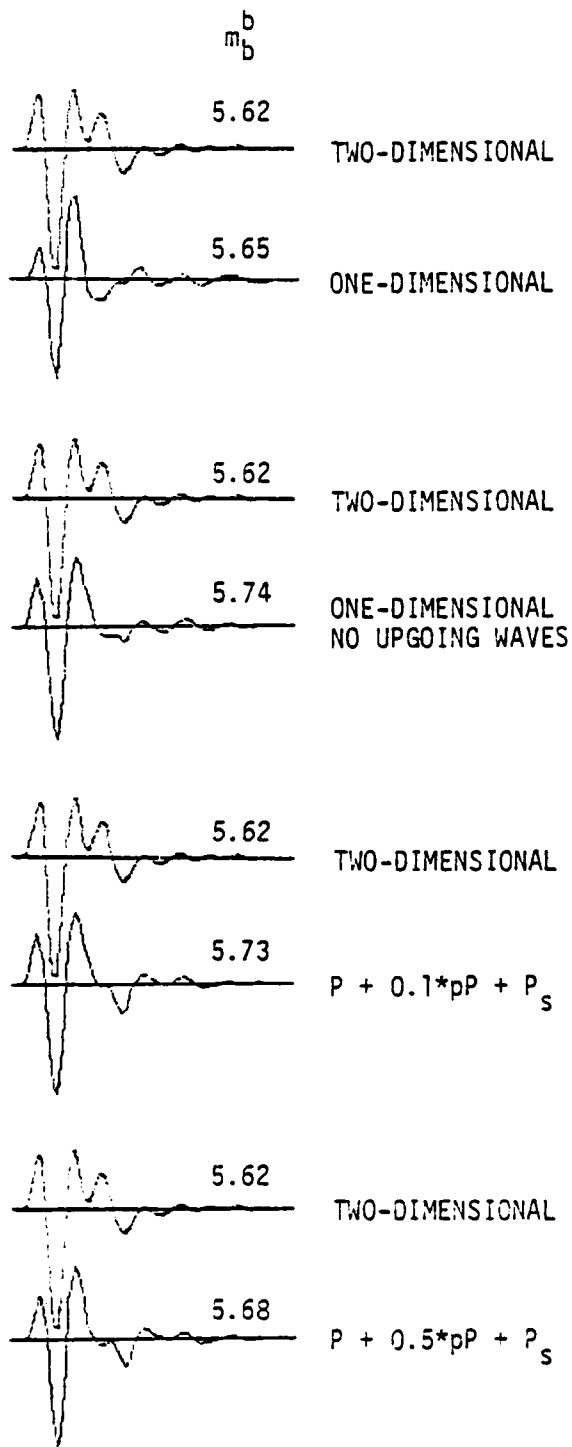
Figure 40. The seismogram for the two-dimensional PILEDRIVER cal-
culation is compared to synthetic seismograms constructed
with elementary point sources. The parameters for P_s are
1.4×10^{16} dyne-sec for the amplitude and 1.7 seconds for
the lag time.

122

If we follow Viecelli (1973) and assume the spall separation is linearly proportional to range, the total impulse is

$$I = \frac{M}{3} (2gh_0)^{1/2} \quad , \tag{30}$$

where g is the gravitational acceleration and h_0 is the maximum height of spall. But if h_0 is only 20 cm, we get

$$I = 2.75 \times 10^{16} \text{ dyne-sec,} \tag{31}$$

which happens to be Viecelli's estimate for the spall impulse for an event of this yield at Pahute Mesa. The actual displacement of the spalled zones is several meters (Rimer, et al, 1979).

In the bottom two seismogram pairs in Figure 40 we compare the 2-D PILEDRIVER calculation to synthetic seismograms computed with the RDP source 469 in which pP is partially suppressed and an impulsive point source has been added at the surface to represent spall closure. The amplitude of the spall impulse is about half the value in (31), so we see that an impulse that large would make a substantial contribution to the seismogram. The waveform comparison in Figure 40 is not very good, indicating that the impulsive point source model for spall closure is too simple.

The point of this analysis is that examination of the dimensions of the spalled region and the amount it is displaced suggests that coherent spall closure would give very large seismic phases. However, a phase that appears to be associated with spall closure is only seen on the shallow source (PILEDRIVER and GRAN3) records and it is not very large there. Thus, the potential energy in spalled material in these calculations is not very efficiently converted to seismic waves.

5.8 BODY WAVE SPECTRA

In Figure 35 we compared body wave seismograms for one- and two-dimensional calculations of the four sources. One step in

123

synthesizing these seismograms is to compute the far-field displacement spectrum at the appropriate takeoff angle (20.3°) at the base of the source structure (Table 6). These far-field displacement spectra are compared in Figure 41. The spectra for the RDP source have the familiar shape that occurs when pP is a spectral replica of P. The spectral peaks and holes occur at multiples of the reciprocal of the P-pP delay time.

As we examine the spectra for the two-dimensional sources, we see that the spectral scalloping is much weaker or absent. The overburied event GRAN2 shows some of the same character as that from the analogous RDP source, but even here the peaks and troughs are less prominent. The spectra for the other events have much weaker and less regular phase interference features. These spectra are evidence of the previously stated conclusion that the pP for the 2-D calculations is relatively small and is not a spectral replica for P. Spectral interference due to much later arriving phases, which we associate with spall closure, is also seen in the shallow source spectra.

5.9   AN EQUIVALENT RDP FROM BODY WAVES

As with the surface waves, we can display the two-dimensional effects in a direct way by computing the RDP that gives the same seismogram. Again, we use (16) in Section 3.4. That is, we divide the 2-D source spectra in Figure 41 by the 1-D source spectra and multiply by the RDP source function used for the latter.

The spectral amplitudes of the equivalent RVP for the four S-Cubed calculations are plotted in Figure 42, together with the appropriate one-dimensional source functions. The high frequency spikes in the $|\hat{\Psi}_e|$ are due to the presence of spectral nulls in the 1-D source spectra that are not replicated in the 2-D spectra.

Our interest in body waves is mainly in the spectral amplitudes of the source function near 1 Hz. Note that the 1-D and 2-D source functions are not very different at that frequency. We saw this in a different way when comparing time domain amplitudes in Figure 35. Also, ignoring the spikes, the high frequency rolloff of the $|\hat{\Psi}_e|$ is about that of the analogous 1-D source.

124
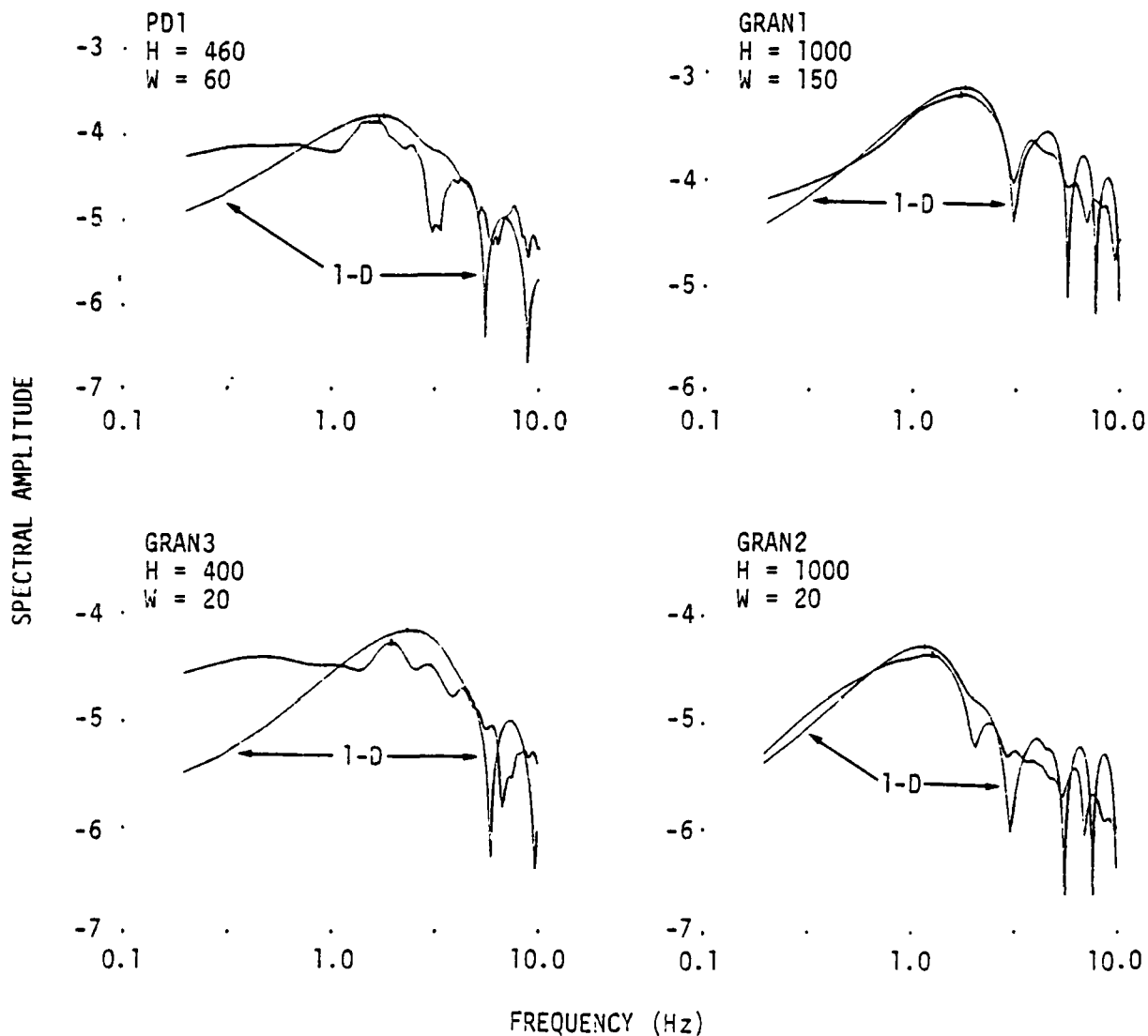
Figure 41. P wave spectra are compared for the one-dimensional and two-dimensional source calculations. The plots are in log-log format with the frequency scaled to 60 KT.

125
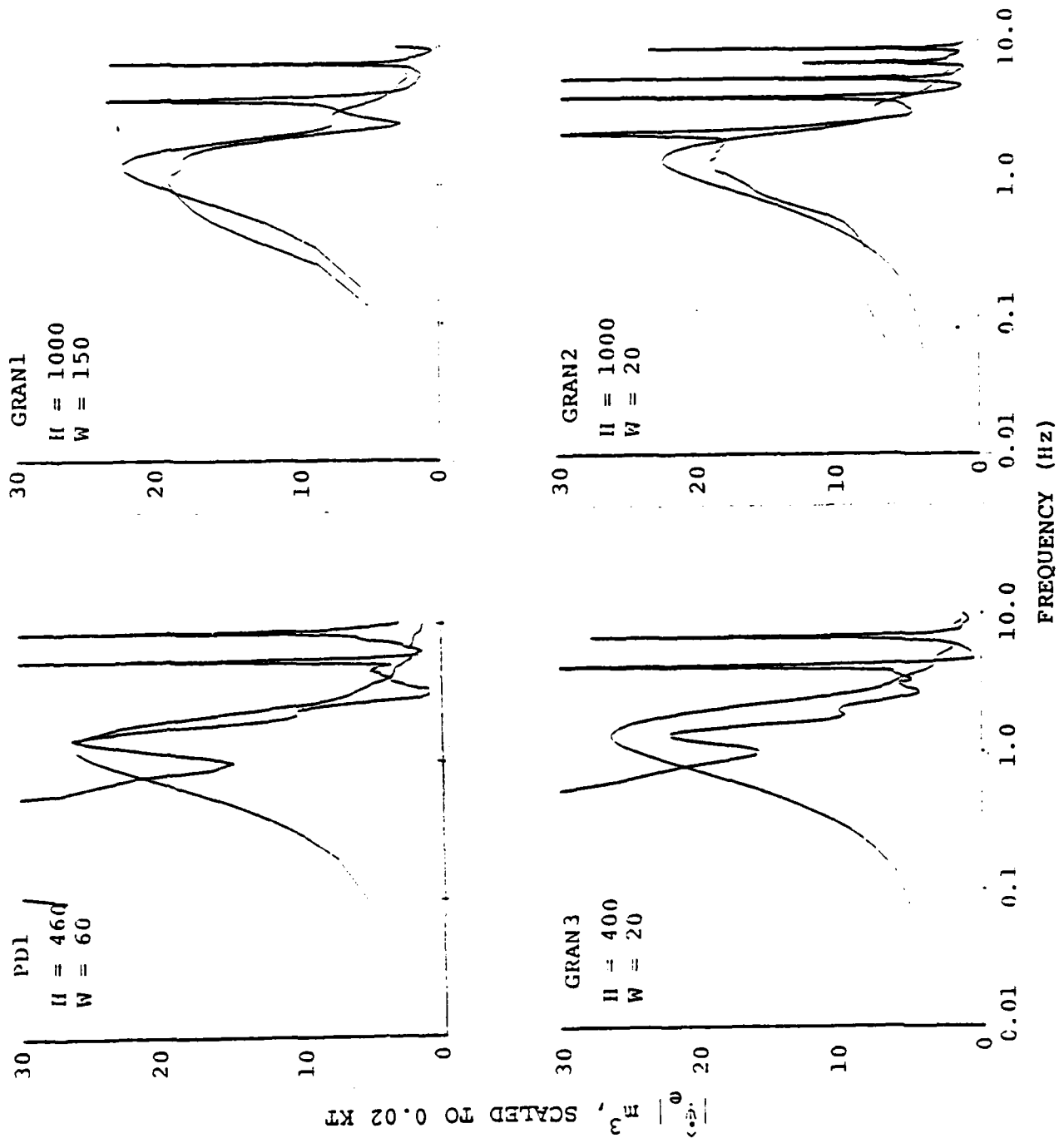
Figure 42. The equivalent RVP, $|\hat{\psi}_e|$, from P waves is compared to the analogous one-dimensional source. The amplitudes have been scaled to 0.02 KT and the frequencies to 60 KT.

126

The $|\hat{\Psi}_e|$ estimated from body waves in Figure 42 should be compared to estimates of the same quantity from surface waves in Figure 32. There are differences, as should be expected. If two-dimensional effects are important, the $|\hat{\Psi}_e|$ should vary with takeoff angle from the source.

The least variation between body and surface wave estimates for $|\hat{\Psi}_e|$ seems to be for the two deep explosions, GRAN1 and GRAN2. Both estimates agree that two-dimensional effects are not very important for these deep events. For the shallow sources, the equivalent RDP estimated from surface waves is rather different from that estimated from body waves, though they do agree that the 2-D source has much more long period energy.

5.10 SUMMARY

Body and surface wave seismograms computed for the four S-Cubed granite calculations give consistent and believable results. Our main conclusions are:

- While the calculations do not ideally satisfy conservation of momentum (the total vertical impulse has a static offset), there is no indication that this has more than a minor effect on the solutions.

- Two-dimensional effects are not very important for the two deep explosions. Both m_b and M_s are little different from the values estimated from an RDP source computed with the same con-stitutive model at the same depth. This is true even though considerable cracking and spallation occur.

- For the shallow events, the two-dimensional ef-fects act to enhance the excitation of surface waves by a factor of two or three.

127

- For body waves, the P phase, which controls m_b^b, is essentially the same for one- and two-dimensional source calculations.

- For the deep events both m_b^b and m_b^c are nearly the same for the one- and two-dimensional sources. However, examination of spectra indicate that pP is not a spectral shadow of P. This is not surprising in view of the cracking that occurs to significant depths.

- For shallow events, the two-dimensional effects substantially alter the portion of the waveform after the initial P wave arrival. This influences the commonly used magnitude, m_b^c, though by less than 0.2 m_b units.

128

VI. COMPARISON OF PREDICTED AND OBSERVED SEISMOGRAMS
FOR PILEDRIVER

6.1 INTRODUCTION

One of the four S-Cubed granite calculations described in Section IV was intended to model the PILEDRIVER event. Rimer, et al. (1979) showed that this two-dimensional calculation gives good agreement with the main features of the recorded near-field ground motions. In this section we will make a careful comparison of the far-field body and surface waves from this calculation with observations of PILEDRIVER.

6.2 COMPARISON OF PREDICTED AND OBSERVED SURFACE WAVES

In Section 5.5, Figure 34, we showed a teleseismic surface wave for the PILEDRIVER calculation. The M_s was computed from a large Airy phase that is a feature of the particular structure that was used for the synthesis. This M_s is 4.55, compared to the observed value for PILEDRIVER of about 3.88 (Eisenhauer, unpublished work). This synthetic M_s value is actually much larger than we would get from an "average" path model, as we will demonstrate.

Bache, Rodi and Harkrider (1978) and Bache, Rodi and Mason (1978) studied the Rayleigh waves from NTS explosions, including PILEDRIVER, at the WWSSN stations ALQ and TUC. In the former study crustal structures were inferred for the NTS-ALQ and NTS-TUC paths. The latter study was concerned with estimating the source (Ψ_∞) amplitudes of NTS explosions, using the crustal models to correct for the path.

In an earlier report, Bache, Gouoillaud and Mason (1977) compared the M_s measured by Eisenhauer with an M_s computed from the Airy phase amplitudes at ALQ and TUC. For eighteen events at Yucca Flat and Pahute Mesa, the residual was minimized by using the formulas:

$$M_s^A = \log A + 2.72 \quad ,$$

for ALQ, and

$$M_S^T = \log A + 2.17 \qquad\qquad (32)$$

for TUC. For PILEDRIVER, these formulas give

$$M_S^A = 3.82 \ ,$$

$$M_S^T = 3.65 \ , \qquad\qquad (33)$$

which are reasonably close to the "mean" value of 3.88.

Using the structures from Bache, Rodi and Harkrider (1978), we computed synthetic seismograms at ALQ and TUC using the 2-D PILEDRIVER source. The results are compared to the data in Figure 43. As was shown in Section V, the 2-D effects do not have much influence on the waveform. The M_S values computed from (32) are 4.19 for ALQ and 3.93 for TUC. These values are 0.36 and 0.62 M_S units smaller than value (4.55) we computed for the central U.S. structure in Section 5.5.

There are some other interesting aspects of the seismogram comparison in Figure 43 that should be discussed. The synthetic and observed waveforms are in excellent agreement at ALQ. At TUC, the agreement is not very good, even though the synthetic and observed records have almost the same phase and group velocity dispersion. This poor waveform agreement at TUC seems to be due to characteristics of the PILEDRIVER source. Figure 44, reproduced from Bache, Rodi and Harkrider (1978), compares synthetic and observed records for typical events at Yucca Flat and Pahute Mesa, as well as for PILEDRIVER. The PILEDRIVER recording at TUC is unique in its disagreement with the synthetic.

Another interesting facet of the comparison in Figure 43 is that the amplitude ratio is not very different at the two stations. Bache, Rodi and Mason (1978) found that the observed amplitudes at ALQ were relatively small compared to the synthetics for an RDP

130
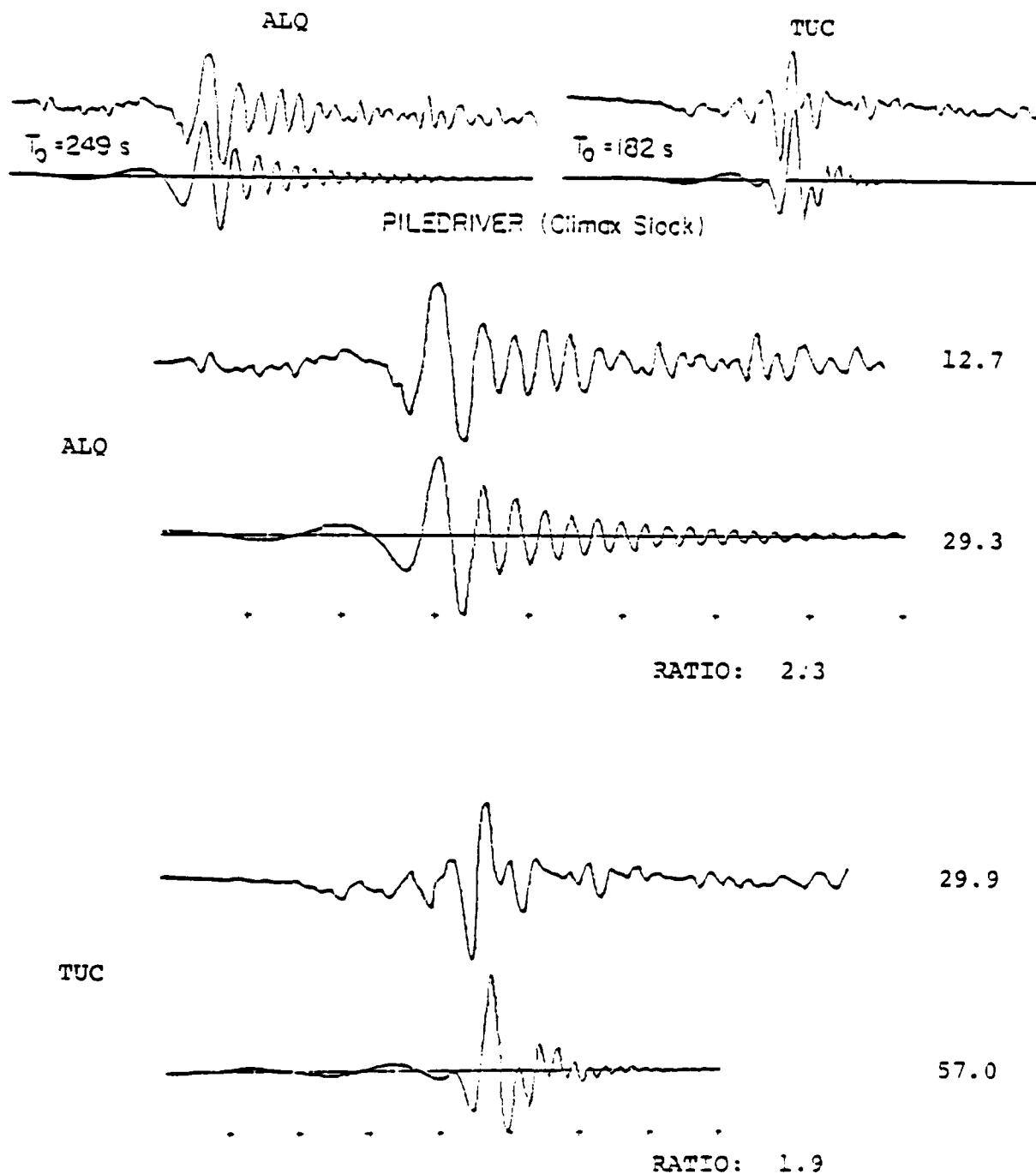
Figure 43. Observations of PILEDRIVER from ALQ and TUC are compared to synthetic seismograms. The synthetics are on the bottom for each pair. The two sets at the top of the page are from Bache, Rodi and Harkrider (1978) and were computed with an RDP source. The other synthetics were computed from the two-dimensional PILEDRIVER calculation. The peak-to-peak amplitude in microns is listed with each record. The time with respect to origin times for the ALQ and TUC records, observed and synthetic, is called T_0.

131
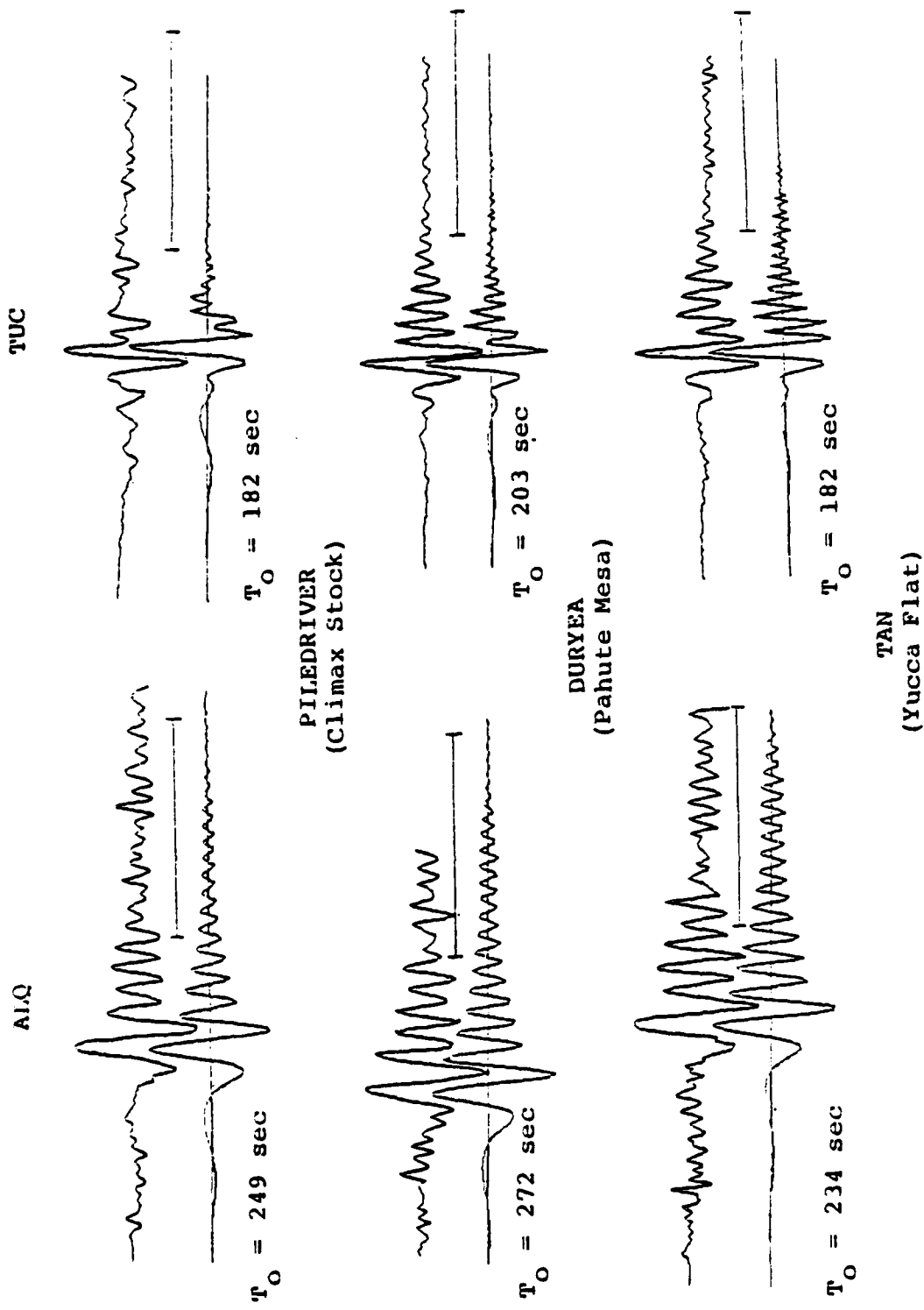
Figure 44. Theoretical and observed seismograms are compared at ALQ (left) and TUC for events in three test areas at NTS. A bar indicating one minute is shown. In each pair the observed and theoretical records start at the same time with respect to the explosion detonation and this time is indicated as T_0. The theoretical seismograms were computed with the same RDP source (reproduced from Bache, Rodi and Harkrider, 1978).

132

source, just as they are here. But in that study, an RDP source that matches the data at TUC was found to give synthetic seismograms that are 50-60 percent too large at ALO and this result seemed independent of test area. However, for the 2-D source, the amplitude ratio difference is only 2.3/1.9 or 20 percent.

An entirely satisfactory explanation of PILEDRIVER surface waves must deal with the observed radiation pattern, which has been interpreted as evidence for a double-couple component being superimposed on the explosion source (Toksöz and Kehrer, 1972). Both ALO and TUC are on positive lobes for the Toksöz and Kehrer (1972) double-couple fit to the data, but at azimuths where the inferred double-couple Rayleigh waves are larger than those from the explosion by factors of 3 to 3.5. This solution suggests that the explosion itself couples rather weakly into surface waves. Such a result is certainly inconsistent with current models for the constitutive behavior of granite represented by the calculations in this report.

Rivers and von Seggern (1979) calculated the seismic moment tensor that fits the observed surface waves for PILEDRIVER. They concluded that the orientation of the superimposed double-couple is consistent with vertical dip-slip faulting, rather than strike-slip faulting. This double-couple reduces the observed surface waves by about a factor of two. The two estimates for the PILEDRIVER double-couple result in surface wave amplitudes that differ by a factor of six.

If the Rivers and von Seggern (1979) double-couple solution were added to our two-dimensional source calculation (with little phase delay), the observed and synthetic seismogram amplitudes in Figure 43 would be in very close agreement. Some additional source complexity could also explain the waveform differences at TUC.

6.3 COMPARISON OF PREDICTED AND OBSERVED BODY WAVES

We begin with a careful comparison of synthetic and observed seismograms at two particular stations that we have used in previous synthetic seismogram studies. We then compare to a suite of WWSSN

133

data collected by Hadley and Hart (1979). The stations to be studied in detail are BFAK (Bluff, Alaska, $\Delta = 33.4°$) and HNME (Houlton, Maine, $\Delta = 36.5°$). The HNME data are taken from the LRSM shot report (SDL Report 165) for this event. The m_b^c at HNME is 5.53. The SDL report also gives a mean m_b of 5.43 for stations with $\Delta > 16°$. At BFAK the m_b^c is 5.54. These values are not much different from a carefully determined network average m_b of 5.47 given by Alewine, Young, Springer and Klepinger (unpublished report).

To compute synthetic seismograms at specific stations we must include the appropriate upper mantle and seismometer responses. For HNME we use the mantle model HWNE (Helmberger and Wiggins, 1971) and account for anelastic attenuation with $t* = 0.8$. This particular earth model and t* were found to be compatible with the HNME recordings of Pahute Mesa explosions studied by Bache, et al. (1979). At this range, the upper mantle response is not too different from a constant geometric spreading factor of 6.4×10^{-5} km^{-1}, as was mentioned in Section 3.6.

For BFAK synthetics we use the path model selected by Bache, et al. (1975) for a study of the relative body wave amplitudes of NTS explosions in different test areas. This upper mantle model is a slightly modified version of the average earth model C2 (Anderson and Hart, 1976). The smooth gradient below the 600 km discontinuity was modified in a way that enhances the theoretical amplitude at the range of BFAK relative to the original C2 model. This amplitude response is roughly equivalent to a constant geometric spreading factor of 10^{-4} km^{-1}, which is 25 percent or so larger than the response at this range from the HNME model (Bache, et al., 1975) or the Jeffreys-Bullen average earth model (Langston and Helmberger, 1975).

For Alaskan observations of NTS explosions, a t* of 1.05 was chosen by Bache, et al. (1975) as the value that seemed to give the best agreement with the observations for several stations and many

134

events. We also must account for differences in the seismometer response. In Figure 45 we plot the response for BFAK together with the LRSM response for PILEDRIVER at HNME and the KS36000 response used for the body wave synthetics in Sections III and V.

Before comparing the PILEDRIVER synthetics to the HNME and BFAK data, it is useful to look at how this comparison turns out for some other events. The HNME synthetic seismograms presented by Bache, et al. (1979) were for three representative large yield Pahute Mesa events, MAST, FONTINA and CAMEMBERT. These synthetics were computed with the Mueller/Murphy tuff/rhyolite source function (Mueller and Murphy, 1971), modified in an ad hoc way to account for nonlinear free surface interaction. The modifications were to multiply the upgoing waves from the source by a constant $\gamma < 1$ (reducing pP) and to add an impulsive downward force at the origin to represent spall closure (Table 11). In Section 5.6 we showed some seismograms computed in this way.

In Figure 46 and Table 12 we compare synthetic and observed seismograms at HNME and BFAK for the three Pahute Mesa events. The path models are as described in previous paragraphs and the source was computed with the γ and spall closure phase P_s, described in Table 11. The frequency content and amplitudes of the observations are matched very well at HNME, which is the station used to infer the parameters in Table 11. At BFAK the frequency content is reproduced pretty well, except for FONTINA where the synthetic has too little high frequency energy. The amplitudes of the synthetics at BFAK are too large by 40 percent or so. Considering the uncertainties in the source and path models, these are quite consistent results.

In Figure 47 and Table 13 we compare the BFAK and HNME observations of PILEDRIVER with synthetics computed with our two-dimensional source. The observations for this event are in analog form, so our measurements do not have the precision they did for the Pahute Mesa events. At BFAK the waveform and frequency

135
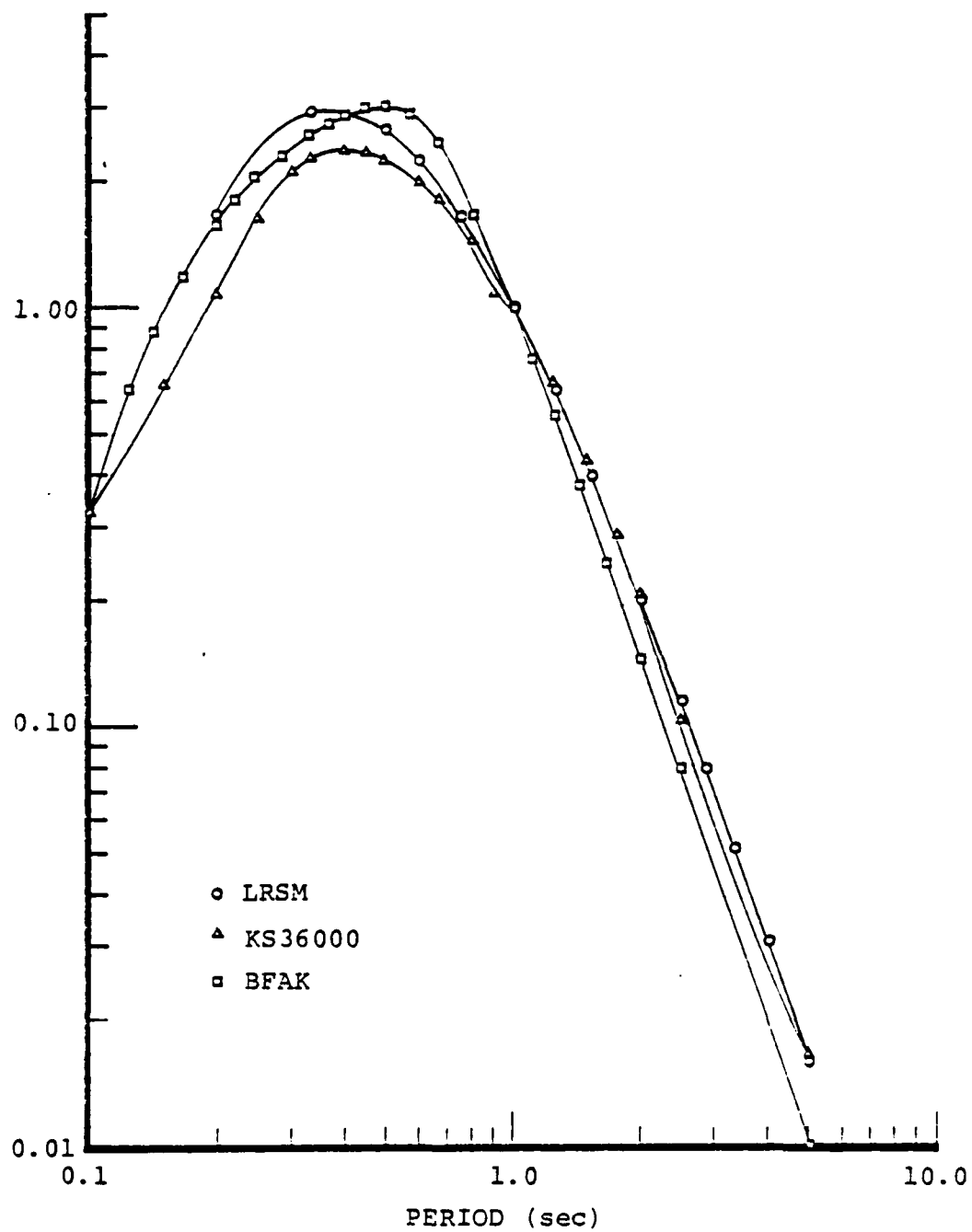
Figure 45. Seismometer amplitude response for the Benioff (LRSM) and
KS36000 seismometers used at HNME and the response of the
BFAK seismometer.

136

TABLE 11. PARAMETERS FOR THE P_s PHASE IN THE
SYNTHETIC SEISMOGRAM CALCULATIONS

	MAST	CAMEMBERT	FONTINA
Spall Impulse (Dyne-sec/kt)	10×10^{14}W	14×10^{14}W	9×10^{14}W
$P-P_s$ lag time (sec)	1.25	1.92	1.86
γ^*	0.60	0.50	0.50

Estimated of spall impulse from near-field data

Viecelli (1973):	3.5×10^{14}W
Sobel (12978):	$21-25 \times 10^{14}$W

Estimated of $P-P_s$ delay from near-field data:

2.0-2.5 seconds.

*Factor multiplying the upgoing waves from the source.

137
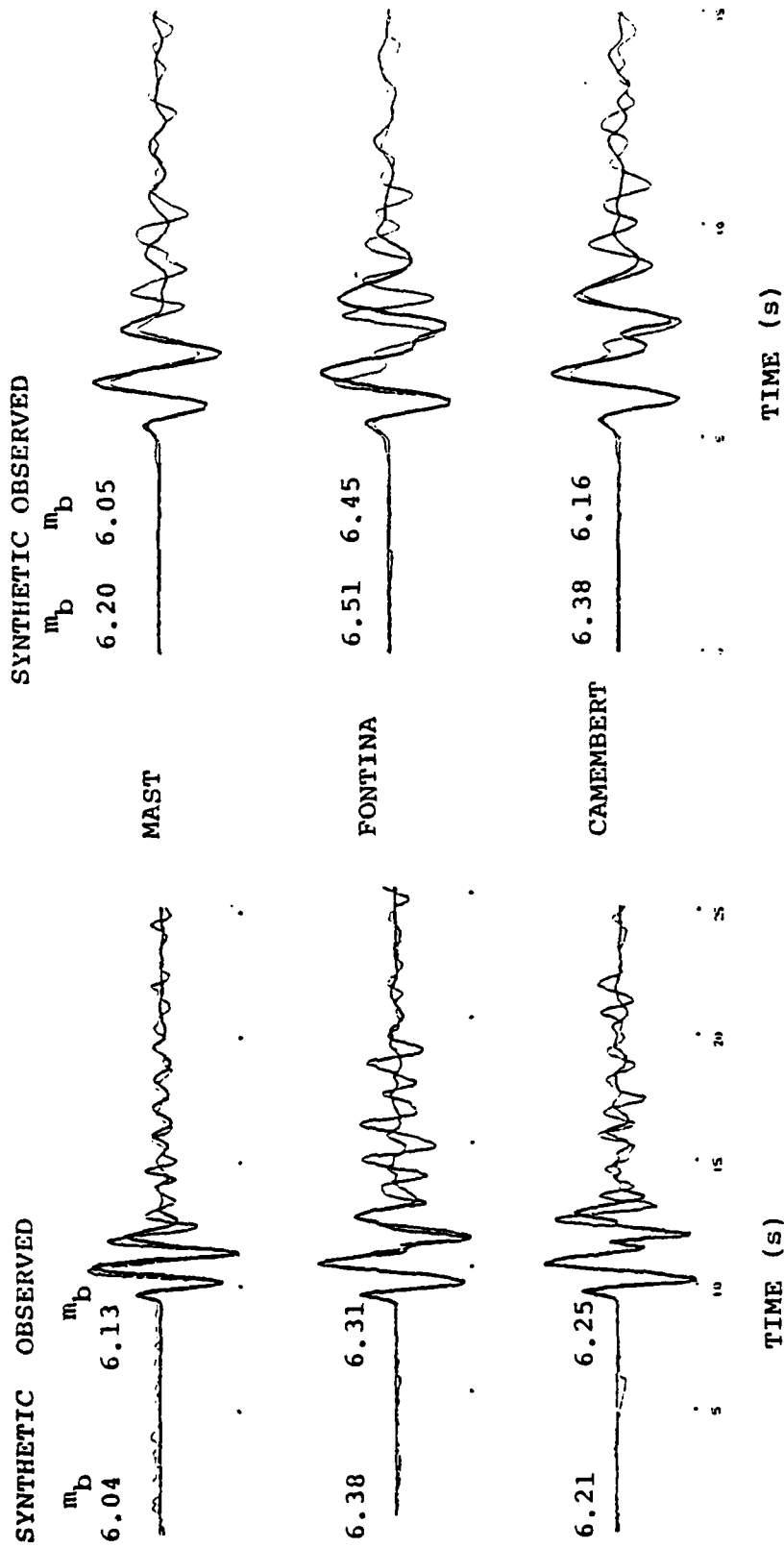
Figure 46. Comparison of synthetic (heavy lines) and observed seismograms at IIMNE and BFAK (Bluff, Alaska).

138

TABLE 12

COMPARISON OF SYNTHETIC AND OBSERVED P-WAVE AMPLITUDES FOR THREE PAHUTE MESA EVENTS

EVENT/STATION	b (nm)	T_b (sec)	m_b^b	c (nm)	T_c (sec)	m_b^c
MAST/HNME						
Observed	594	1.03	5.99	1159	1.12	6.25
Synthetic	524	0.92	5.98	906	1.07	6.16
Ratio	0.9			0.8		
FONTINA/HNME						
Observed	819	0.94	6.17	2014	1.26	6.43
Synthetic	1000	0.99	6.25	2397	1.28	6.50
Ratio	1.2			1.2		
CAMEMBERT/HNME						
Observed	845	0.99	6.16	1506	1.09	6.37
Synthetic	825	0.98	6.16	1453	1.15	6.33
Ratio	1.0			1.0		
MAST/BFAK						
Observed	254	0.99	5.81	466	1.04	6.05
Synthetic	321	0.97	5.92	656	1.04	6.20
Ratio	1.3			1.4		
FONTINA/BFAK						
Observed	729	0.99	6.27	1062	0.95	6.45
Synthetic	719	1.03	6.24	1532	1.20	6.51
Ratio	1.0			1.4		
CAMEMBERT/BFAK						
Observed	375	1.01	5.97	614	1.06	6.16
Synthetic	567	1.02	6.14	1040	1.09	6.33
Ratio	1.5			1.7		
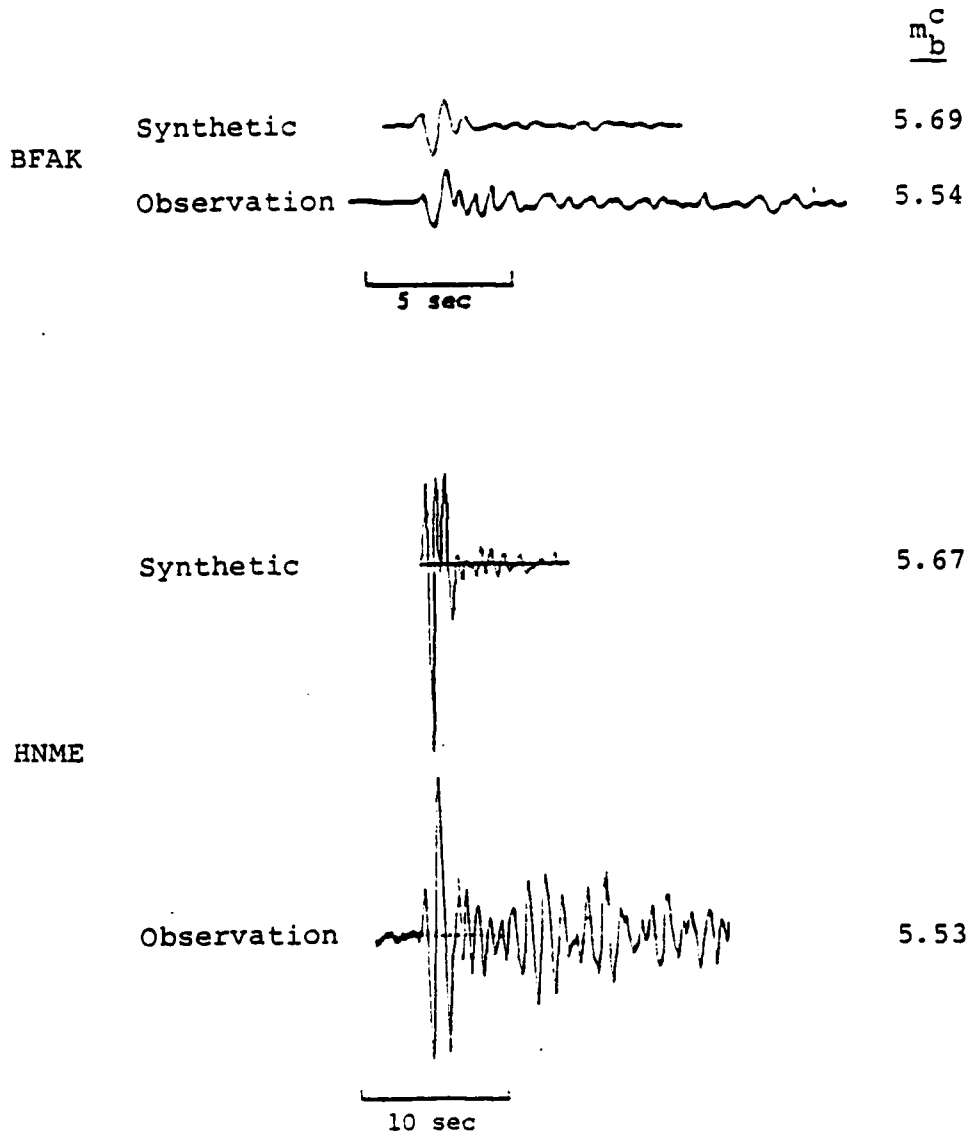
Figure 47. Synthetic seismograms are compared to observations of
PILEDRIVER at stations HNME and BFAK. The observed
records have been hand traced from film chip reproduc-
tions (BFAK) or the record provided with the SDL
report on PILEDRIVER.

140

TABLE 13

COMPARISON OF SYNTHETIC AND OBSERVED P-WAVE AMPLITUDES FOR PILEDRIVER

STATION	b (nm)	T_b (sec)	m_b^b	c (nm)	T_c (sec)	m_b^c
BFAK						
Observed	65	0.8	5.31	111	0.8	5.54
Synthetic	112	0.78	5.55	153	0.79	5.69
Ratio	1.7			1.4		
HNME						
Observed	103	1.0	5.26	210	1.1	5.53
Synthetic	184	0.71	5.66	186 ·	0.70	5.67
Ratio	1.8			0.9		

content agreement is excellent and the synthetic seismogram amplitudes are about 40-70 percent too large. In other words, for PILEDRIVER the match to the BFAK data is about the same as for the Pahute Mesa events.

The waveform and amplitude comparison at HNME is rather poor. Obviously, the relationship between the HNME and BFAK observations is different for PILEDRIVER than it was for the Pahute Mesa events. This can be seen by comparing waveforms. The two stations are compared in terms of their amplitude ratios and their magnitude and period differences for the four events in Table 14. PILEDRIVER is unique in having the HNME record be much longer period than that at BFAK. If the instrument response were indeed as we think it was (Figure 45), it cannot account for such a difference. In fact, we would expect the HNME recording (LRSM seismometer) to be shorter period than that at BFAK.

What can we conclude from the comparison at these two stations? Our PILEDRIVER calculation gives synthetics that match the BFAK data almost as well as did our synthetics for the Pahute Mesa events which, in turn, matched the HNME data even better. However, the PILEDRIVER waveform comparison at HNME is not good. There seem to be some azimuthal effects not present in the Pahute Mesa recordings.

To better resolve the agreement between the synthetic and observed short period P waves for PILEDRIVER, we now look at a more extensive data set. The WWSSN observations of PILEDRIVER were collected by Hadley and Hart (1979). These data are displayed in Figure 48, which is reproduced from the Hadley and Hart report. Also shown in the figure are several synthetic seismograms computed from our two-dimensional PILEDRIVER source, but let us defer discussion of these synthetic records until we have described the main features of the data.

Hadley and Hart (1979) compared the observations of PILEDRIVER to those from the Pahute Mesa explosion JORUM at ten common WWSSN

142

TABLE 14

COMPARISON OF OBSERVED DATA AT HNME and BFAK

AMPLITUDES	MAST	CAMEMBERT	FONTINA	PILEDRIVER
b (HNME/BFAK)	2.3	2.3	1.1	1.6
c (HNME/BFAK)	2.5	2.5	1.9	1.9
MAGNITUDES				
m_b (HNME-BFAK)	0.18	0.19	-0.10	-0.05
m_c (HNME-BFAK)	0.20	0.21	0.31	-0.01
PERIODS				
T_b (HNME-BFAK)	0.04	-0.02	-0.05	0.2
T_c (HNME-BFAK)	0.08	0.03	0.31	0.3
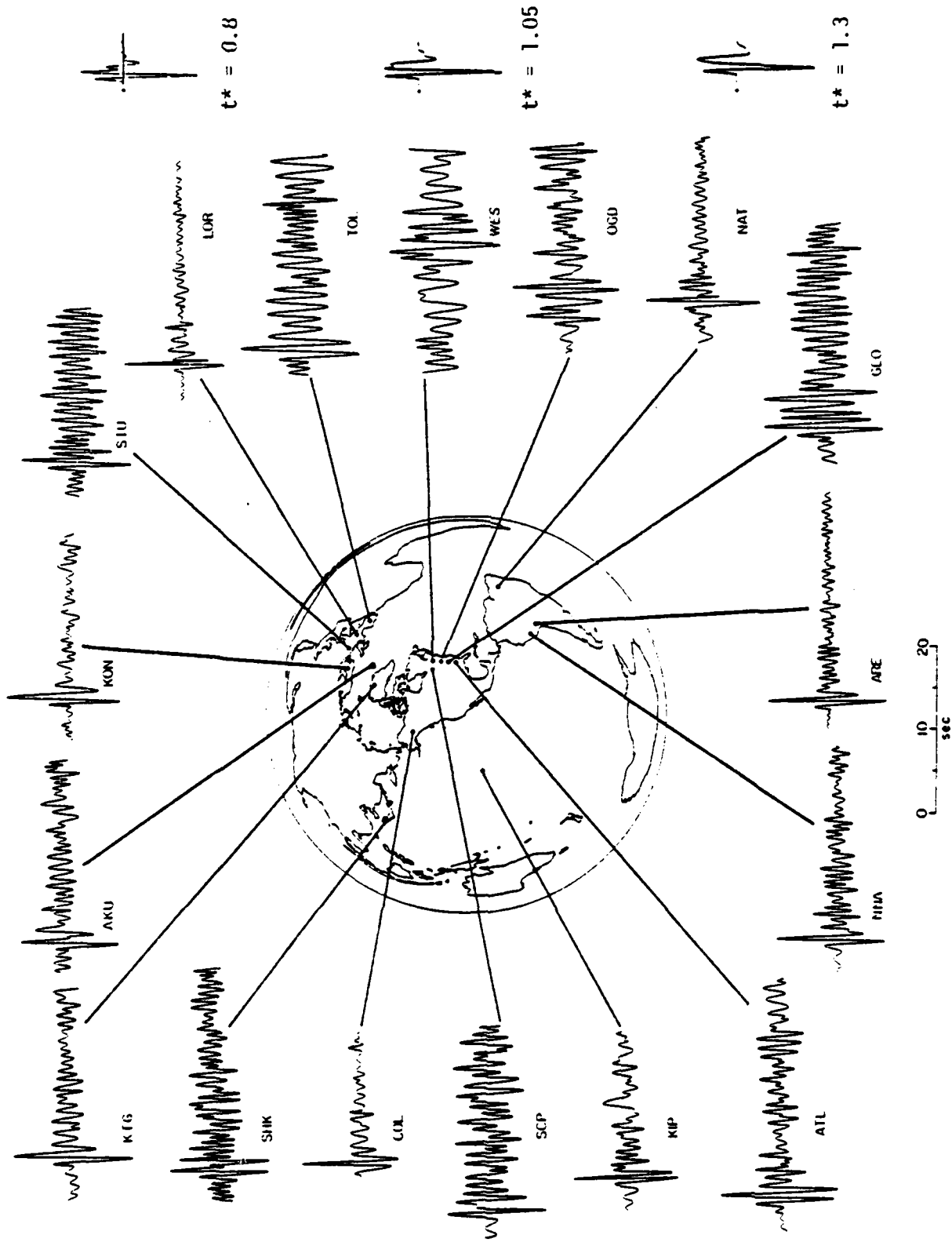
Figure 48. Teleseismic WWSSN recordings of PILEDRIVER (reproduced from Hadley and Hart, 1979). At the right are synthetic seismograms computed with the S-Cubed two-dimensional PILEDRIVER source and three values of t*.

144

stations. The amplitude ratios are listed in Table 15. In the northeast quadrant the PILEDRIVER amplitudes are markedly smaller than the JORUM amplitudes. Hadley and Hart (1979) also point out that at the northeast stations the waveforms for PILEDRIVER are much more complex than those for JORUM. Certainly, we can see in Figure 48 that the waveforms from the stations in the northeast quadrant are more complex than most of the others. Hadley and Hart conclude from these data that the structure beneath PILEDRIVER is introducing strong azimuthal effects.

The azimuth from PILEDRIVER to HNME is 60°, within the region where the WWSSN observations are relatively complex. However, the HNME seismogram, Figure 47, does not seem to be specially complex, so the effect of the near source structure (assuming it exists) is not as strong as it is at nearby WWSSN stations like WES, OGD or SCP. We did see (Table 14) that the amplitude of PILEDRIVER at HNME is relatively small compared to the BFAK amplitude, based on our experience with Pahute Mesa events, though the amplitude anomaly does not seem to be as large as it is for the WWSSN stations. All things considered, the evidence of azimuthal effects is enough to reduce the usefulness of HNME as a standard for comparison of synthetic and observed waveforms.

We now compare our synthetic seismograms to the WWSSN observations of PILEDRIVER. The comparison is shown in Figure 48 and is done taking the observations as a whole, rather than on a station-by-station basis. The simplest seismograms were written at KON, KTG, KIP, NNA, ARE, NAT and LOR. The waveforms at those stations are very similar and serve as a standard for comparison. They are featured by a b-phase amplitude that is 60 percent as large as the c phase.* The second downswing is about half as large as the first, though this is not as consistent as the b/c ratio. Deviations from this basic waveform at the other stations are nearly always associated with lower signal/noise or much larger coda amplitudes,

* The mean b/c for these seven stations is 0.61, with a standard deviation of 0.06.

145

TABLE 15
AMPLITUDE RATIOS, PILEDRIVER/JORUM*

Station	Azimuth ϕ	Ratio
ARE	133.1	0.35
KIP	258.7	0.50
SHK	309.1	0.13
COL	336.1	0.32
AKU	28.3	0.25
STU	32.9	0.27
TOL	46.0	0.13
WES	67.0	0.07
OGD	70.1	0.06
SCP	71.2	0.08

$133 < \phi < 33$:   Mean = 0.30,   standard deviation = 0.12

$45 < \phi < 72$:   Mean = 0.09,   standard deviation = 0.03.

Amplitudes from Figure 3.5., Hadley and Hart (1979).

146

which indicate the influence of structural complexity. An important exception is COL, which happens to be fairly close to BFAK where the waveform (Figure 47) does have the standard pattern.

The synthetic seismograms were computed with the WWSSN seismometer response, but otherwise are as in Figure 47. Seismograms are plotted in Figure 48 for three values of t*, which are 0.8, 1.05 and 1.3. The first two values are preferred for HNME and BFAK, as explained at the beginning of this section. The largest value, 1.3, is the average t* obtained by Helmberger and Hadley (1979) from simultaneous fitting of near- and far-field recordings of the Pahute Mesa events JORUM and HANDLEY.

The synthetic seismograms are not in good agreement with the observed waveforms for any of the t* values. The b/c amplitude ratio is much too small. Also, the secondary arrival that we identified with spall closure in the calculation (Section 5.7) does not seem to appear on the observed records. Both of these deviations from the observed waveforms are consistent with there being too much spallation in the PILEDRIVER source calculation. We had previously remarked that this was the case when examining the near-field velocity data (Section 4.1) and the extent of cracking and spallation (Section 5.7).

For comparing synthetic and observed amplitudes, we essentially follow the procedure used by Hadley and Hart (1979). They list the maximum peak-to-peak amplitude, corrected only for the instrument gain at 1 Hertz. They then corrected the data to a range of 30°, using the effective geometric spreading factors plotted by Langston and Helmberger (1975) for the Jeffreys-Bullen earth model.

In Table 16 we list the corrected amplitude data from Hadley and Hart (1979) for thirteen selected stations. We have not included the North American stations in the northeast quadrant where the amplitudes are anomalously low. We also list the analogous data for the b phase and the m_b computed from the c amplitude. At the bottom of Table 16 is the mean m_b and the (logarithmic) mean b and

147

TABLE 16

AMPLITUDE DATA FOR PILEDRIVER

Station	Range (Degrees)	m_b	Corrected c Amplitude	Corrected b Amplitude
ATL	26	5.63	160	110
COL	33	5.94	365	146
KIP	40	5.84	648	395
KTG	57	5.46	131	89
AKU	60	5.46	137	69
NNA	62	5.90	261	144
ARE	68	6.35	748	464
KON	73	5.86	329	207
LOR	80	5.65	345	173
TOL	81	5.49	180	120
STU	82	5.41	135	103
SHK	82	5.76	234	164
NAT	86	5.87	384	190

Mean m_b: 5.74

   Mean m_b ± one standard deviation = 5.48 to 6.00

Logarithmic Mean c: 266

   Mean c ± one standard deviation = 149 to 475.

Logarithmic Mean b: 157

   Mean b ± one standard deviation = 91 to 270.

148

c amplitudes. Note that the mean m_b is significantly larger than the network m_b values we mentioned at the beginning of this section. These other values may be biased low by including stations in the northeast quadrant with anomalously low (compared to Pahute Mesa events) amplitudes.

For the synthetic seismogram amplitudes we need to use a good "average" value for the geometric spreading. Since most of the data are from stations beyond 40° where most earth models give about the same effective 1/R, the most reasonable procedure is to use the value at 30° for the Jeffreys-Bullen model used to correct the data to this range. This value is 8.4×10^{-5} km^{-1} (Langston and Helmberger, 1975).

The amplitudes for the three synthetic seismograms plotted in Figure 48 are listed below (they are not corrected for period dependent instrument response).

t^*	b Phase	T_b	c Phase	T_c
0.8	375	0.76	425	0.78
1.05	167	0.86	168	0.90
1.3	85	0.97	90	1.39

Since the waveform agreement is not good, the most meaningful comparison is for the b phase. In Table 16 we see that this mean value is 157, with values of 91 to 270 representing one standard deviation from the mean. Thus, the synthetic with $t^* = 1.05$ gives good agreement with the observed amplitudes. For $t^* = 0.8$, the amplitude is too large, and it is too small for $t^* = 1.3$. As far as the frequency content of the waveform is concerned, the $t^* = 1.05$ case seems in reasonable agreement with the data. We believe the best average t^* for NTS explosions recorded at teleseismic stations is near 1.0.

Our conclusion is that the PILEDRIVER source has about the right direct P amplitude (the b amplitude is mainly controlled by

149

direct P). This conclusion cannot be quantified with much precision because of uncertainties about the best average values for the geometric spreading and t*. If the PILEDRIVER source is in error, our general impression, based on many poorly defined factors, is that it is too large.

The two-dimensional source calculation appears to include too much non-linear interaction with the free surface. The later portion of the synthetic P waveform does not match the data, apparently because pP is too greatly suppressed and because the spall closure energy is too large, or is timed incorrectly.

6.4 CONCLUSIONS

A comparison of this kind is always somewhat subjective and subject to qualification. For the surface waves the problem is how to account for the non-axisymmetric component that is present in the source. If we believe the Rivers and von Seggern (1979) solution for this component, our 2-D source gives surface wave amplitudes that match the data. Other assumptions about this component of the source will, of course, change one's perception of how well the surface wave data are matched. Also, the body wave analysis indicates that the free surface interaction effects are too strong in the calculation, at least at body wave periods. Reducing the free surface interaction to better match the PILEDRIVER short-period data would probably reduce the surface wave amplitude, though we cannot estimate the amount of the expected reduction.

For body waves we listed our conclusions at the end of the last section. Our best estimate is that the P wave source amplitude is nearly correct. The two-dimensional calculation does not appear to properly model the free surface interaction at the short periods seen on the P wave recordings, apparently because free surface interaction effects are "overpredicted." This is consistent with the comparison of computed and observed near-field data (Section 4.1), which indicate that the calculation included too much spallation.

150

VII. COMPARATIVE ANALYSIS OF ATI AND S-CUBED GRANITE CALCULATIONS

7.1 INTRODUCTION

We have described eleven two-dimensional calculations of explosions in granite, seven done by ATI and four by S-Cubed. Synthetic body and surface wave seismograms have been computed for all these calculations and we have listed the m_b and M_s values. In this section we present a unified summary of these results so they can be easily compared.

7.2 SUMMARY OF SURFACE WAVE MAGNITUDES

In Section 3.5 we presented the M_s for the ATI granite calculations. The analogous values for the S-Cubed calculations were given in Section 5.5. We now compare the two.

The same path model (Table 2) was used for all the surface wave calculations. In Section 6.2 we pointed out that this path model gives M_s values that are about 0.35 higher than we would expect for an "average" path model. If we are to compare to data, we should correct for this overestimation.

The M_s from the ATI and S-Cubed granite calculations can be directly compared. However, the properties of the granite in the source region are not the same for the two. Differences in elastic properties lead to quite predictable differences in surface wave propagation. Bache, Rodi and Harkrider (1978) point out that for explosions in similar materials, the surface wave amplitude scales with $\mu \psi_\infty$, where μ is the shear modulus. The ψ_∞ is a measure of the static displacement in the material.

The shear modulus for the ATI granite is 172 kbar, compared to $\mu = 206$ kbar for the S-Cubed granite. Thus, if all other factors were equal, we would expect the M_s for the S-Cubed calculations to be 0.08 units higher than for the ATI calculations. Differences other than this may be attributed to differing long period source levels.

151

A good estimate for the source amplitude for long period surface waves is provided by the $|\hat{\Psi}_e|$ plotted in Figures 10 and 32. The amplitudes are all scaled to a common yield, 0.02 Kt. The $|\hat{\Psi}_e|$ at 15 seconds for the ATI calculations is about 4 m^3 for 253 m depth, about 8 m^3 for 531 m depth, and between the two for the others. For the deep (1 km) S-Cubed calculations, the comparable values are 3.5 - 4.0 m^3, while the values for the shallow calculations are 11 to 13 m^3.

The M_s for all the granite calculations are plotted versus source depth in Figure 49. These values have been adjusted to an "average" crust by subtracting 0.35 from the M_s presented earlier. For this comparison all M_s, including the observed value for PILEDRIVER, have been scaled to 150 kt by adding log (150/W). As expected from the $|\hat{\Psi}_e|$, the ATI M_s values fall between the M_s values for shallow and deep S-Cubed calculations.

The M_s for the S-Cubed calculations show a remarkably consistent dependence on depth. As shown in the figure, the parametric dependence is about $h^{-1.46}$. This is a depth dependence that is very much stronger than expected from one-dimensional calculations like those in Figure 29. It may be compared to the depth dependence of $h^{-0.33}$ in the semi-empirical Mueller/Murphy model (Section 3.4).

In Figure 50 we plot the M_s values versus yield. The comparable M_s values computed with the S-Cubed RDP sources 469 and 472 (Figure 29) are also shown. This is simply another display of results that have been amply discussed. The PILEDRIVER observed value is quite close to the M_s for the RDP source at the appropriate depth, but is 0.32 units lower than the M_s for the 2-D PILEDRIVER calculation. However, recall (Section 6.2) that a study of surface wave radiation patterns for PILEDRIVER by Rivers and von Seggern (1979) concluded that the total source includes a double-couple contribution (not accounted for in our solution) which acts to reduce the observed PILEDRIVER Rayleigh wave amplitudes by a factor of two or three. The double-couple contribution should be removed for consistent comparison with the theoretical values in Figure 50.

152
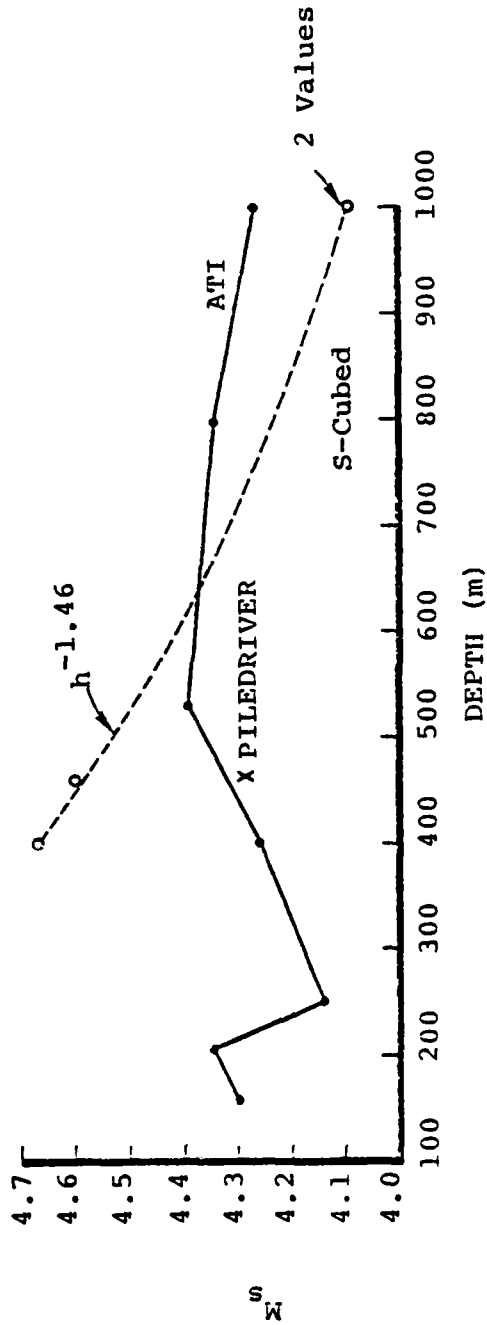
Figure 49. The M_S values for all the two-dimensional calculations are plotted versus source depth. The observed value for PILEDRIVER is also shown. All magnitudes have been scaled to 150 KT.

153

M_s VERSUS LOG YIELD
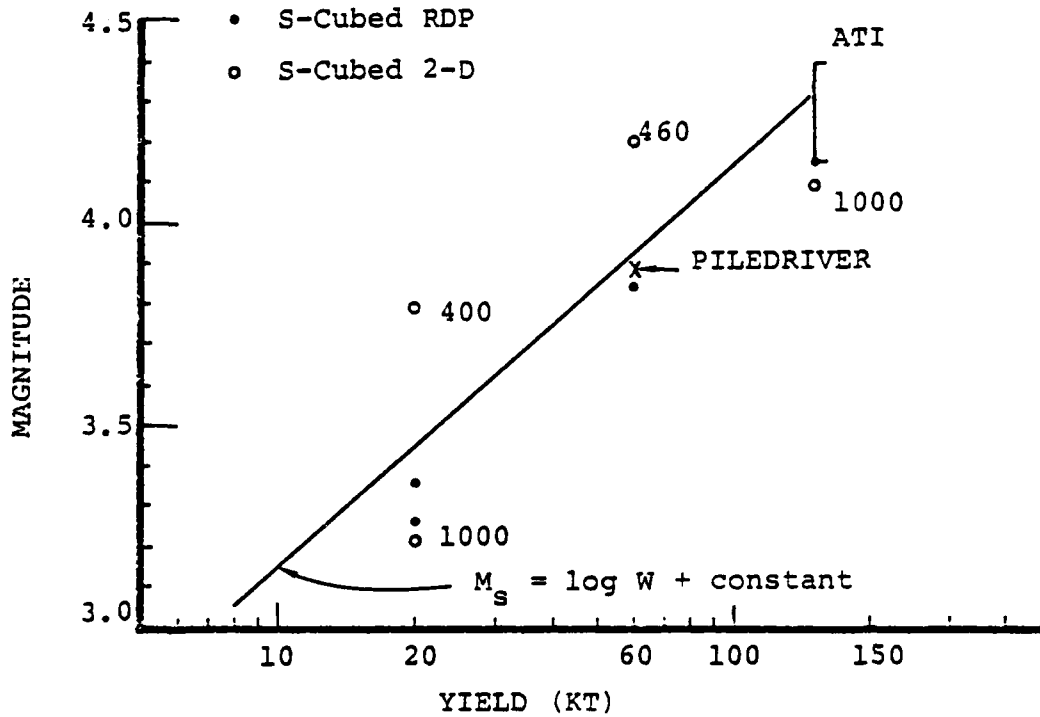
Figure 50. The M_s values for the S-Cubed RDP and two-dimensional source calculations are plotted versus explosion yield. The PILEDRIVER observed value and the range of M_s for the seven 150 KT ATI sources are also shown. The source depth of the S-Cubed two-dimensional calculations is noted with the M_s.

154

7.3 SUMMARY OF BODY WAVE MAGNITUDES

Body wave magnitudes were computed with the same path model for both the ATI (Section 3.6) and S-Cubed (Section 5.6) granite calculations. In comparing these m_b values, it is useful to separate effects due to differing elastic properties from those due to source coupling. Bache, et al. (1975) point out that the P wave amplitude for an RDP source in a realistic earth model is roughly proportional to $\alpha |\hat{\Psi}^R|$, where α is P wave velocity and '$\hat{\Psi}^R$' is the spectral amplitude of the reduced velocity potential at the appropriate period. We computed an effective RDP, $\dot{\Psi}_e$, for the two-dimensional S-Cubed calculations in Section 5.9 and found that it was not too different from the RDP from a one-dimensional calculation in the same material, especially for the deeper events. The same is probably true for the ATI calculations.

The P wave velocities for the ATI and S-Cubed calculations are 4.403 km/sec and 5.35 km/sec. Thus, if the effective source coupling, $\dot{\Psi}_e$, were the same for the two, we would expect the m_b for the S-Cubed calculations to be 0.08 units higher. Note that this is the same as the expected M_s difference due to elastic properties.

We will be plotting the ATI and S-Cubed body wave magnitudes versus source depth and yield. We want to include the observed data on the same plots, so should be sure that the theoretical values include our best estimate of the path parameters. In Section 6.3 we compared observed and computed values for PILEDRIVER as well as we could and concluded that our two-dimensional calculation gives seismograms that are probably about the right amplitude.

We will now plot the ATI and S-Cubed body wave magnitudes versus source depth and yield. We also wish to include the observed data on the same plots. The synthetic seismograms presented in Sections III and V did not include our "best" estimate for the average attenuation and geometric spreading, so these m_b data are shifted (by a constant) from the values we consider suitable for comparison to the data.

155

What about the data? Alewine, Young, Springer and Klepinger (unpublished report) have given m_b values for the granite explosions PILEDRIVER, SHOAL and HARDHAT. These values are comparable to our m_b^c. Based on the ratio of b to c amplitudes for PILEDRIVER (Section 6.3), we estimate that a b phase magnitude (m_b^b) would be about 0.25 units smaller.

The Alewine, et al. m_b^c for PILEDRIVER is 5.47. In Table 16 we saw that the mean m_b^c for thirteen WWSSN stations was 5.74. The b amplitude for our "best" synthetic PILEDRIVER seismogram was in good agreement with the b amplitude from these stations. We do not believe the lower magnitude of Alewine, et al. gives a more accurate estimate for the teleseismic P wave amplitudes, so we feel justified in normalizing all the magnitudes by a factor that causes the synthetic and observed m_b^b for PILEDRIVER to plot close together. For plotting observed values for all three granite explosions, it is more convenient to use the Alewine, et al. magnitudes, so we obtain a PILEDRIVER m_b^b by subtracting 0.25 from the Alewine, et al. m_b^c of 5.47. The result is 5.22. If we subtract 0.3 from the synthetic m_b^b for PILEDRIVER (Table 10), it becomes 5.32, and the 0.1 difference is about right for indicating the agreement between theoretical and observed values. Therefore, we plot the Alewine, et al. observed magnitudes and all theoretical magnitudes are adjusted by subtracting 0.3 units before plotting. Alternatively, we could have added 0.3 to the Alewine, et al. observed magnitudes to make them (at least PILEDRIVER) consistent with the observed WWSSN magnitudes.

In Figure 51 we plot the adjusted body wave magnitudes for the two-dimensional calculations versus source depth. The S-Cubed calculations and the observed m_b have been scaled to 150 kt by adding log (150/W). That is, we scale without accounting for any yield-dependent frequency shift. The dependence on depth of the "b" phase magnitude, m_b^b, is quite weak for both the ATI and S-Cubed calculations. The "c" phase magnitude is more sensitive to free surface effects, but it too has no strong depth trend.

156
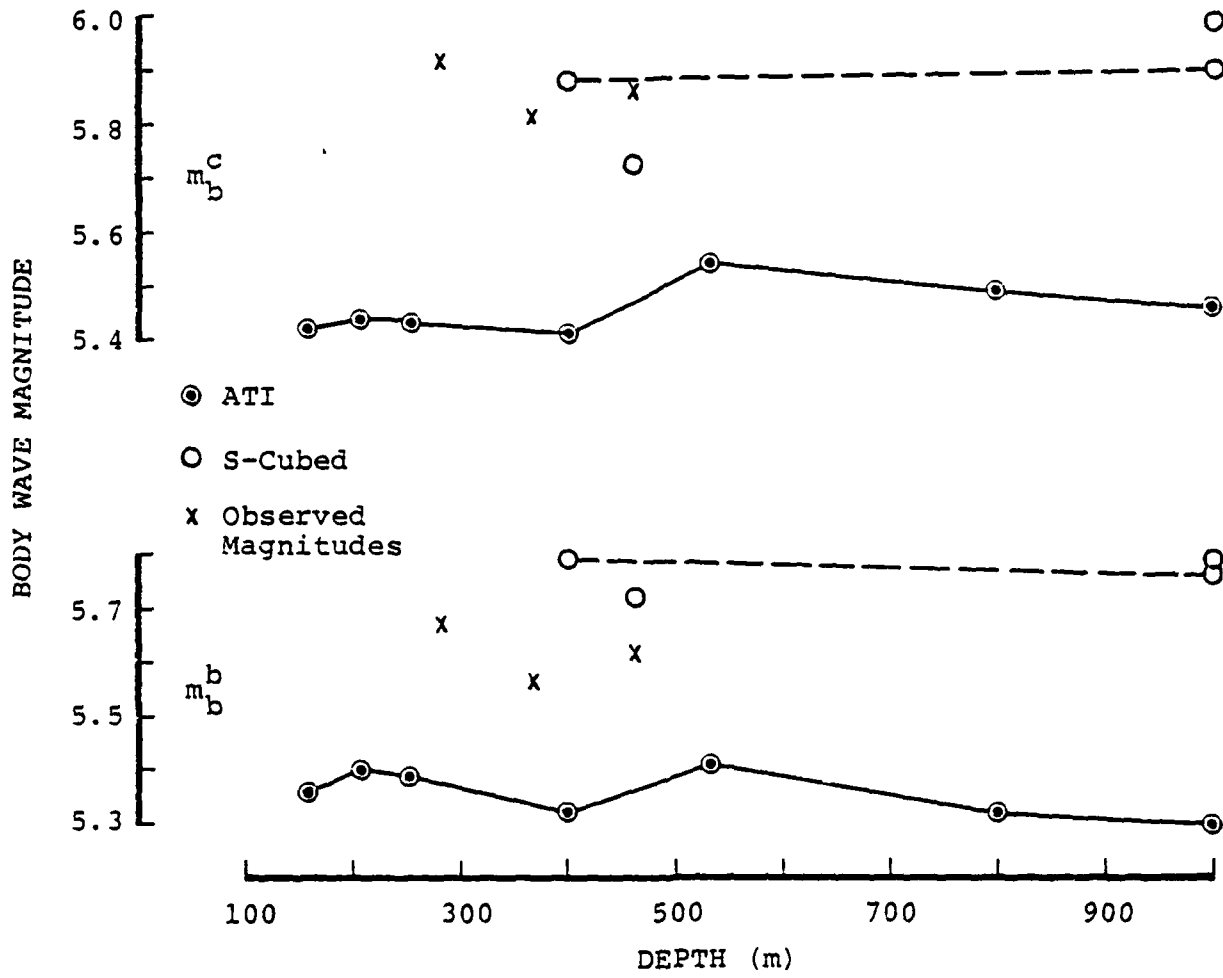
Figure 51. The m_b values for all the two-dimensional calculations are plotted versus source depth. The S-Cubed calculations at the same yield are connected with a dashed line. The observed values for HARDHAT, SHOAL and PILEDRIVER are also plotted with $m_b^b = m_b^c - 0.25$. All magnitudes have been scaled to 150 KT.

157

The S-Cubed calculations show much stronger coupling into short period P waves than the ATI calculations. Accounting for the elastic propagation effect, we estimate that the equivalent RDP for the S-Cubed calculations is about 2.2 times larger near 1 Hertz than that for the ATI granite. Since the long period level of the equivalent RDP for the ATI calculations is between the values for the shallow and deep S-Cubed calculations, this means that the effective RDP source function for the S-Cubed granite is much more peaked.

The body wave magnitudes are plotted versus explosion yield in Figures 52 and 53. As pointed out in Section V, the m_o^b is about the same for the one- and two-dimensional S-Cubed source calculations. The two-dimensional effects are apparent in the m_b^c, especially for the shallow events.

Our final plot, Figure 54, shows the m_b-M_s residual as a function of source depth. We also plot this residual for the Mueller/Murphy RDP source. The difference between the S-Cubed and ATI calculations is, once again, the strong dependence of M_s on source depth for the S-Cubed calculations. The residuals for the Mueller/Murphy RDP source have a similar depth dependence, but for quite different reasons. For an RDP source in an elastic earth model, the m_b is strongly dependent on depth because of the interference of P and pP.

158
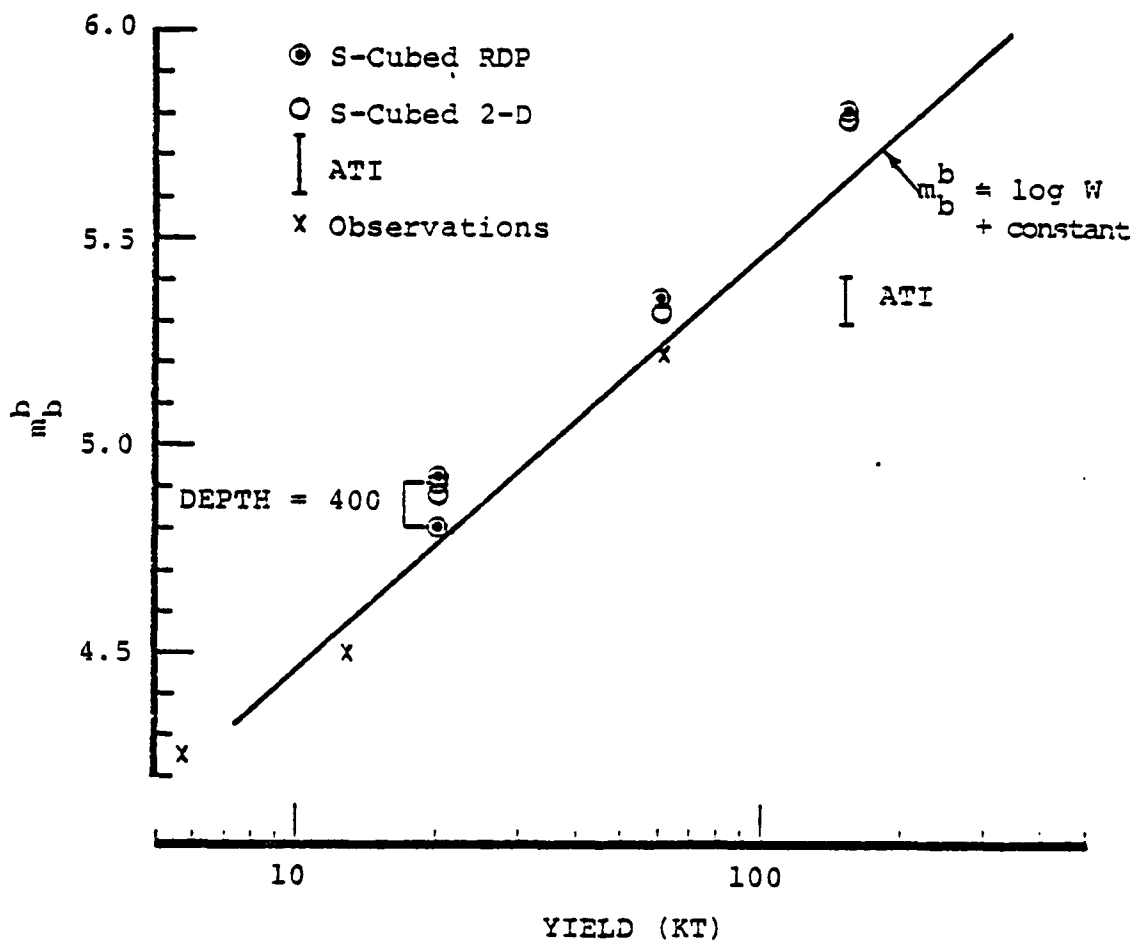
Figure 52. The b phase magnitude, m_b^b, is plotted versus yield. The values for the ATI calculations fall within the indicated range. The observed values are the published m_b^c minus 0.25 for HARDHAT, SHOAL and PILEDRIVER.

159
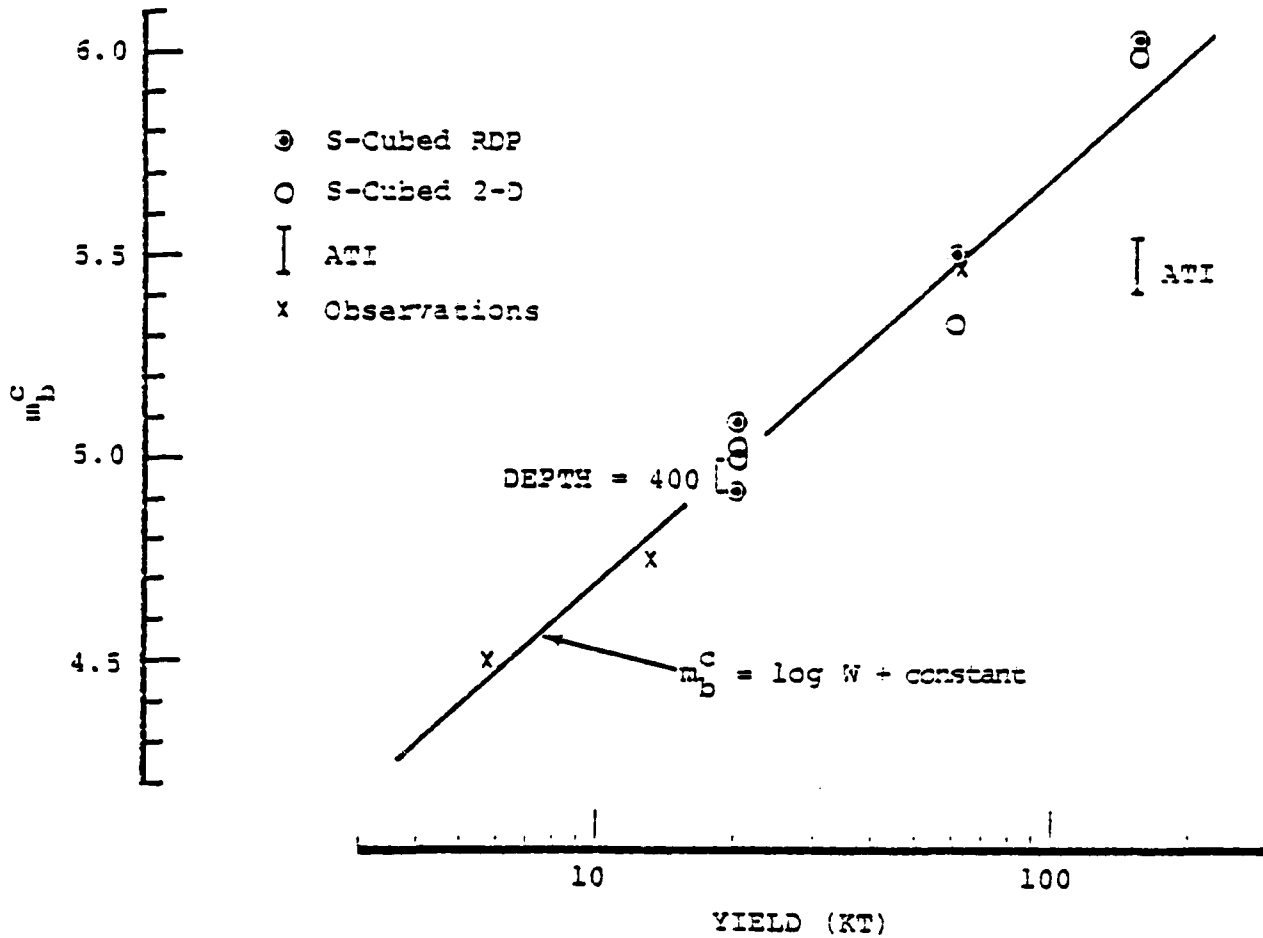
Figure 53. The c phase magnitude, m_b^c, is plotted versus yield. Published (network average) magnitude values for HARDHAT, SHOAL and PILEDRIVER are also plotted.

160
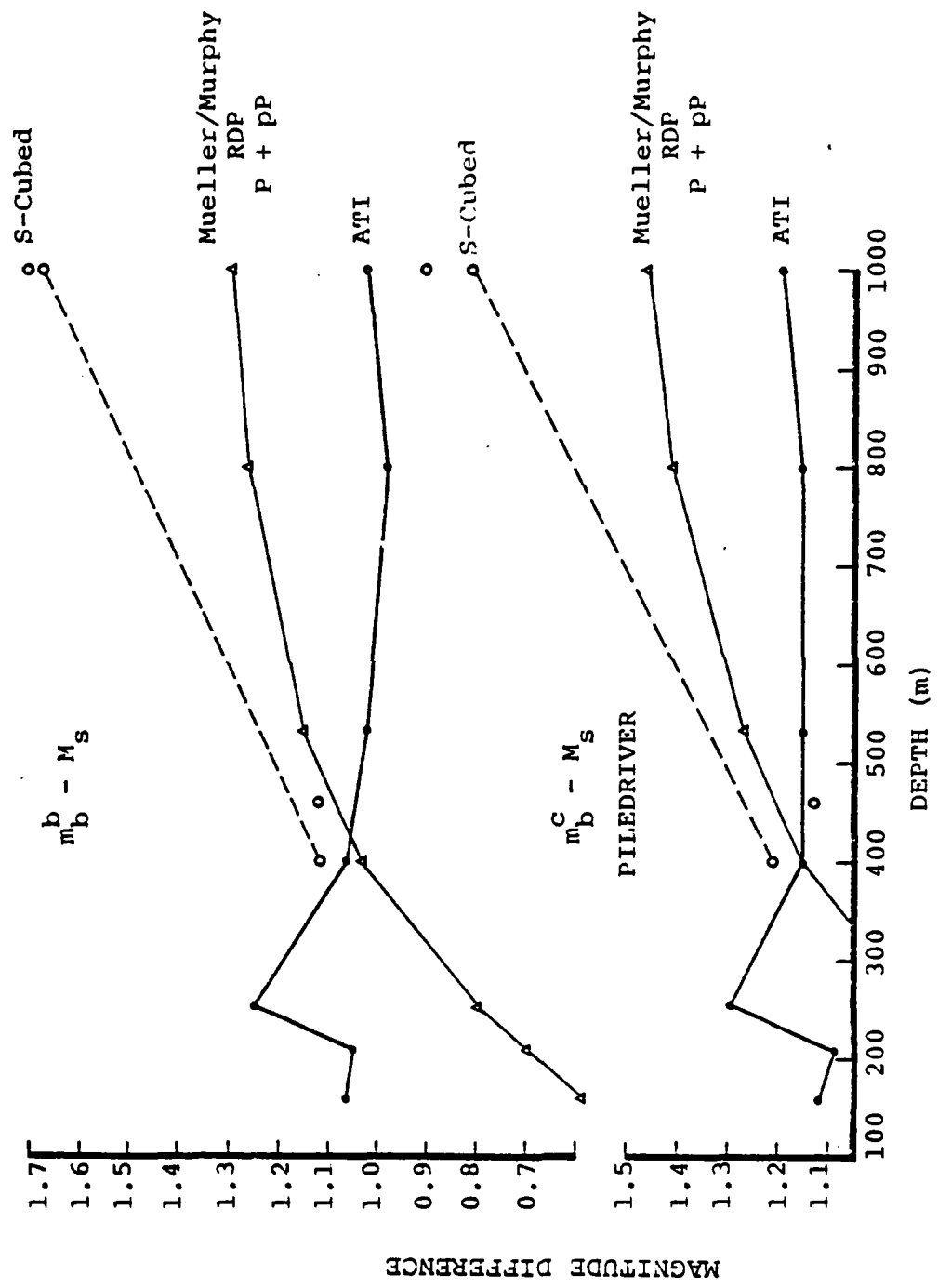
Figure 54. The difference between body and surface wave magnitude is plotted versus source depth.

161

THIS PAGE LEFT BLANK

REFERENCES

Anderson, D. L and R. S. Hart (1976), "An Earth Model Based on Free
    Oscillations and Body Waves," J. Geophys. Res., Vol. 81, pp.
    1461-1475.

Bache, T. C. and J. F. Masso (1978), "Analysis of Two Decoupled
    Explosion Simulations," Systems, Science and Software
    Technical Report, SSS-R-78-3627, April.

Bache, T. C., S. M. Day and J. M. Savino (1979), "Automated
    Magnitude Measures, Earthquake Source Modeling, VFM
    Discriminant Testing and Summary of Current Research,"
    Systems, Science and Software Quarterly Technical Report
    submitted to VSC/ARPA, SSS-R-79-3933, February.

Bache, T. C., W. L. Rodi, and B. F. Mason (1978), "Source Amplitudes
    of NTS Explosions Inferred from Rayleigh Waves at Albuquerque
    and Tucson," Systems, Science and Software Technical Report
    submitted to VSC/ARPA, SSS-R-78-3690, June.

Bache, T. C., P. L. Goupillaud and B. F. Mason (1977), "Seismic
    Studies for Improved Yield Determination," Systems, Science
    and Software Quarterly Technical Report submitted to VSC/ARPA,
    SSS-R-77-3345, July.

Bache, T. C., W. L. Rodi and D. G. Harkrider (1978), "Crustal
    Structures Inferred from Rayleigh Wave Signatures of NTS
    Explosions," Bull. Seism. Soc. Amer., Vol. 68, pp. 1399-1413.

Bache, T. C., D. G. Lambert and T. G. Barker (1979), "A Source Model
    for the March 28, 1975 Pocatello Valley Earthquake from Time
    Domain Modeling of Teleseismic P Waves," Bull. Seism. Soc.
    Amer., Vol. 70, pp. 405-418.

Bache, T. C., J. T. Cherry, N. Rimer, J. M. Savino, T. R. Blake, T.
    G. Barker, and D. G. Lambert (1975), "An Explanation of the
    Relative Amplitudes Generated by Explosions in Different Test
    Areas at NTS," Systems, Science and Software Final Report,
    submitted to the Defense Nuclear Agency, DNA 3958F, October.

Bache, T. C., and D. G. Harkrider (1976), "The Body Waves Due to a
    General Seismic Source in a Layered Earth Model: I.
    Formulation of the Theory," Bull. Seism. Soc. Amer., Vol. 66,
    pp. 1805-1819.

Burridge, R. and L. Knopoff (1964), "Body Force Equivalent for
    Seismic Dislocation," Bull. Seism. Soc. Amer., Vol. 54, pp.
    1875-1888.

Cherry, J. T. , T. C. Bache and D. B. Patch (1975), "The Teleseismic Ground Motion Generated by an Explosion in a Tunnel and Its Effect on the M_s/m_b Discriminant," Systems, Science and Software Final Report, submitted to DNA, DNA 3645F, May.

Cherry, J. T., T. C. Bache, W. O. Wray and J. F. Masso (1976), "Teleseismic Coupling from the Simultaneous Detonation of an Array of Nuclear Explosions," Systems, Science and Software Technical Report SSS-R-76-2865, February.

Cherry, J. T., N. Rimer and W. O. Wray (1975), "Seismic Coupling from a Nuclear Explosion: The Dependence of the Reduced Displacement Potential on the Nonlinear Behavior of the Near Source Rock Environment," Systems, Science and Software Report submitted to the Advanced Research Projects Agency, SSS-R-76-2742, September.

Eisler, J. D. and F. Chilton (1964), "Spalling of the Earth's Surface by Underground Nuclear Explosions," J. Geophys. Res., Vol. 69, pp. 5285-5293.

Frazier, G. A. and C. M. Petersen (1974), "3-D Stress Wave Code for the ILLIAC IV," Systems, Science and Software Final Contract Report, submitted to DNA, DNA 3331F, March.

Fuchs, K. (1966), "The Transfer Function for P Waves for a System Consisting of a Point Source in a Layered Medium," Bull. Seism. Soc. Amer., Vol. 56, pp. 75-108.

Hadley, D. M. and R. S. Hart (1979), "Seismic Studies of the Nevada Test Site," Sierra Geophysics Quarterly Technical Report submitted to VSC/ARPA, SGI-R-79-003, June.

Harkrider, D. G., (1964), "Surface Waves in Multilayered Media I. Rayleigh and Love Waves from Buried Sources in a Multilayered Elastic Half-Space," Bull. Seism. Soc. Amer., Vol. 54, pp. 627-679.

Harkrider, D. G. (1970), "Surface Waves in Multilayered Media II. Higher Mode Spectra and Spectral Ratios from Point Sources in Plane-Layered Earth Models," Bull. Seism. Soc. Amer., Vol. 60, pp. 1937-1987.

Helmberger, D. V. and R. A. Wiggins (1971), "Upper Mantle Structure of the Midwestern United States," J. Geophys. Res., Vol. 76, pp. 3229-3245.

Helmberger, D. V., and D. M. Hadley (1979), "Seismic Source Functions and Attenuation from Local and Teleseismic Observations of the NTS Events JORUM and HANDLEY," submitted to Bull. Seism. Soc. Amer.

Hoffman, H. V. and F. M. Sauer (1969), "Free Field and Surface Motions, PILEDRIVER Event," Stanford Research Institute Report, POR-4000.

Langston, C. A. and D. V. Helmberger (1975), "A Procedure for Modelling Shallow Dislocation Sources," Geophy. J., Vol. 42, pp. 117-130.

Marshall, P. D. and P. W. Basham (1972), "Discrimination Between Earthquakes and Underground Explosions Employing an Improved M_S Scale," Geophys. J., Vol. 28, pp. 431-458.

McEvilly, T. V. (1964), "Central U.S. Crust-Upper Mantle Structure from Love and Rayleigh Wave Velocity Inversion," Bull. Seism. Soc. Amer., Vol. 54, pp. 1997-2016.

Mueller, R. A., and J. R. Murphy (1971), "Seismic Characteristics of Underground Nuclear Detonations Part I. Seismic Spectrum Scaling," Bull. Seism. Soc. Amer., Vol. 61, pp. 1675-1692.

Murphy, J. R., (1977), "Seismic Source Functions and Magnitude Determinations for Underground Nuclear Detonations," Bull. Seism. Soc. Amer., Vol. 67, pp. 135-158.

Perl, N., F. J. Thomas, J. Trulio and W. L. Woodie (1979), "Effect of Burial Depth on Seismic Signals, Volume 1," Pacific Sierra Research Technical Report submitted to DNA/ARPA, PSR Report 815, May.

Perl, N. and J. Trulio (1979), "Effect of Burial Depth on Seismic Signals, Volume II," Pacific Sierra Research Technical Report submitted to DNA/ARPA, PSR Report 815, May.

Perrett, W. R. (1968), "Free Field Ground Motion in Granite, PILEDRIVER Event," Sandia Corporation Report, POR-4001.

Rimer, N., J. T. Cherry, S. M. Day, T. C. Bache, J. R. Murphy and A. Maewal (1979), "Two-Dimensional Calculation of PILEDRIVER, Analytic Continuation of Finite Difference Source Calculations, Analysis of Free Field Data From MERLIN and Summary of Current Research," Systems, Science and Software Quarterly Technical Report submitted to VSC/ARPA, SSS-R-79-4121, August.

Rivers, W. and D. H. von Seggern (1979), "Effect of Tectonic Strain Release on Surface-Wave Magnitudes," to be published as Teledyne Geotech Technical Report SDAC-TR-79-6.

Strick, E., (1970), "A Predicted Pedestal Effect for Pulse Propagation in Constant-Q Solids, Geophysics, Vol. 35, pp. 387-403.

165

Swift, L. M. (1962), "Measurement of Close-In Earth Motion, HARD HAT Event," Stanford Research Institute Report, VUP-2101.

Toksöz, M. N., and H. H. Kehrer (1972), "Tectonic Strain Release by Underground Nuclear Explosions and Its Effect on Seismic Discrimination," Geophys. J., Vol. 31, pp. 141-161.

Tryggvason, E. (1965), "Dissipation of Rayleigh Wave Energy," J. Geophys. Res., Vol. 70, pp. 1449-1455.

Viecelli, J. A. (1973), "Spallation and the Generation of Surface Waves by an Underground Explosion," J. Geophys. Res., Vol. 78, pp. 2475-2487.

APPENDIX A

SYNTHETIC SEISMOGRAMS
FROM COMPLEX SOURCE CALCULATIONS

A.1 INTRODUCTION

There is increasing interest in the use of large scale finite difference or finite element computer programs to simulate the complex nonlinear material behavior that occurs in the region immediately surrounding earthquake or explosion sources. To fully appreciate the significance of the output of these programs, it is important to be able to compute the ground motions at ranges much larger than the maximum dimension of the computational grid. As long as the material response can be assumed to be linearly elastic outside the immediate source region, analytical techniques can be used to continue the wave field to the ranges of interest. In this Appendix we describe these techniques.

When the source is assumed to be embedded in an elastic wholespace, an "equivalent elastic source" representation can be constructed by expanding the outgoing wave field in spherical harmonics (e.g., Bache and Harkrider, 1976). The source is then expressed in terms of multipolar coefficients that can be used as input to programs for computing synthetic seismograms. This technique has been used to study the results from complex explosion (Cherry, et. al., 1975, 1976; Bache and Masso, 1978) and earthquake (Bache, et. al., 1980) sources computed with finite difference programs.

When boundaries (e.g., a free surface) are present in the vicinity of the source, the ground motions at ranges outside the numerical grid can be computed with a wave field continuation method. Based on an elastodynamic representation theorem (e.g., Burridge and Knopoff, 1964). This method requires the convolution of stresses and displacements from the elastic region of the numerical source calculation with Green's functions representing

167

the elastic wave propagation through the medium outside the source region.

In subsequent sections we begin with the formulation of the basic theory. For earthquake sources the wave field continuation must be done in three dimensions. However, many important complex explosion phenomena are axisymmetric and the theory is specialized for this case. Some of the development for the axisymmetric case can also be used for three-dimensional sources in plane-layered earth models, since the Green's functions are azimuth-independent for such structures.

The details of the implementation depend on the choice of Green's functions for the propagation. Our emphasis here is on the Rayleigh wave modes for plane-layered earth models. Test problems which illustrate this case and demonstrate the accuracy that can be achieved are presented. In the body of the report, Sections III and V, we discuss synthetic far-field P wave seismograms. For these synthetic seismograms we used Green's functions computed with the propagator matrix method of Fuchs (1966).

A.2 FORMULATION

For the analytic continuation we use an elastodynamic representation theorem (Burridge and Knopoff, 1964). Assuming no body forces are present, this theorem may be written

$$u_i^F = - \int_{S_M} \left[G_j^i \star T_j^M - S_{jk}^i \star u_j^M n_k \right] dA \quad , \qquad (A.1)$$

where the repeated indices imply summation and the following notation has been used:

$u^F(\underset{\sim}{x}_F, t)$: Components of the displacements at x_F outside the source region;

$G_j^i(\underset{\sim}{x}_M, \underset{\sim}{x}_F, t)$:   Displacement in the direction j at x_M due to a unit impulsive force at x_F in the direction i;

$S_{jk}^i(\underset{\sim}{x}_M, \underset{\sim}{x}_F, t)$:   The components of the stress tensor at x_M due to a unit impulsive force at $\underset{\sim}{x}_F$ in direction $\underset{\sim}{i}$;

$T_j^M(\underset{\sim}{x}_M, t)$:   Components of the monitored traction vector on the monitoring surface;

u_j^M :   Components of the monitored displacement vector on the monitoring surface;

n_k :   Components of the normal to the monitoring surface, with the positive sense being for vector pointing away from the source:

S_M :   Area of the monitoring surface.

Also, convolution is indicated by

$$f*g = \int_0^t f(t-\tau)g(\tau) \; d\tau \quad . \tag{A.2}$$

Thus, the solution at some distant point is obtained by first convolving suitable Green's functions with stresses and displacements monitored on some surface that encloses the region of inelastic material deformation. The final solution is then obtained by integrating the convolution products over the monitoring surface. The restrictions on this technique are, first, that the

169

region outside the monitoring surface must be linearly elastic. Second, if the problem domain is bounded, the Green's functions must satisfy appropriate boundary data. The elastic medium may be anisotropic or have discontinuous properties, though the computation of Green's functions is much more difficult for such media than for homogeneous isotropic media.

To this point the formulation is entirely general. Let us now consider cases where the source and propagation medium are axisymmetric. This is the appropriate geometry for explosions near the free surface (or other horizontal boundaries) in plane-layered earth models.

As shown in Figure A.1, stresses and displacements are monitored on some surface with a typical point M. We wish to compute the displacement field at F. Let the monitored quantities at M be denoted by σ_{rr}^M, σ_{rz}^M, σ_{zz}^M, u_r^M and u_z^M. Then the components of the traction vector and displacement, referred to a local coordinate system (x_1, x_2, x_3) at F, are given by:

$$T_1^M = (\sigma_{rr}^M \cos\theta + \sigma_{rz}^M \sin\theta) \cos\xi ,$$

$$T_2^M = - (\sigma_{rr}^M \cos\theta + \sigma_{rz}^M \sin\theta) \sin\xi ,$$

$$T_3^M = \sigma_{rz}^M \cos\theta + \sigma_{zz}^M \sin\theta ,$$

$$u_1^M = u_r^M \cos\xi , \qquad\qquad\qquad (A.3)$$

$$u_2^M = - u_r^M \sin\xi ,$$

$$u_3^M = u_z^M ,$$

170
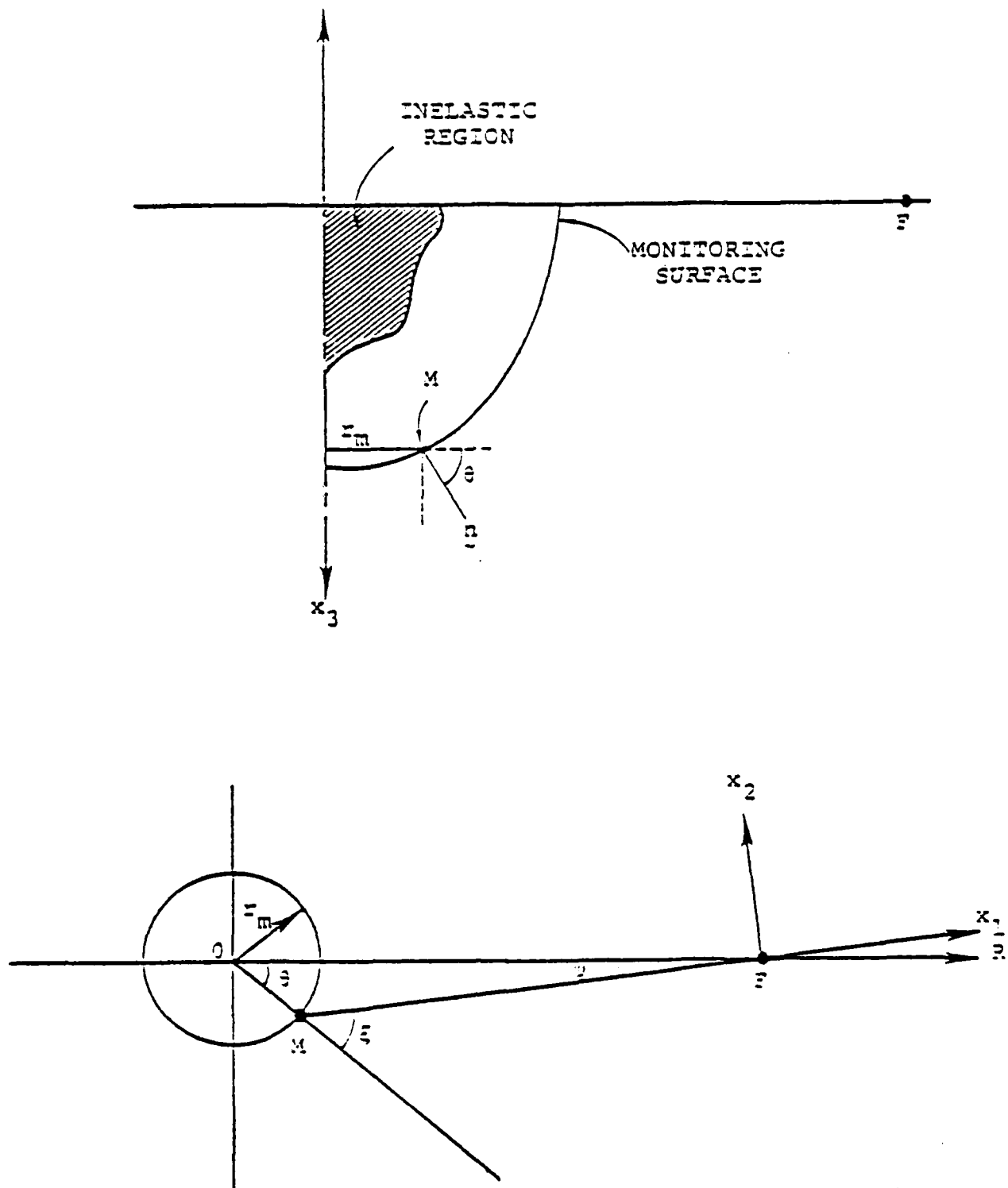
Figure A.1. At the top we show the inelastic region and monitoring surface for a typical axisymmetric problem. At a monitoring point M the outward normal to the monitoring surface is $\underset{\sim}{n}$. The coordinate system for defining the Green's function is shown in the horizontal plane (viewed from positive x_3) at the bottom.

171

$$n_1 = \cos\theta \cos\xi, \quad n_2 = -\cos\theta \sin\xi, \quad n_3 = \sin\theta \quad .$$

Also, the displacements at F in the global R-z system are related to the displacements in the x_1, x_2, x_3 system by

$$u_R^F = u_1^F \cos\psi - u_2^F \sin\psi \quad , \tag{A.4}$$

$$u_z^F = u_3^F \quad .$$

Using these coordinate transformations, (A.1) may be written:

$$u_R^F = -\int_{S_M} r \left[(G_r^R * \sigma_{rr}^M + G_z^R * \sigma_{rz}^M) - (S_{rr}^R * u_r^M + S_{rz}^R * u_z^M) \right] dz$$

$$\qquad - \int_{S_M} r \left[(G_z^R * \sigma_{zz}^M + G_r^R * \sigma_{rz}^M) - (S_{rz}^R * u_r^M + S_{zz}^R * u_z^M) \right] dr \quad ,$$

$$u_z^F = -\int r \left[(G_r^Z * \sigma_{rr}^M + G_z^Z * \sigma_{rz}^M) - (S_{rr}^Z * u_r^M + S_{rz}^Z * u_z) \right] dz$$

$$\qquad - \int r \left[(G_z^Z * \sigma_{zz}^M + G_r^Z * \sigma_{rz}^M) - (S_{rz}^Z * u_r^M + u_r^M + S_{zz}^Z * u_z^M) \right] dr \quad ,$$

where the quantities G_r^R, G_z^R, etc., are azimuthal averages of the Green's functions in the x_1, x_2, x_3 system. The explicit formulas for the azimuthally averaged Green's functions are the following:

$$G_r^R = \int_0^{2\pi} \left[G_1^1 \cos\psi \cos\xi - G_2^1 \sin(\xi+\psi) + G_2^2 \sin\xi \sin\psi \right] d\phi$$

$$G_z^R = \int_0^{2\pi} \left[G_3^1 \cos\psi - G_3^2 \sin\psi \right] d\phi \quad , \tag{A.6}$$

172

$$G_r^z = \int_0^{2\pi} \left[G_1^3 \cos - G_2^3 \sin \right] d\phi ,$$

$$G_z^z = \int_0^{2\pi} \left[G_3^3 \right] d\phi , \qquad\qquad (A.7)$$

where $G_1^1(\underset{\sim}{x}_M, \underset{\sim}{x}_F, t)$, etc., are evaluated at $x_{2F} = 0$. Also, $\underset{\sim}{x}_M = (x_1, x_2, x_3)$, with

$$x_1^2 = R_F^2 + r_M^2 - 2r_M R_F \cos\phi,$$

$$x_2 = 0 ,$$

$$x_3 = z_M - z_F . \qquad\qquad (A.8)$$

For axisymmetric problems formulated to compute the solution in the ω, k domain (e.g., modal solutions), the azimuthal integrations in (A.6) and (A.7) may be computed analytically. In the p, t domain (e.g., generalized ray theory), these integrations cannot, in general, be performed analytically. However, in the far-field, an analytic approximation for these integrals may be used.

The formulas for The azimuthally averaged stress Green's functions, S_{rr}^R, etc., are given by:

$$S_{rr}^R = \int_0^{2\pi} \begin{bmatrix} (S_{11}^1 \cos^2\xi - S_{21}^1 \sin2\xi + S_{22}^1 \sin^2\xi \cos\upsilon \\[2mm] - (S_{11}^2 \cos^2\xi - S_{21}^2 \sin2\xi + S_{22}^2 \sin^2\xi) \sin\upsilon \end{bmatrix} d\phi,$$

$$S_{zr}^R = \int_0^{2\pi} \begin{bmatrix} (S_{31}^1 \cos\xi - S_{32}^1 \sin\xi) \cos\upsilon \\[2mm] - (S_{31}^2 \cos\xi - S_{32}^2 \sin\xi) \sin\upsilon \end{bmatrix} d\phi , \qquad (A.9)$$

$$S_{rr}^z = \int_0^{2\pi} \left[S_{11}^3 \cos^2\xi - S_{21}^3 \sin2\xi + S_{22}^3 \sin^2\xi \right] d\phi ,$$

173

$$S_{zr}^{R} = \int_{0}^{2\pi} \left[S_{31}^{1} \cos \xi - S_{32}^{2} \sin \xi \right] d\theta \; ,$$

$$S_{zz}^{Z} = \int_{0}^{2\pi} \left[S_{33}^{1} \cos \psi - S_{33}^{2} \sin \psi \right] d\phi$$

$$S_{zz}^{Z} = \int_{0}^{2\pi} S_{33}^{3} \; d\phi.$$

If the azimuthal averages in (A.6) and (A.7) can be analytically determined, it is not necessary to use (A.9). Instead, the constitutive equation of the medium at the monitoring point can be used. Thus, for an isotropic medium

$$S_{rr}^{Z} = \lambda \left(\frac{\partial G_{r}^{Z}}{\partial r} + \frac{G_{r}^{Z}}{r} + \frac{\partial G_{z}^{Z}}{\partial z} \right) + 2\mu \frac{\partial G_{r}^{Z}}{\partial r} \; ,$$

$$S_{zz}^{Z} = \lambda \left(\frac{\partial G_{r}^{Z}}{\partial r} + \frac{G_{r}^{Z}}{r} + \frac{\partial G_{z}^{Z}}{\partial z} \right) + 2\mu \frac{\partial G_{z}^{Z}}{\partial z} \; , \qquad \text{(A.10)}$$

$$S_{rz}^{Z} = \mu \left(\frac{\partial G_{r}^{Z}}{\partial z} + \frac{\partial G_{z}^{Z}}{\partial r} \right),$$

where λ and μ are Lame's constants, and formulas of the same type can be written for S_{rr}^{R}, S_{zr}^{R} and S_{zz}^{R}.

The basic formulation for analytical continuation of axi-symmetric source computations is now complete. These equations are valid for a monitoring surface of arbitrary shape. Implementation requires the computation of Green's functions appropriate for the application of interest.

174

A.3 FORMULATION FOR SURFACE WAVES

For many problems the primary interest is in the normal mode contribution to the solution for waves in layered media. For example, the far-field fundamental mode Rayleigh wave is commonly observed and studied for seismic events. For such problems the analysis is more conveniently done in the frequency – wave number domain.

We will develop the solution using Green's functions computed following Harkrider (1964, 1970), though the theory is easily modified to use alternative techniques for computing Rayleigh wave modes.

For the azimuthally averaged Rayleigh wave displacement, Green's functions for a particular mode are:

$$G_r^R = i\pi \underset{\sim}{A}_R \, \epsilon_o \, X_{(z)} \, J_1(kr) \, H_1^{(2)}(kR) \, ,$$

$$G_z^R = i\pi \underset{\sim}{A}_R \, \epsilon_o \, W_{(z)} \, J_0(kr) \, H_1^{(2)}(kR), \qquad\qquad (A.11)$$

$$G_z^Z = \pi \underset{\sim}{A}_R \, X_{(z)} \, J_1(kr) \, H_0^{(2)}(kR) \, ,$$

$$G_z^Z = \pi \underset{\sim}{A}_R \, W_{(z)} \, J_0(kr) \, H_0^{(2)}(kR) \, ,$$

where $X(z)$ and $W(z)$ are the normalized horizontal and vertical displacement eigenfunctions and ϵ_o is the ellipticity. The $\underset{\sim}{A}_R$ is the amplitude response, k is wave number, r is the radial distance to a point on the monitoring surface and R is the range.

The stress Green's functions are easily computed from (A.10) using the following identities given by Harkrider (1970):

175

$$\frac{\partial X(z)}{\partial z} = k \left(W(z) + \frac{\tau(z)}{\mu} \right) \quad ,$$

$$(A.12)$$

$$\frac{\partial W(z)}{\partial z} = - k \left(\frac{\lambda X(z) + \Sigma(z)}{\lambda + 2\mu} \right) \quad ,$$

where $\tau(z)$ and $\Sigma(z)$ are the normalized horizontal and vertical stress eigenfunctions.

A.4   TEST CALCULATIONS

To illustrate the method and determine its accuracy, we compare exact and analytically continued Rayleigh waves for a spherically symmetric explosion source which is represented by the potential plotted in Figure A.2. The exact solution is computed with the method of Harkrider (1964). The monitored solutions for input to the wave field continuation method were computed in two ways, analytically with generalized ray theory and numerically with the SWIS finite element program (Frazier and Peterson, 1974). The geometry for the generalized ray theory calculations of the stresses and displacements at ten evenly spaced monitoring stations is shown in Figure A.3. The elastic properties of the halfspace are $\alpha = 6.0$ km/sec, $\beta = 3.5$ km/sec, $\rho = 2.7$ gm/cm^3. However, the monitored quantities can be scaled to other materials with the same Poisson's ratio by dividing the displacements by the shear modulus, μ, and the time by the velocity, α. This scaling is easily seen from the reduced displacement potential representation for an explosion. The displacement is related to this potential by

$$u = \frac{\partial}{\partial R} \left[\frac{\Psi(t - R/\alpha)}{R} \right] \quad ,$$

$$(A.13)$$

where R is the spherical coordinate. For a pressure profile applied to the surface of a spherical cavity of radius R_e, the Fourier transformed reduced displacement potential is (Mueller and Murphy, 1971)
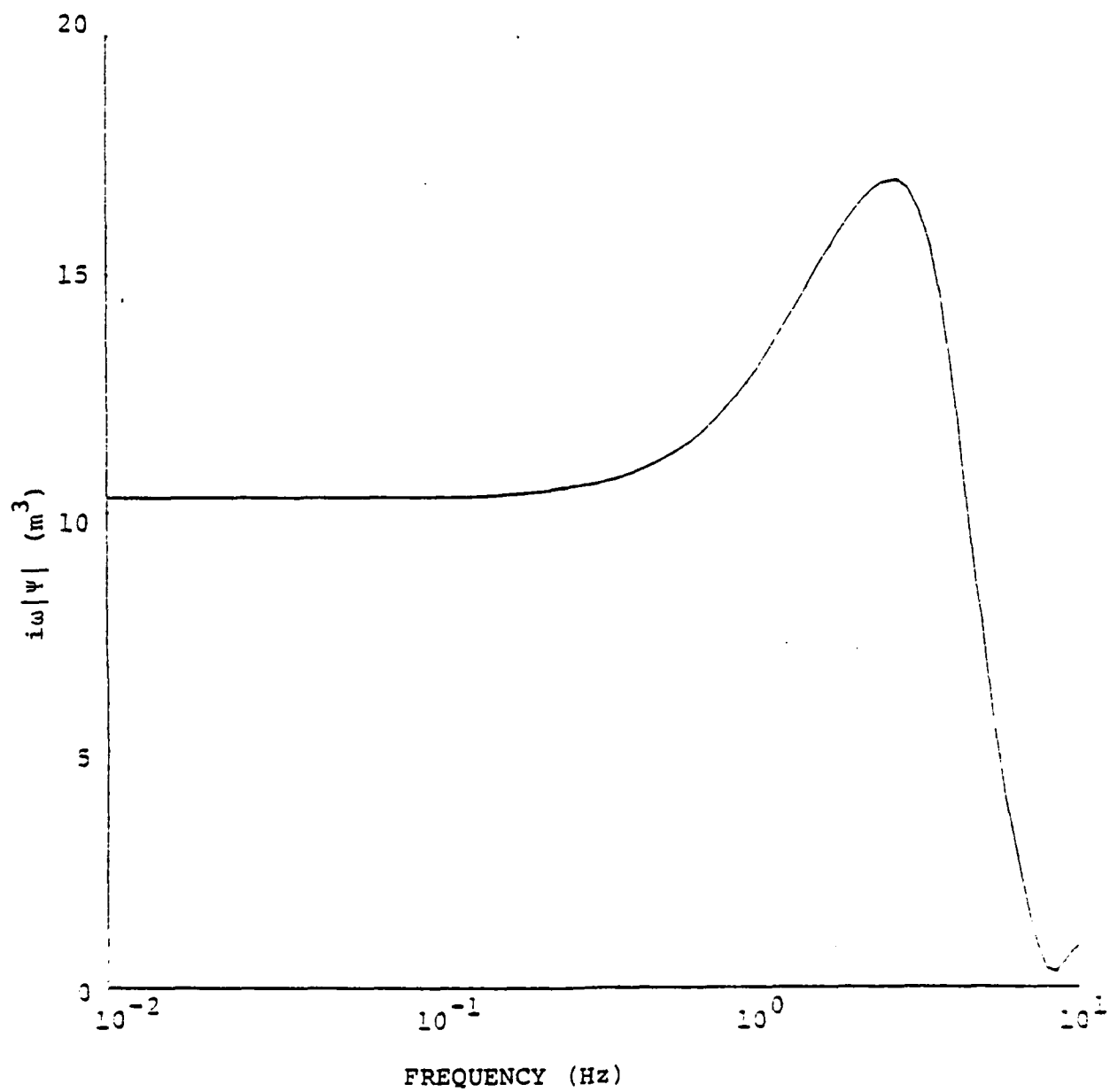
176

Figure A.2. The spectral amplitude of the Fourier transform of the reduced velocity potential used for the explosion simulations.
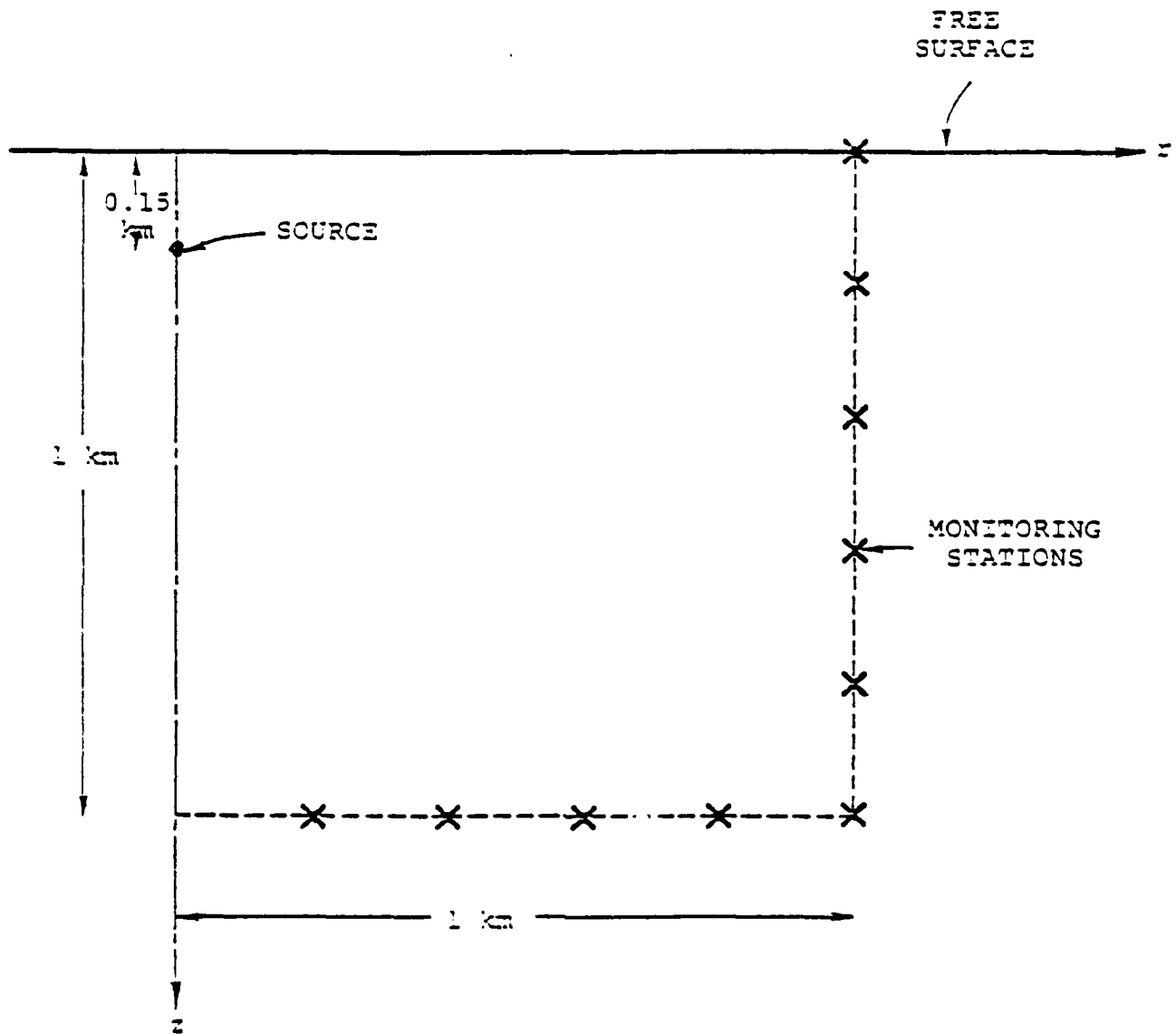
177

Figure A.3. The geometry for the generalized ray theory calculation for a spherically symmetric explosion in a halfspace.

173

$$\hat{\Psi}(\omega) = \frac{\hat{P}(\omega)\ R_e^3}{\mu}\ \frac{\alpha^2}{4\alpha^2 + 4i\omega\alpha R_e - \alpha^2\omega^2 R_e^2\ /\beta^2} \qquad\qquad (A.14)$$

where $P(\omega)$ is the transformed pressure time history. Fixing $P(\omega)$ and R_e, the simple scaling is obtained.

In Figure A.4 we compare the surface wave computed with this method with the exact solution for two propagation media. The first is the elastic halfspace of the source calculation with $Q_\beta = 50$. The second comparison is for a realistic earth model. Bache, et. al., (1978), pointed out that there is often a need to account for the material properties in the immediate source vicinity being different from the average properties along the travel path and presented an approximate techniques for accounting for this difference. An analogous approach was used for the second comparison in Figure A.4. The source region was represented by the NTS/TUC model of Bache, et al., with the top two kilometers replaced by a layer with $\alpha = 3.5$ km/sec, $\beta = 1.75$ km/sec, $\rho = 2.0$ gm/cm^3. The monitored solutions were scaled to be appropriate for this material. Then the source excitation terms in the Green's functions were computed with this modified structure, while the Hankel functions representing the propagation were comput⁺ with the phase velocities for the original NTS/TUC model. The transition between the source region and propagation path models was accounted for by the transmission coefficient

$$T(\omega) = \left(\frac{C_2\ A_{R_2}}{C_1\ A_{R_1}}\right)^{1/2}\qquad , \qquad\qquad (A.15)$$

where subscripts 1 and 2 represent the source and propagation models, respectively.

The exact seismograms are in very close agreement with those from the wavefield continuation method. In Figure A.5 we compare
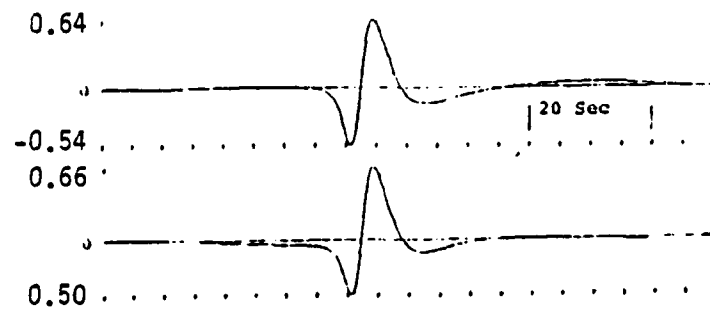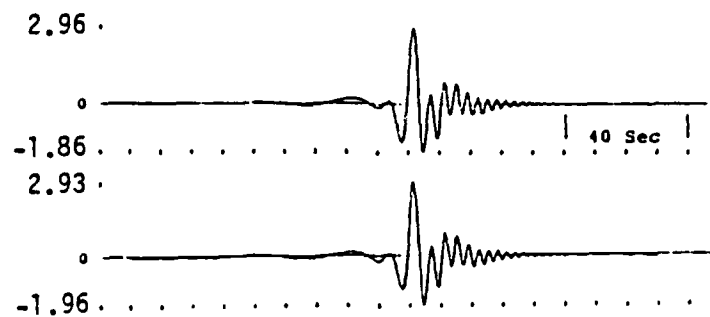
Figure A.4. Comparison of exact (top) seismograms with those computed with the wavefield continuation method. The numbers at the left are peak amplitudes in microns. The range was 1,000 km for the halfspace and 728 km for the NTS/TUC example. The seismograms were filtered by the WWSSN 15-100 instrument response.

130

the two in the frequency domain. We see that the errors are less than 10% over the entire band from 0.5 to 40 seconds. After scaling the halfspace comparison to the source material of the NTS/TUC model, the ratio for the two cases is nearly the same for periods less than 10 seconds. At longer periods the contributions from the integrations (A.5.) along the side and bottom of the cylindrical monitoring surface have opposite sign and are nearly the same size. Then small errors in the static values of the monitored solutions (which were only carried out to 1 second) are weighted by different Green's functions for the two cases, leading to different errors. At shorter periods the primary reasons the exact and wavefield continuation solutions diverge are inaccuracies in the monitored solutions and the lack of resolution of the sparse spatial sampling.

A test problem more closely related to the ultimate problems of interest was done with the SWIS finite element program (Frazier and Peterson, 1974) using the geometry shown in Figure A.6. The grid dimensions were 50 by 50 meters. An exact simulation of an explosion source requires application of a pressure to the surface of a spherical cavity. However, in this geometry it was more convenient to apply the pressure inside a cylindrical cavity with 50 meter radius and height. The stresses and displacements were monitored at the indicated 20 stations and were convolved with the reduced displacement potential of Figure A.2. The amplitudes were normalized by requiring the product of cavity pressure and volume for the cylindrical cavity to be the same as for a spherical cavity consistent with the reduced displacement potential.

The seismograms for the $\alpha = 6.0$ km/sec halfspace are compared in Figure A.6. The spectral comparison is also shown. The comparison is done for a solution using all twenty monitoring stations and for one with alternate modes discarded. With 20 stations, the errors are less than 10 percent from 40 seconds to 0.3 seconds, but the errors are much larger at long periods with fewer stations.

181
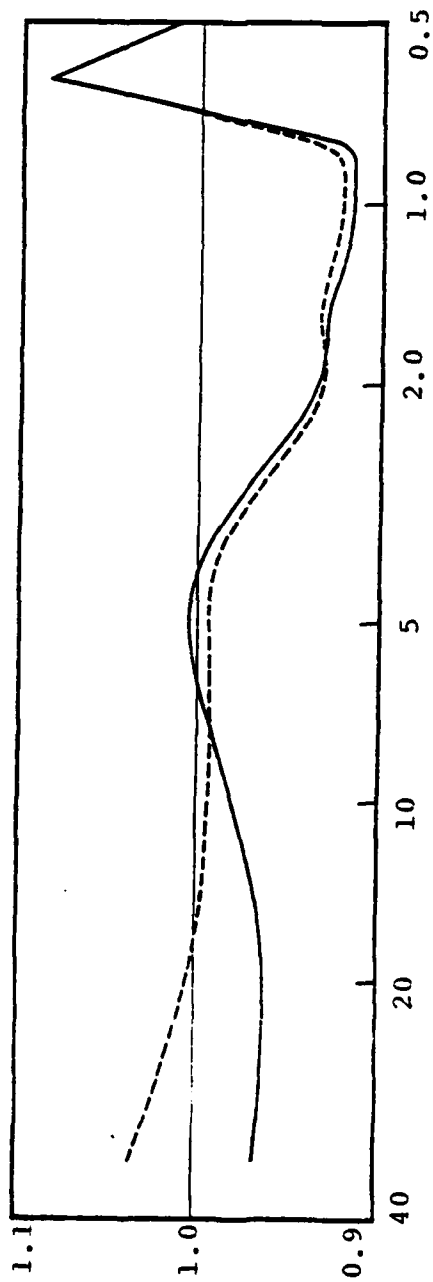
Figure A.5. The seismograms of Figure A.4 are compared via the spectral ratio (wavefield continuation/exact). The solid line is for the halfspace (α = 6.0 km/sec) comparison. This ratio has been scaled to the material of the source layer (α = 3.5 km/sec) for the NTS/TUC comparison by doubling the period.
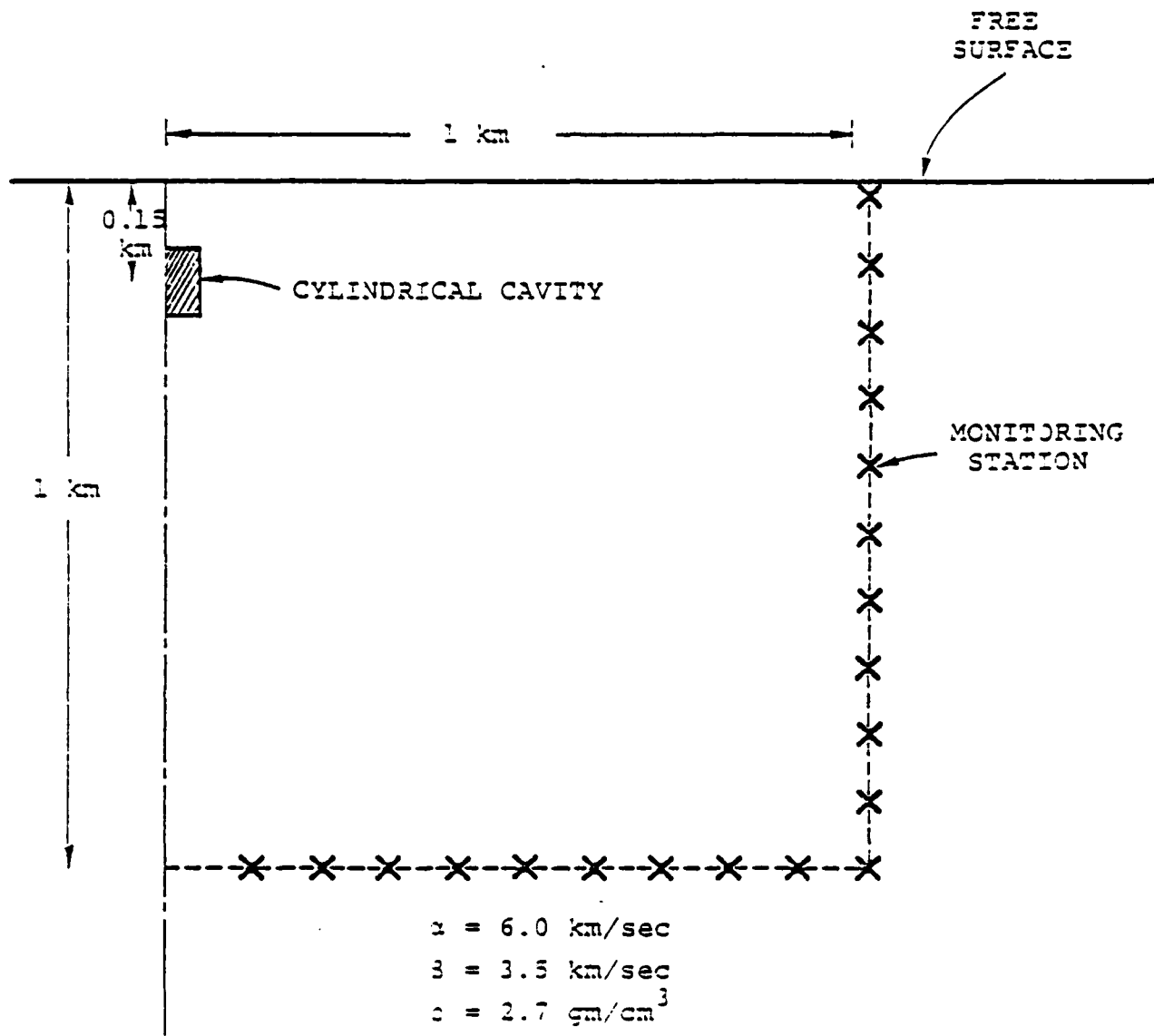
Figure A.6. Schematic view of the axisymmetric grid for the SWIS calculation. The twenty monitoring solutions are indicated.

The figure contains the following labels and values:

- FREE SURFACE
- 1 km (horizontal dimension)
- 0.15 km
- CYLINDRICAL CAVITY
- 1 km (vertical dimension)
- MONITORING STATION

$\alpha = 6.0$ km/sec
$\beta = 3.5$ km/sec
$\rho = 2.7$ gm/cm^3

183

Figure A.7. Temporal and spectral ratio comparison of exact and analytically continued halfspace Rayleigh waves after propagation to 1000 km and filtering by the WWSSN 15-100 instrument response.

A.5   ANALYSIS OF THE LONG PERIOD SOLUTION

The test problems presented in the previous section demonstrate that the technique is quite accurate over most of the period range of interest. However, at long periods the errors can be fairly large, even for these ideal test problems where the late time values of the monitored solutions are defined with considerable accuracy.

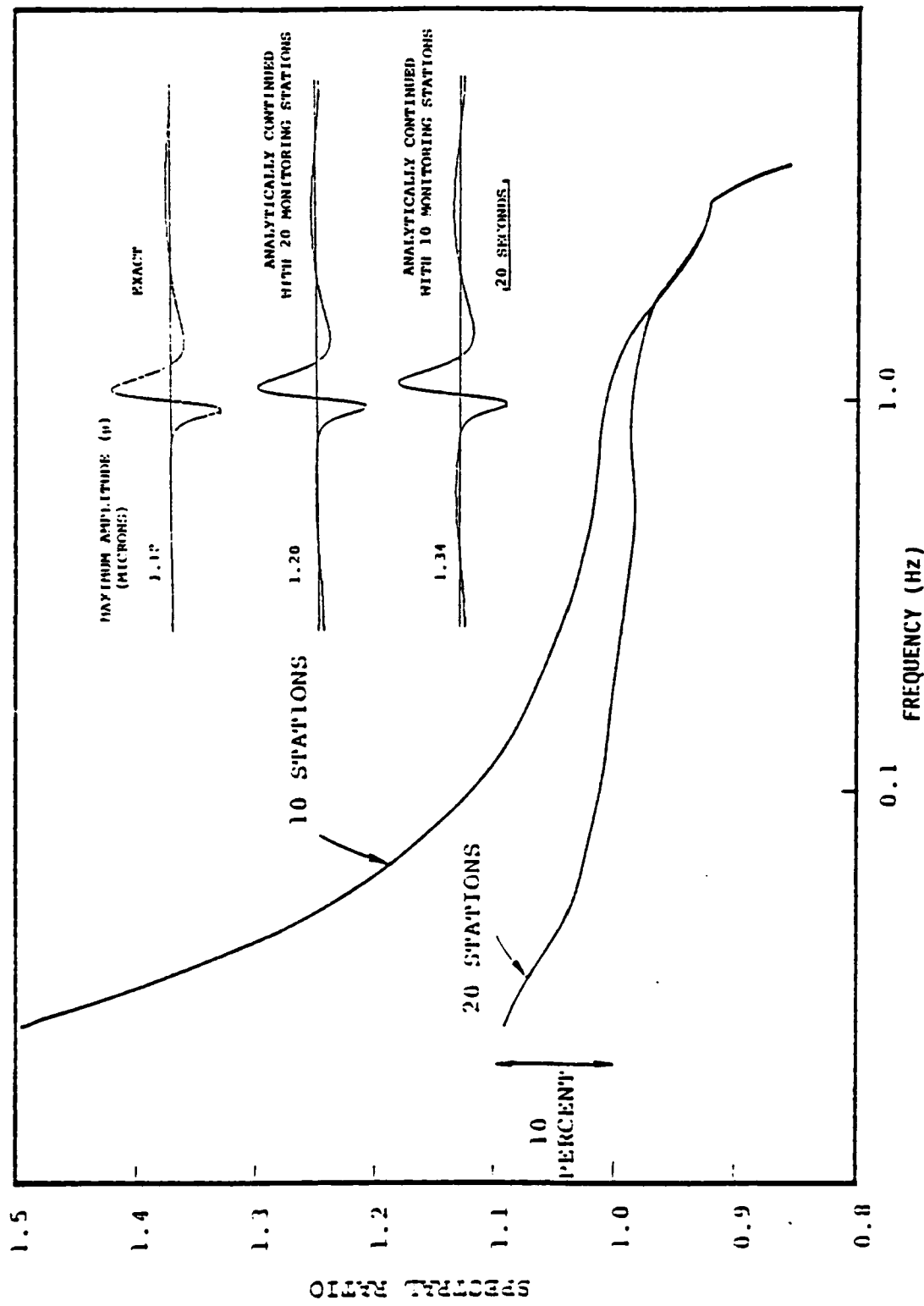In the highly nonlinear complex source calculations of practical interest it is usually impossible to continue until motions entirely cease at the monitoring surface. These calculations generally must be terminated after a few seconds when the motions are small, but finite. Therefore, the static stresses and displacements, which are what determine the solution at periods much larger than the duration of the calculation, will not be determined with great precision.

The test problems were done on a sparse spatial grid and much of the long period error may be attributed to inaccurate spatial quadratures (Figure A.7). This inaccuracy can be nearly eliminated by monitoring at each node in the discrete grid of the source calculation. A more serious concern is with the effect of errors in the computed static solutions, which are generally the values of the monitored quantities at the last time step.

Let us examine the low frequency limit of the vertical Rayleigh wave for axisymmetric problems. Assume that the monitoring surface is a cylinder of radius a and depth b. The monitored stresses and displacements are assumed to reach some static value. In this case their transforms

$$\hat{\sigma}_{zz}^M, \quad \hat{\sigma}_{rz}^M, \quad \hat{u}_z^M, \quad \hat{u}_r^M,$$

are proportional to ω^{-1} at low frequency. Then with some algebra it can be shown that

185

$$\lim_{\omega \to 0} \hat{u}_z^F(r) = -i\pi \underset{\approx}{A}_R H_0^{(2)}(kr) \Bigg\{ \Bigg[\int_0^a \hat{\sigma}_{zz}^M(r,b)\, r_0\, dr_0$$

$$+ \int_0^b a\, \hat{\sigma}_{zr}^M(a,z)\, dz \Bigg]$$

$$- k\, \epsilon_0 \quad b\left(\frac{2\beta^2}{\alpha^2} - 1 \right) \int_0^a \hat{\sigma}_{zz}^M\, r_0\, dr_0$$

$$- \frac{k}{2}\, \epsilon_0 \qquad \int_0^a r_0^2\, \hat{\sigma}_{zr}^M\, dr_0 \qquad\qquad (A.16)$$

$$+ k\, \epsilon_0 \quad a \int_0^b \Bigg[\frac{\mu(3\lambda + 2\mu)}{\lambda + 2\mu}\, \hat{u}_r^M - \frac{a}{2}\, \hat{\sigma}_{rr}^M$$

$$- z\left(\frac{2\beta^2}{\alpha^2} - 1 \right) \hat{\sigma}_{zr}^M \Bigg]\, dz \Bigg\} + 0\left[\omega^2 \right],$$

where all temporal quantities have been Fourier transformed and depend on ω. The λ, μ are the Lamé constants.

The first two terms in the brackets are simply the applied vertical force, $\hat{F}_z(\omega)$. That is,

$$\hat{F}_z(\omega) = \int_0^a \hat{\sigma}_{zz}^M(r_0,b)\, r_0\, dr_0 + \int_0^b a\, \hat{\sigma}_{zr}(a,z)\, dz \, .(A.17)$$

For most source calculations the medium is initially at rest and o external or body forces are applied (the effect of gravity can be subtracted from the monitored solutions). If so, conservation of
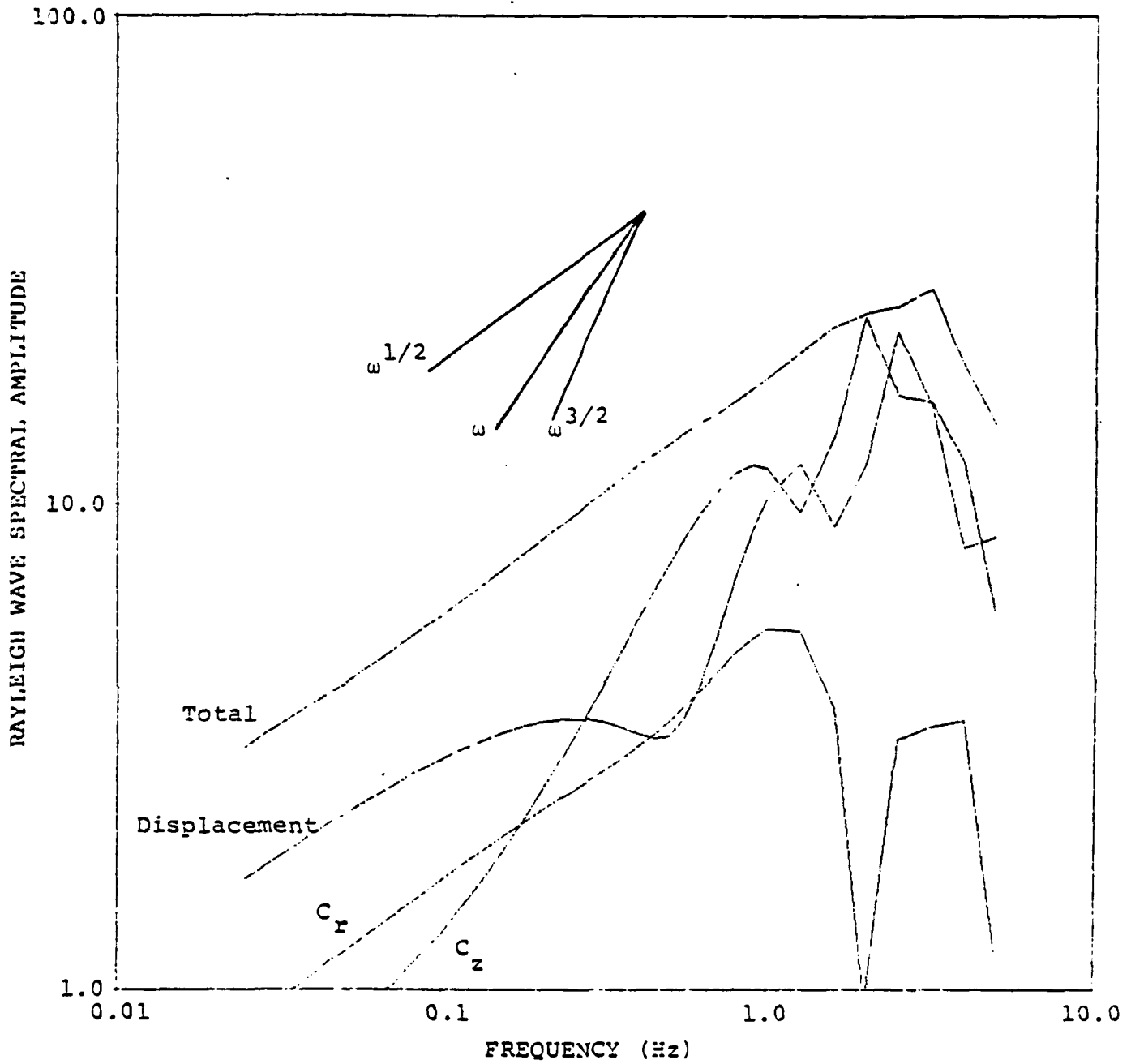
186

Figure A.8. The Rayleigh wave spectral amplitude for the halfspace
example of Figure A.4 is plotted together with the con-
tributions from the monitored displacements, the stresses
associated with vertical tractions (C_z), and the stresses
associated with radial tractions (C_r).

187

linear momentum requires that the vertical force and the vertical impulse vanish at static equilibrium. That is,

$$\lim_{t \to \infty} F_z(t) = 0 \quad ,$$

$$\lim_{t \to \infty} I_z(t) = \lim_{t \to \infty} \int_0^t F_z(\tau) \, d\tau = 0.$$

Then the $\hat{F}_z(\omega)$ terms in (A.16) are proportional to ω at low frequency while all other terms are $O(1)$.

Also, if $F_z(t)$ approaches zero, but $I_z(t)$ does not, then the terms proportional to $\hat{F}_z(\omega)$ in (A.16) are the same order as the others. Further, if $F_z(t) \neq 0$ at late time, this contribution is proportional to $1/\omega$ and dominates the low frequency solution.

When (A.18) is satisfied, the low frequency limit is

$$\lim_{\omega \to 0} \hat{u}_z^F(r) = - i\pi \underset{\approx}{A}_R H_0^{(2)}(kr) \, k \quad \epsilon_0 \left\{ - b \left(\frac{2\beta^2}{\alpha^2} - 1 \right) \int_0^a \hat{\alpha}_{zz}^M \, r_0 \, dr_0 \right.$$

$$\left. + \int_0^a \frac{r_0^2}{2} \hat{\sigma}_{zr}^M \, dr_0 + \int_0^b a \left[\frac{\mu(3\lambda + 2\mu)}{\lambda + 2\mu} \hat{u}_r^M - \frac{a}{2} \hat{\sigma}_{rr}^M - z \left(\frac{2\beta^2}{\alpha^2} - 1 \right) \hat{\sigma}_{zr}^M \right] dz \right\}$$

$$(A.19)$$

Interpretation of this result is more convenient when it is written in terms of tractions, $\hat{T}_r^M$, $\hat{T}_z^M$, instead of stresses and for a monitoring surface of arbitrary shape. Then

$$\hat{F}_z(\omega) = \int_S \hat{T}_z^M(r,z) \, dA \quad , \tag{A.20}$$

188

and (A.19) becomes

$$\lim_{\omega \to 0} \hat{u}_z^F(r) = i \, k \, \pi \, \underset{\sim}{A}_R \, H_0^{(2)}(kr) \; \varepsilon_0 \, \left(\frac{2\beta^2}{\alpha^2} - 1 \right) \int_S z \, \hat{T}_z^M(r,z) \, dA$$

$$+ \int_S \frac{r_0}{2} \, \hat{T}_r^M(r,z) \, dA - \frac{\mu(3\lambda + 2\mu)}{(\lambda + 2\mu)} \int_S r_0 \, \hat{u}_r^M(r,z) \, n_r \, dA \Bigg\} .$$

$$(A.21)$$

Thus, the low frequency behavior of the solution depends only on the vertical and radial tractions and the radial displacements.

As an illustration of the relative importance of the various terms comprising the solution, we examine the halfspace example of Figure A.4. The Rayleigh wave spectral amplitude (before application of the filters for the Q and seismometer) is plotted in Figure A.8 together with the spectra for three contributions that make up the total solution. In this example the displacement contributions dominate at long periods and the radial traction terms are relatively small over the whole frequency band. However, the relative importance of these terms is dependent on details of the problem at hand.

THIS PAGE LEFT BLANK

APPENDIX B

AN "EQUIVALENT" POINT SOURCE FOR COMPLEX SOURCE CALCULATIONS

The method described in Appendix A provides a means for computing the synthetic seismograms from the output of complex source calculations. Such seismograms include both source and path effects. It would be useful to isolate the source effects to the extent possible. One way to do this is to compare two seismograms computed with a simple source and the same path. Differences between the two are then due to differences in the source.

For axisymmetric explosion calculations, the interesting comparison is to a spherical point source representation for the explosion. Let the source function for such an explosion be the reduced velocity potential (ω). Then the Rayleigh waves for this explosion may be written (e.g., Bache, Rodi and Harkrider, 1978),

$$\hat{W}_{EX} = P(r,\omega) \; \hat{\psi} \tag{B.1}$$

where $P(r,\omega)$ represents the path effects. Similarly, the Rayleigh waves computed with the wave field continuation method may be written

$$\hat{W}_{AC} = P(r,\omega) \; \hat{\psi}_e \quad , \tag{B.2}$$

where $\hat{\psi}_e$ represents some "equivalent RDP" representation for the complex source calculation. We have

$$\hat{\psi}_e = \frac{\hat{W}_{AC}}{\hat{W}_{EX}} \quad \hat{\psi} \quad . \tag{B.3}$$

As an example, consider the test problem of Figure A.3. The $|\hat{\psi}|$ for this calculation was plotted in Figure A.2 and ratio $\hat{W}_{AC}/\hat{W}_{EX}$ appears in Figure A.5. In Figure B.1 we show the $|\hat{\psi}|$ and $|\hat{\psi}_e|$ for this comparison. If there were no numerical errors, the two would

191

be identical. On the other hand, if $\hat{w}_{EX}$ had been computed with $\hat{\Psi}$ at a different depth than the 0.15 kilometer depth used for computing the monitoring solutions, we would expect the $\hat{\Psi}_e$ to be much less close to $\hat{\Psi}$.

In analyzing nonlinear axisymmetric finite difference calculations of explosions, we would like to compare the $\hat{w}_{AC}$ to $\hat{w}_{EX}$ computed with a $\hat{\Psi}$ from a one-dimensional calculation in the same material. The differences between the two are then precisely those differences caused by two-dimensional effects.
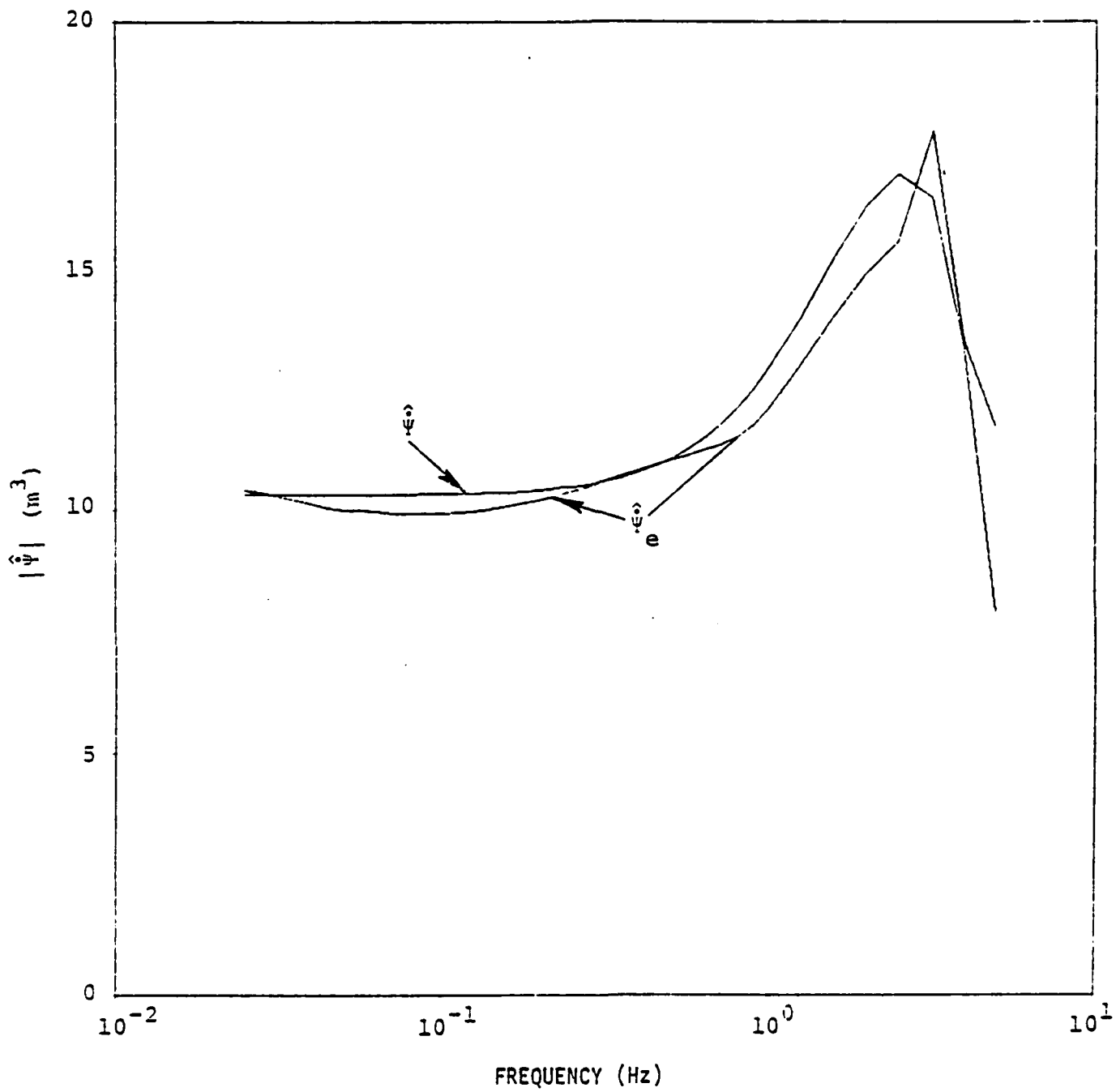
192

Figure B.1. Comparison of the exact source function ($\hat{\overset{\circ}{\psi}}$) with the "equivalent RDP" computed from (B.3.).

193